



IPP Summer University for Plasma Physics



September 14 – September 18, 2015
Garching, Germany

Edited by Roberto Bilato

Contributions from:

C. Angioni, R. Bilato, V. Bobkov, D. Breitschwerdt, R. Dux, T. Eich, C. Hopf, O. Maj, R. McDermott, J. Meyer-ter-Vehn, R. Pitts, E. Poli, T. Pütterich, H.M. Smith, E. Sonnendrücker, R. Stieglitz, W. Suttrop, U. v. Toussaint, T. Windisch

List of speakers

© Copyright by the authors.

- Prof. Dr. Dieter Breitschwerdt TU Berlin
Zentrum für Astronomie und Astrophysik
Hardenbergstr. 36
D-10623 Berlin
- Prof. Dr. Jürgen Meyer-ter-Vehn Max-Planck-Institut für Quantenoptik
Abteilung für Attosekundenphysik
Hans-Kopfermann-Str. 1
D-85748 Garching
- Prof. Dr. Richard Pitts ITER Organization
Building Headquarters
Route de Vinon - CS90046
F-13067 Saint Paul Lez Durance

- Dr. Clemente Angioni Max-Planck-Institut für Plasmaphysik
- Dr. Roberto Bilato Boltzmannstr. 2
- Dr. Volodymyr Bobkov D-85748 Garching
- Dr. Ralph Dux
- Dr. Thomas Eich
- Dr. Christian Hopf
- Dr. Omar Maj
- Dr. Rachael McDermott
- Dr. Emanuele Poli
- Dr. Thomas Pütterich
- Prof. Dr. Eric Sonnendrücker
- Dr. Wolfgang Suttrop
- Dr. Udo von Toussaint

- Dr. Håkan M. Smith Max-Planck-Institut für Plasmaphysik
- Dr. Thomas Windisch Wendelsteinstr. 1
D-17491 Greifswald

Cover page:

The experiment ASDEX-Upgrade in Garching.

Contents

1 Basic plasma physics	13
Monika Bessenrodt-Weberpals, Hugo de Blank, Axel Könies, Emanuele Poli, Ralf Schneider	
1.1 Introduction	13
1.2 Types of plasmas	15
1.2.1 Astrophysical plasmas	15
1.2.2 Laboratory plasmas	15
1.3 Plasma parameters	16
1.3.1 Ionization	16
1.3.2 Degeneracy and thermal wave length	16
1.3.3 Relativistic effects	17
1.3.4 Ideal and non-ideal plasmas	17
1.4 Plasma fundamentals	18
1.4.1 Quasi-neutrality	18
1.4.2 Plasma frequency	18
1.4.3 Debye shielding	19
1.5 Particle collisions	20
1.5.1 Coulomb collisions and Rutherford scattering	20
1.6 Electric resistivity	23
1.7 Motion of charged particles in electromagnetic fields	24
1.7.1 Homogeneous magnetic field	24
1.7.2 Motion in a constant magnetic field due to an additional force	26
1.7.3 $E \times B$ drift, gravitational drift	27
1.7.4 Particle drift in inhomogeneous magnetic fields	27
1.7.5 The guiding centre equations in general geometry	28
1.8 Adiabatic invariants	30

2 Basic nuclear fusion 35

Hans-Stephan Bosch

2.1	Introduction	35
2.2	Energy production on the sun	37
2.3	Fusion on earth	38
2.4	Thermonuclear fusion	40
2.5	Ignition	43
2.6	Magnetic confinement	44
2.6.1	The stellarator	46
2.6.2	The tokamak	47
2.6.3	The fusion reactor	47
2.7	Muon-catalyzed fusion	47

3 An introduction to MHD 51

Bruce D. Scott

3.1	What MHD is	51
3.2	The ideas of fluid dynamics	52
3.2.1	The density in a changing flow field – conservation of particles	52
3.2.2	The advective derivative and the co-moving reference frame	54
3.2.3	Forces on the fluid – how the velocity changes	55
3.2.4	Thermodynamics of an ideal fluid – how the temperature changes	56
3.2.5	The composite fluid plasma system	57
3.3	From many to one – the MHD system	58
3.3.1	The MHD force equation	59
3.3.2	Treating several ion species	59
3.3.3	The MHD kinematic equation	60
3.3.4	MHD at a glance	61
3.4	The flux conservation theorem of ideal MHD	61
3.4.1	Proving flux conservation	61
3.4.2	Magnetic flux tubes	63
3.5	Dynamics, or the wires-in-Molasses picture of MHD	63

<i>CONTENTS</i>	7
3.5.1	Magnetic pressure waves 64
3.5.2	Alfvén waves: magnetic tension waves 65
3.6	The validity of MHD 67
3.6.1	Characteristic time scales of MHD 67
3.6.2	Checking the assumptions 68
3.6.3	A comment on the plasma beta 69
3.7	Parallel dynamics 69
3.8	Towards multi-fluid MHD 71
4	Kinetic theory 73
Emanuele Poli	
4.1	Introduction 73
4.2	The kinetic equation for a plasma 74
4.3	Markovian processes and the Fokker-Planck equation 75
4.4	Landau damping 76
4.5	The Fokker-Planck collision operator 81
5	Plasma Waves and Wave Heating 89
Volodymyr Bobkov	
5.1	Introduction 89
5.2	Wave propagation in cold plasma 91
5.3	Aspects of wave absorption (damping) 94
5.4	Heating in the ion cyclotron range of frequencies 95
5.5	Lower hybrid heating 98
5.6	Electron cyclotron resonance heating 99
5.7	Non-inductive current drive 101
6	Plasma heating: neutral beam injection 103
Christian Hopf, Ursel Fantz, Peter Franzen	
6.1	Introduction 103
6.2	Neutral beam heating physics and current drive 104
6.2.1	Beam ionization 105

6.2.2	Fast ion orbits and orbit losses	107
6.2.3	Slowing down	108
6.2.4	Particle losses	109
6.2.5	Neutral beam current drive (NBCD)	109
6.3	Neutral beam injection systems	111
6.3.1	Generation of the ion beam	112
6.3.2	Neutralization	117
6.3.3	Beam transport	118
6.4	NBI systems based on negative ions	119
6.4.1	Generation of negative hydrogen ions	120
6.4.2	Co-extraction of electrons	123
6.4.3	Wall plug efficiency and neutralization efficiency	123
6.4.4	Development of a negative-ion-based system for ITER	124
7	Plasma wall interaction	129
	Karl Krieger	
7.1	Overview	129
7.1.1	Plasma facing components	130
7.1.2	Bombardment of the walls with plasma particles	130
7.2	The scrape-off layer	131
7.3	Electric coupling of plasma and wall	132
7.4	Hydrogen fuel cycle	133
7.4.1	Reflection	134
7.4.2	Implantation, diffusion and reemission	134
7.5	Impurity production	136
7.5.1	Sputtering	136
7.5.2	Chemical erosion	138
7.5.3	Sublimation, evaporation	139
7.5.4	Desorption	139
7.5.5	Arcing and melting	140
7.5.6	Positive and negative aspects of impurity contamination	140
7.6	Diagnostics for plasma surface interaction	141
7.6.1	In situ diagnostics	141
7.6.2	Laboratory experiments	142

8 Introduction to plasma diagnostics 145

Hans-Jürgen Hartfuß

8.1	Introduction	145
8.2	Categorization	146
8.3	Sightlines	146
8.4	Magnetic diagnostics	147
8.4.1	Rogowski-coil	147
8.4.2	Voltage-loop	148
8.4.3	Diamagnetic-loop	148
8.5	Wave diagnostics	149
8.5.1	Active wave measurements	149
8.5.2	Passive wave measurements	153
8.6	Particle diagnostics	157
8.6.1	Active particle diagnostics	157
8.6.2	Passive particle diagnostics	159
8.7	Langmuir-probes	160
8.8	Summarizing remarks	161

9 Computational plasma physics 163

Eric Sonnendrücker

9.1	Introduction	163
9.2	From a physics problem to a computer code	164
9.3	The Vlasov-Poisson system	165
9.3.1	General features	165
9.3.2	Conservation properties	165
9.4	Linear advection	166
9.4.1	Obtaining a Finite Difference scheme	166
9.4.2	Some classical Finite Difference discretisations	167
9.4.3	Convergence of finite difference schemes	168
9.4.4	Von Neumann stability analysis	170
9.4.5	High-order time schemes	174

9.5	Spectral solution of the Poisson equation	176
9.6	A semi-Lagrangian method for the Vlasov equation	178
9.7	Verification of the 1D Vlasov-Poisson code	181
9.7.1	Test of the field solver	181
9.7.2	Test of the Vlasov solver with a given advection field	181
9.7.3	Comparison with the linearised Vlasov-Poisson system	182
10	Tokamaks: equilibrium, stability and transport	191
	Hartmut Zohm	
10.1	Introduction	191
10.2	Plasma equilibrium	191
10.2.1	The steady state MHD-equations	191
10.2.2	Equilibrium in the linear pinch	192
10.2.3	The Grad-Shafranov equation	194
10.2.4	The tokamak	195
10.3	Stability of an equilibrium state	196
10.3.1	Methods of stability analysis	196
10.3.2	Classification of instabilities	197
10.3.3	Examples	198
10.4	Transport in a fusion plasma	200
10.4.1	Transport equations	200
10.4.2	Transport coefficients	200
11	Experimental results from tokamaks	205
	Wolfgang Suttrop	
11.1	Tokamak plasmas	205
11.1.1	The tokamak principle	205
11.1.2	Components of a tokamak	207
11.1.3	Divertor tokamaks	207
11.1.4	Magnetic configuration	209
11.1.5	Plasma heating	211

<i>CONTENTS</i>	11
11.1.6 Anatomy of a tokamak plasma	212
11.2 Experimental results	213
11.2.1 Confinement and transport	213
11.2.2 Confinement improvement	216
11.2.3 Stability and operational limits	220
11.3 Summary and outlook	226
12 Introduction to stellarator theory	229
Ralf Kleiber, Håkan Smith	
12.1 Introduction	229
12.1.1 Some history	229
12.1.2 Some basic notions	230
12.1.3 Tokamak, stellarator	230
12.1.4 Coil system	233
12.2 Equilibrium	234
12.2.1 Equilibrium equations	234
12.2.2 Straight stellarator	234
12.2.3 Magnetic coordinates	234
12.2.4 Magnetic islands	235
12.2.5 3D equilibrium codes	238
12.3 Pfirsch-Schlüter current	239
12.4 Neoclassical transport	240
12.4.1 Neoclassical transport	240
12.4.2 Quasi symmetry	244
12.5 MHD stability	245
12.6 Stellarator optimisation	247
13 Stellarator experiments	251
Thomas Windisch	
13.1 Introduction	251
13.2 Stellarator concepts	254

13.3	Equilibrium	257
13.3.1	Vacuum magnetic field	257
13.3.2	Plasma Equilibrium and MHD stability	258
13.4	Neoclassical transport	261
13.5	Confinement	264
13.5.1	Impurity transport and divertor concepts	267
13.6	Helical reactor concepts	270
13.7	Summary	271
14	Safety and environmental aspects of fusion	273
Hans-Werner Bartels		
14.1	Introduction	273
14.2	Inventories	273
14.3	Normal operation effluents	278
14.4	Accidents	279
14.5	Waste management	283
14.6	Conclusion	284
15	Dense plasma with intense ion and laser beams	285
M. Roth*, A. Blazevic ^o , N.A. Tahir ^o , D.H.H. Hoffmann* G. Schaumann*, M. Schollmeier*, S. Udrea*, D. Varentsov ^o		
15.1	Introduction	286
15.2	Accelerator and laser facilities at GSI-Darmstadt	286
15.3	High energy density physics	288
15.4	Interaction of heavy ion beams with plasmas	290
15.5	Application to inertial fusion energy	293
15.5.1	Basic issues of ICF target development for heavy ion beams	295
15.5.2	Physics of dense plasmas and fast ignition	297
15.5.3	Ultra-intense lasers	297
15.5.4	Ion acceleration	297
15.5.5	Fast ignition	298
15.5.6	Conclusion	300

Chapter 1

Basic plasma physics

*Monika Bessenrodt-Weberpals,
Hugo de Blank, Axel Könies,
Emanuele Poli, Ralf Schneider*

1.1 Introduction

A plasma is a hot gas consisting of charged and neutral particles which exhibit collective behaviour [1, 2, 3, 4, 5, 6, 7, 8, 9, 10, 11, 12, 13].

The name *plasma* goes back to Langmuir (1929) who discovered electromagnetic oscillations in rarefied gases which he called *plasma oscillations*.

The plasma is often referred to as the fourth state of matter (solid – liquid – gas – plasma). This concept arises from a thermodynamic description but is not completely rigorous. The variation of the basic macroscopic physical quantities like density n and temperature T determines the properties of the matter in the plasma state (see Fig. 1.1). However, the transition from the liquid, gaseous or solid state into the plasma state is not abrupt but continuous. In a gas, for example, more and more of the atoms become ionized with rising temperature and a plasma forms.

We know now that 99% of the matter in the universe is in the plasma state. Plasma can be found in the interior of the stars as well as in the interstellar space and in the core of the planets. Plasma also occurs in gas discharges (*neon light*, lightning) as part of our daily life.

The transition from weakly interacting neutral particles to charged particles which interact over the long-range Coulomb force may alter the properties of the particle system considerably. Therefore, many-body interaction plays an important role. The possible charge separation gives rise to electromagnetic oscillations or waves in a plasma.

Note that today the term plasma is understood in a very broad sense and may be applied to all systems which consist of charged particles as e.g. electrons in a solid or, even more general,

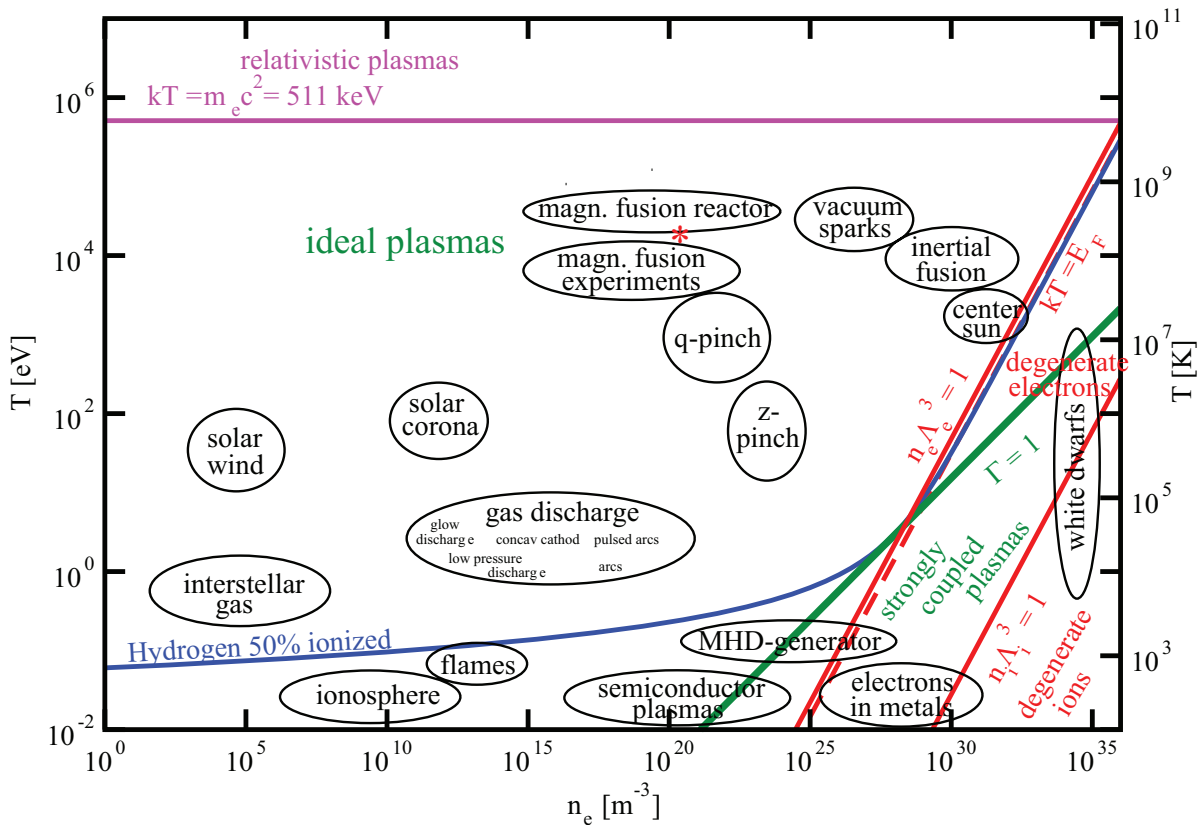


Figure 1.1: Temperatures and densities of astrophysical and laboratory plasmas. The asterisk indicates the fusion relevant parameters used in the examples: $T = 10^4$ eV, $n_e = 10^{20}$ m $^{-3}$, $B = 5$ T.

systems where the bound states of the constituents are broken. The quark-gluon-plasma with its *color* charged constituents, occurring shortly after big bang or at high energy nucleus-nucleus collisions, is a famous example for this concept.

In the course of these lessons we will focus on plasmas made up of ions and electrons which interact over the Coulomb force and which are globally neutral. In this Chapter, we will briefly discuss the types of plasmas in the next section. Then, we go over to the plasma parameters which provide a more quantitative access to the several types of plasmas shown in Fig. 1.1. We will discuss the fundamental concepts of plasma physics, namely the Debye screening, the plasma frequency and the so-called quasi-neutrality. Further we will touch plasma collisions and we will end the lecture discussing the plasma motion in a magnetic field which is of paramount importance for plasmas in magnetic fusion devices.

Finally, appendix A reports some characteristic plasma parameters and their numerical values for typical fusion plasmas ($T = 10^4$ eV, $n_e = 10^{20}$ m $^{-3}$, $B = 5$ T).

1.2 Types of plasmas

1.2.1 Astrophysical plasmas

There are a variety of astrophysical plasmas in nature. They cover a wide range of densities and temperatures. Here, we will mention only a few of them.

The interior of the sun and the stars consists of a very dense and very hot plasma where light atomic nuclei fuse to heavier ones and release the excess of binding energy according to Einstein's famous formula $E = mc^2$, see chap. 2. The plasma density and the plasma temperatures drop the closer one comes to the surface, thus the stellar atmosphere has completely different properties. The solar corona which is even more outside is a dilute magnetized plasma of several million degrees.

The sun emits an extremely dilute supersonic plasma, the solar wind, into its planet system. Near the earth the solar wind has $n_e \approx 5 \text{ cm}^{-3}$ and $T_e = 10^5 \text{ K}$. Because of its high temperature, the plasma has still a high conductivity, see sec. 1.6.

By interaction with the electromagnetic radiation from the sun the atoms of the upper atmosphere become partly ionized. We call this plasma which expands from about 60–2 000 km altitude the ionosphere.

A completely other type of plasmas are the degenerate plasmas within white dwarfs or neutron stars showing extremely high densities and thus behaving differently from the typical ideal plasmas we know from the majority of laboratory plasmas (ideal plasmas are defined below, sec. 1.3.4).

1.2.2 Laboratory plasmas

The tradition of laboratory plasma physics starts with the investigation of the weakly ionized plasmas of flames in the 18th century. Typical applications nowadays are plasma-aided welding and combustion for this type of plasma.

Since the plasma may carry an electric current, plasma discharges of various types are investigated in fundamental research and applied in industry. Low-pressure discharges like glow discharges carry small currents with cold electrodes. They serve for lightening, for gas lasers like the CO₂ laser or the HeNe laser, and for the wide-spread applications of plasma etching and deposition.

High-pressure discharges like arcs may carry larger currents and thereby attain higher temperature. They may also serve for lightening like the well-known high-pressure mercury lamp, for switches, and for plasma-material processing like melting, cutting, and welding.

In order to gain fusion energy in laboratories, high-temperature plasma physics has been started as a classified project around 1950. In 1958, the UN conference on the peaceful use of atomic energy has led to a declassification of fusion research, see chap. 2.

Note that free electrons in metal behave similarly to a high-density, low-temperature plasma (see Fig. 1.1).

1.3 Plasma parameters

To distinguish between different plasma states, let us look at the n - T diagram (see Fig. 1.1). The different physical behaviour is ordered by the four characteristic energies, namely the thermal energy $E_{th} = 3/2k_B T$, the Fermi energy $E_F = (\hbar^2/2m_e) \cdot (3\pi^2 n)^{2/3}$, the electrostatic interaction energy $E_{el} = e^2/(4\pi\epsilon_0 r)$, and the energy of Bohr's ground state $E_I = m_e e^4/(8\epsilon_0^2 \hbar^2)$. For simplicity, we concentrate here on hydrogen with charge $q = e$.

1.3.1 Ionization

First, with $E_{th} \approx E_I$ we can estimate the temperature T_I necessary for ionization from

$$\frac{3}{2}k_B T_I = m_e e^4 / (8\epsilon_0^2 \hbar^2)$$

we get

$$k_B T_I = \frac{m_e e^4}{8\epsilon_0^2 \hbar^2} \cdot 2/3 = 9 \text{ eV} . \quad (1.1)$$

Above this temperature, hydrogen plasmas are partially to fully ionized.

More exactly, the degree of ionization in a plasma in thermodynamic equilibrium is given by the Saha equation [14]

$$\frac{n_z n_e}{n_{z-1}} = 2 \frac{Z_z(T)}{Z_{z-1}(T)} \left(\frac{m_e k_B T}{2\pi\hbar^2} \right)^{3/2} \exp\left(-\frac{E_{I,z}}{k_B T}\right) \quad (1.2)$$

with n_z being the density of the z -th ionization stage and Z_z the corresponding partition function.

From Fig. 1.1, you can read the situation in a hydrogen plasma whose ionization degree is 50%. This shows that the hydrogen plasma is almost completely ionized at $k_B T > 1/10 E_I$. The Saha equation may be applied for low ionization stages and high-density plasmas where collision processes dominate over radiative transitions and thereby determine the equilibrium. For high-ionized atoms like heavy impurities in a fusion plasma, the full set of rate equations has to be solved including both collisional and radiative transitions, see chap. 7.

1.3.2 Degeneracy and thermal wave length

The electrons which are Fermions and thus obey the Pauli principle, have actually to be described by a Fermi distribution of the energy. However, in a wide range of plasma parameters ($E_{th} \gg E_F$) the Maxwell-distribution is an excellent approximation. This is the case for magnetic fusion plasmas, the sun, flames, gas discharges, interstellar plasmas ...

With increasing density or for low temperatures, if the Fermi energy approaches the thermal energy (see Fig. 1.1),

$$k_B T \approx E_F = \frac{\hbar^2}{2m} (3\pi^2 n)^{2/3} .$$

the electron gas becomes more and more degenerate. That means that the quantum statistical behaviour of the electrons does play a role and the Fermi distribution has to be used.

We can express the influence of the quantum character of the particles also using the ratio of the length scales of the thermal (de Broglie) wave length of the particles p

$$\Lambda_p = \frac{h}{\sqrt{2\pi m_p k_B T_p}} \quad (1.3)$$

to their average distance (also called Wigner-Seitz-Radius)

$$r_0 = \left(\frac{4\pi}{3} n \right)^{-1/3}. \quad (1.4)$$

The criterion of non-degeneracy for the particle species p is then given by

$$n_p \Lambda_p^3 \ll 1 \quad (1.5)$$

which is true if the de Broglie wave length is much less than the average particle distance.

1.3.3 Relativistic effects

If the thermal energy of the electrons is of the order of the energy corresponding to the electron rest mass

$$E_{th} \approx m_e c^2$$

at a temperature of approximately 511 keV, we have a relativistic plasma (see Fig. 1.1).

The plasma is called a relativistic degenerate plasma if the Fermi energy is of the order $m_e c^2$.

1.3.4 Ideal and non-ideal plasmas

If the thermal energy of a species of charged particles (e.g. electrons) is much larger than that of their Coulomb interaction, the plasma is called an ideal plasma.

To get a quantitative estimate, let us define the ratio of the Coulomb energy at the average interparticle distance to the thermal energy

$$\Gamma = \frac{Ze^2}{4\pi\epsilon_0 r_0 k_B T}. \quad (1.6)$$

The parameter Γ allows the classification of the degree to which the Coulomb interaction determines the plasma behaviour ($\Gamma \ll 1$ almost ideal, $\Gamma < 1$ weakly non-ideal and $\Gamma > 1$ strongly non-ideal).

The Landau length λ_L is defined as the value of r_0 at which the thermal energy equals the electrostatic energy ($\Gamma = 1$):

$$\lambda_L = \frac{Ze^2}{4\pi\epsilon_0 k_B T}. \quad (1.7)$$

This quantity will reappear in the calculation of the plasma resistivity.

A further parameter may be defined to estimate the particle-particle interaction, namely the ratio of the Landau length and the thermal de Broglie length

$$\xi_p = \sqrt{2\pi} \frac{\lambda_L}{\Lambda_p} = 2 \sqrt{\frac{E_I}{k_B T}}. \quad (1.8)$$

If the plasma parameter ξ is of the order of one then in microscopic scattering processes the quantum mechanical interaction does play an important role and the Born series approximation cannot be applied.

1.4 Plasma fundamentals

1.4.1 Quasi-neutrality

First, let us take a closer look at the electrostatic properties of plasmas. Indeed, plasmas are usually electrically *quasi-neutral*, i.e. local concentrations of charge or external potential are shielded out at a distance which is short compared with the typical system length. A simple estimate shows that a small charge separation causes a large restoring electric field. Consider a non-zero charge density $\rho_E = e(n_i - n_e)$ caused by a small separation x of the electrons from the ions (see Fig. 1.2 left). Application of Poisson's equation $\nabla \cdot \mathbf{E} = \rho_E / \epsilon_0$ yields ($\nabla \cdot \mathbf{E} \approx E/x$)

$$E \approx \frac{n_e e x}{\epsilon_0}. \quad (1.9)$$

A fully ionized plasma at 5 eV and atmospheric pressure has an electron density of $n_e = 6 \times 10^{22} \text{ m}^{-3}$. A charge separation of $x = 1 \text{ mm}$ would lead to a very strong electric field $E = 1 \times 10^{12} \text{ V/m}$ and an electric potential $\phi = 5 \times 10^8 \text{ V}$ over 1 mm. In fact, finite electric fields can be generated by very small deviations of the densities from quasi-neutrality.

1.4.2 Plasma frequency

The strong restoring electric field associated with deviations from quasi-neutrality causes a harmonic oscillation (Langmuir, 1929). In the absence of a magnetic field, electrons react to the electric field of (1.9) with

$$m_e \frac{d^2 x}{dt^2} = -e E = -\frac{n_e e^2 x}{\epsilon_0}.$$

The solution of this equation is an oscillation with the characteristic electron *plasma frequency*

$$\omega_{p,e} = \left(\frac{n_e e^2}{\epsilon_0 m_e} \right)^{1/2}. \quad (1.10)$$

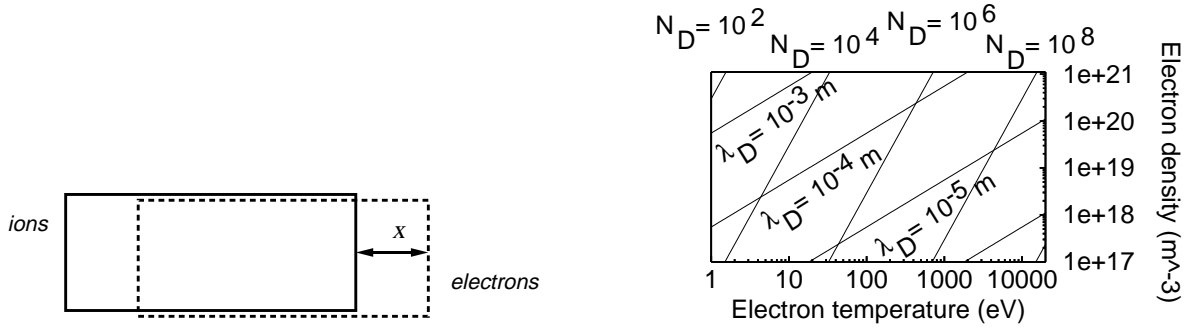


Figure 1.2: Left: Schematic illustration of charge separation in a plasma.

Right: Values of the Debye length λ_D and the plasma parameter N_D plotted against electron temperature and electron density.

The ions do not participate in these oscillations because of their high mass. The plasma frequency is temperature-independent. For typical fusion plasma densities (10^{20} m^{-3}) it is $\nu_{p,e} \approx 100 \text{ GHz}$. Electromagnetic waves with frequencies below $\omega_{p,e}$ cannot propagate in plasmas since their electric fields are screened by the Debye shielding. In this case, the waves are reflected. For larger frequencies, the inertia of the electrons allows the propagation of the waves. This is the reason why metals reflect visible light but not X-rays. The picture becomes more complicated if magnetic fields are present, cf. chap. 5.7. Analogously, the ion plasma frequency is defined as

$$\omega_{p,i} = \left(\frac{n_i Z^2 e^2}{\epsilon_0 m_i} \right)^{1/2} \quad (1.11)$$

and the total plasma frequency

$$\omega_p^2 = \omega_{p,e}^2 + \omega_{p,i}^2. \quad (1.12)$$

1.4.3 Debye shielding

Usually, ions are surrounded by electrons which screen the ion charge. Only at small distances a deviation from charge neutrality may be observed. In the presence of an electric potential ϕ , the electron and ion densities in thermal equilibrium are modified according to Boltzmann's distribution $\sim \exp(-E/k_B T) = \exp[(-mv^2/2 - q\phi)/k_B T]$ with $q = \pm e$. Integration over all velocities yields $\tilde{n}_q = n_q \exp(-q\phi/k_B T_q)$, where n_q are the densities for $\phi = 0$. For small exponents (ideal plasmas!), this can be approximated by $\tilde{n}_q = n_q(1 - q\phi/k_B T_q)$. For singly charged ions, Poisson's equation $\nabla^2 \phi = -\rho_E/\epsilon_0$ in spherical geometry reads

$$\frac{1}{r^2} \frac{d}{dr} \left(r^2 \frac{d\phi}{dr} \right) = \frac{e(\tilde{n}_e - \tilde{n}_i)}{\epsilon_0} = \frac{n_e e^2}{\epsilon_0} \left(\frac{1}{k_B T_e} + \frac{1}{k_B T_i} \right) \phi, \quad (1.13)$$

where the plasma approximation $n_e = n_i$ is used. With the definition of the *Debye length*

$$\lambda_{D,q} = \left(\frac{\epsilon_0 k_B T_q}{n_e e^2} \right)^{1/2}, \quad (1.14)$$

and the total Debye length

$$\lambda_D^{-2} = \lambda_{D,e}^{-2} + \lambda_{D,i}^{-2} \quad (1.15)$$

the solution of (1.13) gives the screened potential

$$\phi(r) = \frac{e}{4\pi\epsilon_0} \frac{\exp(-r/\lambda_D)}{r} \quad (1.16)$$

(the constant derives from assuming that ϕ matches the usual Coulomb potential for $r \rightarrow 0$). The Debye length describes the range of an electric potential inside a plasma, which is much shorter than the range in vacuum.

A more heuristic derivation of the Debye length is the following: Small charge separations arise as a result of thermal fluctuations. In a plasma the thermal energy density of the electrons per degree of freedom is $E_f = (1/2)n_e k_B T$. The electrostatic energy density results from a separation of charge over a length x (see Fig. 1.2 left and (1.9)) as $E_e = (\epsilon_0/2)E^2 = (\epsilon_0/2)(n_e e x / \epsilon_0)^2$. The comparison of E_f and E_e shows that substantial separation of charge can only occur over lengths of up to $x \approx (\epsilon_0 k_B T / n_e e^2)^{1/2}$, which is again the Debye length λ_D given in (1.14).

Averaged over many λ_D , the electron and ion charge densities are equal, i.e. $n_e = n_i$. The thermal electron velocity $v_{th,e} = (3k_B T_e / m)^{1/2}$ is found from (1.10) and (1.14) to be

$$v_{th,e} = \sqrt{3} \lambda_{D,e} \omega_{p,e} .$$

Therefore, $1/\omega_{p,e}$ can be interpreted as the time that a thermal electron needs to pass the Debye length.

The definition of an ideal plasma (see sec. 1.3.4) is equivalent to the call for a large number of particles in a Debye sphere, called the *plasma parameter* N_D

$$N_D = \frac{4}{3}\pi\lambda_D^3 n \gg 1 .$$

1.5 Particle collisions

1.5.1 Coulomb collisions and Rutherford scattering

Collisions in the plasma play an important role for collective effects like e.g. resistivity in the plasma. When an electron collides with a neutral atom, no force is felt until the electron is close to the atom; these collisions are similar to billiard-ball collisions. However, when an electron collides with an ion, the electron is gradually deflected by the long-range Coulomb field of the ion. Nonetheless, an effective cross-section may be derived. We will do it in a classical picture without considering quantum mechanical or relativistic corrections.

We will consider here the scattering of an electron by an ion. Because of the large ratio of ion to electron mass we can assume the ion location in the centre of mass of the two-particle system (see Fig. 1.3 left).

In the absence of Coulomb forces, the electron would have a distance of closest approach called the *impact parameter* ρ .

For the Coulomb interaction of two charges e_1 and e_2 , the potential reads $U(r) = \alpha/r$ with $\alpha = e_1 e_2 / (4\pi\epsilon_0)$.

Following textbooks of theoretical mechanics [17] we introduce cylindrical coordinates and employ the conservation of energy

$$E = \frac{m\dot{r}^2}{2} + \frac{L^2}{2mr^2} + U(r) \quad (1.17)$$

and angular momentum

$$L = mr^2\dot{\phi}. \quad (1.18)$$

Let us assume that the electron has the relative velocity v_∞ if it is at a very large distance from the scattering centre (ion). Then, the (conserved) energy must be equal to $E = mv_\infty^2/2$ and the (conserved) angular momentum $L = m\rho v_\infty$. For very long times the particle should again go to infinity. This allows us to calculate the angle ϕ_0 (see Fig. 1.3) as

$$\phi_0 = \int_{r_{min}}^{\infty} \frac{\rho \frac{dr}{r^2}}{\sqrt{1 - \frac{\rho^2}{r^2} - \frac{2U}{mv_\infty^2}}}. \quad (1.19)$$

The distance of closest approach r_{min} is reached when \dot{r} is zero, i.e. when the kinetic energy of the particle has been converted to energy in the effective potential $U(r) + L^2/(2mr^2)$ ($r = r_{min}$ is a root of the denominator in (1.19)). Integration gives

$$\rho^2 = \frac{\alpha^2}{m^2 v_\infty^4} \cot^2 \frac{\chi}{2} = \rho_0^2 \cot^2 \frac{\chi}{2}, \quad (1.20)$$

with $\chi = \pi - 2\phi_0$, cf. again Fig. 1.3. As we have usually an ensemble of particles which undergo the scattering we define the cross-section σ as

$$d\sigma = \frac{dN}{n}, \quad (1.21)$$

where N shall denote the number of particles being scattered by angles between χ and $\chi + d\chi$, while n is the number of particles per area unit. Assuming a homogeneous beam, we have $dN = n2\pi\rho d\rho$. Expressing this in terms of the solid angle Ω gives

$$d\sigma = \frac{\rho}{\sin \chi} \left| \frac{d\rho}{d\chi} \right| d\Omega. \quad (1.22)$$

Finally, the Rutherford cross-section becomes

$$d\sigma = \left(\frac{\alpha}{2mv_\infty} \right)^2 \frac{d\Omega}{\sin^4(\chi/2)}. \quad (1.23)$$

We can see that the number of collisions with small angles is larger than those of large angles. Furthermore, the value for the cross section diverges for large impact parameters ρ or small angles χ like χ^{-4} with the consequence of an infinite total cross-section. This is due to of the infinite long range of the Coulomb interaction.

From the cross section we can infer an approximate expression for the electron-ion collision time if we define the collision time as the proportionality constant between the initial parallel momentum of the electron and its change during collisions with ions at all possible impact parameters ρ

$$\frac{d}{dt} \langle \Delta p_{\parallel} \rangle = -v_{ei} p_{\parallel} . \quad (1.24)$$

The initial parallel momentum is $p_{\parallel} = p = mv_{\infty}$ while $p_{\parallel}^f = p \cos \chi$, as it can easily be inferred from Fig. 1.3 left. Using trigonometric relations and (1.20) we get

$$\Delta p_{\parallel} = p(\cos \chi - 1) = -2p \frac{1}{1 + \cot^2(\chi/2)} = -2p \frac{1}{1 + (\rho/\rho_0)^2} . \quad (1.25)$$

In the following we will denote v_{∞} by v for brevity. For the net change of momentum per time unit of the electron we have to consider all the ions that the incoming electron can encounter in this time unit

$$\frac{d}{dt} \langle \dots \rangle = 2\pi n_i v \int_0^{\rho_{max}} \rho d\rho \dots . \quad (1.26)$$

The upper limit should actually be taken to be infinity. We will see, however, that the integral diverges for $\rho_{max} \rightarrow \infty$, which is the well known Coulomb divergence due to the r^{-1} dependence of the Coulomb potential. The problem can be cured considering the screening of the particle-particle interaction by the other charges in the system, resulting in the exponentially decaying Debye-potential we have derived in the last section. In a plasma, the typical radius of the interaction is the Debye-length. Therefore, we take this length as the upper cut-off and we obtain

$$\frac{d}{dt} \langle \Delta p_{\parallel} \rangle = -\frac{4\pi n_i}{mv^2} \alpha^2 \frac{1}{2} \left\{ \ln \left| 1 + \left(\frac{\rho_{max}}{\rho_0} \right)^2 \right| \right\} , \quad (1.27)$$

which gives

$$\frac{d}{dt} \langle \Delta p_{\parallel} \rangle \approx -\frac{n_i Z_i^2 e^4}{4\pi \epsilon_0^2 m v^2} \ln \frac{\lambda_D}{\rho_0} = -\frac{n_i Z_i^2 e^4}{4\pi \epsilon_0^2 m v^2} \ln \Lambda , \quad (1.28)$$

if we consider that the Debye length $\rho_{max} = \lambda_D$ is much larger than ρ_0 . The latter condition is true if the number of particles in a Debye sphere is large, i.e. if we have an ideal plasma, see discussion in Sec. 1.3.4. Compare ρ_0 , (1.20), with the Landau length, (1.7). The expression $\ln \Lambda = \ln(\lambda_D/\rho_0)$ is called the Coulomb logarithm.

The cross sections and collision times are fundamental in order to understand the behaviour of the plasma. In the next section we will relate them to the resistivity by very simple physical arguments. Note, however, that the derivation we gave here is heuristic and not rigorous at all. An average over the velocity distribution had actually to be included in the derivation. This is shown in chap. 4.

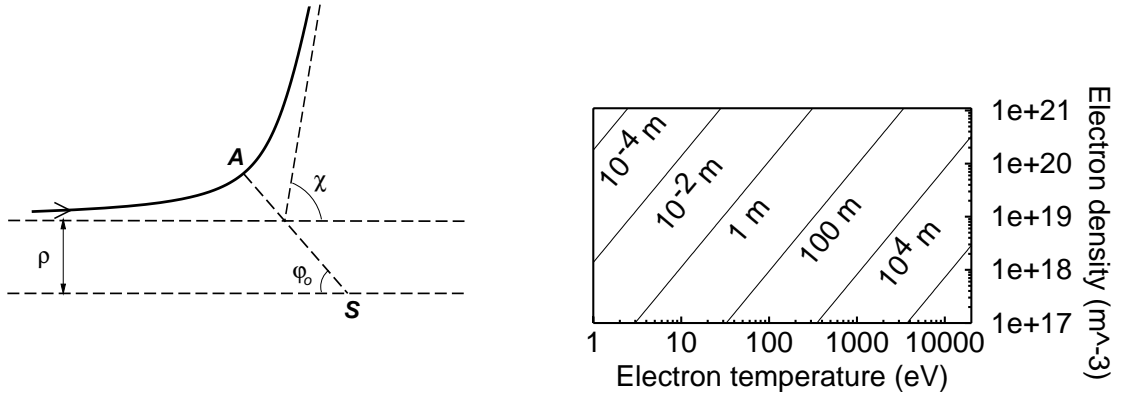


Figure 1.3: Left: Rutherford scattering; S is the centre of mass of the scattering partners. As the Coulomb force is a central force, the orbit is symmetric with respect to A and therefore $\chi = |\pi - 2\phi_0|$.
Right: Values of the mean free path of electrons λ_e plotted against electron temperature and electron density.

The rigorous derivation should start from a kinetic equation. There are a lot of approaches to non-equilibrium processes which give quantum mechanical expressions for cross sections or collision times. These expressions usually include the collective effects like screening which we had to introduce artificially by the cut-off parameter. The expression we have obtained here turns out to be the first order Born approximation of a quantum mechanical cross section. This makes clear that the approximation is valid for high energies of the electron only, i.e. when the thermal energy of a particle is much larger than the Coulomb interaction. Therefore, for non-ideal plasmas the simple classical picture can not be applied and the Coulomb logarithm is a poor approximation.

The collision time for electron-electron collisions follows from comparing (1.24) and (1.28)

$$\tau_{ei} = \frac{4\pi\epsilon_0^2 m_e^2 v_e^3}{Z^2 e^4 n_i \ln \Lambda} . \quad (1.29)$$

From the collision time the mean free path can be calculated as $\lambda_{mfp} = \tau_{ei} v_e$. Fusion plasmas possess a mean free path of about 15 km. This is much larger than the typical laboratory plasma dimensions, leading to the term *collision-less* plasma. The mean free path for fusion reactions is still four orders of magnitude larger at this temperature.

1.6 Electric resistivity

If an electric field is applied to the plasma, the electrons and ions are accelerated in opposite directions. The electrons speed up much faster due to their lighter mass. They deliver the gained energy to the ions by Coulomb collisions, yielding a *resistance* η which, according to Ohm's law, connects the electric field \mathbf{E} with the current density \mathbf{j}

$$\mathbf{E} = \eta \mathbf{j} . \quad (1.30)$$

The net change of electron momentum is supplied by the electric field and by the momentum loss due to collisions

$$\frac{d}{dt} \langle \Delta p_{\parallel} \rangle = -eE - v_{ei} p_{\parallel}. \quad (1.31)$$

Assuming an equilibrium between driving and dissipative forces, the term on the left hand side should vanish. If we further assume that the current is proportional to the relative velocity of electrons and ions $j = -en_e v = -en_e p_{\parallel} / m_e$, we obtain

$$-eE = -\frac{v_{ei} m_e j}{en_e} \quad (1.32)$$

From (1.30) and (1.32) the resistivity is

$$\eta = \frac{v_{ei} m_e}{n_e e^2} \propto T_e^{-3/2}, \quad (1.33)$$

where the temperature dependence follows from the estimate $v_e \sim v_{th} \sim \sqrt{k_B T_e}$ in (1.29). The exact value of the specific resistance was derived in [15] with the help of kinetic theory and the resulting *Spitzer resistivity* is a factor of about two smaller than our first approximation. For $T_e = 1.4$ keV, the plasma resistance is comparable to copper ($1.8 \times 10^{-8} \Omega\text{m}$). Since η is proportional to $T_e^{-3/2}$, fusion plasmas with $T \approx 10$ keV have resistance values which are an order of magnitude smaller than that of copper. The measurement of the resistance can be used to determine plasma temperatures since it depends only very weakly on the density via $\ln \Lambda$ chap. 8. In laboratory plasmas, the effects of different ion species (impurities) on the resistivity often has to be taken into account. For plasmas in strong magnetic fields, additional corrections have to be made to the electrical resistance. The specific resistance η_{\perp} is approximately twice the value of η_{\parallel} .

1.7 Motion of charged particles in electromagnetic fields

Both laboratory and astrophysical plasmas are often immersed in a magnetic field. The motion of a particle with electric charge q and mass m in electric and magnetic fields can be determined from the combined electrostatic and Lorentz force

$$\mathbf{F} = q (\mathbf{E} + \mathbf{v} \times \mathbf{B}).$$

1.7.1 Homogeneous magnetic field

For $E = 0$ and a homogeneous magnetic field, the kinetic particle energy remains constant because the Lorentz force is always perpendicular to the velocity and can thus change only its direction, but not its magnitude. The motion of charged particles is then described in terms of the velocity components parallel and perpendicular to the magnetic field, v_{\parallel} and v_{\perp} . Only v_{\perp} interacts with \mathbf{B} , leading to a circular motion perpendicular to \mathbf{B} . The superposition of this circular motion with a free streaming parallel to the magnetic field gives rise to the helical

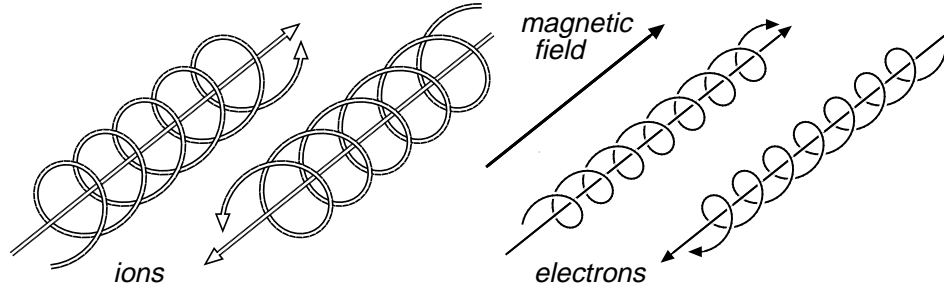


Figure 1.4: Orientation of the gyration orbits of electrons and ions in a magnetic field.

motion depicted in Fig. 1.4. The centrifugal force mv_{\perp}^2/r balances the Lorentz force $qv_{\perp}B$ for a gyration radius r equal to the *Larmor radius*

$$\rho_L = \frac{mv_{\perp}}{|q|B}. \quad (1.34)$$

If $mv_{\perp}^2/2 = k_B T$ is taken for the two-dimensional thermal motion perpendicular to \mathbf{B} , it is

$$\rho_L = \frac{(2mk_B T)^{1/2}}{|q|B}.$$

In a typical fusion plasma ($T = 10$ keV, $B = 5$ T), the electrons have a Larmor radius $\rho_{L,e} = 67 \mu\text{m}$ and deuterons have $\rho_{L,i} = 4.1$ mm. The frequency of the gyration, called *cyclotron frequency* Ω_q , follows from $v_{\perp} = \Omega \rho_L$ to be

$$\Omega_q = \frac{|q|B}{m_q}.$$

In fusion experiments, the electron cyclotron frequency Ω_e is of the same order of magnitude as the plasma frequency $\omega_{p,e}$.

The *Hall parameter*

$$x_q = \Omega_q \tau_{qq} \quad (1.35)$$

counts the number of cyclotron revolutions between succeeding collisions. A magnetized plasma is characterized by $x_e \gg x_i \gg 1$.

The *magnetic moment* μ is defined as the product of the current I times the area A which is surrounded by the current. Thus, the magnetic moment of a single gyrating particle is

$$\mu = I \cdot A = \frac{q\Omega}{2\pi} \cdot \pi \rho_L^2 = \frac{mv_{\perp}^2}{2B} = \frac{\mathcal{E}_{\perp}}{B}, \quad (1.36)$$

where \mathcal{E}_{\perp} is the perpendicular fraction of the kinetic energy. The magnetic field produced by the gyrating particles counteracts the externally imposed magnetic field \mathbf{B} (*plasma diamagnetism*).

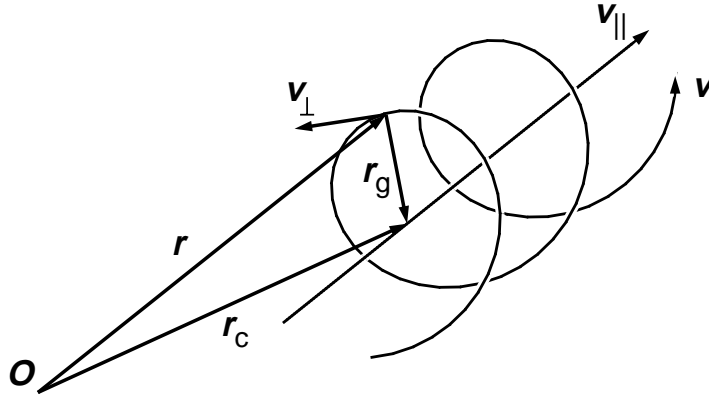


Figure 1.5: Definition of the guiding centre motion.

1.7.2 Motion in a constant magnetic field due to an additional force

If, in addition to the Lorentz force, a force \mathbf{F} acts on the charged particle, the equation of motion is

$$m \frac{d\mathbf{v}}{dt} = q (\mathbf{v} \times \mathbf{B}) + \mathbf{F} .$$

The motion of the particle under the influence of \mathbf{F} can be separated from the gyration due to \mathbf{B} by considering the *guiding centre* of the particle, as shown in Fig. 1.5. The guiding centre “c” is the centre of the gyration cycle. Its position \mathbf{r}_c can be written as

$$\mathbf{r}_c = \mathbf{r} + \mathbf{r}_g , \quad (1.37)$$

where \mathbf{r} is the position of the particle and \mathbf{r}_g the gyration radius vector

$$\mathbf{r}_g = \frac{m}{qB^2} \mathbf{v} \times \mathbf{B} .$$

In *strongly magnetized* plasmas such as in fusion experiments, the Lorentz force dominates other forces \mathbf{F} . Then, ρ_L is often much smaller than other length scales, and Ω much higher than other frequencies. Consequently, the particle orbit is well described by the motion of the guiding centre. With the assumption of a constant B , the velocity of the guiding centre can be obtained by differentiating (1.37)

$$\mathbf{v}_c = \dot{\mathbf{r}}_c = \mathbf{v} + \frac{m}{qB^2} \frac{d\mathbf{v}}{dt} \times \mathbf{B} = \mathbf{v} + \frac{1}{qB^2} [q(\mathbf{v} \times \mathbf{B}) + \mathbf{F}] \times \mathbf{B} . \quad (1.38)$$

Using the vector relation

$$(\mathbf{v} \times \mathbf{B}) \times \mathbf{B} = (\mathbf{v}_\perp \times \mathbf{B}) \times \mathbf{B} = B(\mathbf{v}_\perp \cdot \mathbf{B}) - \mathbf{v}_\perp (\mathbf{B} \cdot \mathbf{B}) = -\mathbf{v}_\perp B^2 ,$$

the guiding centre motion follows to be

$$\mathbf{v}_c = \mathbf{v}_\parallel + \frac{\mathbf{F} \times \mathbf{B}}{qB^2} .$$

The velocity of the guiding centre can be split into components perpendicular and parallel to the magnetic field

$$\mathbf{v}_{c,\perp} = \frac{\mathbf{F}_\perp \times \mathbf{B}}{qB^2}, \quad \frac{dv_{c,\parallel}}{dt} = \frac{F_\parallel}{m}. \quad (1.39)$$

Any force with perpendicular components to the magnetic field leads to a motion perpendicular to \mathbf{B} and \mathbf{F} with the velocity $\mathbf{v}_{c,\perp}$.

1.7.3 $\mathbf{E} \times \mathbf{B}$ drift, gravitational drift

The most important additional force is a constant electric force $\mathbf{F} = q\mathbf{E}$, which leads to a drift

$$\mathbf{v}_E = \frac{\mathbf{E} \times \mathbf{B}}{B^2}. \quad (1.40)$$

This drift velocity does not depend on the sign of the charge or the mass of the particles. Thus, the $\mathbf{E} \times \mathbf{B}$ drift leads to a macroscopic movement of a plasma. More insight into the $\mathbf{E} \times \mathbf{B}$ drift can be gained from Fig. 1.6 left. If the particle accelerates in the electric field, the Larmor radius increases. On the other hand, if it slows down its Larmor radius decreases, leading to the non-closed trajectories shown in Fig. 1.6 left. The net effect is a drift velocity perpendicular to the electric and magnetic fields.

Another drift is due to the gravitation field. If $F_g = mg$ is perpendicular to B , the drift velocity is $v_g = mg/(qB)$.

1.7.4 Particle drift in inhomogeneous magnetic fields

For spatially varying magnetic fields, (1.39) can still be applied if the relative variation of B is small along one gyration of the particle, i.e. in the case of *slowly varying* fields. One important example is the particle drift in a magnetic field with a transverse gradient. The particle orbit has a smaller radius of curvature on that part of its orbit located in the stronger magnetic field. This leads to a drift perpendicular to both the magnetic field and its gradient. Quantitatively, the force on a particle with magnetic moment μ (see (1.36)) can be written as

$$\mathbf{F}_{\nabla B} = -\mu \nabla B,$$

leading to

$$\mathbf{v}_{\nabla B} = -\frac{mv_\perp^2}{2qB^3} (\nabla_\perp B) \times \mathbf{B}. \quad (1.41)$$

Let us consider a curved magnetic field in the case that the plasma current does not play a role, $\nabla \times \mathbf{B} = 0$ or, more generally, $\nabla \times \mathbf{B} \parallel \mathbf{B}$. As sketched in Fig. 1.6, there is a correlation between the field gradient and the curvature radius R_c

$$\frac{R_c}{R_c^2} = -\frac{\nabla_\perp B}{B}. \quad (1.42)$$

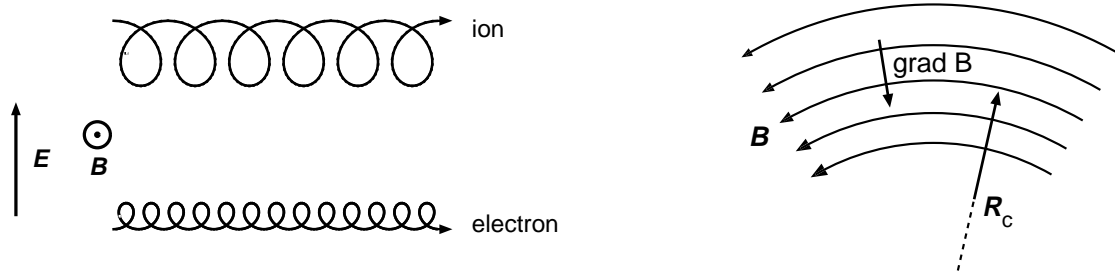


Figure 1.6: Left: $\mathbf{E} \times \mathbf{B}$ drift of ion and electron, $v_E = E/B$.

Right: Inhomogeneous magnetic field. Curvature radius and its relation to the field gradient in the absence of a plasma current ($\nabla \times \mathbf{B} = 0$).

Since the particles follow the curved magnetic field lines, a centrifugal force $F_c = mv_{\parallel}^2 R_c/R_c^2$ is exerted, which is responsible for the drift velocity

$$\mathbf{v}_R = \frac{mv_{\parallel}^2}{qB^2} \frac{\mathbf{R}_c \times \mathbf{B}}{R_c^2}. \quad (1.43)$$

Combination of (1.41), (1.42), and (1.43), yields

$$\mathbf{v}_R + \mathbf{v}_{\nabla B} = \frac{m}{q} \frac{\mathbf{R}_c \times \mathbf{B}}{R_c^2} (v_{\parallel}^2 + \frac{1}{2}v_{\perp}^2).$$

In a very rough approximation $v_{\parallel}^2 + 1/2v_{\perp}^2 \approx v^2$, i.e. the resulting drift is proportional to the particle energy.

As a first application of these drifts, consider the electrons and protons captured in the earth's magnetic field (trapping in a magnetic field will be discussed in the next section). Due to the gradient and curvature of the earth's magnetic field, these electrons and protons drift around the equator, the electrons from west to east and the protons in the opposite direction, producing the so-called ring currents.

1.7.5 The guiding centre equations in general geometry

In fusion plasmas the geometry of the magnetic field is usually fairly complex. Therefore, it is mandatory to derive the guiding centre equations rigorously for arbitrary geometry.

Most elegantly this was done by Littlejohn [16]. He showed that the guiding centre equations can be derived from a generalized Lagrangian. We will outline the general idea and the results only. Littlejohn has shown that there is a non-canonical transformation such that the particle motion can be expressed independently from the gyroangle α to arbitrary order in a small parameter $\epsilon_B = |\rho_L/L_B|$ (where $L_B = B/|\nabla B|$ is the scale length of the magnetic field). This set of phase-space coordinates $(\mathbf{R}, V_{\parallel}, V_{\perp}, \mu)$ is called guiding centre coordinates. In these coordinates, the magnetic moment constructed as

$$\mu = \frac{mV_{\perp}^2}{2ZeB(\mathbf{R})}$$

is conserved. Note, however, that the “true” $\mu = mv_{\perp}^2/(2ZeB)$ resulting from the velocity v_{\perp} in the real space is not conserved in general.

To first order in ε_B and for $d/(\Omega dt) \ll 1$ the following results have been obtained assuming the set of independent variables to be $\mathbf{R}, V_{\parallel}, \mu$

The time derivatives of \mathbf{R} , μ and V_{\parallel} can be obtained from the well known Lagrangian formalism [16] with the single-particle Lagrangian

$$L = Ze\mathbf{A}^* \cdot \dot{\mathbf{R}} + \frac{1}{Ze}\mu\dot{\alpha} - \frac{1}{2}mV_{\parallel}^2 - \mu B - Ze\phi \quad (1.44)$$

which gives the Euler-Lagrange equations

$$Ze(\mathbf{E}^* + \dot{\mathbf{R}} \times \mathbf{B}^*) = m\dot{V}_{\parallel}\mathbf{b} + \mu\nabla B, \quad (1.45)$$

$$\dot{\mu} = 0, \quad (1.46)$$

$$\dot{\alpha} = \frac{ZeB}{m}, \quad (1.47)$$

$$\dot{\mathbf{R}} \cdot \mathbf{b} = V_{\parallel}. \quad (1.48)$$

The modified field quantities are defined as in Littlejohn’s work [16]

$$\mathbf{A}^* = \mathbf{A} + \frac{m}{Ze}V_{\parallel}\mathbf{b}, \quad (1.49)$$

$$\mathbf{B}^* = \mathbf{B} + \frac{m}{Ze}V_{\parallel}\nabla \times \mathbf{b}, \quad (1.50)$$

$$\mathbf{E}^* = -\frac{\partial \mathbf{A}^*}{\partial t} - \nabla\phi, \quad (1.51)$$

$$\mathbf{b} = \frac{\mathbf{B}}{B}. \quad (1.52)$$

Finally we are left with the following equations of motion

$$\dot{\mathbf{R}} = \frac{1}{B_{\parallel}^*} \left[V_{\parallel}\mathbf{B}^* + \frac{1}{Ze}\mathbf{b} \times (\mu\nabla B - Ze\mathbf{E}^*) \right], \quad (1.53)$$

$$\dot{V}_{\parallel} = -\frac{1}{B_{\parallel}^*}\mathbf{B}^* \cdot (\mu\nabla B - Ze\mathbf{E}^*), \quad (1.54)$$

$$\dot{\mu} = 0, \quad (1.55)$$

$$\dot{\alpha} = \Omega = \frac{ZeB}{m}. \quad (1.56)$$

Note, in (1.54), the so-called mirror force (first term on the right-hand side) which is responsible for the *bounce* motion of a part of the particle population in regions of weaker magnetic field, as shown in Fig. 1.7 and Fig. 1.8. This phenomenon can be also understood in terms of adiabatic invariance of the magnetic moment, as explained below.

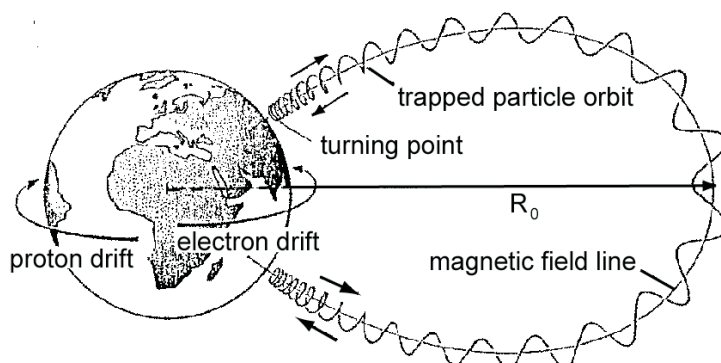


Figure 1.7: Drifts of electrons and protons in the earth's magnetic field.

1.8 Adiabatic invariants

The gyromotion and the bounce motion seen in the previous section are two examples of quasi-periodic motion of a charged particle in a magnetic field. The word *quasi*-periodic is used because it is assumed that the trajectory changes on a time scale which is much slower than the “period” of the motion. For instance, this implies that the Larmor orbit remains nearly unchanged over many gyroperiods $2\pi/\Omega$, or that the trajectory of a trapped particle is approximately the same during many bounce times. In this case, the quantity

$$I \equiv \oint p dq, \quad (1.57)$$

where p and q are conjugate canonical variables and the integral is taken over a complete cycle in q , is called an *adiabatic invariant* of the motion. The period T can be computed directly as $T = \partial I / \partial \mathcal{E}$, where \mathcal{E} is the energy of the system. Using this definition of I , we can immediately prove that the magnetic moment is an adiabatic invariant associated to the cyclotron motion. The relevant Hamiltonian is in this case $H(\mathbf{p}, \mathbf{q}) = (\mathbf{p} - q\mathbf{A})^2 / 2m$ and the canonical momentum $\mathbf{p} = m\mathbf{v} + q\mathbf{A}$. (1.57) becomes then

$$I_1 = \oint m\mathbf{v}_\perp \cdot d\mathbf{r}_\perp + \oint q\mathbf{A} \cdot d\mathbf{r}_\perp = 2\pi\rho m v_\perp - qB\pi\rho^2 = \frac{\pi m^2 v_\perp^2}{qB} \propto \frac{mv_\perp^2}{2B} = \mu,$$

where Stokes' theorem and (1.34) have been used. This shows that the magnetic moment μ , which is proportional to I_1 , is an adiabatic invariant.

We have met this adiabatic invariance in the section before and take the opportunity to recall: for a constant and homogeneous magnetic field guiding centre coordinates and real space coordinates agree what implies that μ is strictly conserved. For inhomogeneous and time dependent magnetic fields we observe that μ is conserved to a certain order in the ordering parameters ϵ_B and $d/(\Omega dt)$ only. Littlejohn's result that a phase space transform exists which finds a redefined μ as a conserved quantity can be regarded as formal expression of the term *adiabatic invariance*.

The invariance of μ is the basis for magnetic mirrors, which is schematically shown in Fig. 1.8. The parallel velocity of a particle in a (spatially or temporally) varying magnetic field is determined by $\mu = \text{const}$ and energy conservation $mv^2/2 = \text{const}$. The combination of these

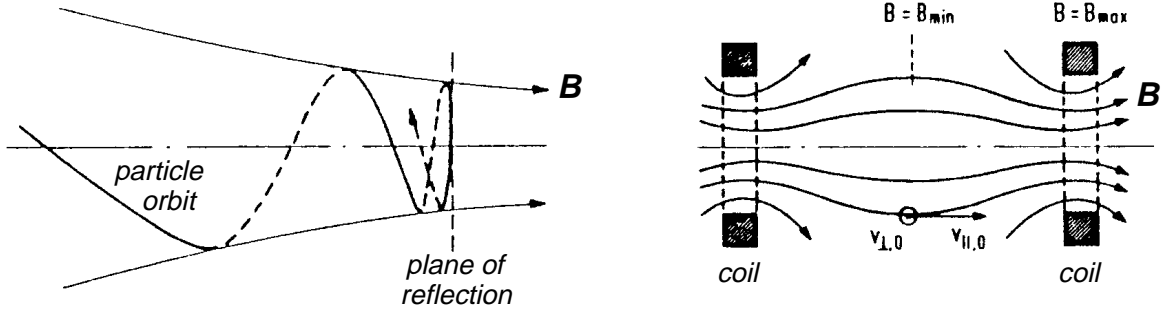


Figure 1.8: Magnetic field lines of a simple axisymmetric magnetic mirror.

conditions, $mv_{\parallel}^2/2 + \mu B = \text{const}$, reveals that v_{\perp}^2 increases with increasing B and hence v_{\parallel} decreases. The criterion for particle reflection ($v_{\parallel} = 0$) at the high field ends of the mirror machine is

$$\frac{1}{2}mv^2 = \frac{1}{2}mv_{\parallel,0}^2 + \mu B_{\min} \leq \mu B_{\max}, \quad (1.58)$$

where $v_{\parallel,0}$ is the parallel velocity in the low field region. If the mirror ratio is defined as $R = B_{\max}/B_{\min}$ and (1.58) is divided by $\mu B_{\min} = 1/2mv_{\perp,0}^2$, the velocity ratio

$$\frac{v_{\parallel,0}}{v_{\perp,0}} \leq \sqrt{R-1} \quad (1.59)$$

describes the criterion for particle confinement. The earth's magnetic field is an example of a magnetic mirror. It forms two belts of confined charged particles originating from the solar wind (see Fig. 1.7). Obviously, particles which do not meet the condition (1.59) are lost from magnetic mirrors. This so called *loss cone* in velocity space is refilled by collisions and therefore pure mirror configurations have a very poor plasma confinement.

The second or *longitudinal invariant* is

$$J = m \oint v_{\parallel} d\ell.$$

Consider a particle between two magnetic mirrors: It bounces between them and therefore has a periodic motion at the bounce frequency. A constant of this motion is $\oint mv_{\parallel} d\ell$ with ℓ being the length between two mirrors and v_{\parallel} the longitudinal velocity. However, the motion is not exactly periodic, because the guiding centre drifts across field lines, and thus the constant of the motion becomes in general an adiabatic invariant. From this we can conclude that the particles will drift on $J = \text{const}$ contours.

If these contours are closed, the drift motion is also periodic and we observe another constant of motion – the so called third adiabatic invariant. Note, however, that to guarantee invariance the perturbations have to be even slower (see 1.8) than the drift period.

The third adiabatic invariant turns out to be the total magnetic flux Φ enclosed by the drift surface. Obviously, the particles will stay on a surface such that the total number of lines of force enclosed remains constant as B varies. This invariant has few applications because most fluctuations of B occur on a time scale short compared with the drift period.

Table 1.1: Characteristic times of motion for typical fusion parameters in a stellarator reactor similar to W7-X: ($B = 5$ T, large radius: 20 m, small radius 2 m, $T = 15$ keV, $n = 3 \cdot 10^{20} \text{ m}^{-3}$).

	gyration time τ_g	bounce time τ_{bounce}	drift time τ_{drift}
electrons	$\approx 7 \cdot 10^{-12} \text{ s}$	$\approx 10^{-6} \text{ s}$	$\approx 6 \cdot 10^{-2} \text{ s}$
deuterons	$\approx 3 \cdot 10^{-8} \text{ s}$	$\approx 10^{-4} \text{ s}$	$\approx 6 \cdot 10^{-2} \text{ s}$
α -particles	$\approx 3 \cdot 10^{-8} \text{ s}$	$\approx 3 \cdot 10^{-5} \text{ s}$	$\approx 10^{-4} \text{ s}$

Appendix A

1.8 summarizes characteristic plasma parameters and their numerical value for typical fusion plasmas, namely $T_e = T_i = 10^4$ eV, $Z = 1$, and $n_e = n_i = 10^{20} \text{ m}^{-3}$, $B = 5$ T for magnetically-confined experiments and $n_e = n_i = 10^{31} \text{ m}^{-3}$ for inertially-confined experiments. In the table, $a = e^4 \ln \Lambda / (6\pi\epsilon_0^2)$.

References

- [1] Y. Eliezer and S. Eliezer: *The Fourth State of Matter*, Bristol: Hilger (1989).
- [2] N.A. Krall and A.W. Trivelpiece: *Principles of Plasma Physics*, New York: McGraw-Hill (1973).
- [3] F.F. Chen: *Introduction to Plasma Physics*, New York: Plenum Press (1974).
- [4] G. Schmidt: *Physics of High Temperature Plasmas*, New York: Academic Press (1979).
- [5] R.B. White: *Theory of Tokamak Plasmas*, Amsterdam: North-Holland (1989).
- [6] R.D. Hazeltine and J.D. Meiss: *Plasma Confinement*, Redwood: Addison-Wesley (1992).

Table 1.2: Characteristic plasma parameters and their numerical value for typical fusion plasmas.

Name	Formula	Magnetic fusion	Inertial fusion
Average distance	$\bar{r} \approx (\frac{4}{3}\pi n)^{-1/3}$	0.2 μm	3×10^{-11} m
Debye length	$\lambda_D = \sqrt{\epsilon_0 k_B T / (n_e e^2)}$	75 μm	2.4×10^{-10} m
Landau length	$\lambda_L = e^2 / (\pi \epsilon_0 k_B T)$	10^{-13} m	10^{-13} m
de Broglie length	$\Lambda_p = \hbar / (\sqrt{m_e k_B T})$	3×10^{-12} m	3×10^{-12} m
Mean free path	$\lambda_{qk} = v_{th,q} \tau_{qk}$	15 km	150 nm
Larmor radius	$\rho_{L,q} = m_q v_{\perp} / (q B)$	67 μm (e), 4.1 mm (i)	
Thermal velocity	$v_{th,q} = \sqrt{3k_B T_q / m_q}$	7.3×10^7 m/s (e), 1.7×10^6 m/s (i)	7.3×10^7 m/s (e), 1.7×10^6 m/s (i)
Plasma frequency	$\omega_{p,e} = (1/2\pi) \sqrt{n_e e^2 / \epsilon_0 m_e}$	90 GHz	2×10^{17} Hz
Cyclotron frequency	$\omega_{c,q} = q B / 2\pi m_q$	140 GHz (e), 40 MHz (i)	
Electron collision time	$\tau_{ee} = \frac{\sqrt{3}}{a} \sqrt{m_e} n_e^{-1} (k_B T_e)^{3/2}$	140 μs	5.4×10^{-15} s
Ion collision time	$\tau_{ii} = \frac{\sqrt{3}}{aZ^4} \sqrt{m_i} n_i^{-1} (k_B T_i)^{3/2}$	6 ms	2.3×10^{-13} s
Electrical resistance	$\eta = m_e / (n_e e^2 \tau_{ei}^E)$	1×10^{-9} Ωm	3×10^{-10} Ωm
Plasma parameter	$N_D = \frac{4}{3}\pi n \lambda_D^3$	2×10^8	500
Coulomb logarithm	$\ln \Lambda = \ln \left(\frac{9}{\sqrt{2}} N_D \right)$	17	4.4
Hall parameter	$x_q = \omega_{c,q} \tau_{qq}$	1×10^8 (e), 3×10^6 (i)	

- [7] B.B. Kadomtsev: *Tokamak Plasma: A Complex Physical System*, Bristol: IOP Publ. (1992).
- [8] P.A. Sturrock: *Plasma Physics*, Cambridge: Cambridge University Press (1994).
- [9] R.J. Goldston and P.H. Rutherford: *Introduction to Plasma Physics*, Bristol: IOP Publ. (1995).
- [10] J.A. Bittencourt: *Fundamentals of Plasma Physics*, Oxford: Pergamon Press (2nd ed, 1995).
- [11] J.A. Wesson: *Tokamaks*, Oxford: Oxford University Press (2nd ed, 1997).
- [12] K. Miyamoto: *Fundamentals of Plasma Physics and Controlled Fusion*, Tokyo: Iwanami Press (1997).
- [13] K.-H. Spatschek: *High Temperature Plasmas*, Weinheim: WILEY-VCH (2012).
- [14] M.N. Saha: *On a Physical Theory of Stellar Spectra*, Proc. Roy. Soc. **A99** (1921) 135.
- [15] L. Spitzer, Jr., and R. Härm: *Transport Phenomena in a Completely Ionized Gas*, Phys. Rev. **89** (1953) 977.
- [16] R.G. Littlejohn, J. Plasma Phys. **29**, 302 (1983).
- [17] L.D. Landau, E.M. Lifshitz, *Course in Theoretical Physics Vol 1: Mechanics*, Butterworth-Heinemann (1982)

Chapter 2

Basic nuclear fusion

Hans-Stephan Bosch

2.1 Introduction

Any energy production from nuclear reactions is based on differences in the nuclear binding energy. Fig. 2.1 shows the nuclear binding energy per nucleon (proton or neutron). It has been derived from measurements of the masses of the nuclei, when it was observed that the masses of nuclei are always smaller than the sum of the proton and neutron masses which constitute the nucleus. This mass difference corresponds to the nuclear binding energy according to Einstein's energy-mass relation $E = \Delta m \cdot c^2$. An explanation of the structure of Fig. 2.1 was given by C.F. von Weizsäcker in 1935. Starting from the very limited range of the strong nuclear force he assumed that each nucleon just influences its nearest neighbours. The binding energy per nucleon would thus be constant. The smaller binding energies for smaller nuclei are due to the relatively large surface to volume ratio. The nucleons at the surface have missing partners and thus their contribution to the total binding energy of the nucleus is reduced. The decrease of binding energy per nucleon for nuclei beyond $A \approx 60$ is due to the repulsive coulomb force of the large amount of positive protons.

The finer structures in Fig. 2.1 are due to quantum mechanical effects, i.e. at certain so-called *magic* proton and neutron numbers the nucleus formed is a very stable configuration. This is roughly comparable to the stable electron configurations of the noble gases, where electron shells are completed. The first magic number is two, which is manifested as a most remarkable example of a local maximum in Fig. 2.1, i.e. the helium nucleus with two protons and two neutrons. From Fig. 2.1 it is clear that there are two ways of gaining nuclear energy:

1. By transforming heavy nuclei into medium-size nuclei: This is done by fission of uranium, which is not a topic of these lectures.
2. By fusion of light nuclei into heavier ones: In particular the fusion of hydrogen isotopes into stable helium offers the highest energy release per mass unit. Doing this in a controlled manner has been the goal of fusion research for about 40 years. Most of the following lectures are dedicated to this goal.

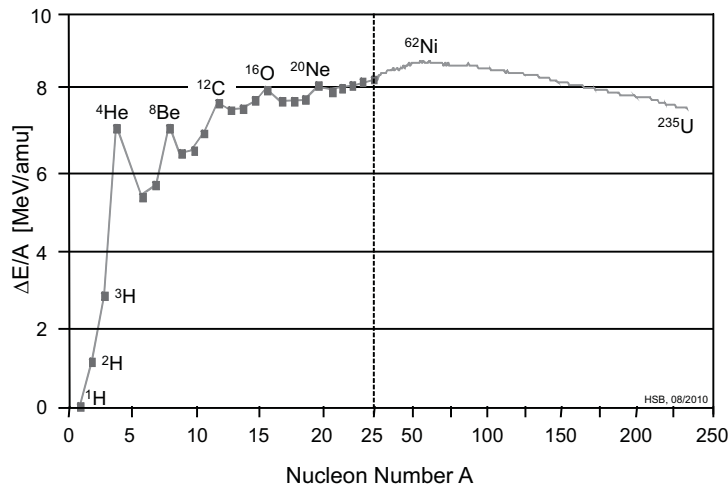


Figure 2.1: Nuclear binding energy per nucleon as a function of the nucleon number A .

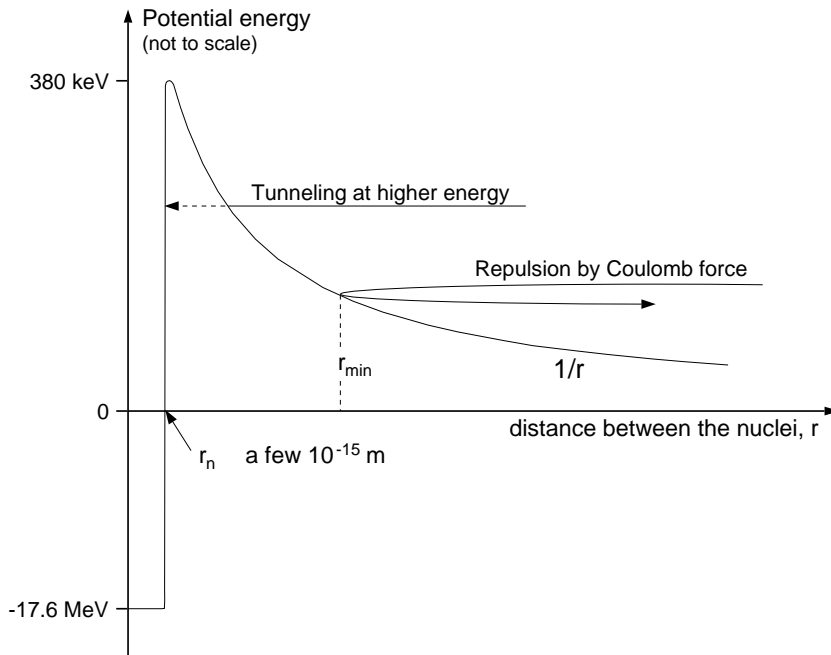


Figure 2.2: Schematic representation of the potential energy U of two nuclei as a function of their distance. The energies quoted are for a system of D ($=^2\text{H}$) and T ($=^3\text{H}$).

The energy release per nucleon is of the order of 1 MeV ($= 10^6$ eV) for fission reactions and in the order of a few MeV for fusion reactions. This is 6–7 orders of magnitude above typical energy releases in chemical reactions, which explains the effectiveness and attractiveness, but also the potential hazard of nuclear power.

All the nuclear reactions are mostly governed by the strong nuclear force which acts over very small distances in the order of the radius of the nuclei, but for distances above a few fermi (i.e. 10^{-15} m) the repulsive Coulomb force between the positively charged nuclei becomes dominant. The potential energy of two nuclei as a function the distance between these nuclei

is shown in Fig. 2.2. The depth of the deep well at small radii is determined by the binding energy, discussed before, while the barrier at a few fermi is given by the Coulomb potential of $Z_1 Z_2 e^2 / 4\pi\epsilon_0 r_m$ which is much smaller, but still poses a principal problem. For alpha-particle decay (where a ${}^4\text{He}$ nucleus separates itself out of a positive nucleus) as well as for fusion of lighter nuclei, this diagram demands a particle energy of the order of 500 keV, and this would make fusion processes almost impossible. However, it was known since the end of the last century, that α -particle decay occurs at room temperature, and in 1928 Gamov [1] explained this by the tunneling effect, which in turn also allows fusion reactions to occur at temperatures far below the Coulomb barrier: Due to quantum mechanical effects the minimum distance between the two nuclei is not fixed (as it is indicated by the repulsion in Fig. 2.2), but there is a finite probability for the nuclei to get closer, and eventually *tunnel* through the Coulomb barrier, as indicated by the dotted line in Fig. 2.2. In terms of wave functions, the amplitude is not zero for $r \leq r_{min}$, but it is finite and decays slowly for smaller radii. Therefore it can still be finite for $r \leq r_n$, i.e. the particles have a possibility to approach close enough for a fusion reaction to occur. This tunneling probability is a strong function of the relative velocity v of the reacting particles with charge Z_1, Z_2 ,

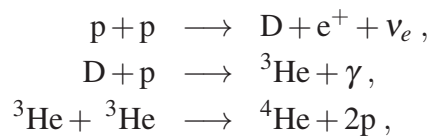
$$P_{tunneling} \sim \exp - \frac{2\pi Z_1 Z_2 e^2}{\hbar v} .$$

This equation shows that reaction partners with small mass (and charge Z) are preferred, and that the reaction probability increases strongly with the relative velocity v , i.e. the temperature.

In the light of the above discussion it becomes clear why fission energy has been much more readily obtained than fusion energy: Fission is triggered by thermal neutron capture, i.e. no force prevents the neutron from entering the uranium nucleus at room temperature and causing a fission reaction.

2.2 Energy production on the sun

Though still a somewhat exotic topic on earth, nuclear fusion is *the* energy source of our universe. The light of all stars is generated by fusion reactions. On the sun the main reactions are the following



where p denotes a proton, D a deuteron, a heavy hydrogen isotope with one proton and one neutron, ${}^3\text{He}$, ${}^4\text{He}$ are helium isotopes, γ stands for a high-energy photon, e^+ for a positron (anti-electron), and ν_e for an electron neutrino.

A very important feature of the energy production on the sun is the need for the weak interaction which transforms protons to neutrons (β^+ -decay), in the first of the above listed reactions. All weak interaction processes involve the emission of neutrinos (thereby keeping the lepton

number constant). As the weak interaction is very slow, it causes the long lifetime of the sun and it is an essential condition for our evolution .

Further reactions which are important at temperatures above about 1 keV, produce ${}^7_4\text{Be}$, ${}^7_3\text{Li}$, ${}^8_5\text{B}$ and ${}^8_4\text{Be}$, which decays into two ${}^4_2\text{He}$ nuclei. Also in these reactions neutrinos are produced, however with a higher kinetic energy than those from the pp-reactions mentioned above.

These neutrinos ignore both the strong and electromagnetic interactions and therefore it is extremely hard to detect them experimentally. Almost all neutrinos produced in the sun travel through it without interaction and thus carry information from the reactions in the core of the sun. It was not till 1992 that the European GALLEX collaboration detected the low energy solar neutrinos from the main energy-producing reactions (pp-chain) listed above. This was the first experimental validation of our theoretical model of energy production in the stars.

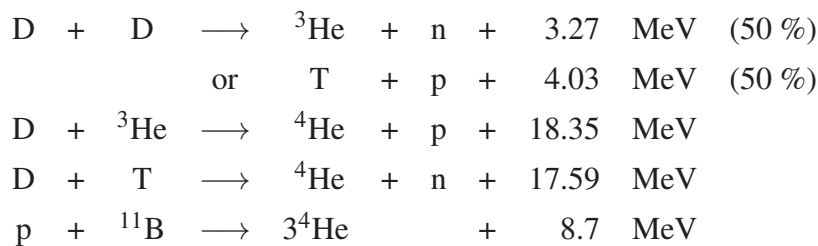
For much higher temperatures ($T \geq 2$ keV), i.e. in stars which with higher mass than the sun, fusion of four protons to ${}^4_2\text{He}$ can also occur in a catalytic process based on ${}^{12}_6\text{C}$. In this so-called Bethe-Weizsäcker cycle oxygen, nitrogen and ${}^{13}_6\text{C}$ are involved only in intermediate stages, and the net reaction again is $4 p \rightarrow {}^4_2\text{He} + 2 e^+ + 2 \nu_e$.

2.3 Fusion on earth

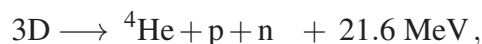
The fundamentals of fusion research are well described in great detail in two (German) books by J. Raeder [4] and U. Schumacher [5].

For energy production on earth the weak interaction has to be avoided since it would lead to unacceptably small reaction rates. The sun (and all other stars) overcome this problem by their huge mass, but a fusion reactor has to be considerably smaller in size than a star.

Possible candidates for using fusion energy on earth are the following reactions (T denoting tritium, the heaviest hydrogen isotope with two neutrons)



Because the kinetic energy of the reactants is much lower than the energy gained in the reaction, the distribution of the reaction energy onto the two product particles is inverse proportional to their mass, i.e. $E_1/E_2 = m_2/m_1$. In the DT-reaction, e.g. the α -particle has an energy of 3.54 MeV, and the neutron has 14.05 MeV. The first four reactions (for which the cross sections are shown in Fig. 2.3) can be summarized as



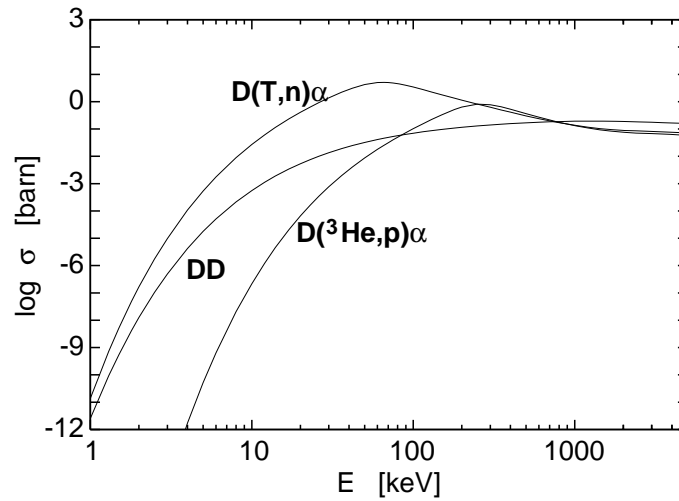
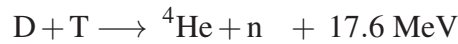


Figure 2.3: Measured cross-sections for different fusion reactions as a function of the center of mass energy [3]. The curve labeled DD shows the sum of the cross sections for both branches of this reaction. Reaction cross sections are usually measured in barn, where $1 \text{ barn} = 10^{-28} \text{ m}^2$.

and therefore rely on deuterium as fuel only. Since the weight fraction of deuterium in water is 3.3×10^{-5} , the energy content of water is about 11.5 GJ per litre, which is about 350 times larger than the chemical energy density of gasoline. This demonstrates the huge potential afforded by nuclear fusion as an energy source.

All the reaction cross sections in Fig. 2.3 show a steep increase with the relative energy, as discussed before, but the D-T reaction



has by far the largest cross-section at the lowest energies. This makes the D-T fusion process the most promising candidate for an energy-producing system. The special role of D-T reactions becomes clear from the energy levels of the unstable ${}^5\text{He}$ nucleus shown in Fig. 2.4. It has an excited state just 64 keV above the sum of the masses of deuterium and tritium. The D-T fusion cross-section therefore reaches its maximum at this energy difference, due to the resonance-like reaction mechanism. The DD reactions (see Fig. 2.4, left part) show no such resonances, and their cross sections are solely governed by the tunneling probability, showing a smooth increase without any maximum, while the D^3He reaction also has a resonance at about 270 keV in the ${}^5\text{Li}$ system, not shown here.

To be a candidate for an energy-producing system, the fusion fuel has to be sufficiently abundant. As mentioned earlier, deuterium occurs with a weight fraction of 3.3×10^{-5} in water. Given the water of the oceans, the static energy range is larger than the time the sun will continue to burn (a few billion years).

Tritium is an unstable radioactive isotope. It decays to



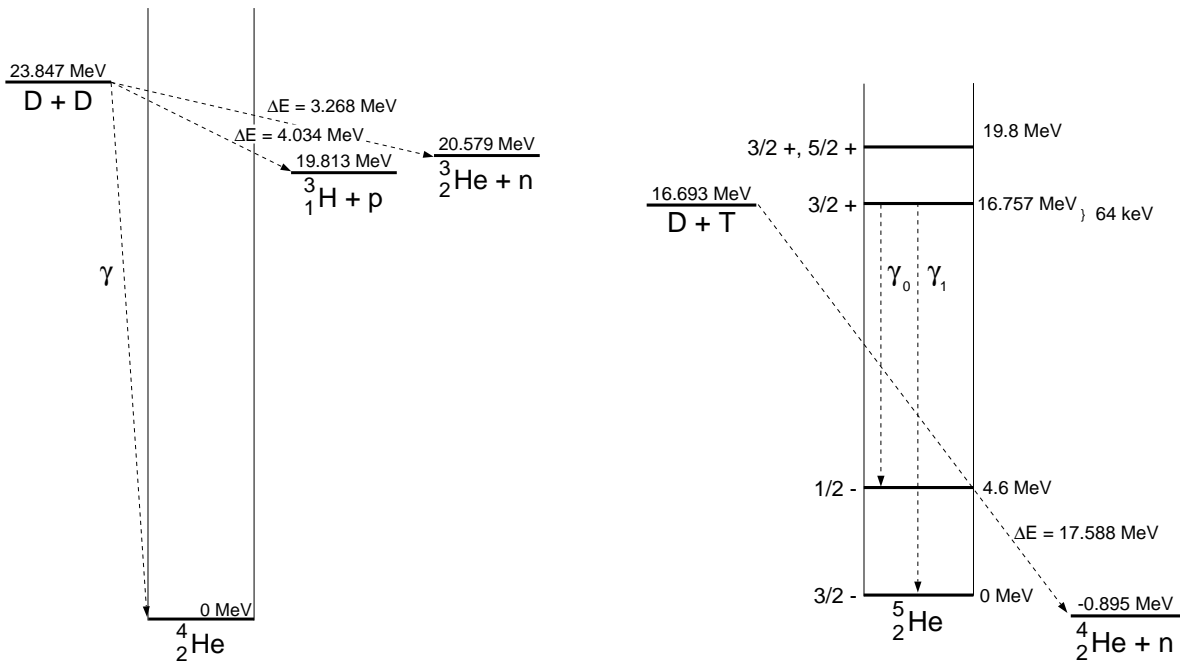
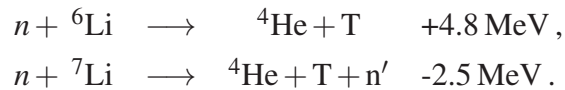


Figure 2.4: Left: Energy diagram of the ${}^4\text{He}$ nucleus and Right: Of the unstable ${}^5\text{He}$ nucleus (right), where the resonance at 16.76 MeV dominates the reaction cross section. The numbers left of the level scheme indicate the J -value and parity of the respective level.

with a half-life of 12.3 years. Note the previously mentioned neutrino production of this β^- decay. Owing to the unstable character of tritium no significant amounts exist, but tritium can be produced with nuclear reactions of the neutrons from the D-T reaction and lithium



The reaction with ${}^7\text{Li}$ is particularly important because it does not consume a neutron and opens the possibility for self-sufficient tritium production in a fusion reactor, i.e. each fusion neutron will produce at least one new tritium nucleus.

The ultimate fusion fuel will thus be deuterium and lithium. The latter is also very abundant and widespread in the earth's crust and even ocean water contains an average concentration of about 0.15 ppm (1 ppm = parts per million). Tab. 2.3 summarizes the estimated world energy resources.

2.4 Thermonuclear fusion

As discussed before, for a fusion reaction to occur, the two nuclei have to *touch* each other since the range of the nuclear force is of the order of the dimensions of the nuclei. The repulsive Coulomb force counteracts all attempts to bring them close together. This is what the difficult

Table 2.1: Estimated world energy resources. The figures are only indicative, being dependent on prices and subject to uncertainty because of incomplete exploration.

Present world annual primary energy consumption	3×10^{11}	
	gigajoules	
Resources		
Coal	10^{14}	300 years
Oil	1.2×10^{13}	40 years
Natural Gas	1.4×10^{13}	50 years
^{235}U (fission reactors)	10^{13}	30 years
^{238}U and ^{232}Th (breeder reactors)	10^{16}	30000 years
Lithium (D-T fusion reactors):		
Land	10^{16}	30000 years
Oceans	10^{19}	3×10^7 years

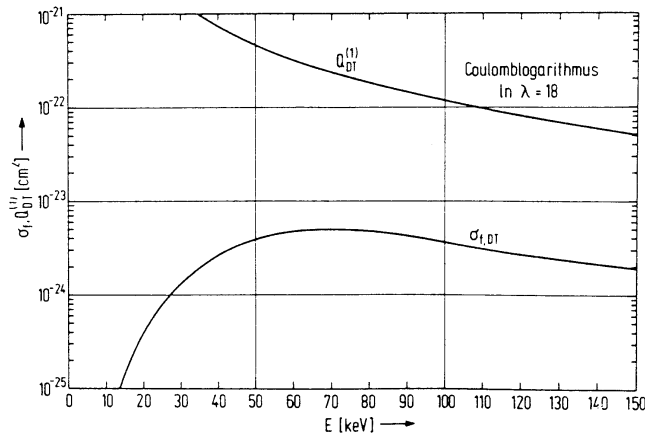


Figure 2.5: Comparison of the D-T fusion cross-section $\sigma_{f,DT}$ and the cross-section for momentum exchange by Coulomb scattering Q_{DT} in a fusion relevant plasma.

research on nuclear fusion is all about: How can the two reaction partners be brought into contact?

The simplest approach to realize the fusion reactions would be to accelerate the reactants to about 100 keV and bring them to collision. This does not lead to a positive energy balance, since the elastic Coulomb scattering as another reaction type has a much larger cross-section, as shown in Fig. 2.5. Thus the two particle beams would just scatter and diverge after one interaction.

A way of overcoming this problem is to confine a thermalized mixture of deuterium and tri-

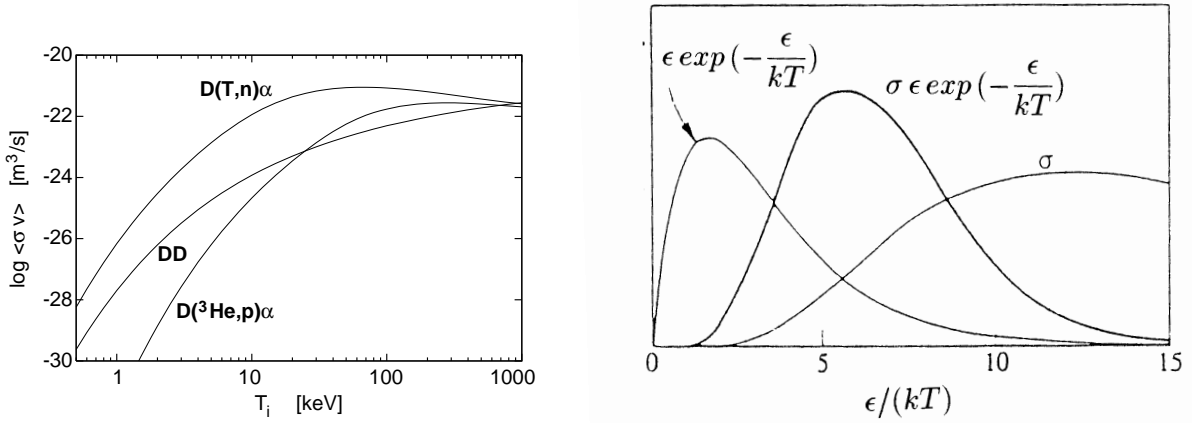


Figure 2.6: Left: Reaction parameter $\langle \sigma v \rangle$ as a function of ion temperature T_i for different fusion reactions [3].

Right: Graph of integrand of the reaction parameter equation and of its two factors $\sigma(\epsilon)$ and $\epsilon \cdot \exp(-\epsilon/kT)$ versus the normalized energy ϵ/T for a D-T plasma at $T = 10$ keV.

tium particles at energies of about 10 keV. Since the average energy of particles at a certain temperature is about kT , where k is the Boltzmann constant, temperatures are often given in electron volt units ($1 \text{ eV} \hat{=} 1.16 \times 10^4 \text{ }^\circ\text{C}$). At energies of 10 keV the hydrogen atoms are completely ionized and form a plasma of charged ions and electrons. The basic physics of plasmas are discussed in chap. 1. For now it should suffice to observe that in a plasma the particles thermalize as a result of many Coulomb scattering processes and thus entail a Maxwellian velocity distribution

$$f(v) = n \left(\frac{m}{2\pi kT} \right)^{3/2} \cdot \exp\left(-\frac{mv^2}{2kT} \right),$$

where f is the number of particles in the velocity interval between v and $v + dv$, n is the density of particles, m is their mass, and kT is their temperature.

The reaction rate per unit volume R can be written as

$$R = n_D \cdot n_T \cdot \langle \sigma v \rangle$$

with v now being the relative particle velocity and $\langle \sigma v \rangle$ being the reaction parameter, i.e. the average of the product of cross-section times velocity.

Calculation of the reaction parameter requires integration over the distribution function of deuterium and tritium. After some numerical transformations one obtains

$$\langle \sigma v \rangle = \frac{4}{(2\pi m_r)^{1/2} (kT)^{3/2}} \int \sigma(\epsilon_r) \cdot \epsilon_r \cdot \exp\left(-\frac{\epsilon_r}{kT} \right) d\epsilon_r,$$

where m_r is the reduced mass, and ϵ_r the relative kinetic energy.

Fig. 2.6 left shows the reaction parameter for some important fusion reactions. At temperatures of interest the nuclear reactions come predominantly from the tail of the distribution. This is illustrated in Fig. 2.6 right, where the integrand of the last equation is plotted versus ϵ_r/T

together with the two factors $\sigma(\varepsilon)$ and $\varepsilon \cdot \exp(-\varepsilon/kT)$ for a D-T plasma at a temperature of 10 keV.

Thermalization is thus not just a way of handling the large cross-sections for elastic Coulomb scattering, it also considerably increases the reaction rate considerably in relation to beam experiments with single particle energies.

2.5 Ignition

In the following the condition which a thermalized D-T plasma has to satisfy to serve as an energy producing system is investigated. Historically, in 1957 John D. Lawson deduced a criterion for a positive energy balance using quantities such as the thermal cycle efficiency η of power reactors [2]. Today the approach has changed slightly to a more physics oriented condition: The aim is an ignited plasma where all energy losses are compensated by the α -particles from the fusion reactions, which transfer their energy of 3.5 MeV to the plasma while slowing down. The neutrons cannot be confined and leave the plasma without interaction.

Transport processes such as diffusion, convection, charge exchange and others are empirically described by an energy confinement time τ_E leading to the power loss term $3nkT/\tau_E$ with $3nkT$ as the inner thermal plasma energy (n is the electron density). Note that this is twice the ideal gas value since every hydrogen atom is split into two particles (electron and nucleus). Another loss mechanism is the bremsstrahlung, which becomes particularly important at high temperatures and impurity concentrations. The power loss due to bremsstrahlung can be written as

$$P_{\text{bremsstrahlung}} = c_1 \cdot n^2 \cdot Z_{\text{eff}} \cdot (kT)^{1/2}$$

with c_1 being the bremsstrahlungs constant ($c_1 = 5.4 \times 10^{-37} \text{ Wm}^3\text{keV}^{-1/2}$), and Z_{eff} the effective charge of the plasma, including all (impurity) species: $Z_{\text{eff}} = \sum_z n_z Z^2 / n$.

The energy balance now reads

$$\left(\frac{n}{2}\right)^2 \langle \sigma v \rangle \cdot \varepsilon_\alpha = 3nkT/\tau_E + c_1 n^2 Z_{\text{eff}} (kT)^{1/2}$$

and this can be rewritten to the ignition condition

$$n\tau_E = \frac{12 kT}{\langle \sigma v \rangle \varepsilon_\alpha - 4c_1 Z_{\text{eff}} (kT)^{1/2}},$$

where ε_α is the energy of the α -particle, 3.54 MeV. This equation shows that the product of the particle density and energy confinement time is only a function of the plasma temperature, with a minimum at about 13 keV. In the range of 10 keV the reaction parameter $\langle \sigma v \rangle$ is roughly proportional to T^2 , which motivated the definition of the so-called fusion product

$$n\tau T = \frac{12 kT^2}{\langle \sigma v \rangle \varepsilon_\alpha - 4c_1 Z_{\text{eff}} (kT)^{1/2}}$$

which has a flat minimum of about $35 \times 10^{20} \text{ s/m}^3 \text{ keV}$ around 10 keV. The fusion product dictates the strategy for developing fusion power as an energy producing system: One has to attain temperatures of around 10 keV (about 100 million °C) and achieve the required density and energy confinement time simultaneously. There are two distinct approaches

1. The hot plasma is confined by strong magnetic fields leading to maximum densities of about $1.5 \times 10^{20} \text{ m}^{-3}$, which is 2×10^5 times smaller than the atom density of a gas under normal conditions. With these densities, the energy confinement time required is in the range of 2–4 seconds. This approach, which is the main line in fusion research, will be covered by most of the following lectures, and is introduced in the next section.
2. The other extreme is to maximize the density. This can be done by strong, symmetric heating of a small D-T pellet. The heating can be done with lasers or particle beams and leads to ablation of some material causing implosion due to momentum conservation. It is clear that the energy confinement time is extremely short in this concept: it is the time required for the particles to leave the hot implosion center. Since it is the mass inertia which causes the finiteness of this time, this approach to fusion is often called *inertial fusion*. The density required is about 1 000 times the density of liquid D-T; the pressure in the implosion center reaches (at temperatures of 10 keV) that in the center of the sun. A detailed description of the actual status in this area can be found in references [7] and [8].

Fig. 2.7 left illustrates the progress of nuclear fusion research in approaching the required $n\tau T$ condition. Today a factor seven is missing for ignition, whereas in the mid-sixties the best experiments fell short of the required conditions by more than five orders of magnitude. However, it has to be kept in mind that achieving ignited plasmas is not sufficient for building fusion reactors. In addition, this plasma state has to be maintained for very long times to allow continuous energy production. One of the most difficult problems will be the interaction of the edge plasma with the surrounding structures and the removal of helium ash. Consequently, edge plasmas constitute an increasingly important research topic.

Impurities from the walls worsen the ignition condition in two ways. They dilute the fuel concentration and even in small amounts they can significantly enhance the radiation losses. Fig. 2.7 right shows the maximum tolerable impurity concentration to reach ignition. Depending on the charge it ranges from a few % for light atoms to the few 10^{-4} level for high Z materials.

2.6 Magnetic confinement

As discussed in chap. 1, plasmas can be confined by magnetic fields, but in linear configurations the end losses are by far too large to reach the necessary energy confinement time τ_E of the order of some seconds. These end losses can be completely avoided in a toroidal system, but in a simple toroidal system with purely toroidal magnetic field, the magnetic field curvature and gradient (approximately as in Fig. 2.8) result in a vertical drift which is in opposite

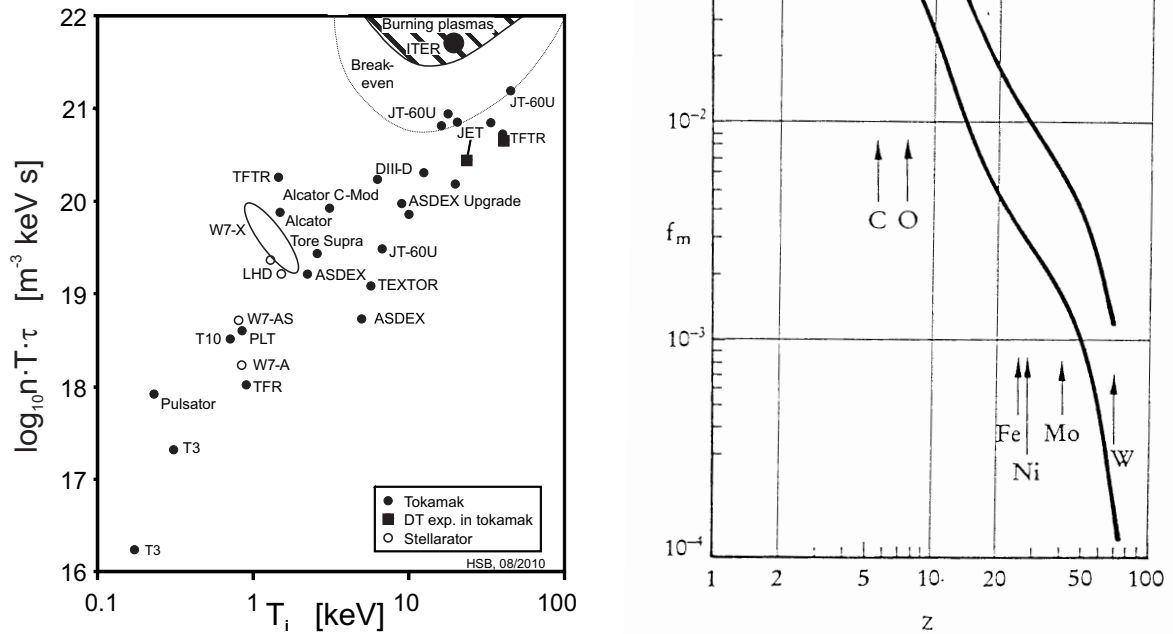


Figure 2.7: Left: Diagram of $nT\tau$ values versus T obtained in different experiments. Right: Maximum tolerable impurity concentrations in a plasma to reach ignition.

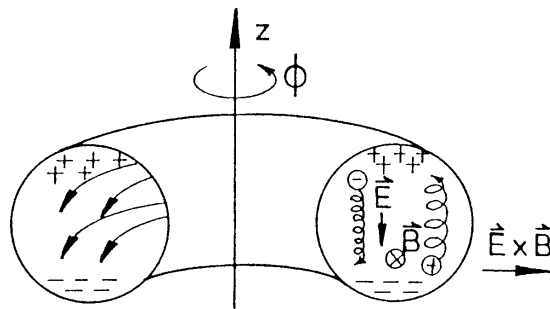


Figure 2.8: Vertical drifts and associated $E \times B$ in a toroidal field.

directions for ions and electrons. The resulting electric field causes an outward $E \times B$ drift of the whole plasma, and therefore such a simple magnetic field configuration will be unstable. To avoid this charge separation, it is necessary to twist the magnetic field lines by additional magnetic field components. Then, single field lines map out so-called flux surfaces. On these flux surfaces, plasma transport is fast, as it is always parallel to B , and therefore plasma parameters usually are constant on a given flux surface. Perpendicular to the flux surfaces, transport

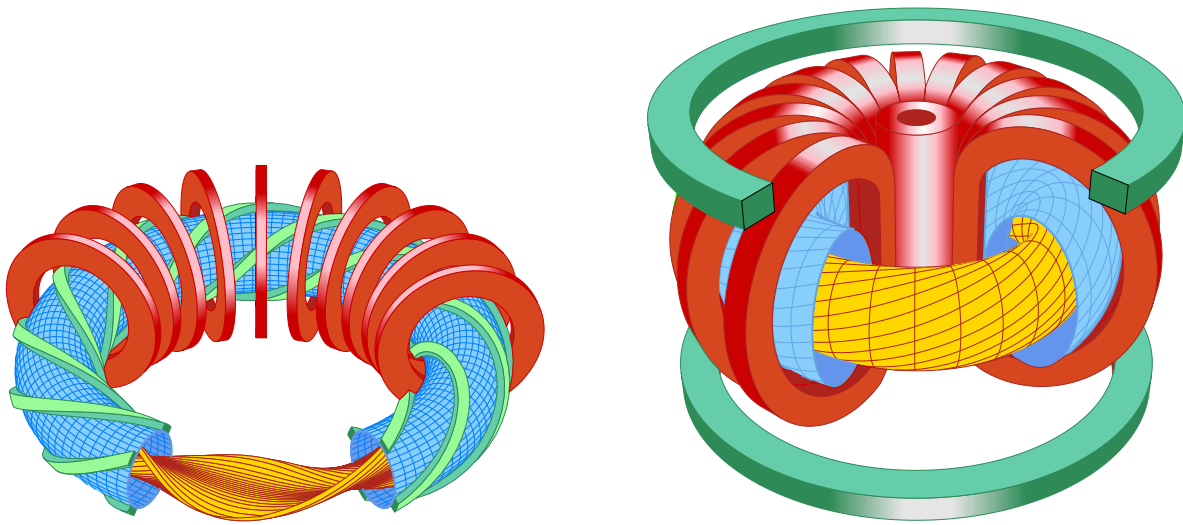


Figure 2.9: Left: Schematic view of a stellarator with four helical coils wound onto the vacuum vessel.
 Right: Tokamak concept. The innermost cylindrical coil is the transformer coil for inducing a plasma current. The toroidal coils above and below the machine create a vertical field for plasma shaping and position control.

is hindered because particle motion perpendicular to B is restricted by the Lorentz force, and therefore plasma parameters can vary strongly in this direction.

Two different principles for twisting the magnetic field lines have been invented in the 50's, and are under investigation worldwide.

2.6.1 The stellarator

The stellarator was invented in 1951 by Lyman Spitzer, Jr. in Princeton. In a stellarator the twist of the field lines is created by external coils wound around the plasma torus, as shown in Fig. 2.9 left. Due to these external currents the plasma shape is not circular, but shows some indentation. In this case, with four coils (neighbouring coils carry opposite current), the plasma has an oval shape.

These external coils have the advantage that the current can be controlled from outside, and can flow continuously, but the configuration shown in Fig. 2.9 left, is very difficult from the engineering point of view, due to the interlinked magnetic coil systems. Also, these *classical* stellarators have shown a rather poor confinement of particles and energy. A solution for both problems has been found by means of numerical optimization of stellarator configurations. Following these studies, *classical* stellarators nowadays have been replaced by *modular* stellarators, where the planar toroidal coils and the helical coils have been replaced by one complex, but modular system of non-planar coils, as will be discussed in chap. 12 and chap. 13.

2.6.2 The tokamak

The second approach is the tokamak proposed by the two Russian physicists I. Tamm and A.D. Sakharov, in the year 1952 and realized by L.A. Artsimovich. The word *tokamak* itself is derived from the Russian words for toroidal chamber with magnetic field. The tokamak concept is outlined in Fig. 2.9 right. The toroidal magnetic field is provided by simple magnets and the necessary twist is produced by the plasma itself, by means of an electric current in the plasma which gives rise to the poloidal component of the twisted magnetic field. The current also serves for plasma build-up and heating. This current is produced by induction, the plasma acting as the secondary winding of a transformer. Tokamaks have proved to be very successful in improving the desired fusion plasma conditions and the today's best experiments are based on the tokamak principle. Of course, a transformer can induce the (dc-) plasma current only during a finite time, while, as mentioned before, a stellarator may principally run steady-state. For truly continuous tokamak operation, alternative current drive methods are being developed. Another disadvantage of the required large plasma current is the potential danger of so-called disruptions: Uncontrolled very fast (~ 10 ms) plasma current decays which can give rise to large forces on the machine.

More details on tokamak physics are described in chap. 10 and chap. 8 and a review on the status of tokamak research is given in [6].

2.6.3 The fusion reactor

The basic geometry of fusion reactors will be a torus (ring) for magnetically confined plasmas. A schematic cross-section of such a reactor is shown in Fig. 2.10. The hot plasma is surrounded by the first wall and blanket. The latter is filled with lithium to produce the tritium, as discussed before, and the majority of thermal energy of the plant is delivered here by neutron moderation. A shield is provided behind the blanket to stop the neutrons not captured by the blanket in order to reduce the heat and radiation loads to the cold structures of the superconducting magnets. The application of superconduction is mandatory for fusion reactors to obtain a positive energy balance.

2.7 Muon-catalyzed fusion

The real issue in achieving nuclear fusion is to overcome the repulsive Coulomb forces of light nuclei. The *conventional* approach is strong heating to reach the ignition conditions described above. Another, more exotic, way is to screen the electric charge by replacing the electron in the hydrogen atom with a muon [9]. This idea was first proposed by A.D. Sakharov in 1948. A muon is an elementary particle, a so-called lepton (*light* particle). This muon has the same properties as an electron, the only difference being that its mass is 200 times larger. Due to its larger mass the muon decays with a half-life of 1.5×10^{-6} seconds

$$\mu^- \longrightarrow e^- + \bar{\nu}_e + \nu_\mu .$$

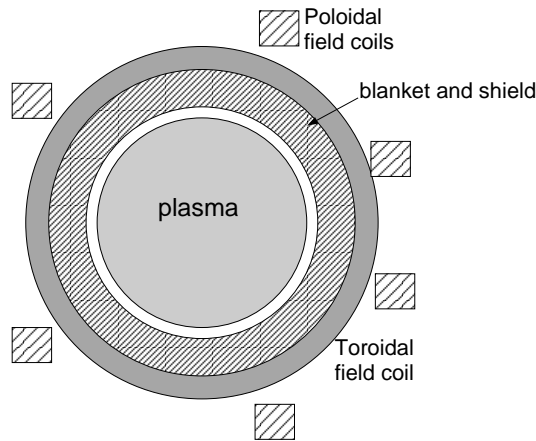


Figure 2.10: Layout of principal components in a conceptual fusion reactor.

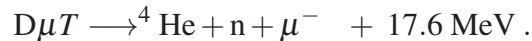
Muons can be produced in accelerators which provide collisions between accelerated protons and some other material. In these collisions many pions are produced. A pion is the lightest elementary particle participating in the strong interaction (so-called hadrons). The three types of pions (π^- , π^+ and π^0) are produced in equal amounts. A negative muon is formed from the decay of a negative pion

$$\pi^- \longrightarrow \mu^- + \bar{\nu}_\mu .$$

In a D-T mixture the muon slows down very fast ($\approx 10^{-9}$ s) and forms a $D\mu$ or $T\mu$ atom with a small Bohr radius of

$$a_\mu = a_e \cdot m_e / m_\mu \approx 2.5 \cdot 10^{-13} \text{ m} .$$

This reduced atomic radius is the key point for possible catalyzed nuclear fusion: If a $D\mu T$ molecule is formed, it takes just 10^{-12} s until quantum mechanical tunnelling triggers a fusion reaction



There are two limiting factors in this approach: the first is the time needed to form a $D\mu T$ molecule. This time can be influenced by some resonance mechanisms. The second limitation comes from the 0.6% probability that the muon will stick to the helium atom after the fusion reaction and will thus be lost for catalyzing more fusion reactions during its lifetime. Recently, experiments obtained fusion rates of more than 100 reactions per muon. For a pure energy producing system this rate is not sufficient, since about 3 GeV ($= 3 \times 10^9$ eV) is needed to produce one negative muon.

References

- [1] G. Gamov; *Zur Quantentheorie des Atomkernes*, Zeitschrift für Physik **51** (1928), p. 204–212.
- [2] J.D. Lawson; *Some Criteria for a Power Producing Thermonuclear Reactor*, Proceedings of the Physical Society **B70** (1967), p.6.

- [3] H.-S. Bosch, G.M. Hale; *Improved Formulas for Fusion Cross-Sections and Thermal Reactivities*, Nuclear Fusion **32** (1992), p. 611–631.
- [4] J. Raeder et al.; *Kontrollierte Kernfusion*, Teubner Verlag, Stuttgart (1981).
- [5] U. Schumacher; *Fusionsforschung*, Wissenschaftliche Buchgesellschaft, Darmstadt (1993).
- [6] J.G. Cordey, R.J. Goldston, R.R. Parker; *Progress toward a Tokamak Fusion Reactor*, Physics Today, January 1992, p. 22–42.
- [7] J.D. Lindl, R.L. McCrory, E.M. Campbell; *Progress Toward Ignition and Burn Propagation in Inertial Confinement Fusion*, Physics Today, September 1992, p. 32–40.
- [8] W.J. Hogan, R. Bangerter, G.L. Kulcinski; *Energy from Inertial Fusion*, Physics Today, September 1992, p. 42–50.
- [9] S.E. Jones; *Muon-Catalysed Fusion Revisited*, Nature **231** (1986), p. 127–133.

Chapter 3

An introduction to MHD, or magnetic fluid dynamics

Bruce D. Scott

3.1 What MHD is

Magneto-hydro-dynamics (MHD) means magnetic fluid dynamics. It is a model system designed to treat macroscopic dynamics of an electrically neutral fluid which is nevertheless made up of moving charged particles, and hence reacts to magnetic fields. Because the magnetic field is in turn produced by electric currents – here, a relative drift between the two fluids of opposite charge density which permeate each other – the resulting dynamical system is rich in nonlinear character.

This is a heuristic introduction to the ideas of fluid dynamics and MHD. Each fluid – they may be termed electrons and ions – is separately treated as a perfect fluid which reacts in a dissipation-free way to the electric and magnetic fields. By perfect fluid, the concept of thermodynamic equilibrium is implied: The effects of dissipation in all forms are taken to be negligible. These include resistivity, thermal conductivity, and viscosity. The two fluids interact only through the electric and magnetic fields they induce. These fields in turn react to changes in the distribution of sources, which are the charge densities and currents represented by the two fluids. Externally imposed fields may also be present. An infinitesimal element of each fluid is assumed to contain an arbitrarily large number of charged particles of the corresponding species, but to be small compared to the spatial scale over which macroscopic thermodynamic or field quantity varies. The picture is a meaningful one if this scale is large compared to the mean-free path between particle collisions, and the radius of gyration of each particle about magnetic field lines is negligibly small. This is the *ideal two-fluid model* of plasma dynamics.

Then, because the mass of an individual electron is so much smaller than that of an individual ion, the contribution of the electrons to fluid inertia may be neglected. With a few additional assumptions which in effect define a parameter regime, the system is treated as a single fluid

which responds to a magnetic force of the Lorentz type, except that the plasma current enters instead of the fluid velocity. The magnetic field, responding to the electric field as usual, is actually advected by the velocity field, since the latter is related in a constitutive way to the electric field. This is the *ideal MHD model* of plasma dynamics, a subset of the two-fluid model.

3.2 The ideas of fluid dynamics

A fluid is in essence a continuous medium. Rather than an ensemble of particles, each individually treated, *populations* of particles are treated. The system is described in terms of a velocity flow field, a density field, and a few thermodynamic state variables. In the simplest picture, the fluid is an ideal gas, in which all state variables are simple relations of the density and temperature.

3.2.1 The density in a changing flow field – conservation of particles

We are first interested in how the density of the fluid evolves, when the flow field is known. This involves the deformation of volumes by the flow. Consider first a volume V , which is fixed in space. The conservation of particles follows simply from counting: The change of the number of particles N , in V is given by the number of particles entering V , less those that leave V . Consider that V is bounded by a surface S , an element of which is ΔS with unit normal \hat{e}_S . For each area element, the number of particles which cross it in a time interval Δt , is given by

$$\delta N = n \Delta x \Delta S, \quad \Delta x = v \cos \theta \Delta t = \mathbf{v} \cdot \hat{e}_S \Delta t,$$

where $n = N/V$ is the density of particles per unit volume, θ is the angle between the velocity vector and the unit normal, and Δx gives the thickness of the region containing particles which cross ΔS during Δt (a note on signs: The unit normal points outward, so a positive δN , indicating particles leaving V , contributes negatively to the change in the total number of particles ΔN).

Since S is a closed surface, we may add up all the contributions from the ΔS 's by performing a surface integral

$$\Delta N = - \oint_S \Delta S n \mathbf{v} \cdot \hat{e}_S \Delta t.$$

Since V is fixed, a change in N affects the density

$$\Delta N = \oint_V dV \Delta n,$$

so upon setting these two expressions equal, we have

$$\oint_V dV \Delta n = - \oint_S dS \cdot (n \mathbf{v}) \Delta t,$$

where ΔS and \hat{e}_S have been combined into dS . Note now that since S is the surface which encloses V , we may apply the Gaussian divergence theorem:

For any volume V enclosed by surface S , with directional element dS , any continuously differentiable vector F satisfies

$$\oint_V dV \nabla \cdot F = \oint_S dS \cdot F .$$

Therefore, we may write

$$\oint_V dV \Delta n = -\Delta t \oint_V dV \nabla \cdot nv .$$

This is valid for arbitrary V ; specifically, it is valid for an infinitesimal volume about any point. This means the integrands must themselves be equal, since in general they do not vanish. Further taking $\Delta t \rightarrow 0$, we obtain

$$\frac{\partial n}{\partial t} = -\nabla \cdot nv$$

as a statement of conservation of particles of number density n , advected by velocity v . It holds for a *fixed* reference frame. The partial time derivative refers to the fact that V is fixed in space.

So what is meant by divergence?

Suppose now that we take the same flow and particle distribution, but now let the boundary surface elements of the volume move with the fluid. Note now that no particles enter or leave V

$$\Delta N = 0 .$$

The volume does, however, change with time: since the density is given by $n = N/V$, its change is inverse to that in V

$$\frac{\Delta n}{n} = -\frac{\Delta V}{V} .$$

At each point, the boundary element moves with the velocity

$$\Delta x = v \Delta t .$$

The separation of points changes according to spatial variations in the velocity

$$\Delta x_2 - \Delta x_1 = (v_2 - v_1) \Delta t .$$

A volume may be expanded in a combination of two ways: Spreading or stretching. If the direction of a surface element dS is taken as the z -direction at some point, spreading is due to the expansion perpendicular to the element: $\partial v_x / \partial x + \partial v_y / \partial y$. Stretching is due to longitudinal variation: $\partial v_z / \partial z$. The sum of these is called the *divergence*, and the divergence of a velocity means the same thing as the expansion of the advected volume

$$\Delta V = V \nabla \cdot (\Delta x) ,$$

or, including Δt , which commutes with spatial derivatives

$$\frac{\Delta V}{\Delta t} = V \nabla \cdot \frac{\Delta x}{\Delta t} = V \nabla \cdot v .$$

With this for the volume change, the density change is given by

$$\frac{\Delta n}{\Delta t} = -\frac{n}{V} \frac{\Delta V}{\Delta t} = -n \nabla \cdot \mathbf{v} ,$$

or

$$\frac{dn}{dt} = -n \nabla \cdot \mathbf{v} ,$$

as a statement of conservation of particles of number density n , advected by velocity \mathbf{v} . It holds for the *co-moving* reference frame. Note that the total time derivative d/dt , gives changes in the frame moving with the fluid at each point, hence the name co-moving.

One final note: A common name for the equation for the conservation of particles is often called the *continuity equation*, since the fact that n and \mathbf{v} are continuously differentiable field quantities has been implicitly used to get it.

3.2.2 The advective derivative and the co-moving reference frame

We now have two statements of the general conservation of particles in terms of the density, n , and the velocity with which they are advected \mathbf{v} . One is in the fixed reference frame

$$\frac{\partial n}{\partial t} = -\nabla \cdot n\mathbf{v} .$$

The other is in the co-moving reference frame

$$\frac{dn}{dt} = -n \nabla \cdot \mathbf{v} .$$

These are actually the same statement in two different coordinate systems. Let the fixed system be denoted as (t, x, y, z) and the co-moving frame as (t', x', y', z') . The transformation between them, which is a *local* transformation, may be written

$$dx' = dx - v_x dt , \quad dy' = dy - v_y dt , \quad dz' = dz - v_z dt .$$

The time derivative transforms as

$$\begin{aligned} \frac{d}{dt} &= \frac{\partial}{\partial t} + \frac{dx}{dt} \frac{\partial}{\partial x} + \frac{dy}{dt} \frac{\partial}{\partial y} + \frac{dz}{dt} \frac{\partial}{\partial z} \\ &= \frac{\partial}{\partial t} + v_x \frac{\partial}{\partial x} + v_y \frac{\partial}{\partial y} + v_z \frac{\partial}{\partial z} , \end{aligned}$$

where the velocity components are not differentiated because the transformation is local. In general form

$$\frac{d}{dt} = \frac{\partial}{\partial t} + \mathbf{v} \cdot \nabla .$$

This is the time derivative in the co-moving frame, written in terms of the time derivative in the fixed frame and the local, instantaneous velocity. It is also known as the *advective derivative*, or in some texts the *substantiative derivative*. Its usefulness is that the laws governing the motion or constitutive change of fluid elements are often most easily formulated in the co-moving frame (or the fluid element's rest frame) and then transformed into the fixed frame. One can readily see that the two equations for the fluid density are equivalent.

3.2.3 Forces on the fluid – how the velocity changes

We now allow the velocity to change, and see how it is caused to change. We examine the forces on the fluid element in the co-moving frame, and then transform to the fixed frame. We consider only fluid pressure and electromagnetic (Lorentz) forces, neglecting such others as gravitation or the effects of moving boundaries.

Consider first the fluid pressure p . Each of the fluid particles is moving with a velocity w , in the co-moving frame, and the average of w over all the particles in a fluid element is zero. Nevertheless, the fluid exerts pressure on any surface, according to the rate at which momentum is transferred by the random particle motion. If p is prescribed, we may compute the net force F , on any fluid element by adding up the forces ΔF , on each surface element dS :

$$\Delta F = p dS .$$

Summing all the force elements over a closed surface gives an area integral

$$F = \oint_S dS p .$$

Since the force is exerted on the enclosed volume, V , we may apply another vector theorem

For any volume V enclosed by surface S , with directional element dS , any continuously differentiable scalar ζ satisfies

$$\oint_V dV \nabla \zeta = \oint_S dS \zeta .$$

It is important to get the correct sign: The force is exerted against the surface from the surrounding fluid; hence the signs in the above should all be negative (except for the theorem). Considering a cubical fluid element, oriented such that the pressure on the right is higher than that on the left: The forces on the top and bottom are equal and opposite, the forces on the front and back are equal and opposite, but the force from the right towards the left is greater than the force from the left toward the right. There is a net force from right to left, given by the pressure difference $\Delta p = p_{\text{right}} - p_{\text{left}}$, times the surface area ΔS . If the coordinates are set up such that z increases towards the right, we can see that the force from right to left is *opposite* to the directional gradient in the pressure. Since the size of the element is Δz , then the force is given by

$$F = -\Delta p \Delta S \hat{e}_z = -\Delta z \Delta S (\Delta p / \Delta z) \hat{e}_z = -\Delta V \nabla p \rightarrow -\oint_V dV \nabla p .$$

This force acts to accelerate the fluid element. The mass in the element is given by the mass of each particle m , times the number of particles N , in the volume V . The element accelerates according to

$$Nm \frac{dv}{dt} = F ,$$

or taking the volume to zero about a given point, the velocity change can be taken inside the integral

$$\oint_V dV nm \frac{dv}{dt} = -\oint_V dV \nabla p .$$

Dispensing with the volumes as before, we obtain

$$nm \frac{dv}{dt} = -\nabla p ,$$

in the co-moving frame, and

$$nm \left(\frac{\partial}{\partial t} + \mathbf{v} \cdot \nabla \right) \mathbf{v} = -\nabla p ,$$

in the fixed frame.

This is the force law which determines how the fluid velocity field changes in reaction to gradients in its pressure. Standing alone, it is the force law for a neutral fluid.

Adding the Lorentz force is straightforward, since the force is a body force, one which acts on the element as a whole and not through the surface. The force on N particles of charge q in the fixed frame is

$$\mathbf{F} = Nq \left(\mathbf{E} + \frac{\mathbf{v}}{c} \times \mathbf{B} \right) = \oint_V dV nq \left(\mathbf{E} + \frac{\mathbf{v}}{c} \times \mathbf{B} \right) ,$$

so that the integrand is added to the neutral fluid force law to obtain the force law for a charged fluid

$$nm \left(\frac{\partial}{\partial t} + \mathbf{v} \cdot \nabla \right) \mathbf{v} = -\nabla p + nq \left(\mathbf{E} + \frac{\mathbf{v}}{c} \times \mathbf{B} \right) .$$

Note that one could just as easily derive the Lorentz force term in the co-moving frame as well, with \mathbf{v} zero, and then transform to the fixed frame via the Lorentz transformation (the low-velocity form of which is the transformation used in sec. 3.2.2.

We now have equations describing the evolution of the density and velocity of a fluid in general, so we could build up the two-fluid system consisting of one set of these for each species, and then close the system with Maxwell's equations for the electric and magnetic fields. This would only be complete for an isothermal system, though, so we do need to discuss how the pressure changes.

3.2.4 Thermodynamics of an ideal fluid – how the temperature changes

The simplest system is the ideal fluid: One which evolves quasi-statically through successive states of local thermodynamic equilibrium. Changes are expected to be slow enough such that equilibrium is maintained, but fast enough so that fluid elements do not exchange entropy.

In thermodynamic equilibrium with only isentropic changes considered, the first law reads

$$\Delta E + p \Delta V = \Delta Q \rightarrow 0 .$$

E is the internal energy of a given fluid element of N particles. For the ideal gas law

$$E = \frac{3}{2} NkT .$$

V is the volume occupied by the N particles. Over infinitesimal time intervals

$$\frac{dE}{dt} + p \frac{dV}{dt} = 0,$$

in the co-moving frame.

We already know how the volume changes

$$\frac{dV}{dt} = V \nabla \cdot \mathbf{v}.$$

Given that the number of particles is kept fixed

$$\frac{3}{2} N k \frac{dT}{dt} + p V \nabla \cdot \mathbf{v} = 0,$$

and since the density is $n = N/V$,

$$\frac{3}{2} n k \frac{dT}{dt} + p \nabla \cdot \mathbf{v} = 0.$$

Now, transforming to the fixed frame, we have the relation governing the change of the fluid's temperature given the flow field and all the thermodynamic state variables

$$\frac{3}{2} n k \left(\frac{\partial T}{\partial t} + \mathbf{v} \cdot \nabla T \right) + p \nabla \cdot \mathbf{v} = 0.$$

3.2.5 The composite fluid plasma system

Under the preceding conditions: Perfect fluid with an ideal gas law, no reactions that create or destroy particles of any species, maintenance of local thermodynamic equilibrium...

The system of several fluids each made up of charged particles of species α evolves according to

$$\begin{aligned} \frac{\partial n_\alpha}{\partial t} + \nabla \cdot n_\alpha \mathbf{v}_\alpha &= 0, \\ n_\alpha m_\alpha \left(\frac{\partial}{\partial t} + \mathbf{v}_\alpha \cdot \nabla \right) \mathbf{v}_\alpha &= -\nabla p_\alpha + n_\alpha q_\alpha \left(\mathbf{E} + \frac{\mathbf{v}_\alpha}{c} \times \mathbf{B} \right), \\ \frac{3}{2} n_\alpha k \left(\frac{\partial T_\alpha}{\partial t} + \mathbf{v}_\alpha \cdot \nabla T_\alpha \right) + p_\alpha \nabla \cdot \mathbf{v}_\alpha &= 0, \end{aligned}$$

while the electric and magnetic fields evolve according to Maxwell's equations

$$\begin{aligned} \nabla \cdot \mathbf{E} &= 4\pi \sum_\alpha n_\alpha q_\alpha, \\ \frac{1}{c} \frac{\partial \mathbf{E}}{\partial t} &= \nabla \times \mathbf{B} - \frac{4\pi}{c} \sum_\alpha n_\alpha q_\alpha \mathbf{v}_\alpha, \\ \nabla \cdot \mathbf{B} &= 0, \\ \frac{1}{c} \frac{\partial \mathbf{B}}{\partial t} &= -\nabla \times \mathbf{E}. \end{aligned}$$

Note that the charge density and the current have been specified in terms of the fluid variables

$$\rho_{ch} = \sum_{\alpha} n_{\alpha} q_{\alpha}, \quad \mathbf{J} = \sum_{\alpha} n_{\alpha} q_{\alpha} \mathbf{v}_{\alpha},$$

The above constitutes a closed system governing the evolution of several charged ideal fluids and the electric and magnetic fields they induce. Note that external fields may also be imposed.

3.3 From many to one – the MHD system

In many cases, the regime of parameters in which the plasma finds itself allows considerable simplification of the multi-fluid system. The fact that the electron mass is so much smaller than that of any ion allows one to neglect the electron inertia in comparison to that of the ions, with the result that the electron force equation becomes a relation for the electric field in terms of the velocity and magnetic field.

For purposes of illustration it is useful to consider that there is only one ion species.

The following assumptions are made:

1. The *displacement current*, which is the term involving the time derivative of \mathbf{E} , is negligible because the time for a light wave to cross the system is much shorter than any relevant dynamical scale.
2. The electron mass is sufficiently small that parallel force balance on the electrons is maintained at all times. This allows the neglect of electron inertia. For the ideal MHD system we assume that the parallel electron dynamics are generally negligible; this means the components of both ∇p_e and \mathbf{E} parallel to the magnetic field.
3. The drift velocity of the electrons relative to the ions due to the current is small compared to the ion velocity. This allows one to assume that all species move with the same velocity, when specifying velocities.
4. Pressure forces are negligible compared to Lorentz forces on all the fluids.
5. The system is approximately neutral, such that the total charge density is negligible compared to that of any constituent.

Note that this does not mean that $\mathbf{E} \rightarrow 0$, but that the spatial scale of any variation is large compared to the Debye length of the plasma, and that the plasma frequency is faster than any rate of change. This means, however, that we can use the relation of zero charge density as a good approximation for the electron density in terms of the ions. For one ion species with charge Ze , this means

$$n_e \approx Zn_i.$$

These assumptions will be checked once we explore the dynamical scales of the MHD system.

3.3.1 The MHD force equation

The electron and ion force equations appear as

$$\begin{aligned} n_i M_i \left(\frac{\partial}{\partial t} + \mathbf{v}_i \cdot \nabla \right) \mathbf{v}_i &= -\nabla p_i + n_i Z e \left(\mathbf{E} + \frac{\mathbf{v}_i}{c} \times \mathbf{B} \right), \\ 0 &= -\nabla p_e - n_e e \left(\mathbf{E} + \frac{\mathbf{v}_e}{c} \times \mathbf{B} \right), \end{aligned}$$

Adding these and using the charge neutrality relation, we obtain

$$\rho \left(\frac{\partial}{\partial t} + \mathbf{v} \cdot \nabla \right) \mathbf{v} = -\nabla p + \frac{1}{c} \mathbf{J} \times \mathbf{B}.$$

This is the MHD force equation. To get it, we have written p for the total pressure $p = p_e + p_i$, and $\rho = n_i M_i$ for the mass density. We have further dropped the subscript on the ion velocity, using this as the bulk fluid velocity. The electron velocity is obtainable from \mathbf{v} and \mathbf{J} . Note that the current is

$$\mathbf{J} = n_i Z e \mathbf{v}_i - n_e e \mathbf{v}_e.$$

The electrons have two roles:

1. They provide pressure, and can be dominant in doing so (but only if the temperatures are allowed to be unequal).
2. They keep the system quasi-neutral through their ability to move arbitrarily fast along the magnetic field lines.

3.3.2 Treating several ion species

One can easily generalise the MHD force equation to a system of several ion species by defining the total velocity as the velocity of the *center of mass*

$$\rho \mathbf{v} = \sum_i n_i M_i \mathbf{v}_i,$$

where the sum is over all the ion species. The mass density evolves according to the continuity equations for all ion species

$$\frac{\partial \rho}{\partial t} + \nabla \cdot \rho \mathbf{v} = 0.$$

Provided all the temperatures are equal, this can be done for the energy equation as well

$$C_v \left(\frac{\partial}{\partial t} + \mathbf{v} \cdot \nabla \right) T + p \nabla \cdot \mathbf{v} = 0,$$

where the specific heat at constant volume is

$$C_v = \frac{3}{2} k \sum_{\alpha} n_{\alpha},$$

and the sum is over all species, including the electrons. Alternatively, this may be combined with the continuity equation to reflect the fact that p/ρ^γ , with $\gamma = 5/3$, is conserved in the dynamics, even for several species (see below).

One very important note: The system can be treated as ideal either if the heat exchange among the particle populations is (1) negligible or (2) so fast that the temperatures are all kept equal. In laboratory plasmas the first of these limits is usually well-satisfied for dynamics, and the second is usually valid for quasi-static equilibria.

3.3.3 The MHD kinematic equation

We need now only determine how the magnetic field evolves, and since the current is given by

$$\mathbf{J} = \frac{c}{4\pi} \nabla \times \mathbf{B} ,$$

that will be enough to close the system.

The magnetic field evolves according to

$$\frac{1}{c} \frac{\partial \mathbf{B}}{\partial t} = -\nabla \times \mathbf{E} ,$$

and from the electron force equation we have

$$\mathbf{E} + \frac{\mathbf{v}_e}{c} \times \mathbf{B} = -\frac{1}{n_e e} \nabla p_e .$$

For the dynamical scales of interest, it will become clear that the pressure gradient is negligibly small in this equation (recall we are neglecting parallel electron dynamics). This is assumption (4) above. We have already assumed that \mathbf{J} is small enough that the electron and ion velocities are equal to high accuracy (assumption 3). This implies that the component of the fluid velocity across the magnetic field is given by the $\mathbf{E} \times \mathbf{B}$ velocity

$$\mathbf{v} = \frac{c}{B^2} \mathbf{E} \times \mathbf{B} ,$$

which means that all the particles $\mathbf{E} \times \mathbf{B}$ drift together across the magnetic field lines, preventing any significant charge build-up. Substituting for \mathbf{E} in the equation for \mathbf{B} , we obtain

$$\frac{\partial \mathbf{B}}{\partial t} = \nabla \times (\mathbf{v} \times \mathbf{B}) .$$

This is the MHD kinematic equation. Whether or not the magnetic field has important effect on the dynamics, it describes how the magnetic field is advected by the flow velocity. Much of the character of MHD springs from this equation, especially its most important consequence: Flux conservation. We will see what this is and what it means in a moment.

3.3.4 MHD at a glance

The complete ideal MHD system is collected here for clarity.

The continuity equation

$$\frac{\partial \rho}{\partial t} + \nabla \cdot \rho \mathbf{v} = 0.$$

The MHD force equation

$$\rho \left(\frac{\partial}{\partial t} + \mathbf{v} \cdot \nabla \right) \mathbf{v} = -\nabla p + \frac{1}{c} \mathbf{J} \times \mathbf{B}.$$

The adiabatic pressure equation

$$\left(\frac{\partial}{\partial t} + \mathbf{v} \cdot \nabla \right) p + \frac{5}{3} p \nabla \cdot \mathbf{v} = 0.$$

The MHD kinematic equation

$$\frac{\partial \mathbf{B}}{\partial t} = \nabla \times (\mathbf{v} \times \mathbf{B}).$$

Ampere's law

$$\mathbf{J} = \frac{c}{4\pi} \nabla \times \mathbf{B}.$$

3.4 The flux conservation theorem of ideal MHD

There is an important result that arises immediately from the MHD kinematic equation. This is that the magnetic flux through any surface element advected by the fluid remains constant no matter what the flow field. Closely related is that the flux through the surface defined by any closed curve within the fluid is also conserved. The result gives rise to the concept of the magnetic flux tube.

3.4.1 Proving flux conservation

Consider an arbitrary, infinitesimal surface defined by a triangle of infinitesimal sides. Three points, x_0 , x_1 , x_2 , are given, and the surface element is

$$d\mathbf{S} = \frac{1}{2} (\mathbf{x}_1 - \mathbf{x}_0) \times (\mathbf{x}_2 - \mathbf{x}_0).$$

The magnetic flux through the surface is given by $\mathbf{B} \cdot d\mathbf{S}$, and it changes according to

$$\frac{d}{dt} \mathbf{B} \cdot d\mathbf{S} = \frac{d\mathbf{B}}{dt} \cdot d\mathbf{S} + \mathbf{B} \cdot \frac{d}{dt} d\mathbf{S}.$$

Remembering that the surface and magnetic field are advected by the fluid

$$\frac{d\mathbf{B}}{dt} = \frac{\partial\mathbf{B}}{\partial t} + \mathbf{v} \cdot \nabla\mathbf{B}.$$

Now find how the surface element changes

$$\frac{d}{dt}d\mathbf{S} = (\mathbf{x}_1 - \mathbf{x}_0) \times \frac{1}{2}(\mathbf{v}_2 - \mathbf{v}_1) + \frac{1}{2}(\mathbf{v}_1 - \mathbf{v}_0) \times (\mathbf{x}_2 - \mathbf{x}_1),$$

noting that $d\mathbf{x}/dt = \mathbf{v}$. Reform this in terms of contributions to $\Delta\mathbf{x} \times \mathbf{v}$

$$\begin{aligned} \frac{d}{dt}d\mathbf{S} &= -(\mathbf{x}_1 - \mathbf{x}_0) \times \frac{1}{2}(\mathbf{v}_1 + \mathbf{v}_0) - (\mathbf{x}_2 - \mathbf{x}_1) \times \frac{1}{2}(\mathbf{v}_2 + \mathbf{v}_1) \\ &\quad - (\mathbf{x}_0 - \mathbf{x}_2) \times \frac{1}{2}(\mathbf{v}_0 + \mathbf{v}_2) \\ &= -\sum_j \Delta\mathbf{x}_j \times \mathbf{v}_j, \end{aligned}$$

where j tracks the midpoint of each line segment. Employ a vector identity to replace this expression by

$$\frac{d}{dt}d\mathbf{S} = -(\mathbf{dS} \times \nabla) \times \mathbf{v}.$$

We require to further re-form this; using the component-index representation of the right side, we have

$$\begin{aligned} [(\mathbf{dS} \times \nabla) \times \mathbf{v}]_i &= \varepsilon_{ipq}(\varepsilon_{plm} \Delta S_l \partial_m) v_q \\ &= \varepsilon_{pqi}(\varepsilon_{plm} \Delta S_l \partial_m) v_q \\ &= \Delta S_q \partial_i v_q - \Delta S_i \partial_q v_q, \end{aligned}$$

which may be written in vector form as

$$\frac{d}{dt}d\mathbf{S} = \mathbf{dS}(\nabla \cdot \mathbf{v}) - (\nabla\mathbf{v}) \cdot \mathbf{dS}.$$

Inserting this back into the original expression for the flux evolution, we obtain

$$\begin{aligned} \frac{d}{dt}\mathbf{B} \cdot \mathbf{dS} &= \left(\frac{\partial\mathbf{B}}{\partial t} + \mathbf{v} \cdot \nabla\mathbf{B} \right) \cdot \mathbf{dS} + \mathbf{B} \cdot [\mathbf{dS}(\nabla \cdot \mathbf{v}) - (\nabla\mathbf{v}) \cdot \mathbf{dS}] \\ &= \mathbf{dS} \cdot \left(\frac{\partial\mathbf{B}}{\partial t} + \mathbf{v} \cdot \nabla\mathbf{B} - \mathbf{B} \cdot \nabla\mathbf{v} + \mathbf{B}\nabla \cdot \mathbf{v} \right) \\ &= \mathbf{dS} \cdot \left(\frac{\partial\mathbf{B}}{\partial t} - \nabla \times \mathbf{v} \times \mathbf{B} \right) = 0, \end{aligned}$$

since the expression in parentheses vanishes according to the MHD kinematic equation.

This proves the flux conservation theorem for an infinitesimal surface element advected by the fluid. It follows that the flux through any *surface* advected by the fluid is also conserved; simply add up all the surface elements.

3.4.2 Magnetic flux tubes

As a result of the fact that the magnetic flux through any surface advected by the fluid is conserved, we may find a group of field lines which serve as the boundary for a definite volume. Define a closed curve which is the boundary for a small but finite surface, the magnetic flux through which is not zero. Follow each field line an arbitrary distance away from the original curve, and define another curve which intersects the same field lines. This is a *magnetic flux tube*. Note that the magnetic flux through the sides of the tube is zero, and because the flux is conserved it stays zero.

Under advection of a flow which deforms the flux tube, the identity of the flux tube is maintained, even though the flux tube may be very greatly twisted and tangled with several other flux tubes. The consequence of this is that the field line topology is not allowed to change.

Consider two flux tubes which may be defined in a sheared magnetic field. Shear in the magnetic field may be thought of as follows: Consider a horizontal plane in which parallel lines are drawn. Now consider a plane immediately above or below the first one, in which parallel lines are also drawn. If the orientation of each set of parallel lines changes from plane to plane, then the field represented by the drawn lines is said to be *sheared*, and the shear can be quantified by giving the rate of change of this angle of orientation with perpendicular distance. Label two very narrow flux tubes, one lying in one such plane and another lying initially in a plane immediately below the first one, “a” and “b”, respectively. Due to the shear, when the flux tubes are brought together by a flow field, they cross. Propose that they might pass through each other as they are forced together. Before the interaction, the magnetic flux through the sides of both tubes is zero. If they are allowed to pass through each other, the field lines due to tube “a” would intersect the sides of tube “b”, and vice versa. The magnetic flux through the sides of the tubes would no longer be zero. This is in obvious contradiction to the flux conservation theorem, so the conclusion is that the flux tubes are never allowed to cross. Note that this conclusion holds as well for flux tubes of infinitesimal cross-section, and hence for individual field lines.

In ideal MHD, magnetic flux tubes and field lines cannot be advected through each other, because of the magnetic flux conservation theorem.

Below, we will explore how this constraint is relaxed by a finite plasma resistivity.

3.5 Dynamics, or the wires-in-Molasses picture of MHD

Note that the magnetic force term in the MHD force equation can be split into two pieces using an elementary vector identity

$$\frac{1}{c} \mathbf{J} \times \mathbf{B} = \frac{1}{c} \left(\frac{c}{4\pi} \nabla \times \mathbf{B} \right) \times \mathbf{B} = -\nabla \frac{B^2}{8\pi} + \frac{\mathbf{B} \cdot \nabla \mathbf{B}}{4\pi}.$$

These two contributions denote *magnetic pressure* and *magnetic tension*, respectively. Magnetic pressure may be combined with gas pressure

$$\rho \left(\frac{\partial}{\partial t} + \mathbf{v} \cdot \nabla \right) \mathbf{v} = -\nabla \left(p + \frac{B^2}{8\pi} \right) + \frac{\mathbf{B} \cdot \nabla \mathbf{B}}{4\pi},$$

where one notes that it behaves like an energy density with two degrees of freedom (for which the pressure and energy density are equal).

The other contribution is magnetic tension. It is part of what gives MHD its unique character (flux conservation, or the advection of magnetic field lines is the other part). To see why it is called tension, consider the magnetic field due to a wire carrying current, surrounded by a vacuum. The field lines are described by loops centered upon the wire, and the forces are obviously zero because it is a vacuum. A cylindrical coordinate system may be defined, with z in the direction of the wire and r perpendicular to it. The only nonzero component of $\mathbf{B} \cdot \nabla \mathbf{B}$ is

$$\mathbf{B} \cdot \nabla \mathbf{B} = -\frac{B^2}{r} \hat{\mathbf{e}}_r.$$

This shows that magnetic tension is a force which acts in the direction of the curvature vector (towards the loop's center), a general result for a curved field line. Since the current outside the wire vanishes, the tension and pressure forces must be in balance: since $B \sim I/r$,

$$-\nabla \frac{B^2}{8\pi} = 2 \frac{B^2}{8\pi} \frac{1}{r} \hat{\mathbf{e}}_r = \frac{B^2}{4\pi r} \hat{\mathbf{e}}_r = -\mathbf{B} \cdot \nabla \mathbf{B}.$$

In such a situation, which can also exist in a plasma where the current is not zero, magnetic pressure and tension are in balance, and the configuration is termed *force-free*.

3.5.1 Magnetic pressure waves

Consider a compression in a magnetised plasma in equilibrium, perpendicular to the magnetic field. The velocity depends only on the direction perpendicular to the field, and it is itself directed perpendicular to the field. In this situation

$$\mathbf{B} \cdot \nabla \mathbf{B} = 0,$$

since \mathbf{B} is compressed perpendicular to its direction. The field lines are compressed together with the fluid, according to the MHD kinematic equation

$$\frac{\partial \mathbf{B}}{\partial t} = -\mathbf{v} \cdot \nabla \mathbf{B} - \mathbf{B} \nabla \cdot \mathbf{v},$$

where the third piece, $\mathbf{B} \cdot \nabla \mathbf{v}$, vanishes due to the geometry. This equation states that \mathbf{B} reacts exactly as would a density

$$\frac{\partial \mathbf{B}}{\partial t} + \nabla \cdot \mathbf{v} \mathbf{B} = 0.$$

With the vanishing magnetic tension, the force equation reads

$$\rho \left(\frac{\partial}{\partial t} + \mathbf{v} \cdot \nabla \right) \mathbf{v} = -\nabla \left(p + \frac{B^2}{8\pi} \right).$$

The result is exactly analogous to sound waves, since both the pressure and magnetic field are perturbed in the same way. Consider small perturbations of short wavelength, on which scale the equilibrium pressure and magnetic field is homogeneous. We *linearise* the equations by retaining terms only to first order in the perturbations, which are denoted by a tilde symbol. For example, B^2 becomes $B^2 + 2\mathbf{B} \cdot \tilde{\mathbf{B}}$, with the term quadratic in $\tilde{\mathbf{B}}$ neglected. The velocity requires no symbol, since it is understood to belong to the perturbations. Both pressure and magnetic perturbations are induced by compression in the velocity

$$\frac{1}{\gamma p} \frac{\partial \tilde{p}}{\partial t} = \frac{1}{B} \frac{\partial \tilde{\mathbf{B}}}{\partial t} = -\nabla \cdot \mathbf{v},$$

with $\gamma = 5/3$. The perturbed force equation reads

$$\rho \frac{\partial \mathbf{v}}{\partial t} = -\nabla \left(\tilde{p} + \frac{B\tilde{\mathbf{B}}}{4\pi} \right),$$

and note the factor of two arising from perturbing B^2 . These may be combined into a wave equation

$$\frac{\partial^2 \tilde{\mathbf{B}}}{\partial t^2} - \left(\frac{B^2}{4\pi\rho} + \frac{\gamma p}{\rho} \right) \nabla_{\perp}^2 \tilde{\mathbf{B}} = 0,$$

where it is noted that the derivatives are all perpendicular to \mathbf{B} .

The second term in the parentheses will be recognised as the square of the adiabatic sound velocity v_s . The first term introduces the characteristic velocity of MHD in general, and the velocity of propagation of small magnetic disturbances in particular. It is the square of the *Alfvén velocity*

$$v_A^2 = \frac{B^2}{4\pi\rho},$$

after Hannes Alfvén, who is recognised as the founder of the MHD description of plasma fluid dynamics. Magnetic pressure waves, like sound waves, are longitudinal waves, but unlike sound waves they are in their pure form only when the disturbance propagates perpendicular to the magnetic field. In general, when both gas pressure and magnetic pressure are present, they both contribute to the actual wave speed: $v^2 = v_s^2 + v_A^2$. More on the ratio of gas to magnetic pressure shortly.

3.5.2 Alfvén waves: magnetic tension waves

Because the magnetic field also exhibits tension, transverse waves similar to waves on a taut string also occur in MHD. Assume now that there is a divergence-free perturbation of a magnetised plasma in equilibrium, still perpendicular to the magnetic field. The velocity now

depends only on the direction parallel to the field, although it is itself directed perpendicular to the field. In this situation

$$\nabla \cdot \mathbf{v} = \tilde{p} = \mathbf{B} \cdot \tilde{\mathbf{B}} = 0,$$

since the disturbance is a transverse-shear perturbation. The field lines are not compressed, but are bent, according to the MHD kinematic equation

$$\frac{\partial \mathbf{B}}{\partial t} = -\mathbf{v} \cdot \nabla \mathbf{B} + \mathbf{B} \cdot \nabla \mathbf{v},$$

where the divergence piece, $\mathbf{B} \nabla \cdot \mathbf{v}$, vanishes due to the geometry. Field line bending becomes clearer when this expression is re-cast in the co-moving frame

$$\frac{d\mathbf{B}}{dt} = \mathbf{B} \cdot \nabla \mathbf{v}.$$

The single contribution arises due to the fact that the field line is moved in alternate directions according to position along it.

This is a new situation, in which the pressure is unperturbed, and the magnetic field is perturbed only through the component perpendicular to the equilibrium field. For homogeneous perturbations

$$\begin{aligned} \frac{\partial \tilde{\mathbf{B}}_{\perp}}{\partial t} &= \mathbf{B} \cdot \nabla \tilde{v}_{\perp}, \\ \rho \frac{\partial \tilde{v}_{\perp}}{\partial t} &= \frac{\mathbf{B} \cdot \nabla \tilde{\mathbf{B}}_{\perp}}{4\pi}, \end{aligned}$$

where there is no factor of two since the perturbed field component is perpendicular. These may be combined into a wave equation

$$\frac{\partial^2 \tilde{\mathbf{B}}_{\perp}}{\partial t^2} - \frac{B^2}{4\pi\rho} \frac{(\mathbf{B} \cdot \nabla)^2}{B^2} \tilde{\mathbf{B}}_{\perp} = 0,$$

where note now that the derivatives are all parallel to \mathbf{B} .

This type of disturbance propagates parallel to \mathbf{B} , and it is a transverse wave. It is called an *Alfvén wave*, since it is the type of propagating wave which exists in MHD but not in neutral fluid dynamics. Its propagation speed is purely the Alfvén velocity. The detection of Alfvén waves in the solar wind by spacecraft in the 1960s gave evidence that MHD phenomena do occur in nature and are not a theoretical artifice.

The concept of field line tension is now clear, since the behavior of the field line in MHD is the same as that of a taut string: *Pluck it, and transverse waves run down the line*. The concept of *field line bending* is closely related: curvature of a field line gives rise to the magnetic tension force. However, field line bending should not be considered as a force in itself, but a cause of one.

A general description of MHD can be that of *molasses threaded by wires*. The wires are magnetic field lines, which exert force on the fluid and which are advected by the fluid as it moves. Additions to this are that the wires exert pressure as well as tension, tending to repel each other, and that in the ideal limit the fluid is not viscous.

One final note: The attractive force between two wires is due to magnetic tension overcoming magnetic pressure.

3.6 The validity of MHD

The Alfvén velocity as just introduced determines the natural time scale of any MHD phenomena of a confined system. With this in hand, we are in a position to judge the validity of MHD by providing *a posteriori* checks on its fundamental assumptions. The Alfvén times are discussed first, and then the checks are made.

3.6.1 Characteristic time scales of MHD

Although they were derived for small disturbances on a homogeneous background, the wave velocities for propagation perpendicular and parallel to the magnetic field indicate the characteristic time scales for adjustment to equilibrium for general perturbations of any confined MHD system. This is much the same as the way the time it takes for a sound wave to cross a neutral fluid in hydrostatic equilibrium under gravity gives the characteristic adjustment time for that fluid. The reason is that a global free oscillation is nothing more than the longest-wavelength limit of the appropriate wave. Examples of the neutral fluid case would be an ocean layer, the Earth's atmosphere, or the Sun. In that case, for a scale length a , the sound-wave transit time is

$$\tau_s = a/c_s ,$$

which is also the inverse of the frequency of the fundamental global mode of oscillation (cf. the five-minute oscillation observed on the Sun).

For a confined plasma in equilibrium the sound speed is replaced by the Alfvén velocity, v_A . It must be noted, though, that the geometry of the confined system is important, since different types of waves propagate parallel to and perpendicular to the magnetic field. With characteristic scale lengths L_\perp perpendicular to the field and L_\parallel parallel to the field, two time scales are of interest. Due to the propagation of magnetic pressure waves, we have the *fast Alfvén*, or compressional Alfvén time: $\tau_A = L_\perp/v_A$. From the propagation of magnetic tension waves (Alfvén waves) we have the *slow Alfvén*, or shear Alfvén time: $\tau_A = L_\parallel/v_A$.

Both of these are usually written as τ_A in the literature, and one has to extract the meaning from the context. The name *shear Alfvén time* originates from the fact that parallel length scales for many laboratory plasma instabilities arise from the existence of magnetic shear in the equilibrium configuration.

These time scales and characteristic velocities can be deduced directly from the MHD force and kinematic equations by *scaling* them. Assuming that the spatial scale is a , the kinematic equation yields

$$\frac{\partial \mathbf{B}}{\partial t} = \nabla \times (\mathbf{v} \times \mathbf{B}) \quad \rightarrow \quad \frac{B}{\tau} \sim \frac{Bv}{a} ,$$

and the force equation yields

$$\rho \frac{dv}{dt} = -\nabla p + \frac{1}{c} \mathbf{J} \times \mathbf{B} \quad \rightarrow \quad \rho \frac{v}{\tau} \sim \frac{B^2}{4\pi a},$$

if the gas pressure is negligible. These similarity relations may be solved for v and τ , given B and a , and the result is $v \sim v_A$ with $\tau \sim a/v_A$.

3.6.2 Checking the assumptions

With a as a representative spatial scale and τ_A as the corresponding time scale, we may now examine the MHD assumptions listed in sec. 3.3, a little out of order.

1. The displacement current is neglected because $v_A \ll c$. This is easily satisfied for laboratory and space plasmas.
5. Quasineutrality depends additionally on both $\tau_A \omega_{pe} \gg 1$ and $\rho_i \gg \lambda_D$. The latter three parameters in this list are the electron plasma frequency ($\omega_{pe}^2 = 4\pi n e^2 / m_e$), the ion Larmor gyroradius ($\rho_i^2 = c^2 M_i T_i / e^2 B^2$), and the Debye screening length ($\lambda_D^2 = T / 4\pi n e^2$). The former inequality is needed to neglect the parallel electric field, as the time scale for the electrons to equilibrate charge is ω_{pe} . The latter is needed in order to use the Lorentz force in the fluid description, since the Lorentz force has the gyroradius as its implicit length scale and the particles are not supposed to individually interact.
3. Fluid elements of all species move with velocity v , with the relative drift implied by \mathbf{J} negligible. This requires $J \ll n e v_A$, or using Ampere's law to express J in terms of B (as magnitudes), we find

$$\frac{\rho_i^2}{a^2} \equiv (\text{drift parameter})^2 \ll \text{plasma beta} = \beta \equiv \frac{8\pi p}{B^2}.$$

(The plasma beta is discussed below.) Neglecting ion inertia as a correction to the $\mathbf{E} \times \mathbf{B}$ velocity for ions depends on the same limit, since $\tau_A \Omega_i \gg 1$ is an equivalent statement ($\Omega_i = eB/M_i c$ is the ion gyrofrequency). The statement that the drift parameter be smaller than some limit is a requirement on how strongly the plasma is magnetised, and that it must be smaller than $\beta^{1/2}$ is usually well-satisfied in any fusion or space plasma application.

2. Electron inertia is negligible because $m_e \ll M_i$ in general. It is negligible compared to the pressure gradient if $n m_e v_A / \tau \ll p/a$, which implies $\beta \gg m_e / M_i$. This has no impact on the MHD kinematic equation, since ∇p is negligible to that anyway. But this serves as a check that electron inertia is negligible even when ion inertia is very strong compared to pressure corrections, which is why a limit on β makes sense (see below).
4. That ∇p is negligible compared to the Lorentz force term is implied as well by (3), since $\mathbf{J} \times \mathbf{B} / c$ is comparable to ∇p and $J \ll n e v_A$. If $\beta \ll 1$, then this is even more so.

3.6.3 A comment on the plasma beta

The *plasma beta*, defined by

$$\frac{\text{gas pressure}}{\text{magnetic pressure}} = \frac{8\pi p}{B^2} \equiv \beta,$$

is very important in plasma fluid dynamics. It gives the relative importance of the gas pressure to the magnetic field as the restoring force to any disturbance. If $\beta \gg 1$, then the magnetic force has a negligible effect on the dynamics, but the magnetic field is still advected by the flow. This is called *MHD kinematics*. It is important in studies of the generation of a magnetic field by a conducting fluid undergoing motion forced by other means, such as convection in a gravitational field. The generation of a large-scale magnetic field by convective turbulence is called the *dynamo effect*, and it is thought to be the most likely scenario for the origin of planetary and stellar magnetic fields. (A note: Some treatments define β with 4π instead of 8π .)

In the opposite limit, $\beta \ll 1$, the gas pressure drops out of the MHD force equation to lowest order in β , but it remains as a slight correction to the geometry of any equilibrium. For such a *low-beta* plasma, the gas pressure is still important because it can break the tendency of magnetic pressure and tension to cancel. A consequence is that a finite gas pressure prevents the establishment of a force-free equilibrium, to which the plasma tends to relax in many important configurations, even in a situation with a nonzero current density. In addition, the gas pressure can cause instability in an equilibrium which would otherwise be stable to MHD perturbations (*MHD-stable*). In the tokamak configuration for a fusion plasma, for example, this fact is responsible for limiting the plasma beta to quite low values.

The tendency of magnetic pressure and tension to cancel is ultimately the reason that assumptions (3) and (5) have to be separately checked.

3.7 Parallel dynamics and resistivity, or relaxing the ideal assumption

One limit which was not examined above is the role of parallel dynamics: The general case of flows parallel to the magnetic field. If we compare the drift velocity implied by \mathbf{J} not to v_A but to v_s , we get a different limit: $\beta \gg \rho_i/a$ (the reader is invited to check this). The drop of one power of the drift parameter places a rather strict limit on how low the beta can be allowed to go. In solar plasmas the drift parameter is really very small, so this point can be ignored. In fusion plasmas, especially tokamak and stellarator plasmas in which β is quite limited by effects arising from the gas pressure, the limit can be violated, and it is nearly always violated in the boundary regions of the plasma. It is important to realise that a perturbation compressing the gas purely parallel to the magnetic field involves no disturbance of the field. A small disturbance of this type merely leads to longitudinal sound waves propagating parallel to the field lines. Such parallel effects may be neglected for any disturbance of the general equilibrium or violent instability, since these evolve on Alfvén time scales. However, transport

phenomena may give rise to force imbalances along the field lines, and these would relax on the parallel sound transit time scale. If phenomena on this scale are of global importance, then the kinematic MHD equation will be affected since although these effects are parallel, the forces they cause may have a nonzero perpendicular curl. When this is the case, studies of the consequences must treat the electron and ion fluids separately, on an equal footing. Further inquiry along these lines is beyond the scope of this introduction to MHD.

A simpler effect which breaks the ideal MHD constraints but still allows treatment of the system as MHD and as a single fluid is electrical resistivity. Resistivity means an exchange of momentum between electrons and ions as their respective fluids drift past each other. The details of the electron-ion collision process are complex, due to the fact that the angle through which an electron is scattered upon close approach to an ion depends strongly on the relative velocity. Nevertheless, by the inclusion of a simple momentum exchange term loosely based on a collision frequency, a qualitative picture of the most important consequence can be given: Magnetic field line diffusion, or how those flux tubes tangled together at arbitrarily small scale eventually relax. MHD with electrical resistivity is called *resistive MHD*.

Consider a plasma with a single ion species of charge e , and allow the ions and electrons to exchange momentum. The continuity and energy equations are unaffected, but the electrons lose momentum to the ions on a time scale given by a collision frequency ν_{ei}

$$0 = -\nabla p_e - n_e e \left(\mathbf{E} + \frac{\mathbf{v}_e}{c} \times \mathbf{B} \right) - n_e m_e \nu_{ei} (\mathbf{v}_e - \mathbf{v}_i),$$

in which inertia is still neglected. To conserve momentum, the same term appears with opposite sign in the ion momentum equation

$$n_i M_i \frac{d\mathbf{v}_i}{dt} = -\nabla p_i + n_i e \left(\mathbf{E} + \frac{\mathbf{v}_i}{c} \times \mathbf{B} \right) + n_e m_e \nu_{ei} (\mathbf{v}_e - \mathbf{v}_i).$$

We now add these two to obtain the resistive MHD force equation

$$\rho \left(\frac{\partial}{\partial t} + \mathbf{v} \cdot \nabla \right) \mathbf{v} = -\nabla p + \frac{1}{c} \mathbf{J} \times \mathbf{B}.$$

Note that since the MHD force equation is one for *total* momentum, the addition of resistivity does not alter its form.

Now consider the MHD kinematics. Solving the electron momentum equation for \mathbf{E} , obtain

$$\mathbf{E} + \frac{\mathbf{v}_e}{c} \times \mathbf{B} = -\frac{\nabla p_e}{n_e e} - \frac{m_e \nu_{ei}}{n_e e^2} n_e e (\mathbf{v}_e - \mathbf{v}_i).$$

As before, we neglect the pressure force and assume that \mathbf{v}_e is \mathbf{v} . Note as well that $n_e e (\mathbf{v}_e - \mathbf{v}_i) = \mathbf{J}$. (The astute reader will note the slight complications that arise when the charge state of the ions differs from $+1$; let this be left as an exercise.)

The electron force balance, modified by resistivity, now reads

$$\mathbf{E} + \frac{\mathbf{v}}{c} \times \mathbf{B} = \eta \mathbf{J},$$

where $\eta = m_e v_{ei} / n_e e^2$ is the resistivity. Inserting this relation into the MHD kinematic equation, we find

$$\frac{\partial \mathbf{B}}{\partial t} = \nabla \times (\mathbf{v} \times \mathbf{B}) - \nabla \times \left(\frac{\eta c^2}{4\pi} \nabla \times \mathbf{B} \right).$$

Assuming for the moment that η is homogeneous, the double-curl operation may be reduced, re-casting the kinematic equation as

$$\frac{\partial \mathbf{B}}{\partial t} = \nabla \times (\mathbf{v} \times \mathbf{B}) + \frac{\eta c^2}{4\pi} \nabla^2 \mathbf{B}.$$

This has the form of a diffusion, which is the role that resistivity plays. The eventual fate of tangled magnetic flux tubes is now apparent. Supposing that

$$\frac{v_A}{a} \gg \frac{\eta c^2}{4\pi a^2},$$

or in terms of the *Lundquist number* S and *resistive decay time* τ_R

$$S \equiv \frac{\tau_A}{\tau_R} \gg 1, \quad \tau_R = \frac{a^2}{\eta c^2 / 4\pi},$$

the system evolves according to ideal MHD on large scales. When flux tubes are tangled on ever-smaller scales, however, some scale, λ , is reached at which $S(a \rightarrow \lambda) \sim 1$. At that scale the magnetic field lines lose their identity through diffusion and *re-connection*, and the tangles are smoothed out.

3.8 Towards multi-fluid MHD

Further relaxing the assumptions of MHD brings one eventually to the necessity of treating all the constituent fluids on an equal footing, especially when further *collisional* phenomena become important. This is in any case beyond the goal of this study, which is to introduce the ideas of MHD. Interested readers will no doubt find it stimulating both to explore MHD phenomena further, and to consider in more depth the different effects one finds in two- or more-fluid dynamics. For this purpose a set of references is provided.

References

A good MHD text, both for an introduction to MHD and for further study of the basic phenomena (it is the very best book containing reconnection and MHD turbulence): *Nonlinear Magnetohydrodynamics*, by D. Biskamp (Cambridge, 1993). It cites all of the references below.

A perhaps more introductory text which is less like a review is *Ideal Magnetohydrodynamics*, by J.P. Freidberg (Plenum Press, New York, 1987).

The standard text for astrophysical MHD applications is *Cosmical Magnetic Fields*, by E.N. Parker (Clarendon Press, Oxford, 1979). Convection of magnetic flux tubes and dynamo theory form the centerpiece of this book.

A tokamak-oriented text which includes the basic MHD problems as well as the more complicated phenomena one encounters is *Theory of Tokamak Plasmas*, by R.B. White (North Holland, Amsterdam, 1989).

The best source on two-fluid dynamics is still the review article by S.I. Braginskii, in *Reviews of Plasma Physics*, M.A. Leontovich, ed. (Consultants Bureau, New York, 1965), Vol. 1, p. 205. It contains a systematic derivation of the equations from kinetic theory as well as a clear introduction to the effects represented by the individual terms (and why they appear). One obtains a good understanding of the dependence of both the two-fluid and MHD models on the kinetic theory of plasmas, and their range of validity.

Chapter 4

Kinetic theory

Emanuele Poli

4.1 Introduction

The most complete description of a plasma composed by N particles would rely on the solution of the $3N$ equations of motion $\mathbf{F}_i = m_i \mathbf{a}_i$, where in the calculation of the force acting on the i -th particle one has to take into account the influence of all the particles in the system. The solution of this formidable set of coupled differential equations for realistic parameters is of course prohibitive from a computational point of view and would, moreover, require the knowledge of the $6N$ initial values of position and velocity of each particle. But perhaps even more important than this is the fact that a complete solution of Newton's equations would simply yield a tremendous amount of unnecessary information, since we will never perform an experiment aiming at determining the *microscopic* behaviour of each particle in the plasma. What we are going to measure are *macroscopic* quantities like density, temperature, currents and so on. To connect these two levels, a statistical approach, in the sense that will be specified in the next section, is required. This is the scope of kinetic theory.

The importance of kinetic theory is twofold. First of all, it constitutes a theoretical foundation for the macroscopic descriptions of a plasma, like fluid theory and magnetohydrodynamics. Moreover, processes whose treatment requires the knowledge of the velocity distribution of the particles in the plasma must be examined in the framework of kinetic theory. In these notes, the first point is not addressed. The focus will be rather on the second aspect. After sketching the derivation of the kinetic equation (see sec. 4.2) and of the Fokker-Planck term (see sec. 4.3), we will consider two of the most known applications of kinetic plasma theory, namely the Landau damping (see sec. 4.4) and the Coulomb collision operator (see sec. 4.5).

In order to be able to fit the content of this lecture in roughly fifteen pages, the standard derivation of the Landau damping, which can easily be found in standard textbooks, has been omitted. A short list of references is given at the end.

4.2 The kinetic equation for a plasma

The fundamental quantity in kinetic theory is the *distribution function*. It expresses the particle density in a six-dimensional phase space $\{\mathbf{r}, \mathbf{v}\}$, in a way which can be easily understood if we first introduce the so-called Klimontovitch distribution function

$$f_K(\mathbf{r}, \mathbf{v}, t) \equiv \sum_{i=1}^N \delta^{(3)}(\mathbf{r} - \mathbf{r}_i(t)) \delta^{(3)}(\mathbf{v} - \mathbf{v}_i(t)) , \quad (4.1)$$

where the sum runs on the position and velocity of the N plasma particles. As stated in the introduction, we do not want to be bound to the knowledge of position and velocity of each particle. Hence, we can introduce a smoother distribution function by averaging f_K over a volume $\Delta\mathbf{r}\Delta\mathbf{v}$ in phase space,

$$f(\mathbf{r}, \mathbf{v}, t) \equiv \frac{1}{\Delta\mathbf{r}\Delta\mathbf{v}} \int_{\Delta\mathbf{r}} d^3\mathbf{r} \int_{\Delta\mathbf{v}} d^3\mathbf{v} f_K = \frac{N_p}{\Delta\mathbf{r}\Delta\mathbf{v}} . \quad (4.2)$$

Here, N_p is the number of particles in the volume $\Delta\mathbf{r}\Delta\mathbf{v}$, which is taken to be large enough to contain a large number of particles (so that the averaging procedure implied by (4.2) is meaningful in a statistical sense); at the same time, this volume should be small compared to the macroscopic scale of the system, in such a way that the coordinates \mathbf{r} and \mathbf{v} can be still be thought as *local*. According to these considerations, we can denote the level of description expressed by the distribution function $f(\mathbf{r}, \mathbf{v}, t)$ as *mesoscopic*. Since the distribution function has the meaning of a phase-space density, its integral over the whole phase space gives the total number of particles in the system, $\int d^3\mathbf{r}d^3\mathbf{v}f = N$. Alternatively, the distribution function can be normalised as $\int d^3\mathbf{r}d^3\mathbf{v}f = 1$, in which case $f\Delta\mathbf{r}\Delta\mathbf{v}$ should be interpreted as the *probability* of finding a particle in the volume $\Delta\mathbf{r}\Delta\mathbf{v}$.

We turn now to the problem of determining an evolution equation for the distribution function. Being a particle density in phase space, f must satisfy a continuity equation, expressing the fact that the total number of particles must be conserved. Such an equation reads

$$\frac{\partial f}{\partial t} + \nabla_{\mathbf{r}, \mathbf{v}} \cdot [(\mathbf{v}, \mathbf{a})f] = 0 ,$$

where $\nabla_{\mathbf{r}, \mathbf{v}} \cdot$ is the divergence in the six-dimensional space. Writing $\mathbf{a} = \mathbf{F}/m$, the previous equation becomes

$$\frac{\partial f}{\partial t} + f \frac{\partial}{\partial \mathbf{r}} \cdot \mathbf{v} + \mathbf{v} \cdot \frac{\partial f}{\partial \mathbf{r}} + f \frac{\partial}{\partial \mathbf{v}} \cdot \frac{\mathbf{F}}{m} + \frac{\mathbf{F}}{m} \cdot \frac{\partial f}{\partial \mathbf{v}} = 0 . \quad (4.3)$$

At this point, we write the force \mathbf{F} as $\mathbf{F}^{\text{ext}} + \mathbf{F}^{\text{int}}$, i.e. we separate the forces *external* to the volume $\Delta\mathbf{r}\Delta\mathbf{v}$ (those acting equally on each particle in this volume), from the *internal* forces arising from the particle interaction (*collisions*) inside $\Delta\mathbf{r}\Delta\mathbf{v}$ (for these internal forces the point-like nature of the plasma is still important). Let us first neglect the contribution of the internal forces and suppose that, at the each *mesoscopic* point of the system, the Hamiltonian equations of motion $\mathbf{v} = \partial H / \partial \mathbf{p}$ and $\mathbf{F}^{\text{ext}} = \dot{\mathbf{p}} = -\partial H / \partial \mathbf{r}$ (with $\mathbf{p} = m\mathbf{v}$) are satisfied. It is then immediate to see that (4.3) simplifies to

$$\frac{\partial f}{\partial t} + \mathbf{v} \cdot \frac{\partial f}{\partial \mathbf{r}} + \frac{\mathbf{F}}{m} \cdot \frac{\partial f}{\partial \mathbf{v}} = 0 \quad (4.4)$$

(the apex ^{ext} will be omitted from now on). This is the collisionless kinetic equation, also called the *Vlasov equation*. Introducing the total time derivative in phase space as $d/dt \equiv \partial/\partial t + \mathbf{v} \cdot \partial/\partial \mathbf{r} + (\mathbf{F}/m) \cdot \partial/\partial \mathbf{v}$, we see immediately that (4.4) can be written simply as $df/dt = 0$. This means that f is constant along trajectories (*characteristics*) satisfying the Hamiltonian equations of motion. Moreover, it conserves entropy.

The influence of the internal forces can be modelled simply by introducing on the right-hand side of (4.4) a collision term, which will be calculated explicitly later (cf. sec. 4.3 and sec. 4.5). The kinetic equation becomes then

$$\frac{\partial f}{\partial t} + \mathbf{v} \cdot \frac{\partial f}{\partial \mathbf{r}} + \frac{\mathbf{F}}{m} \cdot \frac{\partial f}{\partial \mathbf{v}} = \left. \frac{\partial f}{\partial t} \right|_{\text{coll}}. \quad (4.5)$$

In this form, the kinetic equation is also called the *Boltzmann equation*. It exhibits the following important properties, which are reported here without proof. First of all, Boltzmann's H-theorem holds, i.e. the time derivative of the quantity $H \equiv \int f \ln f d^3\mathbf{v}$ is never positive. It can be easily shown that H is (except for a constant term) proportional to $-s$, where s is the entropy density of the system. Moreover, at thermal equilibrium, the distribution function is a Maxwellian, which hence corresponds to the state with maximum entropy. Due to its importance, we report here its explicit form¹

$$f_M = n \left(\frac{m}{2\pi k_B T} \right)^{3/2} \exp(-mv^2/2k_B T), \quad (4.6)$$

where n is the density and T is the temperature. An important quantity connected with the exponent of f_M is the *thermal velocity*

$$v_{\text{th}} \equiv \sqrt{\frac{2k_B T}{m}}. \quad (4.7)$$

Despite their rather compact form, (4.4), (4.5) are by no means easy to solve. This is essentially due to the fact that the forces acting on the system can depend in some complicated way on the distribution function itself. This makes these equations, in general, nonlinear integro-differential equations. An explicit solution of the Vlasov equation is considered in sec. 4.4.

4.3 Markovian processes and the Fokker-Planck equation

In this section, we obtain an equation for the evolution of the distribution function under the influence of the microscopic (internal) forces. In the approach presented here, the effect of these forces is modelled as a stochastic process introducing a probability $\psi(\mathbf{Z}, \Delta\mathbf{Z})$ that the position \mathbf{Z} of a particle in *phase space* changes by an amount $\Delta\mathbf{Z}$ in a time Δt . This probability function does not depend explicitly on the time t , i.e. each transition is independent of the previous history of the particle. Such a process is called *Markovian*. The perhaps best-known example

¹The form reported in (4.6) corresponds to the normalisation $\int d^3\mathbf{r} d^3\mathbf{v} f = N$.

of Markovian process is the Brownian motion. Clearly, the function ψ must be normalised in such a way that its integral over all possible displacements $\Delta\mathbf{Z}$ is equal to one, $\int d(\Delta\mathbf{Z})\psi = 1$.

The distribution function at a given position \mathbf{Z} and time t is supposed to be related to the distribution function at $\mathbf{Z} - \Delta\mathbf{Z}$ and $t - \Delta t$ by the Chapman-Kolmogorov equation

$$f(\mathbf{Z}, t) = \int d(\Delta\mathbf{Z}) f(\mathbf{Z} - \Delta\mathbf{Z}, t - \Delta t) \psi(\mathbf{Z} - \Delta\mathbf{Z}, \Delta\mathbf{Z}), \quad (4.8)$$

which represents a *sum* over all possible displacements $\Delta\mathbf{Z}$ leading to a given position \mathbf{Z} , each term of the *sum* being weighted with its probability ψ . If the changes $\Delta\mathbf{Z}$ are small compared to the size of the system, $|\Delta\mathbf{Z}| \ll |\mathbf{Z}|$, the right-hand side of (4.8) can be expanded as follows

$$f(\mathbf{Z}, t) = \int d(\Delta\mathbf{Z}) \left[f\psi - \Delta\mathbf{Z} \cdot \frac{\partial}{\partial\mathbf{Z}} (f\psi) - \Delta t \frac{\partial f}{\partial t} \psi + \frac{1}{2} \Delta\mathbf{Z} \Delta\mathbf{Z} : \frac{\partial^2 (f\psi)}{\partial\mathbf{Z} \partial\mathbf{Z}} \right], \quad (4.9)$$

where all quantities are evaluated at the position \mathbf{Z} and the dyadic notation has been used in the last term on the right-hand side of (4.9). In this expansion, it has been taken explicitly into account that ψ does not depend on time. Moreover, the expansion is performed up to the second order in \mathbf{Z} but only to the first order in t . This is consistent with the fact that, in a random walk ansatz, the mean square displacement is found to scale linearly with time.

Let us introduce the average changes in $\Delta\mathbf{Z}$ (*friction coefficient*) and $\Delta\mathbf{Z}\Delta\mathbf{Z}$ (*diffusion coefficient*) during the time Δt as

$$\langle \Delta\mathbf{Z} \rangle \equiv \frac{1}{\Delta t} \int d(\Delta\mathbf{Z}) \Delta\mathbf{Z} \psi(\mathbf{Z}, \Delta\mathbf{Z}), \quad (4.10)$$

$$\langle \Delta\mathbf{Z}\Delta\mathbf{Z} \rangle \equiv \frac{1}{\Delta t} \int d(\Delta\mathbf{Z}) \Delta\mathbf{Z}\Delta\mathbf{Z} \psi(\mathbf{Z}, \Delta\mathbf{Z}). \quad (4.11)$$

With these definitions, dividing both sides of (4.9) by Δt and recalling the normalisation condition for ψ (and that f is not a function of $\Delta\mathbf{Z}$) we obtain finally

$$\frac{\partial f}{\partial t} = - \frac{\partial}{\partial\mathbf{Z}} \cdot (\langle \Delta\mathbf{Z} \rangle f) + \frac{1}{2} \frac{\partial^2}{\partial\mathbf{Z} \partial\mathbf{Z}} : (\langle \Delta\mathbf{Z}\Delta\mathbf{Z} \rangle f). \quad (4.12)$$

This is the Fokker-Planck equation², which we will use in the following section to obtain a physical picture of Landau damping and in sec.4.5 to calculate an explicit form for the collision operator.

4.4 Landau damping

The basic difference between a gas and a plasma is the fact that the plasma is composed by charged particles, which react to electromagnetic forces. As mentioned above, this makes the solution of the kinetic equation very complicated even in the collisionless limit, because

²This name is also used for the equation resulting from substituting (4.12) into the right-hand side of the Boltzmann equation (4.5).

the electromagnetic fields that determine these forces are functions of the charge and current distributions in the plasma, and hence of the distribution function itself.

As an example, we consider here the propagation of an electrostatic wave in a collisionless electron plasma (the ions will be supposed to give simply a neutralising static background). For these waves (which do not exist in vacuum, but can propagate in a plasma), the oscillating magnetic field is zero and the electric field is parallel to the wave vector, as can be deduced from the Maxwell equation for the curl of the electric field in the electrostatic limit, $\nabla \times \mathbf{E} = 0$, which yields in Fourier space $\mathbf{k} \times \mathbf{E} = 0$. To account for the interaction between this wave and the plasma, we need then the Vlasov equation (4.4), where the force $\mathbf{F} = -e\mathbf{E}$ must be calculated from

$$\nabla \cdot \mathbf{E} = \frac{\rho_{\text{ch}}}{\epsilon_0} = -\frac{e}{\epsilon_0} \int f d^3\mathbf{v}. \quad (4.13)$$

In the last step, the charge density ρ_{ch} has been expressed as an integral over velocity space of the distribution function. If we substitute (4.13) into the Vlasov equation, we see immediately that it becomes a nonlinear equation for f . However, if we suppose that the influence of the wave is just to produce a small perturbation of the background plasma, we can write the distribution function as $f = f_0 + f_1$, with $|f_1/f_0| \ll 1$, where f_1 represents the effect of the wave. Retaining then only the first-order terms in f_1 (i.e. in a *linear* picture), the coupled Vlasov-Maxwell set of equations becomes

$$\begin{aligned} \frac{\partial f_1}{\partial t} + \mathbf{v} \cdot \frac{\partial f_1}{\partial \mathbf{r}} - \frac{e\mathbf{E}}{m} \cdot \frac{\partial f_0}{\partial \mathbf{v}} &= 0, \\ \nabla \cdot \mathbf{E} &= -\frac{e}{\epsilon_0} \int f_1 d^3\mathbf{v}. \end{aligned} \quad (4.14)$$

The solution derived by Landau (1946) for these equations can be found in many textbooks and is not reported here.

An instructive physical interpretation of the Landau damping can be obtained from a direct calculation of change in the velocity of an electron in the presence of an electrostatic wave and is discussed in the remainder of this section. Since the problem is one-dimensional, we simply write the wave field as

$$\mathbf{E} = E_0 \hat{\mathbf{x}} \cos(kx - \omega t),$$

where again the field amplitude is supposed to be small enough that it leads just to a small perturbation of the electron orbit. If this is the case, we can integrate the equation of motion

$$m \frac{dv}{dt} = -eE_0 \cos(kx - \omega t) \quad (4.15)$$

along the unperturbed orbit $x = x_0 + v_0 t$, to obtain

$$\begin{aligned} \Delta v &= -\frac{eE_0}{m} \int_0^t dt' \cos [kx_0 + (kv_0 - \omega)t'] \\ &= -\frac{eE_0}{m} \frac{1}{kv_0 - \omega} (\sin [kx_0 + (kv_0 - \omega)t] - \sin(kx_0)). \end{aligned} \quad (4.16)$$

The resonant denominator appearing in (4.16) indicates that the energy exchange between wave and particle is particularly effective if the velocity of the particle is close to the phase

velocity of the wave, $v_0 \approx \omega/k$, because in this case the particle does not experience a rapidly oscillating field (with a vanishing average effect), but rather a constant one. Whether Δv is then positive or negative depends on the relative phase kx_0 between wave and particle (in other words, it depends on whether the particle travels in phase with a positive or negative electric field).

At this point, we assume that it is possible to treat the wave-particle interaction as a Markovian process. This amounts to say that we suppose that there is some random process (e.g. binary collisions) running in the background that destroys the phase coherence between particles and wave on a typical time scale τ . We can then calculate the average values of Δv and $(\Delta v)^2$ using (4.10) and (4.11), assuming $\Delta t = \tau$ and that the values of the phase between wave and particle are uniformly distributed (i.e., that the probability ψ is constant). The integral over all the possible *displacements* Δv for a given electron is equivalent to an integral over all the initial phases between the wave and the electron. We obtain immediately

$$\langle \Delta v \rangle = \frac{1}{2\pi\tau} \int_0^{2\pi} d(kx_0) \Delta v|_{t=\tau} = 0$$

and, employing the trigonometric relation $\sin \alpha - \sin \beta = 2 \cos[(\alpha + \beta)/2] \sin[(\alpha - \beta)/2]$ in (4.16),

$$\langle (\Delta v)^2 \rangle = \frac{1}{2\pi\tau} \int_0^{2\pi} d(kx_0) (\Delta v)^2|_{t=\tau} = \frac{e^2 E_0^2}{m^2} \frac{2}{(kv_0 - \omega)^2 \tau} \sin^2 \left[\frac{(kv_0 - \omega)\tau}{2} \right]. \quad (4.17)$$

As we see, $\langle (\Delta v)^2 \rangle$ is proportional to E_0^2 . If we want to use (4.12) to determine the change in the distribution function due to the wave-particle interaction, we need for consistency to calculate $\langle \Delta v \rangle$ also to the second order in E_0 . This can be achieved by integrating the equation of motion, (4.15), along the orbit perturbation Δx given by

$$\Delta x = \int_0^t \Delta v(t') dt' = -\frac{eE_0}{m} \frac{1}{kv_0 - \omega} \left[\frac{-\cos[kx_0 + (kv_0 - \omega)t] + \cos(kx_0)}{kv_0 - \omega} - t \sin(kx_0) \right],$$

where Δv has been taken from (4.16). In calculating the second-order expression for Δv we make the further assumption that $k\Delta x(\tau) < 1$, which implies that the electric field in the equation of motion can be expressed as $E \approx (\partial E / \partial x)\Delta x$. The result is then

$$\begin{aligned} \Delta v = -\frac{e}{m} \Delta x \int_0^t dt' \frac{\partial E}{\partial x} &= \frac{e^2 E_0^2}{m^2} \frac{k}{(kv_0 - \omega)^2} \\ &\times \left[\frac{-\cos[kx_0 + (kv_0 - \omega)t] + \cos(kx_0)}{kv_0 - \omega} - t \sin(kx_0) \right] \\ &[\cos[kx_0 + (kv_0 - \omega)t] - \cos(kx_0)], \end{aligned} \quad (4.18)$$

which allows us to obtain finally

$$\langle \Delta v \rangle = \frac{1}{\tau} \frac{e^2 E_0^2}{m^2} \frac{k}{(kv_0 - \omega)^2} \left[\frac{-1 + \cos[(kv_0 - \omega)\tau]}{kv_0 - \omega} + \frac{\tau}{2} \sin[(kv_0 - \omega)\tau] \right]. \quad (4.19)$$

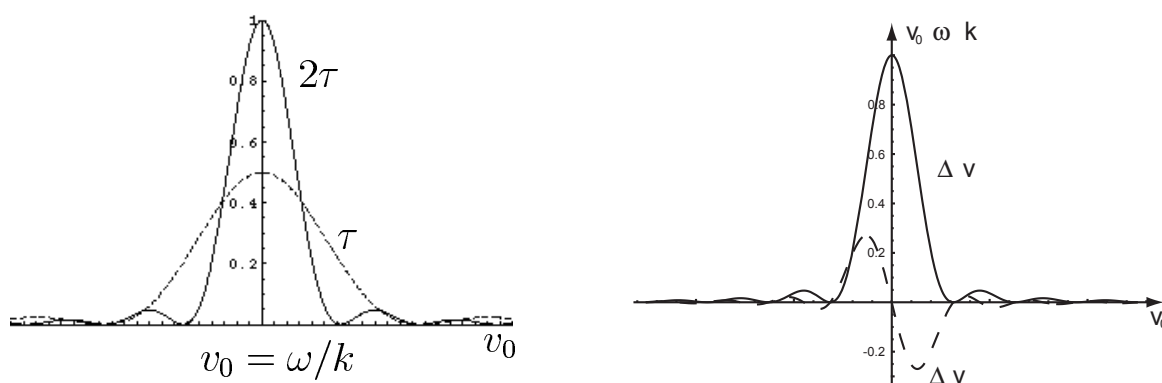


Figure 4.1: Left: The quantity $\langle(\Delta v)^2\rangle$ as a function of v_0 .
Right: The quantities $\langle\Delta v\rangle$ and $\langle(\Delta v)^2\rangle$ as functions of v_0 .

We can now make some comments on these results. First of all, we notice that $\langle(\Delta v)^2\rangle$ is peaked around $v_0 = \omega/k$, as shown in Fig. 4.1 left for two different values of the parameter τ . The fact that the peak value of $\langle(\Delta v)^2\rangle$ increases with τ but its width decreases can be explained as follows. When the interaction time becomes longer, more energy can be exchanged between the electron and the wave, but only if the velocity of the particle is closer to the resonance condition, because otherwise it will be kicked away from the resonance by the wave field. For this reason, the net energy exchange turns out to be independent of τ . In the limit $\tau \rightarrow \infty$ we have³ $\langle(\Delta v)^2\rangle \rightarrow \pi(eE_0/m)^2 \delta(kv_0 - \omega)$ i.e. only particles which exactly satisfy the resonance condition contribute to the energy exchange, according to the standard result for Landau damping.

Before turning to the Fokker-Planck equation to determine the variation of the kinetic energy of the electrons interacting with the wave, we point out that the following relation holds

$$\langle\Delta v\rangle = \frac{1}{2} \frac{\partial}{\partial v_0} [\langle(\Delta v)^2\rangle] , \quad (4.20)$$

as can be verified from a direct differentiation of (4.17) employing the trigonometric identity $\sin^2(\alpha/2) = (1 - \cos \alpha)/2$. The dependence of $\langle\Delta v\rangle$ and $\langle(\Delta v)^2\rangle$ on v_0 is shown in Fig. 4.1 right.

The $\langle\Delta v\rangle$ term, which has been computed going up to the second order in the evaluation of wave-particle interaction, has also a simple meaning. Consider first the particles which are (slightly) slower than the wave: Those which have a phase such that they are accelerated by the wave field are brought into resonance and exchange energy for a longer time than those which are decelerated by the wave. On average, hence, slower particles are accelerated. Similarly, particles which are faster than the wave will, on average, lose energy while interacting with the wave.

Using (4.12) we can now determine the energy gained (or lost) by an electron distribution interacting with an electrostatic wave. In the picture given here, the distribution function f determines the distribution of the initial velocities v_0 . Let us now drop the subscript from v_0

³We recall the representation of the δ -function as $\delta(x) = \lim_{a \rightarrow 0} (a/\pi x^2) \sin^2(x/a)$.

for simplicity. The time derivative of the kinetic energy \mathcal{E} of the plasma is

$$\frac{\partial \mathcal{E}}{\partial t} = \int dv \frac{mv^2}{2} \frac{\partial f}{\partial t} = \int dv \left[mv \langle \Delta v \rangle + \frac{1}{2} m \langle (\Delta v)^2 \rangle \right] f, \quad (4.21)$$

where the first term on the right-hand side of (4.12) has been integrated once by parts and the second term twice.

We can now discuss the different mechanisms that contribute to the change in the particle energy.

1. The energy is quadratic in the velocity. Random changes in v lead to a non-vanishing change in the energy $m \langle (\Delta v)^2 \rangle / 2$.
2. The average $\langle \Delta v \rangle$ is odd in v around ω/k . However, $\int v \langle \Delta v \rangle dv < 0$. If f is not a function of v then the first term on the right-hand side of (4.21) will give a negative contribution. It turns out that in this case the negative contribution exactly cancels the positive contribution of $m \langle (\Delta v)^2 \rangle / 2$. This can be immediately seen if we substitute (4.20) into the first term on the right-hand side of (4.21) and then integrate this first term by parts to obtain $\partial \mathcal{E} / \partial t = -(m/2) \int dv \langle (\Delta v)^2 \rangle v \partial f / \partial v$, which is clearly zero if f is independent of v .
3. If f is a function of velocity such that there are more particles for which $v < \omega/k$ than for $v > \omega/k$ (which usually the case), there is a net increase in particle energy, i.e. an absorption of energy from the wave.

Summarising, there will be a net absorption of wave energy if the gradient of the distribution function at $v = \omega/k$ is negative, as we know from the standard picture of Landau damping. That the absorption is proportional to the gradient of the distribution function can also be seen by combining (4.12) with (4.20) to obtain

$$\frac{\partial f}{\partial t} = \frac{1}{2} \frac{\partial}{\partial v} \left[\langle (\Delta v)^2 \rangle \frac{\partial f}{\partial v} \right] \quad (4.22)$$

i.e. by writing the Fokker-Planck equation as a diffusion equation in velocity space. If the gradient of the distribution function is zero, no diffusion takes place and f is constant in time. If the gradient of the distribution function is positive, then the particles give energy to the wave. This will lead to an instability in which the wave amplitude is exponentially increasing.

Finally, let us briefly discuss the limits of applicability of our description of Landau damping. If the coherence time τ becomes too long, particles can make multiple bounces in the potential of the wave, i.e. they are trapped in this potential, making our (quasi-)linear ansatz invalid. Indeed, we decided to ignore such a process when we have assumed that $k\Delta x(\tau) < 1$. The absorption in the case of multiple bounces goes down. Another point deserves particular attention. The mechanism of Landau damping does not rely explicitly on collisions. However, there has to be some random process which destroys the coherence between the particles and the wave on a short enough time scale. As mentioned before, in a plasma this role is usually played by collisions. Since the amount of energy absorption is independent of the coherence time (if it is not too long), the collision frequency can determine the coherence time without appearing explicitly in the expression for the amount of damping of the wave.

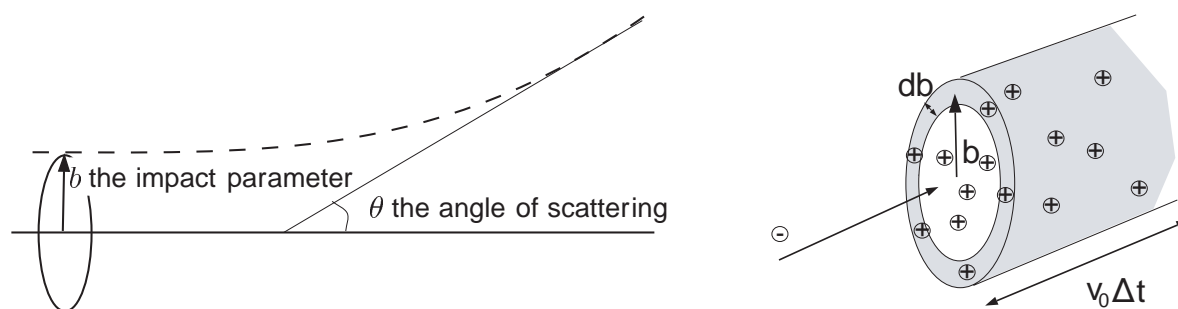


Figure 4.2: Left: Scattering of the particle in the center of mass frame.
Right: Scattering of an electron by ions as the electron travels for a time Δt .

4.5 The Fokker-Planck collision operator

As mentioned in sec. 4.2, the discreteness of the particles reveals itself through the appearance of *internal* forces, i.e. of collisions. Coulomb collisions can be regarded as a Markovian process leading to a change of the particle velocity, if we suppose that each collision event can be regarded as independent of the previous ones. So, we want to employ (4.12) to determine the right-hand side of (4.5). Before calculating the average changes in the particle velocity for a single electron according to (4.10) and (4.11), let us briefly recall some basic features of Coulomb scattering.

A Coulomb interaction between two particles labeled one and two leads to a scattering over an angle θ in the center of mass frame as sketched in Fig. 4.2 left. This angle is determined by the impact parameter b through the equation

$$\tan \frac{\theta}{2} = \frac{b_0}{b}, \quad (4.23)$$

where b_0 is the impact parameter for 90° angle scattering

$$b_0 = \left| \frac{e_1 e_2 (m_1 + m_2)}{4\pi \epsilon_0 m_1 m_2 |\mathbf{g}|^2} \right|, \quad (4.24)$$

where the relative velocity $\mathbf{g} \equiv \mathbf{v}_1 - \mathbf{v}_2$ has been introduced. In the following, we will denote with \mathbf{v}_1 the velocity of particle one before the collision and with \mathbf{v}'_1 its velocity after it.

What we want to calculate is the average value of $\Delta \mathbf{v}_1 \equiv \mathbf{v}'_1 - \mathbf{v}_1$. Introducing the centre-of-mass velocity $\mathbf{v}_{cm} \equiv (m_1 \mathbf{v}_1 + m_2 \mathbf{v}_2) / (m_1 + m_2)$, and recalling that in the absence of external forces (neglected on the time scale of the collision process) $\mathbf{v}_{cm} = \mathbf{v}'_{cm}$, it is easy to show that

$$\Delta \mathbf{v}_1 = \frac{m_2}{m_1 + m_2} \Delta \mathbf{g} = \frac{m_2}{m_1 + m_2} g (\sin \theta \cos \phi, \sin \theta \sin \phi, \cos \theta - 1).$$

In the last step, we have chosen the reference frame in such a way that \mathbf{g} is in the direction of the z -axis, $\mathbf{g} = (0, 0, g)$ and we have employed cylindrical coordinates. As expressed by (4.23), there is a one-to-one correspondence between θ and b , so that an average in θ can be substituted by an average over b . In fact, the probability that particle one is scattered by particle

two between an angle θ and an angle $\theta + d\theta$ during the time Δt is given by the probability of finding particle two inside a cylindrical cell of radius between b and $b + db$ and of length $|\mathbf{v}_1 - \mathbf{v}_2|\Delta t = |\mathbf{g}|\Delta t$ (see Fig. 4.2 right for the case of an electron scattered by an ion population). We can hence write

$$\langle \Delta \mathbf{v}_1 \rangle = \frac{m_2}{m_1 + m_2} \int d\phi \int b db \int d^3 \mathbf{v}_2 |\mathbf{g}| f(\mathbf{v}_2) \Delta \mathbf{g}. \quad (4.25)$$

Before proceeding with the calculation of this integral, it is important to understand whether 90° -scattering processes are likely to occur, or if small-angle diffusion dominates. To this aim, we can calculate the mean value of b_0 over the velocity distribution, for instance in the case of a Maxwellian distribution (4.6). We can then compare this value with the typical distance between particles in the plasma, to know whether they come close enough to experience 90° -degree scattering. In general, the mean value of a quantity $A(\mathbf{v})$ over the distribution function is obtained from

$$\bar{A} \equiv \frac{\int A(\mathbf{v}) f_M(\mathbf{v}) d^3 \mathbf{v}}{\int f_M(\mathbf{v}) d^3 \mathbf{v}}.$$

In order to calculate \bar{b}_0 , according to (4.24) we have to evaluate the average distribution of the initial inverse squared velocities $1/v_0^2$

$$\overline{1/v_0^2} = \int \frac{f_M(v_0)}{v_0^2} d^3 \mathbf{v}_0 = 4\pi \int_0^\infty \frac{f_M(v_0)}{v_0^2} v_0^2 dv_0 = \frac{m}{k_B T},$$

where the integral over the polar angles has been performed in the first step and the formula $\int_0^\infty \exp[-x^2] dx = \pi^{1/2}/2$ has been used in the second. This yields

$$\bar{b}_0 = \frac{e_1 e_2}{4\pi \epsilon_0 k_B T} \equiv \lambda_L,$$

which is the definition of the *Landau length* λ_L . This quantity must be compared with the average distance of the plasma particles. This can be easily done by evaluating the number of particles within a sphere of radius λ_L , taking $e_1 = e_2 = e$. Recalling the definition of the Debye length $\lambda_D^2 = \epsilon_0 k_B T / e^2 n$ one obtains immediately

$$\frac{4\pi}{3} \lambda_L^3 n = \frac{1}{3} \left(\frac{1}{4\pi \lambda_D^3 n} \right)^2 = \frac{1}{27 N_D^2} \ll 1,$$

$N_D \equiv (4\pi/3) \lambda_D^3 n \gg 1$ being the number of particles inside the Debye sphere. This result shows that the particles are usually not close enough in order for large-angle scattering to occur, so that the plasma is dominated by small-angle collisions. In other words, the Coulomb potential is usually much smaller than the mean kinetic energy of the particles.

It follows from these considerations that the integral over b in (4.25) can safely be performed taking b_0 as the lower integration bound, because below this value no scattering process occurs. In the opposite limit, it is known that for distances larger than the Debye length the potential of a charged particle is screened by the others, so that also for $b > \lambda_D$ no scattering takes

place. Moreover, since small-angle collisions dominate, we can approximate $\sin \theta \approx \theta$ and $\cos \theta \approx 1 - \theta^2/2$. (4.25) becomes then

$$\begin{aligned} \langle \Delta \mathbf{v}_1 \rangle &= \frac{m_2}{m_1 + m_2} \int_0^{2\pi} d\phi \int_{b_0}^{\lambda_D} b db \int d^3 \mathbf{v}_2 f(\mathbf{v}_2) g^2 \left(\theta \cos \phi, \theta \sin \phi, -\frac{\theta^2}{2} \right) \\ &= -\frac{2\pi m_2}{m_1 + m_2} \int_{b_0}^{\lambda_D} b db \int d^3 \mathbf{v}_2 g \mathbf{g} \frac{\theta^2}{2} \end{aligned}$$

(remember that \mathbf{g} points by definition in the z -direction). Since from (4.23) it is $\theta^2/2 \simeq 2b_0^2/b^2$, using the definition of b_0 (4.24) we arrive finally at

$$\langle \Delta \mathbf{v}_1 \rangle = -\frac{e_1^2 e_2^2 \ln \Lambda}{4\pi \epsilon_0^2 m_1^2} \frac{m_1 + m_2}{m_2} \int d^3 \mathbf{v}_2 f(\mathbf{v}_2) \frac{\mathbf{g}}{g^3}, \quad (4.26)$$

where we have introduced the *Coulomb logarithm* $\ln \Lambda \equiv \ln(\lambda_D/b_0) \gg 1$.

The same exercise can be performed for $\langle \Delta \mathbf{v}_1 \Delta \mathbf{v}_1 \rangle$. First of all, let us write down the elements of the symmetric matrix $\{\Delta g_i \Delta g_j\}$

$$\begin{aligned} \Delta g_1 \Delta g_1 &= g^2 \theta^2 \cos^2 \phi, & \Delta g_2 \Delta g_2 &= g^2 \theta^2 \sin^2 \phi, & \Delta g_3 \Delta g_3 &= g^2 \frac{\theta^4}{4}, \\ \Delta g_1 \Delta g_2 &= g^2 \theta^2 \cos \phi \sin \phi, & \Delta g_1 \Delta g_3 &= -g^2 \frac{\theta^3}{2} \cos \phi, & \Delta g_2 \Delta g_3 &= -g^2 \frac{\theta^3}{2} \sin \phi. \end{aligned}$$

The only non-vanishing elements after the integration over ϕ are the elements “11” and “22” (neglecting terms of order θ^4), for which we have

$$\int_0^{2\pi} d\phi \Delta g_1 \Delta g_1 = \int_0^{2\pi} d\phi \Delta g_2 \Delta g_2 = \pi g^2 \theta^2, \quad (4.27)$$

where again we can approximate $\theta^2 = 4b_0^2/b^2$. This yields

$$\begin{aligned} \langle \Delta v_{1i} \Delta v_{1j} \rangle &= \left(\frac{m_2}{m_1 + m_2} \right)^2 \int_0^{2\pi} d\phi \int_{b_0}^{\lambda_D} b db \int d^3 \mathbf{v}_2 f(\mathbf{v}_2) g \Delta g_i \Delta g_j \\ &= \frac{e_1^2 e_2^2 \ln \Lambda}{4\pi \epsilon_0^2 m_1^2} \int d^3 \mathbf{v}_2 f(\mathbf{v}_2) \frac{g^2 \delta_{ij} - g_i g_j}{g^3}, \end{aligned} \quad (4.28)$$

where the last expression derives from the fact that $g_1 = g_2 = 0$, $g_3 = g$. The two following identities, which can be checked employing the definition of \mathbf{g}

$$-\frac{\mathbf{g}}{g^3} = \frac{\partial}{\partial \mathbf{v}_1} \left(\frac{1}{g} \right) \quad \frac{g^2 \delta_{ij} - g_i g_j}{g^3} = \frac{\partial^2 g}{\partial v_{1i} \partial v_{1j}} \quad (4.29)$$

help us put the previous expressions in a more compact form

$$\langle \Delta \mathbf{v}_1 \rangle = \gamma \frac{\partial H}{\partial \mathbf{v}_1}, \quad (4.30)$$

$$\langle \Delta v_{1i} \Delta v_{1j} \rangle = \gamma \frac{\partial^2 G}{\partial v_{1i} \partial v_{1j}}, \quad (4.31)$$

where $\gamma \equiv e_1^2 e_2^2 \ln \Lambda / 4\pi \epsilon_0^2 m_1^2$ and

$$H(\mathbf{v}_1) \equiv \frac{m_1 + m_2}{m_2} \int d^3 \mathbf{v}_2 \frac{f(\mathbf{v}_2)}{|\mathbf{v}_1 - \mathbf{v}_2|} \quad G(\mathbf{v}_1) \equiv \int d^3 \mathbf{v}_2 f(\mathbf{v}_2) |\mathbf{v}_1 - \mathbf{v}_2| \quad (4.32)$$

are the *Rosenbluth potentials*. Substituting (4.30) and (4.31) into the Fokker-Planck equation we obtain the following form for the Coulomb collision term

$$\left. \frac{\partial f}{\partial t} \right|_{\text{coll}} = -\gamma \frac{\partial}{\partial \mathbf{v}_1} \cdot \left(f(\mathbf{v}_1) \frac{\partial H}{\partial \mathbf{v}_1} \right) + \frac{\gamma}{2} \frac{\partial^2}{\partial \mathbf{v}_1 \partial \mathbf{v}_1} : \left(f(\mathbf{v}_1) \frac{\partial^2 G}{\partial \mathbf{v}_1 \partial \mathbf{v}_1} \right). \quad (4.33)$$

The collision operator is local, i.e. all quantities are evaluated at the same position. Moreover, it is nonlinear in the distribution function, which appears once explicitly and once implicitly in the Rosenbluth potentials.

Before applying (4.33) to the case of a *test particle* in a uniform plasma in thermal equilibrium, we observe that the collision operator conserves particle number, momentum and energy. Furthermore, as stated in sec. 4.2, it satisfies Boltzmann's H-theorem.

Consider now the simple case in which a single particle with velocity $\mathbf{V}(t)$ collides with a thermal background, for which the distribution of the velocities \mathbf{v}_2 is Maxwellian

$$f(\mathbf{v}_2) = \frac{n}{\pi^{3/2} v_{\text{th}}^3} e^{-v_2^2/v_{\text{th}}^2} \quad (4.34)$$

with $v_{\text{th}}^2 \equiv 2k_B T/m$, see (4.7). The distribution function for the colliding particle is simply

$$f(\mathbf{v}_1) = \delta^{(3)}[\mathbf{v}_1 - \mathbf{V}(t)]. \quad (4.35)$$

The moments of (4.33) can be calculated to obtain expressions for the rate of change of velocity, energy, etc. as shown below. Let first multiply (4.33) by \mathbf{v}_1 and integrate over $d^3 \mathbf{v}_1$. On integrating twice by parts, the last term on the right-hand side of (4.33) vanishes. The other term can be integrated once by parts. The result is an evolution equation for the velocity of the test particle

$$\frac{\partial \mathbf{V}}{\partial t} = \gamma \frac{\partial H}{\partial \mathbf{V}}. \quad (4.36)$$

This confirms the interpretation of the first term on the right-hand side of the Fokker-Planck equation (4.12) as a dynamical friction decelerating the particle. Using (4.34), the Rosenbluth potential H and its derivative can be computed analytically as

$$H(\mathbf{v}) = \left(\frac{m_1 + m_2}{m_2} \right) \frac{n}{v} \phi \left(\frac{v}{v_{\text{th}}} \right),$$

where the index one has been dropped for simplicity and

$$\phi(x) \equiv \frac{2}{\sqrt{\pi}} \int_0^x dt e^{-t^2} \quad (4.37)$$

is the error function. Noting that H is in our case an isotropic function, we can write (4.36) as

$$\frac{\partial \mathbf{V}}{\partial t} = \gamma \frac{\partial H(\mathbf{V})}{\partial \mathbf{V}} \equiv -\mathbf{v}_f(\mathbf{V}) \mathbf{V}, \quad (4.38)$$

which defines the frictional coefficient ν_f . Computing explicitly the derivative of H we have

$$\nu_f = \frac{2\gamma}{V} \left(\frac{m_1 + m_2}{m_2} \right) \frac{n}{v_{th}^2} \psi \left(\frac{V}{v_{th}} \right), \quad (4.39)$$

where

$$\psi(x) \equiv \frac{\phi(x) - x\phi'(x)}{2x^2} \quad (4.40)$$

is the Chandrasekhar function. The functions ϕ and ψ have the following limits

$$\begin{aligned} \lim_{x \rightarrow 0} \phi(x) &= \frac{2x}{\sqrt{\pi}}, & \lim_{x \rightarrow \infty} \phi(x) &= 1, \\ \lim_{x \rightarrow 0} \psi(x) &= \frac{2x}{3\sqrt{\pi}}, & \lim_{x \rightarrow \infty} \psi(x) &= \frac{1}{2x^2} \end{aligned}$$

and they are constants of order one for $x = 1$.

From (4.39) we see that the frictional coefficient is proportional to density and inversely proportional to temperature. For very fast test particles, $V/v_{th} \rightarrow \infty$, ν_f is proportional to $1/V^3$, while it is independent of V at low speeds, $V/v_{th} \rightarrow 0$. Eq. (4.38) then implies that the frictional force increases with V at small speeds, but decreases as V increases in the opposite limit. This means that a current in a plasma is usually carried by fast electrons in the tail of the distribution function. Another interesting consequence is the phenomenon of the so-called *runaway electrons*, for which the friction becomes too small to balance a constant accelerating force, like for instance a constant electric field.

As a second example, we multiply (4.33) by $v_{1\perp}^2$ and integrate over d^3v_1 , assuming again that the distribution functions for the colliding particles are given by (4.34) and (4.35). Here, $v_{1\perp}^2$ is the sum of the squares of the components of v_1 perpendicular to $V(0)$. In this case, only the second term on the right-hand side of (4.33) is found to contribute and we obtain

$$\frac{\partial V_{\perp}^2}{\partial t} = \frac{2\gamma}{V} \frac{\partial G}{\partial V}. \quad (4.41)$$

For a Maxwellian plasma, the Rosenbluth potential G and its derivative can again be computed analytically. A *collision frequency* ν can be defined by imposing the right-hand side of (4.41) to equal to νV^2 , with the result

$$\nu = \frac{2\gamma}{V^3} n \left[\phi \left(\frac{V}{v_{th}} \right) - \psi \left(\frac{V}{v_{th}} \right) \right]. \quad (4.42)$$

In order to evaluate the collision frequency, (4.42), we will assume that a test electron travels at a speed $V = v_{th,e}$ and a test ion at $V = v_{th,i}$.

For the case of electron-electron and ion-ion scattering we take then $\phi(1) - \psi(1) \approx 1$ and recalling the definition of γ we get (taking the ion charge equal to absolute value of the electron charge)

$$\begin{aligned} \nu_{ee} &= \frac{ne^4 \ln \Lambda}{2\pi\epsilon_0^2 m_e^2 v_{th,e}^3}, \\ \nu_{ii} &= \frac{ne^4 \ln \Lambda}{2\pi\epsilon_0^2 m_i^2 v_{th,i}^3}. \end{aligned}$$

For the case of an electron scattered by ions and of an ion scattered by electrons we have to take in ϕ and ψ the limit for $x \rightarrow \infty$ and $x \rightarrow 0$, respectively

$$\begin{aligned} \nu_{ei} &= \frac{ne^4 \ln \Lambda}{2\pi\epsilon_0^2 m_e^2 v_{th,e}^3} \left[1 - \frac{1}{2(v_{th,e}/v_{th,i})^2} \right] \propto \frac{1}{m_e^2 v_{th,e}^3}, \\ \nu_{ie} &= \frac{ne^4 \ln \Lambda}{2\pi\epsilon_0^2 m_i^2 v_{th,i}^3} \frac{4}{3\sqrt{\pi}} \frac{v_{th,i}}{v_{th,e}} \propto \frac{1}{m_i^2 v_{th,e} v_{th,i}^2}. \end{aligned}$$

For nearly equal electron and ion temperatures, $T_e \approx T_i$, we have $v_{th,i} \approx v_{th,e}(m_e/m_i)^{1/2}$. The resulting ordering of these collision frequencies is then

$$\nu_{ee} : \nu_{ii} : \nu_{ei} : \nu_{ie} = 1 : \left(\frac{m_e}{m_i}\right)^{1/2} : 1 : \left(\frac{m_e}{m_i}\right). \quad (4.43)$$

The ions have a smaller (by a factor $(m_e/m_i)^{1/2}$) thermal velocity need more time than the electrons to meet and be deflected by each other. An even longer time is needed for a heavy ion to be deflected by the much lighter electrons.

As a last application of (4.33), we derive the so-called energy exchange times, which are related to the typical time scale required for a particle population to relax to a Maxwellian. Indicating by \mathcal{E} the kinetic energy of the test particle, we can write $\Delta\mathcal{E} = m[v_1^2 - V(0)^2]/2$. Following again the procedure outlined before, i.e. multiplying both sides of (4.33) by $(\Delta\mathcal{E})^2$ and integrating over v_1 , it is possible to derive an equation for the evolution of $\Delta\mathcal{E}$ in the form

$$\frac{\partial(\Delta\mathcal{E})^2}{\partial t} = \nu^E \left(\frac{mV^2}{2}\right)^2,$$

where the energy exchange frequency defined in the previous equation is found to be

$$\nu^E = \frac{8\gamma}{V^3} n \psi\left(\frac{V}{v_{th}}\right). \quad (4.44)$$

Assuming again v_1 of the order of the thermal speed, we first see that $\nu_{ee}^E \sim \nu_{ee}$ and $\nu_{ii}^E \sim \nu_{ii}$. Moreover, in analogy with (4.43), we can write an ordering of these frequencies for different species

$$\nu_{ee}^E : \nu_{ii}^E : \nu_{ei}^E (\sim \nu_{ie}^E) = 1 : \left(\frac{m_e}{m_i}\right)^{1/2} : \left(\frac{m_e}{m_i}\right). \quad (4.45)$$

In other words, thermal equilibration is reached first by electrons (on the electron-electron collision time scale), then by ions (on the ion-ion collision time), whereas equilibration between these two species takes place after a time which is longer than the electron thermalisation time by a factor m_i/m_e .

Acknowledgments

I wish to thank Dr. R. Bilato and Dr. A. G. Peeters for making available the scripts of their previous lectures on this subject.

References

Most of the material of this lecture is exhaustively covered in Chapters 7 and 8 of T.J.M. Boyd and J.J. Sanderson, *The Physics of Plasmas*, Cambridge University Press, and for Landau damping in Chapter 8 of T.H. Stix, *Waves in Plasmas*, AIP (1992). The physics of Coulomb scattering is described in H. Goldstein, *Classical Mechanics* (2nd edition), Addison-Wesley, 1980.

For a more advanced reading on the derivation of the collision operator the review article of Trubnikov in *Reviews of Plasma Physics*, Ed. M.A. Leontovich, Consultants Bureau, NY, 1965, Vol. 1 is still an undying masterpiece.

For insatiable readers, we recommend the seminal (original) papers of Landau on Coulomb interactions in Plasmas, *Zh. Eksper. Theor. Fiz.* **t**, p. 203 (1937), and on Landau Damping, *J. Phys (Moscow)* **10**, p. 25 (1946): They are examples of rare clarity and rigorous logic.

Chapter 5

Plasma Waves and Wave Heating

Volodymyr Bobkov

5.1 Introduction

In a fusion reactor, a temperature of 10 to 20 keV is required to exploit the reaction $D + T \rightarrow {}^4\text{He} + n + 17.6 \text{ MeV}$ successfully. In the ignited plasma, temperature is sustained by the heating via the α -particles (${}^4\text{He}$) which are created in the reaction and are confined in the plasma. However, to reach the ignition and to control the ignited plasma, additional heating and current drive systems are required.

Generally, heating of the plasma means that the kinetic energy of the electrons and of ions is increased. However, the commonly used heating schemes do not act on the different plasma species in the same way. Rather, velocity increments are given only to a fraction of the plasma particles. Furthermore, this velocity increase is not isotropic. It is the subsequent collisions between the heated fraction and the bulk plasma that lead to randomization and equipartition of the additional energy. On the other hand, this energy also causes enhanced radiation losses and particle losses to the walls. Eventually, the plasma reaches a new steady-state where the energy input per time balances the energy losses. This power flow is schematically shown in Fig. 5.1. There the conversion efficiency of the electric power into heating power and the loss in the process of coupling the heating power to the plasma have been included.

Different heating methods have been developed and are successfully applied to plasmas:

- Ohmic heating (OH) is specific to a tokamak. It is the Joule dissipation of the toroidal plasma current that is driven by the tokamak central solenoid. By itself this heating does not suffice to drive the plasma to reactor relevant temperatures, because its effectiveness deteriorates with increasing temperature (lower resistivity) while the losses due to bremsstrahlung radiation increase. At the same time, with increasing plasma current, MHD stability limits plasma performance. OH is not usable for stellarators since it would unduly modify the magnetic field structure.

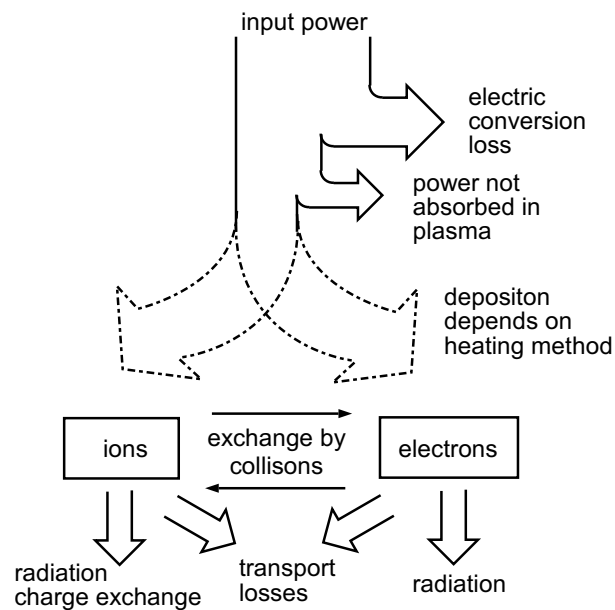


Figure 5.1: Principle of power flow for plasma heating.

- Neutral beam injection (NBI) heating consists of injecting a beam of neutral fuel atoms at high energy that can cross the magnetic field lines into the plasma and can be ionized in the confined plasma region. By prudent choice of neutral beam geometry, energy and plasma density one can obtain heating profiles peaked either closer to the plasma center ("on-axis" heating) or to the plasma periphery ("off axis"). Through collisions the beam ions transfer their energy to the bulk plasma.
- Wave heating, or in other words Radio Frequency heating (RF) consists of launching high power electromagnetic waves into the plasma. Depending on the choice of frequency, antenna (launcher) geometry, plasma density and composition, different species and locations of the plasma can be heated. RF heating is predominantly applied in the range of low frequency Alfvén waves (1–10 MHz), ion cyclotron frequencies (30–100 MHz, IC range), lower hybrid frequencies (1–10 GHz, LH range) and electron cyclotron frequencies (50–150 GHz, EC range).

In a fusion reactor based on the tokamak principle, a non-inductive current drive in the plasma (not attributed to the OH current induced by the solenoid) is required, in order to increase the pulse length and to improve power plant economy. Current drive systems also provide a tool to control MHD activity in the plasma and to tailor current profile for better performance. The current drive can be done either with NBI (by making the injection angle more oblique one) or by the wave systems (e.g. by launching waves predominantly in one direction). In stellarators, current drive might also be necessary in order to compensate for the bootstrap current (self-generated toroidal current associated with trapped particles in the plasmas with high pressure gradients).

In this chapter we discuss wave heating. The challenge of launching RF power into the plasma can be separated to: wave generation, coupling, propagation and absorption. Methods used for wave generation and coupling at the interface between the launcher and the plasma vary

depending on the frequency range used. In many cases in typical magnetic fusion plasmas, the propagation of the RF waves is well described by the cold plasma approximation, because the plasma pressure is much smaller than the magnetic pressure. However when describing wave resonances, wave absorption and particular wave modes which might exist in hot plasma, expansions to the cold plasma model or full kinetic description (warm plasma) are often required.

5.2 Wave propagation in cold plasma

Wave propagation is characterized by a dispersion relation which determines \mathbf{k} (wave vector) as a function of ω (frequency). Generally, the dispersion relation is derived after the Maxwell equations for the perturbed quantities (assuming plane waves) and generalized Ohm's law are used to achieve the wave equation for Fourier amplitude of the electrical field $\mathbf{E}_{\omega,k}$:

$$\mathbf{k} \times (\mathbf{k} \times \mathbf{E}_{\omega,k}) + \frac{\omega^2 \overset{\leftrightarrow}{\mathbf{K}}}{c^2} \mathbf{E}_{\omega,k} = 0,$$

here $\overset{\leftrightarrow}{\mathbf{K}}$ is dielectric tensor, ω is generator frequency and c is speed of light. For E_x, E_y, E_z components of $\mathbf{E}_{\omega,k}$ in Cartesian coordinates, this equation represents a system of homogeneous linear equations. For this system to have non-zero solutions, determinant of the matrix of the coefficients in front of E_x, E_y, E_z should be 0, in other words:

$$\det \left[\mathbf{N} \times (\mathbf{N} \times \mathbf{I}) + \overset{\leftrightarrow}{\mathbf{K}}(\omega, \mathbf{N}) \right] = 0$$

which is known as a dispersion relation, with $\mathbf{N} = (\mathbf{k} \cdot c)/\omega$ being the refractive index.

Assuming \mathbf{N} to be in x, z plane, assigning z -axis as a direction of external magnetic field, the wave equation above can be re-written as:

$$\begin{pmatrix} K_{xz} - N_z^2 & K_{xy} & K_{xz} + N_x N_z \\ K_{yx} & K_{yy} - N_x^2 - N_z^2 & 0 \\ K_{xz} + N_x N_z & 0 & K_{zz} - N_x^2 \end{pmatrix} \begin{pmatrix} E_x \\ E_y \\ E_z \end{pmatrix} = 0.$$

The cold plasma approximation allows to determine the dielectric tensor $\overset{\leftrightarrow}{\mathbf{K}}$. The approximation is made when the equations are combined with the equation of motion of particles where only the Lorentz force balances the inertial term. One gets:

$$\overset{\leftrightarrow}{\mathbf{K}} = \begin{pmatrix} K_{xx} & K_{xy} & 0 \\ K_{yx} & K_{yy} & 0 \\ 0 & 0 & K_{zz} \end{pmatrix}$$

with $K_{xx} = K_{yy} = 1 - \sum_s \omega_{ps}^2 / (\omega^2 - \Omega_s^2) \equiv \epsilon_{\perp}$, $K_{yx} = -K_{xy} = i \sum_s \Omega_s / \omega \cdot \omega_{ps}^2 / (\omega^2 - \Omega_s^2) \equiv \epsilon_{yx}$, $K_{zz} = 1 - \sum_s \omega_{ps}^2 / \omega^2 \equiv \epsilon_{\parallel}$, where $\omega_{ps}^2 = q_s^2 n_s / (M_s \epsilon_0)$, $\Omega_s = q_s B / M_s$ are the squares of the plasma frequency and the cyclotron frequency correspondingly, related to plasma species s .

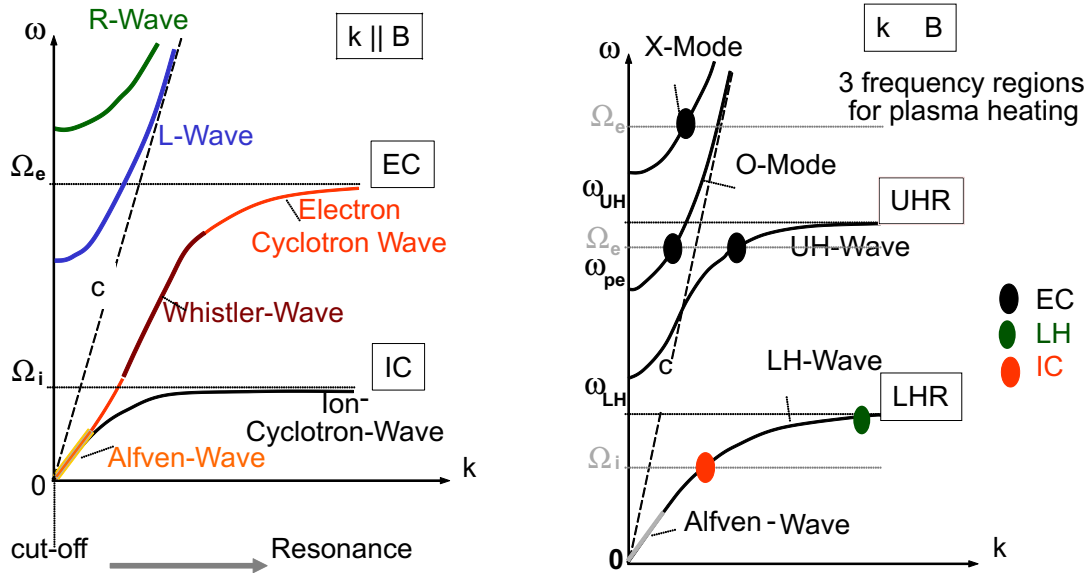


Figure 5.2: Left: Wave propagation parallel to B_0 in cold plasma.
Right: Wave propagation perpendicular to B_0 in cold plasma.

Here q_s is particle charge, B is magnetic field, M_s is particle mass and ϵ_0 is permittivity of vacuum.

For simplicity, let us consider two-component plasma with electrons and ions and two particular cases of wave propagation: parallel to the external magnetic field B_0 (i.e. $k \parallel B_0$) and perpendicular to the magnetic field ($k \perp B_0$).

For wave propagation along the main magnetic field ($k \parallel B_0$), i.e. defining $N_x = 0$ and $N_y = 0$, dispersion relation yields two solutions for propagative waves:

$$N_z^2{}_{1,2} = \frac{\omega^2 \pm \omega\Omega_e + \Omega_e\Omega_i - \omega_{pe}^2}{(\omega \pm \Omega_i)(\omega \pm \Omega_e)}.$$

These solutions correspond to either right-hand (R, solution with +) or left-hand (L, solution with -) circularly polarized waves, the sign being also determined by the ratio $(iE_x)/E_y = \pm 1$. The corresponding diagrams for the solutions in the (ω, k) space are shown in Fig. 5.2 left which includes particular cases of the two solutions: Whistler-wave and Electron Cyclotron wave for the R-solution; Alfvén wave (so-called shear Alfvén wave) and Ion Cyclotron wave for the L-solution.

For wave propagation perpendicular to the main magnetic field ($k \perp B_0$), i.e. defining $N_z = 0$ and $N_y = 0$, two existing solutions are:

1. Ordinary (O-) wave for which electric field of the wave is parallel to B_0 and dispersion is equal to that without B_0 :

$$N_x^2{}_{1} = 1 - \frac{\omega_{pe}^2}{\omega^2}.$$

2. Extraordinary (X-) wave for which the electric field is perpendicular to \mathbf{B}_0 .

$$N_x^2 = \frac{(\omega^2 + \omega\Omega_e + \Omega_e\Omega_i - \omega_{pe}^2)(\omega^2 - \omega\Omega_e + \Omega_e\Omega_i - \omega_{pe}^2)}{(\omega^2 - \omega_{LH}^2)(\omega - \omega_{UH}^2)},$$

where ω_{LH} and ω_{UH} are lower and upper hybrid frequencies correspondingly, defined via $1/\omega_{LH}^2 = 1/(\Omega_i^2 + \omega_{pi}^2) + 1/(|\Omega_e\Omega_i|)$ and $\omega_{UH}^2 = \Omega_e^2 + \omega_{pe}^2$. While at the frequencies close to ω_{LH} and ω_{UH} the waves are called lower hybrid and upper hybrid waves, the wave below Ω_i is the so-called compressional Alfvén wave (Fig. 5.2 right).

The extrema of the solutions where $N = 0$ (wave cut-off) or $N = \infty$ (wave resonance) are of particular interest. Cut-offs mark regions of the plasma where the wave cannot propagate and resonances mark regions where the phase and group velocity go to zero, thus where the wave energy is bound to pile up, unless something happens. In the latter region the phase velocity becomes smaller than the thermal velocity of the plasma particles and the cold plasma dispersion relation is no longer sufficient to describe the plasma properly. Here thermal effects need to be included. This can be done in an orderly fashion through a finite Larmor radius (FLR) expansion where the smallness parameter is the ratio of the Larmor radius to the perpendicular wavelength. This increases the order of the dispersion relation and leads to the appearance of new waves that were not present in the solution of the cold plasma dispersion relation. At the former resonances coupling to the new waves occurs. The dispersion relation also predicts damping of the waves. This does not come as a surprise since the Kramers-Kronig relations state (based on causality) that resonances in the real part of the dispersion relation are connected with a non-vanishing imaginary part (usually predicting damping).

In the case of the perpendicular propagation, the cold plasma dispersion relation yields resonances at the lower hybrid frequency, the upper hybrid frequency and at the ion-ion-hybrid frequency (close to the ion cyclotron frequencies). The latter occurs only in a multi-ion species plasma (not described above). Surprisingly, no resonances occur at the ion cyclotron or the electron cyclotron frequencies Ω_i and Ω_e , respectively. At these frequencies the cyclotron motion of the ions and electrons short-circuits the circularly polarized wave component that rotates in the same direction as the considered species, thus completely quelling a possible resonance. In the case of wave absorption on electrons (LH and EC range), to account for the absorption correctly, FLR contributions and relativistic corrections need to be included to obtain the cyclotron resonances.

Perpendicular wave propagation properties define the predominant frequency ranges (IC, LH, EC) used for RF plasma heating in today's large magnetic confinement experiments, because one usually wants to deliver RF power from the plasma periphery across the magnetic field to the confined plasma. The particular frequency ranges will be discussed in detail later.

In reality, the finite size of the plasma bounded by a conducting wall and the shape of the antenna imposes boundary conditions. In particular, the antenna often fixes the values of k_{\parallel} of the launched waves (and accordingly N_{\parallel} with the latter being N_z using the convention above), i.e. their k_{\parallel} -spectrum, for a given frequency (ω) of the RF generator. This together with the values of the plasma density and magnetic field determine the corresponding response of the plasma and N_{\perp} values (or N_x). It can be shown that for an arbitrary direction of wave

propagation in cold plasma (prior to going to the limits of the parallel and perpendicular wave propagation), the dispersion relation yields two distinctive solutions for N_{\perp}^2 , the so-called slow and fast waves. The waves are distinguished by the corresponding phase velocity ω/k , with that being small for the slow wave and high for the fast wave.

5.3 Aspects of wave absorption (damping)

The damping process of the wave on plasma species can be understood on a kinematic level. If a charged particle moves in the same direction and with about the same speed as the phase velocity of a wave, the wave electric field in the moving frame of the particle stays constant and the particle is accelerated or decelerated depending on its position with respect to the wave. If there are more particles that are decelerated than there are particles that are accelerated then there is net energy transfer from the wave to these resonant particles. The wave is damped and the average velocity of the particles is increased. For a Maxwellian velocity distribution wave damping can become significant for waves with phase velocities between one and three times the thermal velocity. Since collisions only partially restore the distribution function such an absorption process leads to a local deviation in velocity space.

The motion along the magnetic field still separates out and a wave-particle resonance is possible if the wave has an electric field component along the magnetic field and its phase velocity component and the particle velocity component v_{\parallel} fulfil the requirement for wave-particle resonance (not to be confused with wave resonance): $v_{\parallel} - \omega/k_{\parallel} \approx 0$. This requirement allows for the so-called Landau damping of the wave on the particles, known from the kinetic theory.

If the wave has circularly polarized component it can also couple to the gyro-motion of the particles. Resonant interaction requires $v_{\parallel} - \omega/k_{\parallel} - l\Omega/k_{\parallel} \approx 0$ where l is the number of the harmonic. Such transfer of energy from wave to particles is called Landau cyclotron damping. The resonance condition says that energy transfer between the wave and the resonant particles is possible not only if the Doppler-shifted wave frequency matches the gyro-frequency of the particle Ω , but also if it is a multiple l of this frequency. If $l \neq 1$, it is necessary that the wave field has a gradient perpendicular to the magnetic field, for wave energy to be transferred to a particle.

Let us consider heating at the first harmonic ($l = 2$, usually referred as "second harmonic" in experiments). Let us say that at one point particle and electric field point in the same direction and the particle is being accelerated (see Fig. 5.3 at $t = 0$). After the particle has rotated half a gyro-orbit, the electric field has already completed a full revolution (see Fig. 5.3 at $t = T$). Thus the electric field points again in the same direction, yet the velocity direction of the particle is reversed and the particle is decelerated during the second half of its gyro-motion. On average, net energy transfer takes place only if the electric field changes magnitude over the plane of the gyro-orbit of the particle. In other words, if the wave electric field has a gradient, net energy transfer does become possible.

Similar processes exist involving the interaction between the magnetic moment of the gyrating particle and the magnetic field of the wave. They are called transit time magnetic pumping (TTMP).

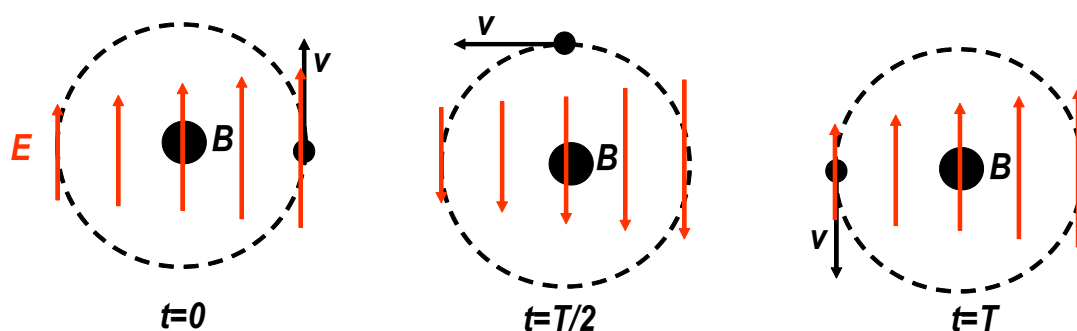


Figure 5.3: Net acceleration of gyrating particles for the first harmonic resonance (usually referred as "second harmonic") with wave electric field having a gradient.

Concludingly, an RF wave which can propagate into plasma and is not hindered by cut-offs from accessing a perpendicular wave resonance, can be absorbed there. The absorption efficiency depends on:

1. the amount of the power that is converted into a wave that has the
2. proper polarization and phase velocity to be resonant with particles of the plasma and
3. the slope of the velocity distribution function of the resonant particles.

In addition, large field amplitudes can lead to a non-linear enhancement of the wave absorption process.

The changes in the distribution function, in particular if a tail of fast, confined particles with decreased collision frequencies is created, can be useful for current drive if the toroidal symmetry is broken and the waves are predominantly launched into one direction.

5.4 Heating in the ion cyclotron range of frequencies

To launch waves in the IC frequency range, and in particular, the fast wave in the plasma, an antenna is used near the plasma edge. The antenna is usually an arrangement of current carrying poloidal conductors, called current straps. The fast wave travels almost perpendicular to the magnetic field lines into the plasma center where they can be absorbed at an ion cyclotron resonance or an ion-ion-hybrid resonance. The location of these resonances depends predominantly on the magnetic field strength. In a tokamak, for example, the toroidal magnetic field decreases radially proportional to $1/R$, thus the resonant zones are vertical layers where $\Omega_i(R) = \omega$.

In this frequency range $\omega \approx \Omega_i$ the slow wave is evanescent except at very low density. Then $|\epsilon_{\parallel}| \gg |\epsilon_{\perp}|$, $|\epsilon_{yx}|$ and the fast wave dispersion relation is given by:

$$N_{\perp}^2 = \epsilon_{\perp} - N_{\parallel}^2 - \frac{\epsilon_{yx}^2}{\epsilon_{\perp} - N_{\parallel}^2}.$$

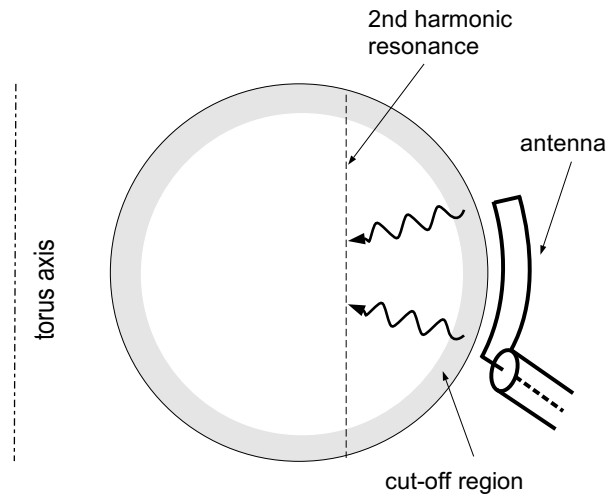


Figure 5.4: Principle of 2nd harmonic ion cyclotron heating.

This wave is elliptically polarized with a small component of the electric field in the direction of the magnetic field. There is a cut-off at the plasma edge for densities below a typical value of several times 10^{18} m^{-3} . Note that, as said before, for single species plasma this dispersion relation does not have a resonance even though ϵ_{\perp} goes to infinity at the ion cyclotron resonance. The situation changes if finite Larmor radius effects are taken into account or the plasma is allowed to have more than one ion species.

After FLR contributions have been added to the fast wave dispersion relation one finds that due to the parallel electric field component and for higher electron temperatures there is weak Landau and TTMP damping of the electrons even if no ion resonance is present in the plasma. Using this process is called "fast wave heating" and can be used to drive a current in the plasma by phasing the current straps such that the radiated k_{\parallel} -spectrum is skewed. The current is not only an effect of the local changes in the velocity distribution function but also due to the decreasing collision frequency at higher velocities that alleviates sustaining the changes in the distribution function.

With the addition of the FLR contribution to the dielectric tensor elements absorption zones appear in the vicinity of the harmonics of the ion cyclotron layers and Landau cyclotron damping can occur. The resonance width is usually small compared to the minor radius of the plasma. Using this process is called cyclotron harmonic damping. To determine the strength of the damping also the polarization of the wave in the vicinity of the resonance has to be included. Even with FLR effects, the damping at the fundamental resonance is small due to the unfavourable polarization. It has its maximum at the second harmonic (here, $l = 2$ is referred as in the experiments) and decreases to higher harmonics. Fig. 5.4 shows the evanescent zone near the plasma edge where $N_{\perp} < 0$ and the resonance layer for the second harmonic heating in a tokamak-like cross-section. For the heating at harmonics, typically a tail of fast particles is created that becomes more anisotropic with velocity since the particles predominantly gain perpendicular energy.

If the plasma includes other species of low concentration, for example, the omnipresent hydrogen in a deuterium plasma, absorption at the hydrogen resonance becomes very strong due

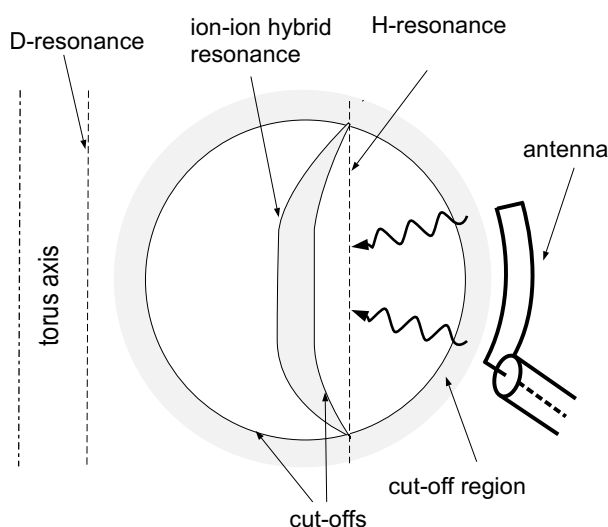


Figure 5.5: Principle of mode-conversion heating.

to Landau cyclotron damping on the hydrogen. This is possible because in the vicinity of the hydrogen resonance, a considerable fraction of the wave power is left circularly polarized because the polarization is determined by the majority deuterium. This scheme is called minority heating. Because a dominant fraction of the power is absorbed by the minority ions, a strong tail in the distribution function is created. The energies are often high so the tail relaxes mostly due to collisions with electrons.

For a higher concentration of the second species, the beneficial effect on the polarization in the vicinity of the resonance decreases, and so does the damping. However, above a critical concentration of a few per cent, a new resonance and an associated cut-off occur: the ion-ion hybrid resonance. The location of cut-offs and resonances are shown schematically in Fig. 5.5 right for the case of hydrogen in deuterium. The resonance calls again for a more detailed analysis using the FLR expansion. It is found that near this resonance a mode-conversion of the fast wave to an ion-Bernstein wave occurs. The ion-Bernstein wave has an electric field component in the direction of the magnetic field and is strong Landau damped on electrons. Now the location of the antenna becomes important. If it is located on the low field side the wave is only weakly damped at the cyclotron resonance. At the cut-off it is partly reflected and it partly tunnels to the resonance layer where it then couples to an IBW. Often, there is an upper limit of about 25% of the power of the fast wave that can mode convert to an IBW on a single pass. If the antenna is located on the high field side direct coupling to the IBW is possible. Except for some stellarator-like experiments RF antennas are usually installed on the low field side for practical reasons.

Low loss coaxial transmission lines and generators (that were developed for radio communications etc.) are readily available. Usually in antennas the radiated power is only a small fraction of the reactive power. Therefore the antennas are coupled with other reactive elements to form a resonant circuit. This causes large electric fields in the antenna that need to be screened from the plasma.

Good absorption efficiency, in particular in dense and hot plasmas, have been obtained. The large electric fields in the antenna and the dependence of the plasma coupling on the plasma

properties intrinsically link the RF system to the plasma such that separate testing and conditioning are of limited use only.

Present research focuses on a better understanding of the antenna plasma coupling, improving the compatibility of the antennas with first wall (due to enhanced non-linear RF-wall interactions leading to a production of impurities and enhanced heat loads at the walls), more detailed investigation of the absorption mechanisms and the development of higher power cw generators.

5.5 Lower hybrid heating

In the LH range, a slow wave is launched with a wave guide. In the plasma it travels at a small angle with respect to the magnetic field lines, this causes the wave to circle the torus several times until the center of the plasma is reached. Landau damping along the path often becomes more important than ion damping near the lower hybrid resonance.

In the lower hybrid frequency domain the ordering is $\Omega_e \gg \omega_{LH} \gg \Omega_i$. The dispersion relation of the slow mode is approximately given by:

$$N_{\perp}^2 = \epsilon_{\parallel} \left(1 - \frac{N_{\parallel}^2}{\epsilon_{\perp}} \right).$$

As in the preceding RF heating schemes the wave has to tunnel through an evanescent region in front of the antenna until a minimal density given by the perpendicular Alfvén resonance is reached. A typical cut-off density is 10^{18} m^{-3} .

Depending on the k_{\parallel} of the launched spectrum, the slow wave can couple to the fast wave and since the group velocity of the fast wave is such as to transport the power back to the plasma edge the wave energy then becomes trapped in the plasma periphery. This occurs for N_{\parallel} smaller than a critical value N_c given by:

$$N_c^2 = \frac{1}{1 - \omega^2 (|\Omega_e \Omega_i|)^{-1}}.$$

For typical parameters this means that the parallel wavelength needs to be shorter than about 0.2 m. For the slow waves which fulfil this requirement well, the ratio of group velocity perpendicular and parallel to the magnetic field is independent of k_{\parallel} , thus the wave energy travels into the plasma as well collimated beams, mainly along the toroidal direction. With approaching the resonance, the angle to the magnetic field lines decreases further. This behaviour is schematically shown in Fig. 5.6.

Even though the wave might not yet have reached the resonance, its electric field component parallel to the toroidal magnetic field causes Landau damping on the electrons. Since the k_{\parallel} -spectrum of the launched waves is often quite wide (limited by the accessibility condition and the upper end of the antenna spectrum) the resonant velocities extend from the electron thermal velocities up to a substantial fraction of the speed of light. Thus an electron tail is

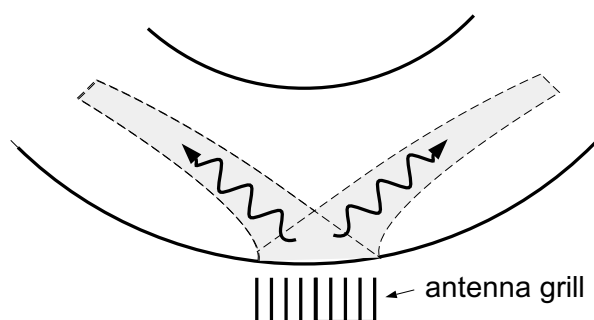


Figure 5.6: Wave propagation for lower hybrid heating.

created extending to very high energies. Near the lower hybrid resonance strong ion damping occurs, predominantly through nonlinear stochastic damping on the ion cyclotron motion.

The antenna (or a "grill") arrays consist of a phased array of open rectangular waveguides arranged with the RF electric field aligned with the magnetic field. The shape of the antenna face resembles the plasma shape to be able to move the antenna as close as possible to the plasma surface. However, experiments have shown that the antenna can create its own plasma in front of it, thus the coupling problem is less severe. The RF generators used are klystrons.

5.6 Electron cyclotron resonance heating

In contrast to the two preceding RF heating methods, at the EC range of frequencies the evanescent region between the antenna and the plasma can be avoided. Thus the proper polarization can be chosen at the antenna and the desired plasma wave can be excited with good conversion ratio. Only since the mid-70s, generators, the so-called gyrotrons, have become available that operate in the frequency range of the electron cyclotron resonance. In this range only electrons respond to the waves since $\omega \approx \Omega_e \approx \omega_{pe} \gg \Omega_i, \omega_{pi}$.

The O-mode and the X-mode can be used. Whereas the O- solution of the dispersion relation for the perpendicular propagation in the EC range remains as described above, the X- solution takes the following form:

$$N_{\perp}^2 = \left(1 - \frac{\omega_{pe}^2}{\omega^2} - \frac{\Omega_e}{\omega}\right) \left(1 - \frac{\omega_{pe}^2}{\omega^2} + \frac{\Omega_e}{\omega}\right) \left(1 - \frac{\omega_{pe}^2}{\omega^2} + \frac{\Omega_e^2}{\omega^2}\right)^{-1}.$$

The O-mode at the fundamental frequency (O1) has a cut-off at the electron plasma frequency ω_{pe} . The X-mode at the fundamental frequency (X1) has a cut-off below the electron plasma frequency and above the upper hybrid frequency. Thus the X1 electron cyclotron resonance is only accessible from the high field side. To enable heating from the low field side and to get a stronger absorption, usually X2 heating is used instead. Fig. 5.7 left shows schematically heating scheme for O1 or X2 EC heating. Fig. 5.7 right shows the location of resonances and cut-offs for X1 heating.

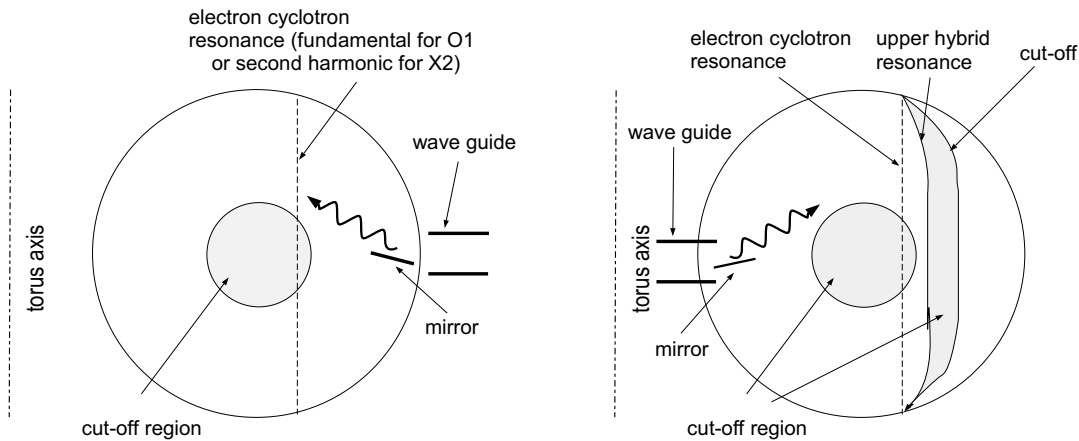


Figure 5.7: Left: Principle of fundamental O-mode or second harmonic X-mode heating.

Right: Principle of fundamental X-mode heating from high field side.

The absorption process in the EC range is dependent on thermal (FLR) and relativistic corrections, yet the absorption region is usually very narrow and much smaller than the plasma radius, thus making ECRH also useful for localized heating in order to suppress MHD activity.

The limitation to use ECR heating at densities higher than cut-off can be overcome by using X3 and O2 heating, albeit with lower absorption (or the need of high electron temperatures to get a good absorption). Another method is by coupling from an O-mode to an X-mode that finally mode-converts to an Electron-Bernstein-wave. This tricky scheme is possible at a particular angle of incidence. The experimental proof is a fine example of the predictive power of the warm plasma dispersion relation as well as how sophisticated ECRH experiments have become.

The RF power in the electron cyclotron range of frequencies is generated using gyrotrons. In these devices an electromagnetic wave is coupled to spiraling electrons in a steady magnetic field. The bunching of the electrons in phase space amplifies the wave. Care is taken to amplify only one waveguide mode, e.g. the TE_{02} . Output powers of up to 1000 kW for continuous operation at frequencies of 28–170 GHz have been obtained and research is aiming at 2 MW cw gyrotrons. The RF power is coupled out of the gyrotrons using ceramic and lately diamond windows. Latter have very low absorption and high thermal conduction coefficients allowing cooling through edges.

Transmission lines consist of waveguides with different mode converters to change the gyrotron output mode into an TE_{11} -mode for O-mode heating or an HE_{11} for X-mode heating. Transmission of Gaussian beams using quasi-optical lines have recently also become available. Finally inside of the torus the direction of the beam can be changed using movable mirrors, allowing off-axis heating without changing the frequency or magnetic field.

The pinpoint accuracy of ECRH due to its narrow deposition profile and the possibility of ray-tracing calculations in an inhomogeneous plasma have made ECRH a valuable and reliable tool. Technical development and testing can be done independently of the plasma.

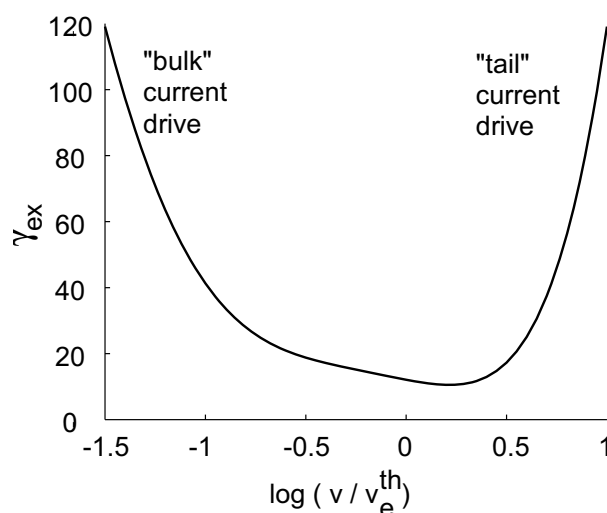


Figure 5.8: Normalized current drive efficiency for Landau damping.

5.7 Non-inductive current drive

The discussed heating schemes usually heat only a small fraction of the plasma particles. This can be taken advantage to drive a current in the plasma. This is useful in order to reduce or eliminate the necessity of ohmic current in a tokamak or to compensate for the pressure-driven bootstrap current in a stellarator.

A current drive efficiency γ_{th} can unambiguously be defined as the ratio of local driven parallel current density, j , and the local absorbed power density p : $\gamma_{th} = j/p$. Different experiments are often compared using a scaled figure of merit γ_{ex} defined as

$$\gamma_{ex} = \frac{\bar{n}_e [10^{20} \text{ m}^{-3}] R [\text{m}] I [\text{A}]}{P [\text{W}]},$$

where \bar{n}_e is the line-averaged density, R is the major radius of the plasma, i.e. the distance between the torus axis and the center of the plasma column, I is the integrated driven plasma current and P is the total absorbed power. With $I = \pi a^2 j$, $P = \pi a^2 \cdot 2\pi R$ and $j/p \propto 1/\bar{n}_e$, it is easy to confirm that $\gamma_{th} \propto \gamma_{ex}$.

To drive a current in a plasma by waves, "pushing of electrons" and asymmetric electron collisionality can be used.

Electrons are being pushed along the magnetic field lines using Landau damping of waves that are launched into the plasma. This changes the velocity distribution of the resonant electrons until the collisional relaxation balances the driving force. If the antenna current straps are phased properly, the waves are launched predominantly in one direction inside the torus, thus a net electron current appears. For $\omega/k_{\parallel} \ll v_e^{th}$, the absolute change in electron momentum for a given loss of energy of the wave is large, but a large fraction of the electrons are trapped in the toroidal field ripple and the collision frequency is large. For $\omega/k_{\parallel} \gg v_e^{th}$, the collision frequencies are small, but there are also few electrons in the distribution function. The compilation of these two effects leads to a theoretical curve shown in Fig. 5.8 identifying

the regions of bulk and tail current drive. Lower hybrid, fast wave and ion-Bernstein wave mode-conversion change the tail of the electron distribution function.

Electron cyclotron heating predominantly changes the perpendicular temperature of the electrons and does not impart much parallel momentum. Still current drive is possible, because the electrons that fulfill the resonance condition $v_{\parallel} = (\omega - \Omega_e)/k_{\parallel}$ (relativistic effects are neglected) and are heated, will attain a lower collision frequency due to their higher velocity. Therefore their collisional relaxation will be reduced. Actually, this effect is also of great importance for current drive based on Landau damping. Yet there is a small caveat. Because of the radial dependence on the magnetic field, this resonance occurs only a small region next to the location where $\omega = \Omega(r)$. Electrons on the high field side of this resonance will also meet the requirement $v_{\parallel} = (\omega - \Omega_e)/k_{\parallel}$, albeit for reversed velocity. Therefore it is necessary that the wave is strongly damped. Otherwise one creates a shear layer in the current profile without any change in the total current.

Acknowledgements

Current script is a modified and extended version of the script on the wave heating written initially by Dr. Dirk Hartmann for the IPP Summer University.

References

- [1] V. Erckmann and U. Gasparino: *Electron cyclotron resonance heating and current drive in toroidal fusion plasmas*, Plasma Phys. Control. Fusion **36** (1994) 1869.
- [2] V. Erckmann et al.: *20 years of ECRH at W7-A and W7-AS*, Nucl. Fusion **43** (2003) 1313.
- [3] R.A. Cairns: *Radiofrequency Heating in Plasmas*, Hilber, Bristol (1991).
- [4] T.H. Stix: *Waves in Plasmas*, AIP, New York (1992).
- [5] *Fusion Physics ed. by M. Kikuchi, K. Lackner, M.Q Tran*, IAEA Vienna (2013), pp 609-755.

Chapter 6

Plasma heating: neutral beam injection

Christian Hopf, Ursel Fantz, Peter Franzen

6.1 Introduction

A temperature of about 20 keV is required to ignite a magnetically confined fusion plasma. Once ignited, the plasma maintains its temperature by heating through the alpha particles that are produced in the D–T fusion reaction and carry 3.5 MeV or 1/5 of the fusion energy. Initially, however, auxiliary heating is necessary to reach ignition. Furthermore, contemporary fusion experiments are too small to reach ignition at all and, with few exceptions, do not use a D/T mix as fuel. In these experiments all heating has to be achieved with external power. Various heating methods have been developed and are successfully applied in fusion experiments.

Ohmic heating (OH) is a beneficial side effect of the presence of an inductively driven plasma current I_p in a tokamak. The primary purpose of this current is to create the poloidal component of the confining magnetic field. Due to the finite conductivity of the plasma the current leads to heating by dissipation of the power $P = \mathcal{R}I_p^2$, where \mathcal{R} is the Ohmic resistance of the plasma. However, with increasing temperature the resistance of the plasma decreases, leading to a decrease of the deposited heating power. The maximum achievable temperatures depend on the machine parameters and the confinement regime but are generally too low for plasma ignition. In addition, ohmic heating is not the method of choice for stellarators since the current would heavily modify the magnetic field created by the external coils. Only before alternative auxiliary heating methods became readily available was ohmic heating applied in stellarators too.

Radio frequency heating (RF) uses high power electromagnetic waves to transfer energy to the plasma. Depending on the choice of frequency, plasma density and composition, different constituents of the plasma can be heated. RF heating is predominantly applied in the range of low frequency Alfvén waves (1–10 MHz), ion cyclotron frequencies (30–100 MHz), lower hybrid frequencies (1–10 GHz) and electron cyclotron frequencies (50–150 GHz).

Neutral beam injection heating (NBI), the topic of this article, is the major work horse among the auxiliary heating methods on most of the world's fusion experiments. The concept is

straightforward and was suggested back in the early 1950s: neutral atoms can penetrate the confining magnetic field and are ionized in the plasma via collisions with electrons and ions. The fast ions thus generated are now confined by the magnetic field as well. If their kinetic energy is large compared to that of the ions and electrons in the plasma they will on average transfer energy to the plasma particles by collisions, thereby heating the plasma.

Neutral beam heating has played an important role in many “milestone experiments” of fusion research. To mention a few, in 1980 NBI heating enabled the first demonstration of a current-free stellerator operation at relevant temperatures and densities and several hundred kW heating power on Wendelstein 7-A [1]. In 1982 the spontaneous transition of the plasma above a heating power threshold into a regime of significantly improved confinement, called high confinement mode or H mode, was discovered on ASDEX in NBI-heated discharges [2]. The so far highest D–T fusion power of 16 MW was achieved on JET in discharges heated with both D and T neutral beams. In the peak of the fusion reaction rate still approximately half of the rate was due to beam–plasma interaction [3, 4].

Like RF heating, NBI is not only useful for plasma heating, but also for *current drive*. If a neutral beam is injected with a toroidal velocity component the current profile is also changed. This *non-inductive current drive* is desirable in order to attain steady-state operation in a tokamak and to access advanced regimes of superior confinement that often depend on achieving a tailored current profile.

Even in a fusion reactor’s burning plasma control of the current profile might still require additional ohmic heating or non-inductive current drive.

6.2 Neutral beam heating physics and current drive

The basic idea behind neutral beam heating is simple: A beam of fast particles is injected into the plasma. If the energy of the beam particles is very much greater than the thermal energy of the target plasma the plasma will be heated by collisional energy transfer from the fast particles. Acceleration of particles requires electrically charged particles, i.e. in practice ions or electrons. On the other hand, a beam of charged particles will be deflected by the confining magnetic field even before reaching the plasma. Therefore, the beam of fast charged particles must be neutralized after acceleration. This requirement rules out electrons as beam particles and leaves ions as the only choice. Usually, one of the principal atom species in the plasma is selected as the neutral beam species, i.e. H or D in a fusion experiment running in hydrogen or deuterium, and D or T in a D–T fusion reactor. This choice avoids a change in plasma composition due to NBI.

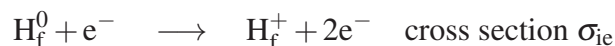
When the neutral atoms enter the plasma they become ionized by collisions with the plasma ions and electrons and hence also confined by the magnetic field. Due to collisions they thermalize and thereby heat the plasma.

The two main design parameters of an NBI system are the beam energy and the injection geometry. These two parameters determine the collision cross sections and the direction of the fast particles which in turn determine the heating profile and the current-drive properties of the injection system. An outline of the underlying physics is given in this section.

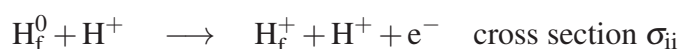
6.2.1 Beam ionization

When the neutral beam atoms—unaffected by the magnetic field and hence travelling in straight lines—enter the plasma they become ionized due to mainly three collisional processes. These are:

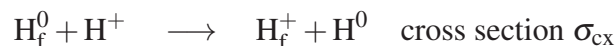
- *Collisional ionization by electrons:*



- *Collisional ionization by plasma ions:*



- *Charge exchange with plasma ions:*



In these reactions H stands for any hydrogen isotope and can be replaced also by D or T. The index “f” indicates the fast beam particle.

For each of these processes the cross section σ_k ($k \in \{ii, ie, cx\}$) depends on the relative velocity of the colliding particles, $v_{\text{rel}} = |\mathbf{v}_b - \mathbf{v}_{(i \text{ or } e)}|$, where \mathbf{v}_b is the beam velocity, index “i” stands for the plasma ions and “e” stands for the plasma electrons. While the beam velocity is well defined, the plasma ions and electrons have a broad velocity distribution. Considering that neutral beam heating requires $v_i \ll v_b$ and, due to the electrons’ much lighter mass, $v_b \ll v_e$ we can neglect the contribution of the ion velocity to the relative velocity in beam–ion collisions and write the total ionization cross section as

$$\sigma_{\Sigma} = \sigma_{cx}(v_b) + \sigma_{ii}(v_b) + \frac{\langle \sigma_{ie} v \rangle}{v_b}.$$

The expression in the numerator of the last term is the rate coefficient defined by

$$\langle \sigma_{ie} v \rangle = \frac{\int \sigma_{ie}(v_{\text{rel}}) v_{\text{rel}} f(v_{\text{rel}}) dv_{\text{rel}}}{\int f(v_{\text{rel}}) dv_{\text{rel}}}$$

where $f(v_{\text{rel}})$ is the distribution function of the relative velocity.

In the ideal case of a uniform, pure hydrogen plasma of density n ionization leads to an exponential attenuation of the neutral beam of intensity I_0 along its direction x ,

$$I = I_0 \exp\left(-\frac{x}{\lambda}\right),$$

where λ is the mean free path for ionizing collisions, given by

$$\lambda = \frac{1}{n \sigma_{\Sigma}}.$$

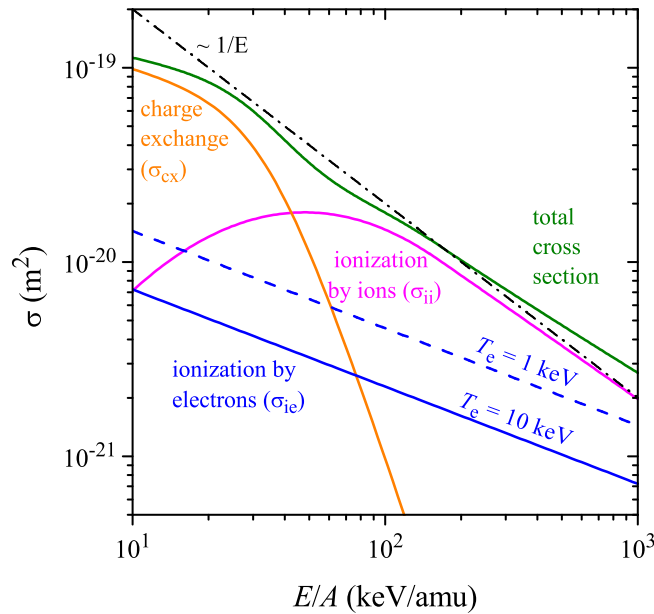


Figure 6.1: Ionization cross sections taken from reference [5].

The ionized fast beam particles are no longer unaffected, but confined, by the magnetic field.¹

The cross sections as a function of beam energy per nucleon are shown in Fig. 6.1. At injection energies below 50 keV/amu, commonly found in many present-day NBI systems, charge exchange dominates beam ionization. At higher energies ionization by ions takes over the leading role, while ionization by electron impact is always only a minor contribution.

The total ionization cross section falls roughly as $1/E$. This pronounced energy dependence makes it possible to choose the mean free path by variation of the beam energy. In order to achieve central heating of the plasma the mean free path should approximately match the minor radius a . We can test this match for typical ASDEX Upgrade parameters using the total cross section in Fig. 6.1. For the 93 keV deuterium beams and a plasma density of $5 \times 10^{19} \text{ m}^{-3}$ we obtain $\lambda = 0.66 \text{ m}$. ASDEX Upgrade’s minor radius is $a = 0.65 \text{ m}$. To obtain $\lambda = a = 2 \text{ m}$ for ITER at $n = 10^{20} \text{ m}^{-3}$ a very much higher energy of 500 keV/amu is required. In fact, the ITER NBI system is designed to deliver 1 MeV deuterium beams. More detailed calculations show that the power deposition profile is already peaked in the plasma center for $\lambda > (1/4) \cdot a$. Hence, the reason for the choice of the high acceleration voltage for ITER is not only central heating but also achieving the necessary heating power.

If the mean free path is long—a condition that can occur for example when the plasma density is low during plasma startup—not the whole beam may be ionized in the plasma. The non-ionized fraction of the beam that hits the far wall is called *shine through*. As the power load to the wall caused by shine through can be substantial—for 100% shine through it is of the order

¹The ionization of the neutral beam is sometimes also referred to as *beam trapping* or as *beam absorption*. Both these terms tend to be misleading. “Beam trapping” does not necessarily create “trapped” ions, i.e. ions on a banana orbit. “Beam absorption” only means that the absorbed particles are not transmitted through the plasma. However, the energy of the beam particles is only absorbed much later after slowing down of the fast ions.

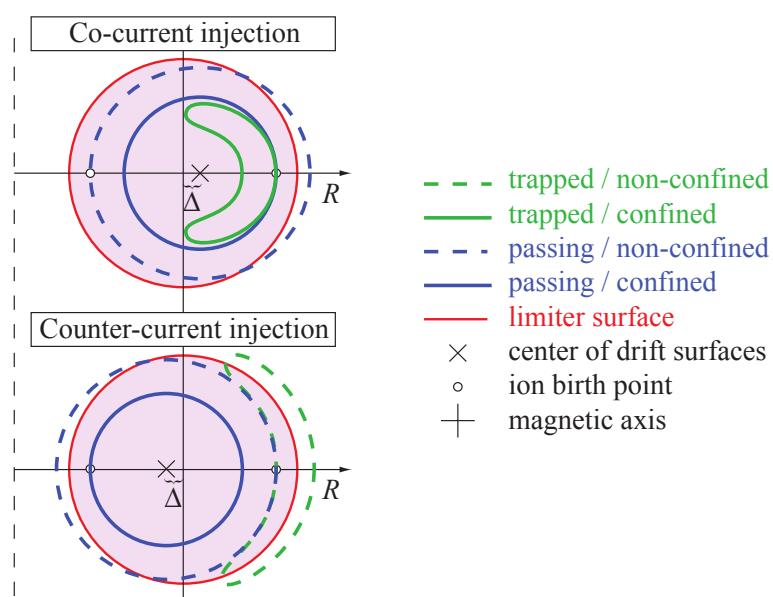


Figure 6.2: Schematic of passing (blue) and trapped (green) ion orbits. The orbits are projected into a poloidal plane. The birth locations of the ions are indicated by small open circles. The dashed black line indicates the center of the torus. The red solid line indicates the limiter surface. Orbits intersecting the limiter (dashed) are not confined because the ion collides with the limiter.

of several tens of MW/m^2 —appropriate safety interlocks are required to protect the wall from excessive shine-through heat load.

6.2.2 Fast ion orbits and orbit losses

The now confined fast ions follow drift orbits and exchange energy with the plasma particles in collisions. As the ion mean free path in the plasma is very much larger than the circumference of the torus, $\lambda_i \gg 2\pi R$ ($R =$ major radius), the ions will on average complete several full orbits before being substantially scattered or slowed down. Therefore we discuss the fast ion orbits first. Fig. 6.2 illustrates various types of orbits.

Two general types of orbits can be distinguished: Passing orbits (blue in Fig. 6.2) and trapped “banana” orbits (green in Fig. 6.2). While travelling around the torus the ions see a periodically varying magnetic field strength as they follow the helically twisted field lines. When moving in the direction of increasing magnetic field the ion’s kinetic energy parallel to the magnetic field decreases and is converted into perpendicular kinetic energy. If the ion’s initial ratio of momentum parallel to the magnetic field to the momentum perpendicular to the magnetic field is too low, the ion’s parallel velocity becomes zero at a certain magnetic field and it is reflected. The ion is trapped and travels back and forth between two such reflection points.

Due to the $\text{grad-}B$ and curvature drifts the ions in a toroidal device do not exactly follow the magnetic field lines but their guiding center orbits are slightly shifted by a distance Δ with respect to the flux tube that the ion was born on, i.e. where ionization occurred. As a result

the poloidal projection of a passing orbit looks approximately like the shifted cross section of a flux tube, while a trapped orbit looks like a banana. If the resulting orbit intersects the wall the ion will be lost. Such losses are called first orbit losses.

Whether the shift of a passing particle's drift surface is inward or outward and whether banana orbits lie inside or outside the ion's birth location depends on the direction of the toroidal velocity component of the beam. If this velocity component is in the direction of the plasma current the situation is called *co-current injection*. As can be seen from Fig. 6.2 only the orbits of ions born on the high field side close to the inner wall may intersect the wall. In the opposite case, counter-current injection, the banana orbits lie outside the birth location and may intersect the outer wall. Additionally, passing orbits of ions born close to the edge on the outer mid plane may intersect the inner wall. This is the reason why first orbit losses are especially high for counter-current, near-radial NBI.

6.2.3 Slowing down

Ions on confined orbits, i.e. orbits that do not intersect the walls, travel many times around the torus and transfer their energy to ions and electrons in successive collisions. The energy dependence of the instantaneous energy loss per unit path length is fairly well described by

$$\frac{dE}{dx} = \underbrace{-\frac{\alpha}{E}}_{\text{to ions}} - \underbrace{\beta\sqrt{E}}_{\text{to electrons}}, \quad (6.1)$$

where α and β are coefficients that depend on the beam and plasma species as well as plasma density and electron temperature. While the energy transfer to the ions decreases with increasing beam energy, the transfer to the electrons increases. The energy at which the cross over occurs is called *critical energy* and given by,

$$E_c = \left(\frac{\alpha}{\beta}\right)^{2/3} = 14.8 T_e \left(\frac{A^{3/2}}{n_e} \sum \frac{n_j Z_j^2}{A_j}\right)^{2/3},$$

where A_j , Z_j , and n_j are the atomic mass, charge, and density of plasma ion species j , n_e is the electron density, and A is the atomic mass of the beam species. For a pure hydrogen plasma this gives

$$\text{H}^0 \rightarrow \text{H}^+ (\text{D}^0 \rightarrow \text{D}^+) : \quad E_c[\text{keV}] = 14.8 (18.6) T_e[\text{keV}].$$

The fractions of energy transferred to ions and electrons during the entire slowing down process can be calculated by integration of the terms in (6.1). The result is that the threshold for dominant electron heating is at $2.5 E_c$

$$E \begin{cases} < 2.5 E_c & \text{dominant ion heating,} \\ > 2.5 E_c & \text{dominant electron heating.} \end{cases}$$

In contemporary experiments ion heating usually clearly dominates. In ITER, however, both NBI and α -particle heating will predominantly heat the electrons.

The time it takes for ions to slow down to thermal energies can also be obtained by integration using (6.1). For present-day machines the *slowing down time* is typically 20–100 ms. In ASDEX Upgrade the ion circles the torus about 10^4 times during this time, as we will see later.

6.2.4 Particle losses

Besides the first orbit losses already mentioned also fast ions born on confined orbits can be lost in the course of slowing down. Two mechanisms are mainly responsible for these losses.

First, *pitch angle scattering*, i.e. a change in the ratio of parallel to perpendicular velocity due to collisions, can scatter ions into non-confined orbits such as banana orbits that intersect the wall. These losses are typically of the order of 5–10% of the heating power.

Second, in the presence of neutral hydrogen in the plasma charge exchange collisions can convert the fast ions into fast neutrals that escape the confining magnetic field. This mechanism accounts for typically a loss of 5% of the beam power.²

6.2.5 Neutral beam current drive (NBCD)

If the neutral beam is injected tangentially into the plasma, the ionized fast particles will travel around the torus in a well defined direction. As they are charged particles an electric current is associated with this motion of fast particles. This current is called the *circulating current*.

We can estimate the circulating current, taking ASDEX Upgrade as an example. ASDEX Upgrade has two tangential current drive beams operating at 93 kV in deuterium with a power of 2.5 MW per beam. Hence, the injected current is $I_0 = P_{\text{NBI}}/U_{\text{acc}} = 54 \text{ A}$. For the mean velocity during slowing down we make the crude, yet for our purposes sufficient, assumption that it is half the beam velocity, $\langle v \rangle = v_0/2 = 1.5 \times 10^6 \text{ m/s}$. The slowing down path length is then given by $\langle v \rangle \tau_s$, where τ_s is the slowing down time. In ASDEX Upgrade $\tau_s \approx 70 \text{ ms}$ and $\langle v \rangle \tau_s \approx 10^5 \text{ m}$. With a circumference of $2\pi R \approx 10 \text{ m}$ this means the ions travel on average 10^4 times around the torus. Hence, the circulating current can be estimated as

$$I_{\text{circ}} = 10^4 I_0 = 550 \text{ A}$$

or about half the plasma current.

Unfortunately, this simple picture leaves out an important process; if fast ions travel through a plasma they drag along plasma electrons. These electrons cancel a part or all of the ion current. Cancellation of the ion current is complete when beam and plasma have the same effective charge, $Z_{\text{beam}} = Z_{\text{eff}} = \sum Z_j^2 n_j / (Z_j n_j)$, where Z_j and n_j are the charge and density of plasma species j . To make this last point plausible, let us consider two groups of ions at two different velocities v_a (e. g. background plasma) and v_b (e. g. beam). We can find a frame of reference in which the associated ion currents cancel, i.e. $v'_a n_a = -v'_b n_b$. If these two

²The numbers are taken from typical results of Monte Carlo simulations of NBI heating of ASDEX Upgrade discharges.

groups of ions produce equal drag on the electrons, the resulting electron current in this frame of reference—and hence the resulting Lorentz-invariant total current—also vanishes. Only if the two groups of ions produce *different* drag, e.g. by having different charge (collision cross section $\propto Z^2$, current $\propto Z$), the resulting electron currents do not cancel.

In other words, one way to rescue current drive is to increase Z_{eff} —an approach that opposes the usual quest for a clean plasma. There is, however, another aspect that was missed in the simple picture so far.

In a toroidal geometry a certain fraction of the electrons are on trapped orbits due to a low ratio of parallel to perpendicular velocity. These electrons cannot contribute to a toroidal current as they are toroidally confined. Hence, the cancellation of the circulating current by the electrons is reduced by the trapped electron fraction

$$I_{\text{cd}} = I_{\text{circ}} \left[1 - \frac{Z_{\text{beam}}}{Z_{\text{eff}}} \left(1 - G(Z_{\text{eff}}, \varepsilon) \right) \right].$$

In this equation I_{cd} is the driven current, I_{circ} is the circulating current, and $G(Z_{\text{eff}}, \varepsilon)$ is the trapped electron fraction that depends of Z_{eff} and the torus' inverse aspect ratio $\varepsilon = r/R$. Due to the effect of trapped electrons the driven current in a tokamak is typically more than half of the circulating current. A detailed prediction of driven current (density profiles) is done with numerical codes.

When the neutral beam is switched on the beam-driven fast ion current does not immediately manifest as a net current in the plasma. The onset of the beam current induces an opposing current in the plasma that exactly cancels the beam-driven current. This induced current decays resistively with characteristic times that are typically of the order of seconds.

Neutral beam current drive is considered as one of the possible means of achieving steady state operation in a tokamak reactor. For this application the energetic efficiency of the current drive is an important factor. The efficiency (gain/investment) of a current drive system is defined as the current driven per power coupled to the plasma,

$$\varepsilon_{\text{cd}} = \frac{I_{\text{cd}}}{P} \left[\frac{\text{A}}{\text{W}} \right].$$

As for all current drive systems

$$I_{\text{cd}} \propto P \cdot \frac{1}{n_e} \cdot \frac{1}{R}$$

a more convenient figure of merit to compare systems is

$$\eta_{\text{cd}} = R n_e \frac{I_{\text{cd}}}{P}, \quad \text{usually given in } \left[\frac{10^{20} \text{A}}{\text{Wm}^2} \right].$$

The current drive efficiency as a function of beam energy calculated for a deuterium beam deposition at half minor radius and for $Z_{\text{eff}} = 2$ is shown in Fig. 6.3. For a given electron temperature the curves go through a broad maximum. The beneficial consequence of this observation is that at given electron temperature the beam energy can be substantially reduced

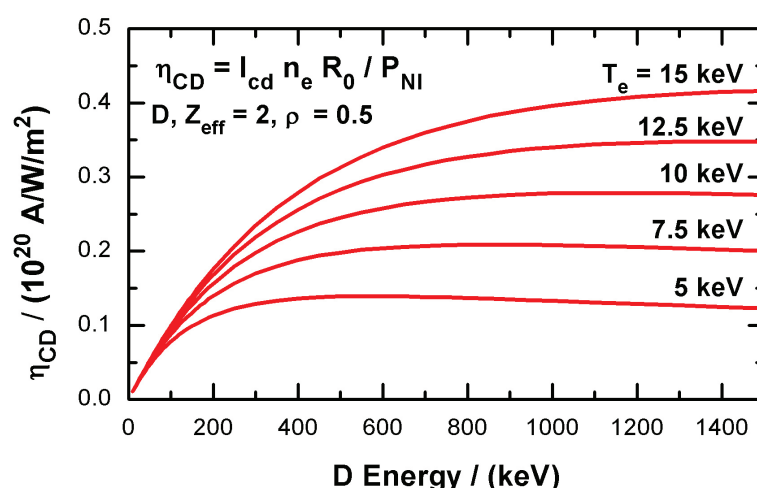


Figure 6.3: Calculated current drive efficiency as a function of beam energy. Parameters are given in the figure.

without sacrificing much of the current drive efficiency. At about half the energy of the maximum the efficiency is still 90% of the maximum efficiency. As the value of the acceleration voltage has a huge impact on the installation cost of an NBI system one wants to keep the beam energy as low as possible. We can also see from the graph that at high beam energies only an increase of the electron temperature can increase the efficiency further whereas at low beam energies an increase of the beam voltage has more effect. In ITER, up to 2 MA current can be driven by the neutral beams operating at 1 MV, 33 MW heating power, $R = 6.2$ m, $n_e = 10^{20} \text{ m}^{-3}$ and $T_e = 15$ keV.

Experimentally, fully non-inductive current drive using NBCD has been demonstrated in JT-60U in low-density, low-current, high- T_e discharges [6]. The bootstrap current, a self generated plasma current due to radial gradients in the plasma, also delivered an important contribution to the total driven current.

6.3 Neutral beam injection systems

The generation of a neutral beam can be divided into three successive steps, schematically shown in Fig. 6.4:

- the generation of a powerful ion beam in the ion source,
- the neutralization of the ion beam in the neutralizer, and
- the transport of the neutral beam to the plasma vessel.

Generation of the ion beam is accomplished by extraction of the ions from a hydrogen plasma.

The neutralization of the extracted ions occurs in the neutralizer via charge exchange collisions of the fast ions with the cold hydrogen molecules. The neutralizer is usually a drift tube directly attached to the ion source with a permanent inflow of hydrogen gas.

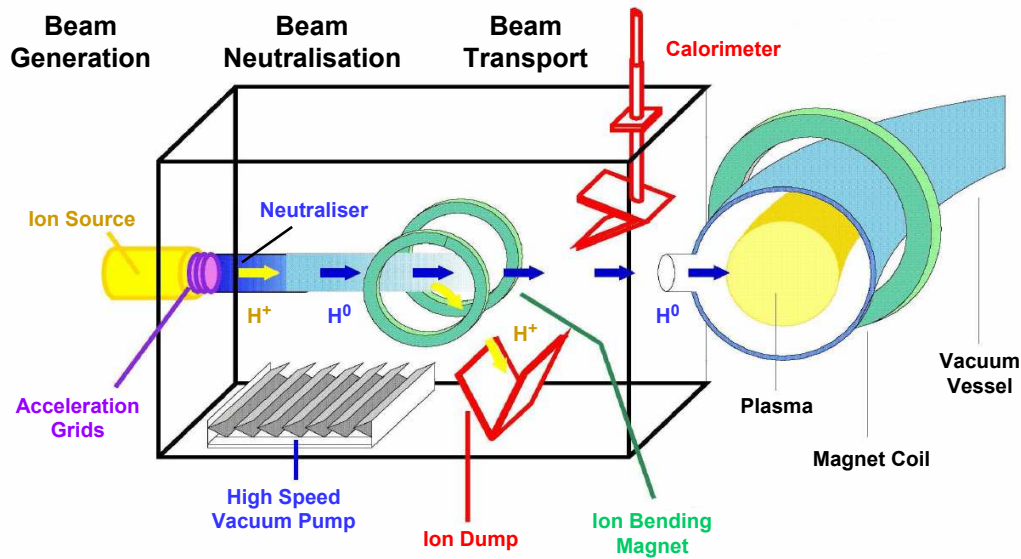


Figure 6.4: Schematic view of a neutral beam heating system.

After leaving the neutralizer a significant fraction of the beam is still ionized. During the transport of the neutral beam these ions are removed from the beam by a bending magnet and they hit an efficiently water cooled residual ion dump.

A further indispensable component of a neutral beam system is a calorimeter that can be moved into the beam. It usually consists of efficiently cooled target plates of a design similar or identical to the beam dumps. It allows to fire beams for test or conditioning purposes when no plasma is available as absorbing target. Furthermore, the deposited heating power can be derived from the known flow of cooling water through the calorimeter plates and the temperature difference between inlet and outlet.

A cutaway view of the NBI system on JET is shown in Fig. 6.5. The beamline has eight sources. Parameters are given in Tab. 6.1.

In the following sections ion beam generation, neutralization, and beam transport are discussed in more detail.

6.3.1 Generation of the ion beam

Sources for positive ions

The general principle of ion beam generation by extraction of ions from a plasma is well established and applied for many purposes. The unique requirement that NBI ion sources have to fulfill is the high beam power of several MW at reasonably low beam divergence in order to satisfy the heating power demands and accomplish good beam transmission through often narrow ports. The acceleration voltage is determined by the required mean free path of

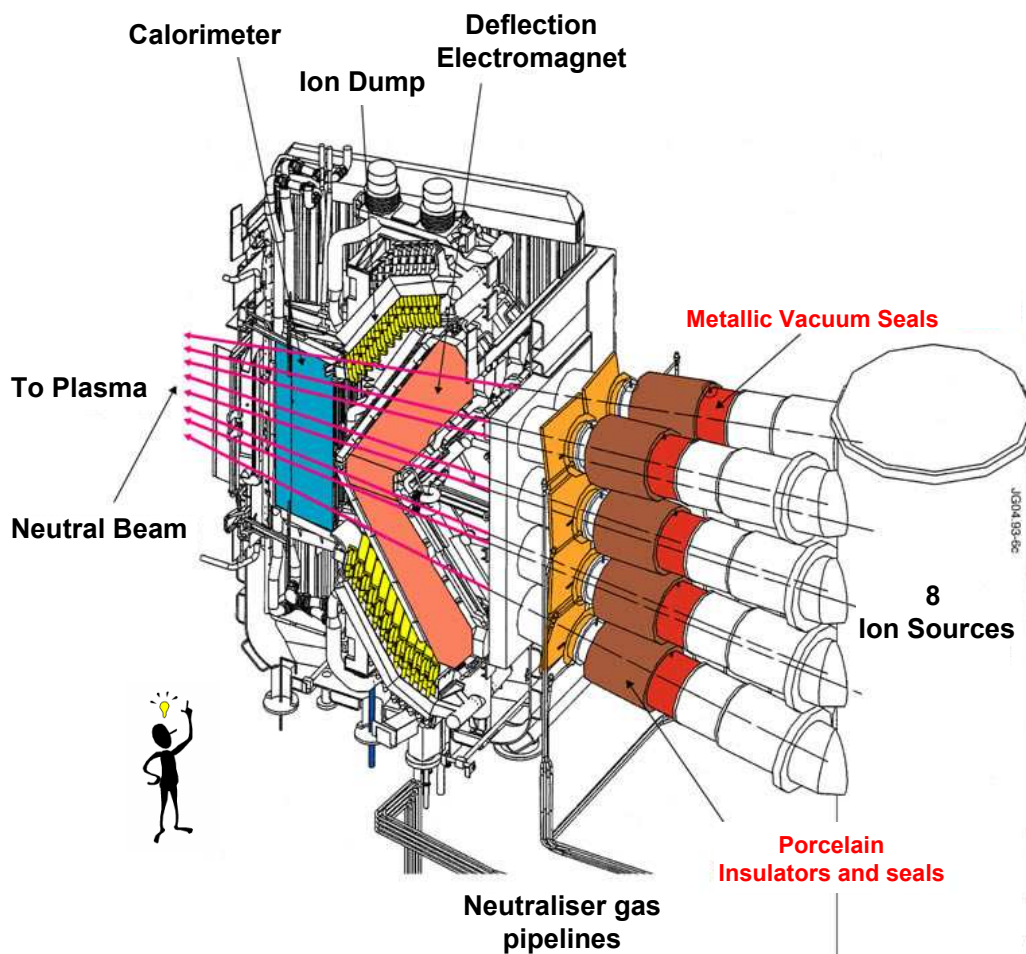


Figure 6.5: NBI System at JET with eight ion sources.

the neutrals in the plasma and, hence, ultimately by the geometric dimensions of the fusion experiment. It is between several tens of keV on existing devices and 1 MeV for ITER. Consequently, the beam current has to be of the order of several tens of amperes which in turn demands a large cross section of the beam of several hundreds of cm^2 . The necessary high ion flux densities of typically a few hundred mA/cm^2 over the large area demands a sufficiently high plasma density and a reasonable uniformity in space and time ($< 10\%$).

Two different types of ion sources have become popular for NBI systems, arc sources and RF sources.

In an *arc sources* electrons are thermally emitted by a number of hot tungsten-filament cathodes and accelerated into the ion source volume by a DC voltage of about 100 V. There they ionize the gas molecules and create the plasma. The arc current is of the order of 1 kA.

In an *RF source* the power is coupled to the plasma via a coil wound around the electrically non-conducting walls of the plasma source. The coil is powered by radio frequency (RF) in the 1 MHz range. The coil's time-dependent magnetic field induces oscillating, closed electric

Table 6.1: Performance of the NBI systems on various fusion experiments. The maximum current density for positive ion systems is limited by the power supplies, not by the source.

Fusion Device	AUG		W7-X*	JET	LHD	JT-60U	
	H ⁺ /D ⁺	H ⁻	H ⁺ /D ⁺	H ⁻ /D ⁻			
Type of Source	Arc	RF	RF	Arc	Arc	Arc	Arc
Extraction Area (cm ²)	390		390	300	1150	128	1660
Max. Energy (keV)	55/60	72/93	55/60 (72/100)	80/130	180	75/95	360/380
Injected Power per Source (MW)	1.6/2.5	1.4/2.5	1.4/2.5	1.5/1.4	3.75	0.9/1.4	3.3/2.7
Sources per Beamline	4		1 (4)	8	2	2	2
Number of Beamlines	1 + 1		2	3	3	14	1
Total Power (MW)	12/20		2.8/5 (11.2/20)	36/32	15	27/40	13.2/10.8
Pulse duration (s)	4/8	4/8	10	10	10	5	10
Max. Current Density (mA/cm ²)	250/200	160/160	250/200	160/160	35	270/210	13/9

*Two stage construction planned, otherwise copy of the AUG RF system.

field lines that periodically accelerate the electrons and lead to ionization. A plasma generated by this concept is called inductively coupled plasma (ICP). The typical RF power is around 100 kW.

RF sources have a number of advantages compared to arc sources. The RF power delivered by the generator can be quickly adjusted, allowing for a rapidly responding feedback control of the ion current extracted from the source. In arc sources such a quick feedback is not possible due to the thermal inertia of the filaments. Furthermore, while in an arc source every of the several tens of filaments has to be individually connected with a cable, an RF source needs only one high voltage connection and the connection for the coil. As the whole ion source is at acceleration voltage with respect to the grounded torus this greatly simplifies the wiring. The RF can even be supplied to the coil via an electrically insulating transformer such that the RF generator can be kept at ground potential.

For long pulse operation and operation in environments that require remote handling an additional advantage is that the RF sources require almost no maintenance due to the absence of filaments with limited lifetime.

Independent of their type, positive ion sources do not only produce H⁺ ions, but also molecular H₂⁺ and H₃⁺ ions that are also accelerated. After acceleration these molecular ions have the same kinetic energy as the atomic ions. Hence, the energy per H in the ion is only a half and a



Figure 6.6: Photograph of a grid of the ASDEX Upgrade NBI system. The grid consist of 774 apertures with 8 mm in diameter.

third of the full energy, respectively. The neutral atoms produced from these molecular ions in the neutralizer also have half and third energy. Generally, the molecular ion fraction decreases with the coupled power density and increases with pressure. As an example, the RF sources on ASDEX Upgrade have a ratio of $H^+ : H_2^+ : H_3^+$ of approximately 7:2:1 when running at full parameters.

Extraction and acceleration of positive ions beams

It is intuitively clear that in order to create not too inhomogeneous acceleration field the diameter of the extraction aperture should not be very much larger than the acceleration gap. Hence, the large extraction area means that the beam has to be extracted through multiple apertures, e.g. 774 in the case of the ASDEX Upgrade grids. This is achieved by assembling a set of carefully aligned grids. A photograph of a grid is shown in Fig. 6.6. The holes of the aligned grids form multiple channels through each of which one beamlet is extracted, accelerated, and focussed. The geometry of the accelerating channels, shaping and gap distances, are carefully designed to control beam optics by proper use of electrostatic lenses. In contrast to single beam extraction systems, such as accelerators in high energy physics, where additional beam optics can be placed anywhere along the beamline, the NBI beam receives its final properties already at this point.

The extraction system consists of three or more metallic grids. Fig. 6.7 shows a three-grid system. The first grid, called plasma grid, separates the source plasma from the accelerator. The acceleration field is generated by the potential difference between plasma grid and grounded grid. The decel grid, a third grid in between plasma grid and grounded grid, is negatively biased by a few kV with respect to the grounded grid. Its role is twofold. First, it serves to prevent electrons created in ionizing collisions in the neutralizer from being accelerated in opposite beam direction into the source and damaging the back of the source by excessive heat flux. A potential barrier of a few hundred volts is sufficient for the purpose. Second, the decel grid exerts an electrostatic divergent lens effect upon the ion beam.

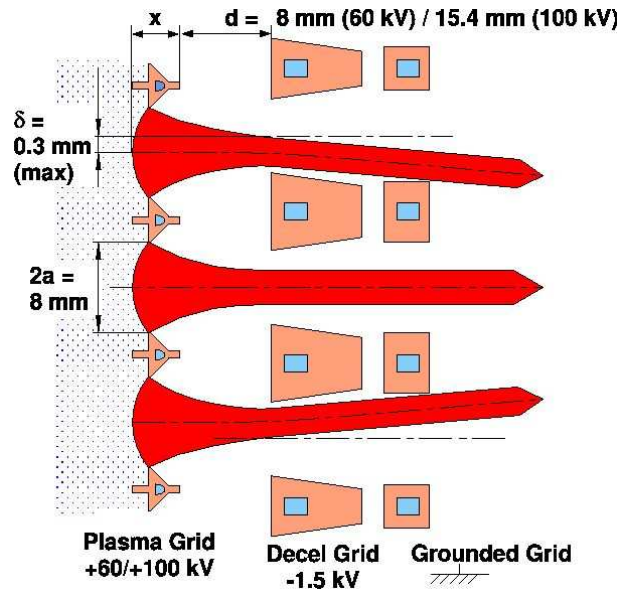


Figure 6.7: Extraction geometry for a three-electrode system for three circular beamlets with offset focussing (beam steering). Dimensions are given for the ASDEX Upgrade NBI system.

In the following paragraphs we will briefly discuss three concepts important in beam extraction. These are perveance, divergence, and steering.

Perveance: The current that can be extracted from a single aperture is basically determined by the space-charge-limited flow described by the Langmuir-Child law for non-relativistic charged particles

$$I = \Pi \cdot V^{3/2},$$

where I is the extracted current and V is the applied extraction voltage. The factor Π is called *perveance* and inversely proportional to the square of acceleration gap d ,

$$\Pi \propto \frac{1}{d^2}.$$

The perveance of an extraction system, and hence the extracted current, is ultimately limited by the minimum gap d required between the grids to hold the acceleration voltage without electrical breakdowns. Furthermore, for a given extraction system there is an optimum perveance at which the beam divergence is minimal.

In practice, the extracted current of an NBI ion source is not limited by space charge, but by the plasma density in front of the plasma grid. Nevertheless, perveance remains a useful quantity for reasons explained in the next paragraph.

Divergence: In contrast to electron emitters there is no fixed boundary from where the ions are emitted. Instead, the boundary between the undisturbed, field-free source plasma and the acceleration region is a curved surface (see Fig. 6.7) that is the self-consistent solution of the space-charge-limited flow of ions. For a given extraction geometry there is an optimum match between the ion flux density delivered by the plasma and the electrostatic acceleration potential V , i.e. an optimum perveance, such that the resulting plasma curvature yields a minimum

beam divergence. In practice, the minimum achievable divergence is limited by aberrations, space-charge forces and transverse beam energy due to a finite ion temperature in the source plasma. Typical values are of the order of 0.8° for the ASDEX Upgrade injectors. Because the matching condition for optimum beam divergence has to be met in every single aperture, the ion source has to produce an ion flux density which is reasonably uniform in space and time. Typically, non-uniformities larger than 10% lead to a degradation of beam divergence.

Steering: The beam dimensions at some distance from the ion source, e.g. at the porthole of the plasma device, are determined on the one hand by the divergence of the single beamlets and on the other hand by the finite dimensions of the plasma grid. The latter effect can be made negligibly small by aiming or steering the individual beamlets or groups of beamlets onto a common focal point or line. Apart from the obvious techniques of curving the electrodes or subdividing them and tilting the subsections with respect to each other there is a more subtle way of utilizing the defocusing effect of the electrostatic divergent lens formed by the electrostatic field distribution behind the decel electrode. Displacing an aperture in the negative grid with respect to the corresponding aperture in the plasma grid results in a deflection of the beamlet. The direction of deflection is opposite to the direction of displacement, i.e. it requires an outward (with respect to the axis of the whole beam) displacement of the decel aperture to create the desired inwards deflection of the beamlet. Beam steering is schematically shown in Fig. 6.7.

6.3.2 Neutralization

Neutralization happens via charge exchange collisions of the fast ions with the cold hydrogen molecules with the cross section shown in Fig. 6.1. The neutralizer is usually a drift tube directly attached to the ion source with a relatively high pressure $p_n > 10^{-3}$ mbar that is maintained by a constant inflow of neutral hydrogen gas.

Once neutralized, the fast atoms may also be ionized again in subsequent collisions. After a sufficient length ℓ of the neutralizer, or more precisely a sufficient $p_n \ell$, a steady state is reached in which the reaction rates of both neutralization and re-ionization are equal and the ratio of neutral to charged fast beam particles does no longer change. The ratio depends on the cross sections of both reactions that in turn depend on velocity. The optimal length of a neutralizer is such that the mentioned steady state is just reached. If the neutralizer is shorter, less ions are neutralized, if it is longer the losses of beam particles due to scattering in collisions increase.

The resulting neutral fraction of the beam at the end of the neutralizer is called neutralization efficiency. It is shown in Fig. 6.8. At low ion energies of < 20 keV/amu the efficiency can be as high as 90%. Above ~ 20 keV/amu the efficiency decreases for positive ions and becomes smaller than 50% above ~ 100 keV/amu. The decrease is mainly due to the decrease of the neutralization cross section shown in Fig. 6.1. Neutralization efficiencies smaller than 50% are unattractive because more than half of the energy invested for beam acceleration is wasted on the non-neutralized fraction of the beam.

Fig. 6.8 also shows that for negative ions the neutralization efficiency stays high throughout the depicted energy range. For negative ions neutralization happens via the stripping of the weakly bound additional electron. It is hence obvious that injection energies in excess of

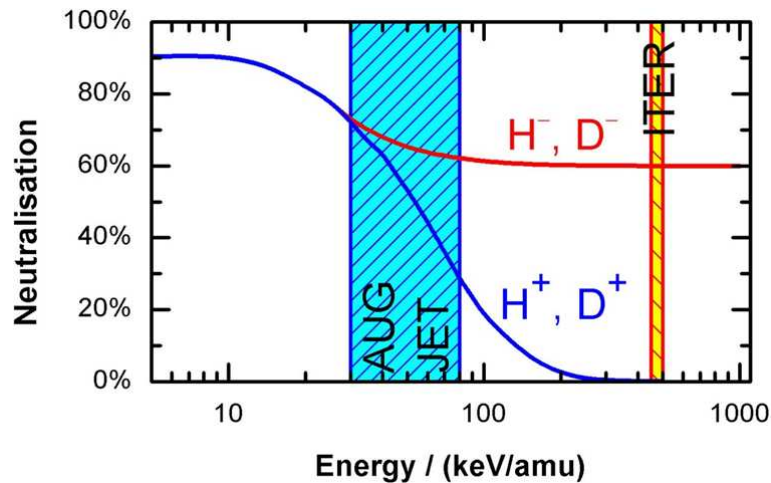


Figure 6.8: Optimum neutralization efficiency for positive and negative hydrogen ions versus beam energy per nucleon.

~ 100 keV/amu require negative-ion-based systems. Negative-ion-based NBI is used on the LHD stellarator in Japan, was used on the JT-60U tokamak and will be operated on its upgrade, JT-60SA, also situated in Japan (see Tab. 6.1). The NBI system for ITER, designed for 1 MV acceleration voltage, will necessarily have to start from negative ions.

6.3.3 Beam transport

Ion removal

When the beam leaves the neutralizer it is only partially neutralized. The previous argument that neutralization efficiencies lower than 50% are unattractive implies, on the other hand, that up to 50% of the beam can still be ionized and the ions carry up to the same power as the neutral beam. If no provisions were made these ions would be deflected by the fringe field of the fusion experiment and strike the walls of the beam line somewhere. On unprotected walls severe melting damage would occur. Therefore, the ions are removed from the beam in a controlled fashion and directed on specially designed residual ion dumps.

Removal of the ion beam is accomplished by the magnetic field of a bending magnet. The angle by which the beam is bent may be up to 180° , as in the case of the ASDEX Upgrade injectors.

The beam dumps are copper panels with a dense arrangement of cooling channels close to the surface. High pressure cooling water ensures a fast flow of water through these channels. A typical figure of merit for these advanced thermal sinks is a power density limit of 25 MW/m^2 perpendicular to the surface. To reduce the power density of the ion beam to below these acceptable limits the panels are inclined with respect to the direction of incidence.

Vacuum requirements

Downstream of the neutralizer the pressure should be significantly lower than in the neutralizer for mainly two reasons.

First, ionization and scattering of beam neutrals outside the neutralizer leads to a loss of particles and hence power from the beam. Furthermore, the ionized fast atoms are deflected by the fusion experiment's fringe field and hit the wall of the beam line. High fluxes of such ions can cause thermal damage to the walls. Moreover, ions hitting the walls can lead to desorption of gas from the surface that it turn leads to more ionization. This positive feedback can eventually lead to a catastrophic event known as beam blocking, in which most of the beam is becoming ionized in the beam line and hits the walls. The condition can be detected by the strong light emission associated with it and an interlock can stop the beams.

Second, NBI beam lines have to be connected to the torus via a duct with rather large diameter. A high pressure in the beam line would consequently also lead to a high flux of cold neutral gas to the torus. Such a huge flow of gas would render density control difficult to impossible, especially in low density discharges.

Both, estimates and experience tell that the pressure must be below 10^{-4} mbar to avoid both problems. The necessary pumping speed is determined by this allowed upper limit of the pressure and the gas flow into the beam line. This flow of gas comes from gas inlets into the ion source and the neutralizer and amounts to approximately 20 mbar ℓ /s of H₂ on each of the eight ion sources per beam line on JET.

The resulting total gas flow of the order of 100 mbar ℓ /s requires a pumping speed of several 10^6 ℓ /s to reach a pressure below 10^4 mbar. This cannot be achieved by conventional turbo or diffusion pumps as the open diameter of their flanges limits their pumping speed. Instead, large area cryo-condensation pumps cooled to 4 K with liquid He or titanium getter pumps (operated at room temperature) are used. In these systems a specific pumping speed of 10–20 ℓ /(s · cm²) for H₂ can be achieved perpendicular to the pump's front surface. Hence, a total pumping surface of several 10 m² is required. This is one of the reasons why conventional neutral beam systems are so big.

6.4 NBI systems based on negative ions

As discussed in sec. 6.2.1 ITER's NBI system is specified to have an acceleration voltage of 1 MeV for reasons of achieving the required heating power and central heating. Future devices such as DEMO or a fusion power plant—if they will have NBI—may require even higher beam energies. At these energies the neutralization efficiency for positive hydrogen ions is unacceptably low (see Fig. 6.8). For negative hydrogen ions, on the other hand, it never drops below 60%. Hence, the designs of NBI systems for ITER and for other large devices are based on negative hydrogen ions despite the fact that negative ion beams are much more difficult to produce than beams of positive ions.

The use of negative ions comes at a price. The additional electron has a low binding energy of 0.75 eV and can be easily detached in collisions with electrons or ions. While this is an

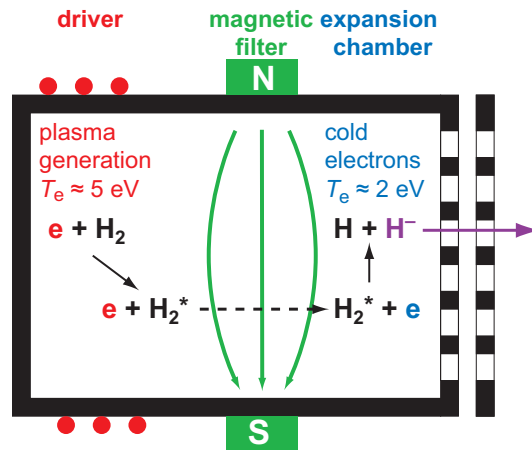


Figure 6.9: Volume production of H^- in a tandem source.

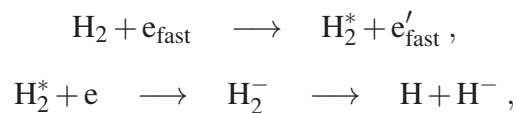
advantage in terms of beam neutralization, it also means that the negative ions have a very limited lifetime in the source plasma. Therefore, the extracted current densities from negative ion sources are typically a factor of ten lower than those from positive ion sources. The low current densities have to be compensated by the size of the extraction area.

6.4.1 Generation of negative hydrogen ions

There are basically two mechanisms that create negative hydrogen ions in a plasma source, *volume production* and *surface production*.

Volume production

Volume production is a two-step process. It is schematically shown in Fig. 6.9. In the first step a hydrogen molecule is excited in a collision with a sufficiently energetic electron to a high vibrational level ($v \geq 4$). In the second step, an additional electron is captured by the excited molecule forming an intermediate molecular negative ion. The molecular ion then dissociates into a neutral hydrogen atom and a negative hydrogen ion. The whole reaction reads



where the prime on the electron in the first reaction indicates that its energy has changed.

The vibrational excitation of the hydrogen molecules requires a high electron temperature, typically $T_e \sim 5\text{--}10\text{ eV}$. On the other hand, a low T_e around $1\text{--}2\text{ eV}$ maximizes the dissociative attachment reaction rates and simultaneously minimizes the destruction of H^- by electronic and ionic collisions. For this reason, the most common type of volume-production source, the tandem source shown in Fig. 6.9, has two distinct regions separated by a magnetic filter field, the driver and the extraction chamber. In the driver either an arc or an RF discharge is generated in hydrogen gas as described earlier for positive ion sources. External magnets create the

magnetic filter near the plasma grid perpendicular to the extraction direction. The filter field reduces electron transport from the driver leading to reduced n_e and T_e in the extraction region.

Efficient volume production requires a high density of all species involved in the two-step reaction. On the other hand, a high density also shortens the mean free path of negative ions before destruction. Furthermore, a high density in the source also increases the gas density and hence the stripping losses in the acceleration system. For this reason volume production is not a viable concept for the large ion sources used for NBI.

Surface production

The generation mechanism better suited for large ion sources is surface production. In surface production, a neutral hydrogen atom or a or a positive hydrogen ion captures one or two electrons upon backscattering from a surface with a low work function,



The probability of this electron capture reaction depends on the work function Φ of the surface, the affinity A of the electron—being 0.75 eV for negative hydrogen ions—and also on the perpendicular velocity v_\perp of the escaping ion. The negative ion yield per H impact on a wall can be predicted by

$$Y(\text{H}^-/\text{H}^+) = \exp\left(-\frac{\Phi - A}{Cv_\perp}\right),$$

where C is a constant, and $(\Phi - A)$ represents the difference of energy between the Fermi level of the surface and the affinity level; it should be as small as possible to enhance the electron capture probability.

The most widely used method to lower the surface work function is to cover a metal with cesium. The optimal coverage with cesium is about 0.6 monolayers (3.3×10^{14} Cs/cm²) with an energy-dependent production yield of up to 0.67 H⁻ per incident H atom. For tungsten, for example, the work function of W(110) is reduced to 1.45 eV compared to 5.25 eV for pure tungsten. For the surface conditions found on most cesiated sources, the expected yield $Y(\text{H}^-/\text{H})$ or $Y(\text{H}^-/\text{H}^+)$ is in the range 10^{-2} – 10^{-1} , in agreement with experiments.

The cesium coating is usually achieved by evaporating Cs into the chamber and redistribution through the plasma. The transport in these cesium-seeded discharges is governed by complex physics and plasma chemistry. Achieving long pulse stability therefore requires a basic understanding of the dynamical behaviour of the cesium distribution in the source.

Due to the short survival path length of H⁻ only negative ions produced on surfaces in direct proximity to the extraction holes have a sufficient chance of being extracted. However, negative ions created at the plasma grid surface are accelerated by the plasma sheath backwards into the source. Thus, they initially start in the wrong direction and have to effectively turn towards the extraction grid. Two processes are mainly responsible for this required change of direction. Firstly, the magnetic fields of the electron-deflection magnets in the extraction grid and the filter field bend the trajectories of the negative ions such that they may eventually become extracted. Secondly, charge exchange collisions of the type $\text{H}^- + \text{H} \rightarrow \text{H} + \text{H}^-$

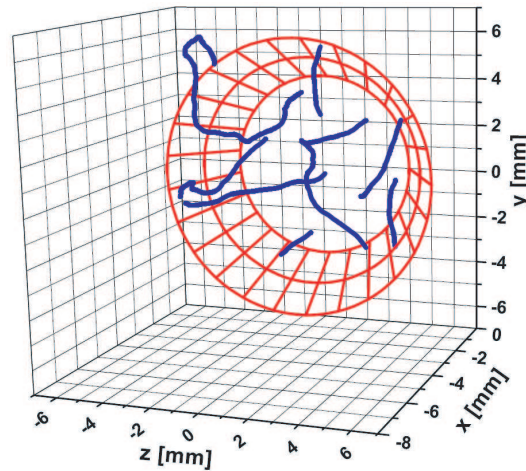


Figure 6.10: Simulated extraction trajectories from a chamfered plasma grid aperture.

can transfer the additional charge to a hydrogen atom that travels in a different direction. The use of chamfered apertures instead of a flat design improves the extraction probability by increasing the effective area for production of negative ions and by providing a more favorable starting angle of H^- from the surface. Simulated trajectories of H^- are shown in Fig. 6.10. The sharp bends correspond to charge exchange while the smooth bends are a result of the magnetic fields.

Destruction of H^-

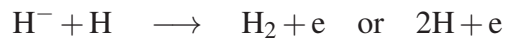
The destruction of negative ions in the plasma is dominated by three processes. These are electron stripping



which is very effective for electron temperatures in the range of a few electronvolts, mutual neutralization



that depends slightly on the ion temperature, and, finally, associative detachment



that has a weak dependence on the temperature of the atoms.

Electron stripping can be minimized by reducing T_e to approximately 2 eV, but then mutual neutralization will take over. In either case this results in survival lengths for the negative ions that are short compared to the source dimensions. Nevertheless, a reduction of the electron temperature below 2 eV helps to increase the survival length and is achieved by the magnetic filter field. Furthermore, the formation of H^- has to be maximized on surfaces close to the extraction holes, i.e. on the plasma grid surface.

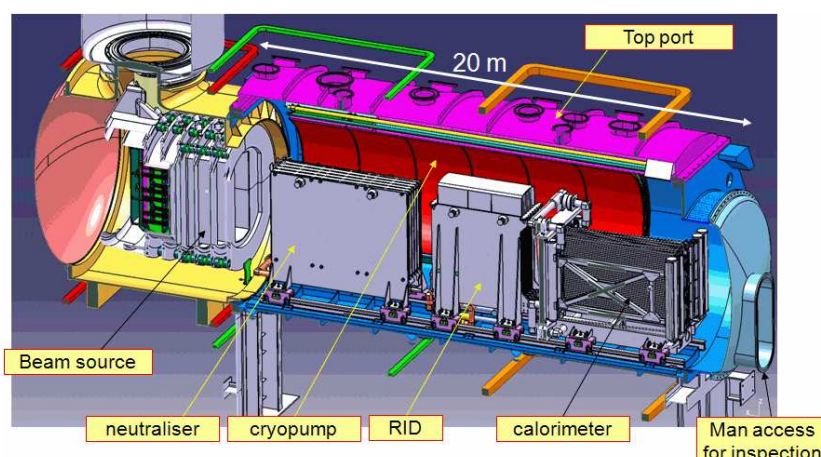


Figure 6.11: Sketch of the ITER neutral beam test facility MITICA at RFX.

6.4.2 Co-extraction of electrons

Extracting negative ions will unavoidably also lead to the extraction of electrons, as the charges of both have the same sign. Accelerating these electrons to full beam energy is a waste of energy (and money) and bears the risk of causing heat flux damage at the locations struck by these electrons. Therefore, the extraction systems for negative ions have a first stage with rather low acceleration voltage of $\sim 10\text{kV}$ between the plasma and the *extraction grid*. The extraction grid is equipped with permanent magnets to bend the electron trajectories onto this heavily cooled grid. Besides, biasing the plasma grid positively with respect to the source body reduces the co-extracted electron current and can increase the extracted negative ion current significantly.

6.4.3 Wall plug efficiency and neutralization efficiency

The current drive efficiency defined in sec. 6.2.5 relates the driven current to the heating power coupled to the plasma and is determined by the physics of current drive. From an engineering and economic standpoint it is more important to ask how much of the electric power produced by the fusion power plant P_{el} is the gross power P_{NBI} needed to run the NBI system to achieve the required non-inductive current drive. P_{NBI} is larger than the coupled power P_c by all the power losses in the system and the power needed for auxiliary systems. The ratio P_{NBI}/P_{el} is called circulating power fraction. The wall plug efficiency is defined by

$$\eta_{wp} = \frac{I_{cd}}{P_{NBI}} = \frac{I_{cd}}{P_c} \frac{P_c}{P_{NBI}} = \epsilon_{cd} \eta_{syst}.$$

For DEMO, $\eta_{syst} > 0.6$ is required.

The main losses of present-day NBI systems are the power carried by the non-neutralized beam fraction, i.e. the power to the residual ion dump, and, in the case of negative ions, the power carried by the co-extracted and co-accelerated electrons. Minimizing these losses is of paramount importance if NBI is used in DEMO or a power plant.

Table 6.2: Parameter of the ITER NBI system.

Current Density	20 mA/cm ² D ⁻
Electron Content (j_e/j_{ion})	<1
Accelerated Current	40 A
Beam Energy	1 MeV
Pulse Length	3600 s
Extraction Area	2000 cm ²
Source dimensions	1.9 × 0.9 m ²
Homogeneity	10%

Like positive ions, negative ion beams are conventionally neutralized during the transit through a neutral hydrogen-gas-filled tube, however by stripping of the additional electron instead of charge exchange. The achievable neutralization efficiency is $\approx 60\%$ at high extraction voltages. The remaining $\approx 40\%$ of the beam are more or less equally partitioned between H⁻ and H⁺.

A totally different concept might provide still higher neutralization efficiencies and therefore less energy loss. Photo detachment, the detachment of the additional electron by the photons of a laser in an optical cavity, could be of interest for future NBI systems.

6.4.4 Development of a negative-ion-based system for ITER

ITER will have two NBI beamlines with one source each. According to ITER's specifications each source will have to deliver 16.7 MW of 1 MeV neutral deuterium. The extracted current will be 40 A. Given the comparatively low extracted current densities achievable with negative ion sources this requires a huge extraction area of 2000 m². The total cross section of the source will be 1.9 × 0.9 m². The parameters of the ITER NBI are given in Tab. 6.2.

Fig. 6.11 shows a sketch of the neutral beam test facility MITICA (Megavolt ITER Injector & Concept Advancement) that will be constructed by Consorzio RFX in the next few years in Padua, Italy. It will be a complete prototype of the ITER injectors comprising ion source, accelerator, neutralizer, residual ion dump (RID), and calorimeter. It is designed in close collaboration with other European associations. IPP Garching contributes strongly to the design of the RF source and the RF circuits as well as to diagnostics and modelling of the RF driven plasmas.

Acceleration system

In addition to plasma and extraction grid the ITER accelerator has five additional grids, forming five acceleration stages of 200 keV each (see Fig. 6.12). The gaps between the grids are 90 mm each. Due to the large number of grids beam alignment is a difficult task. The advantage of this multiple gap design is that—in contrast to a single gap design—stripped off,

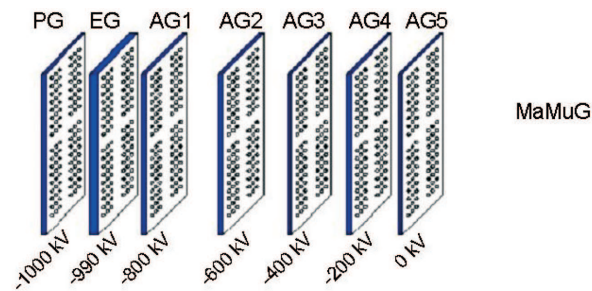


Figure 6.12: Sketch of the ITER-NBI acceleration system.

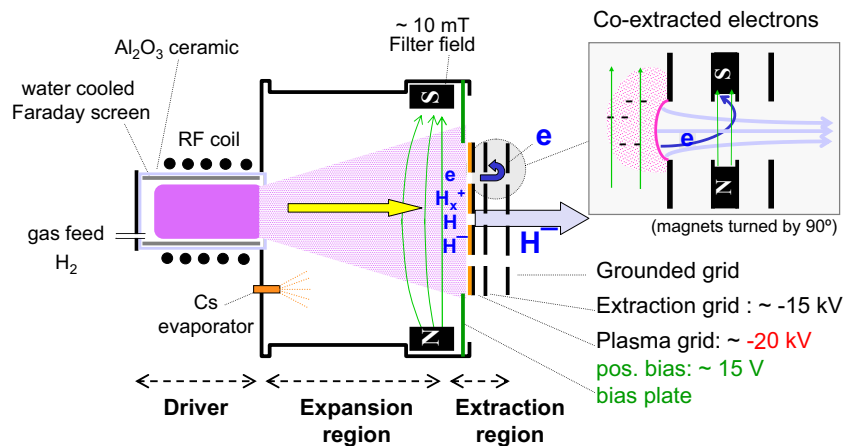


Figure 6.13: Basic layout of the IPP RF driven negative ion source.

co-accelerated electrons can be removed from the beam onto the grids before they are accelerated to full energy. Additionally, it was found that the design with multiple gaps has better voltage holding properties.

Stripping losses, i.e. losses of the additional electron of negative ions, in the accelerator system due to collisions with the background gas depend on the source pressure. These stripping losses lead to non-fully accelerated ions and to additional heat loads on the grid system. As a compromise between these stripping losses and stable source operation ITER requires a source pressure of 0.3 Pa. For comparison, positive ion sources run at a few Pa. Even at this low pressure, the stripping losses in the ITER NBI acceleration system are estimated to about 30%.

RF-driven ion source

The development of large negative ion sources was started in the early 90s in Japan with filamented arc sources for the fusion experiments LHD and JT-60U. This development was the basis for the design of the ITER neutral beam injection system. Due to the advantages of the RF source mentioned above and due to the good experience with the positive ion based RF sources on the NBI system for ASDEX Upgrade, IPP Garching started the development of an RF driven negative ion source in the end of the 90 s. In July 2007 the RF source was chosen

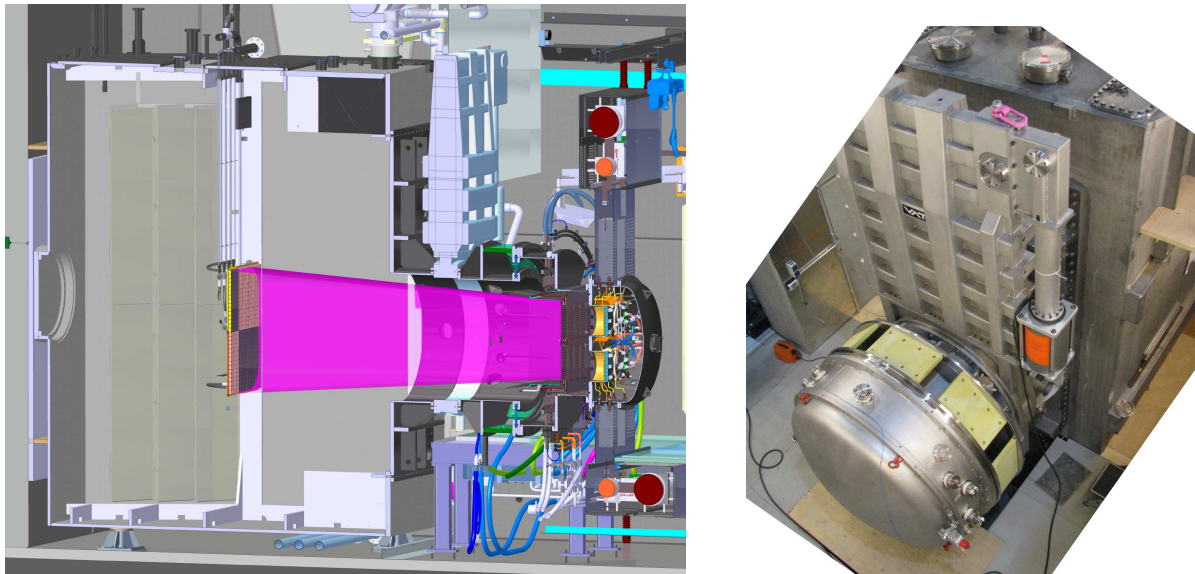


Figure 6.14: CAD drawing of the half-ITER-size source on the testbed ELISE (left side) and a photograph taken during construction in late 2011 (right side). To give an impression of the size: the big vacuum vessel is over 4 m high.

by the ITER board as the reference design. Details of the source and the current status can be found in [16].

Fig. 6.13 shows the principle design of the IPP RF-driven negative ion source. This RF source consists of three parts: the driver, where the RF is coupled to the plasma, the expansion region, where the plasma expands into the actual source body, and the extraction region. The latter two are separated by a magnetic field of the order of 10 mT parallel to the plasma grid, called filter field. This field is necessary in order to keep the hot electrons generated by the RF with energies of around 10 eV away from the extraction region. There electron temperatures below 2 eV are necessary in order to minimize the destruction rate of the negative hydrogen ions by electron collisions. The driver is mounted on the back of the source body and consists of an alumina cylinder (245 mm in diameter) with a water-cooled RF coil connected to a 1 MHz oscillator. An internal, water-cooled copper Faraday screen protects the alumina cylinder from the plasma and reduces capacitive coupling.

Current densities of 33 mA/cm^2 with H^- and 23 mA/cm^2 with D^- have been achieved with the IPP RF source on the small test facility BATMAN (Bavarian Test Machine for Negative Ions) at the required source pressure of 0.3 Pa and electron/ion ratio < 1 , but with a small extraction area of only 74 cm^2 and limited pulse length $< 4 \text{ s}$. BATMAN is equipped with the standard size IPP RF source, a rectangular body with the dimensions of $32 \times 59 \text{ cm}^2$ and 23 cm depth.

Long pulses were investigated on the long pulse test facility MANITU (Multi Ampere Negative Ion Test Unit). Its extraction area could be extended up to 300 cm^2 and the pulse length up to 3600 s, using the same driver and source body as on BATMAN.

The extension of the source dimensions to those required for ITER follows a modular concept; instead of upscaling the whole driver eight drivers of the size used on the previous test beds will be mounted on the back of the source. The feasibility of the modular concept and the achievable plasma uniformity were investigated on the test bed RADI, featuring four drivers on a half-ITER-size source without beam extraction.

At present the all parameters defined in the ITER NBI specifications have been achieved one at a time, but not yet simultaneously. This is partly due to the lack of adequate large-scale and long-pulse test facilities so far. As a consequence, the European ITER domestic agency F4E has defined an R&D roadmap for the construction of ITER's NBI system. An important step herein is IPP's new test bed ELISE (see Fig. 6.14), a half-ITER-size RF-driven ion source with the aim of demonstrating the extraction of a 60 kV, 20 A beam, that will commence operation in 2012. ELISE will give significant input for the design of neutral beam test facility PRIMA, currently under construction by Consorzio RFX in Padua, Italy. PRIMA will comprise two individual test facilities, SPIDER, a full-size ion source with 100 kV extraction, and the full power NBI prototype MITICA, entering operation in 2017.

Further reading

A general overview of heating methods can be found in Wesson's book [7]. The physics of NBI heating are treated in detail by Cordey [8] and in Speth's review article [9]. Fish [10] gives an extensive overview of current drive methods in general while Mikkelsen and Singer [11] focus on NBI current drive. Good overviews of neutral beam systems are in Duesing's [12] and Speth's [9] articles. The physics of negative ion generation was compiled by Pamela [13] and details on the development of negative ion based systems can be found in references [14, 15, 16]. The current status of the development of RF-driven negative ion sources for ITER is reported in references [17, 18].

References

- [1] W7-A Team, Proceedings of the IAEA Fusion Energy Conference (1980) 185.
- [2] F. Wagner et al., Phys. Rev. Lett. 49 (1982) 1408
- [3] R. J. Hawryluk et al., Rev. Mod. Phys. 70 (1998) 553
- [4] M. Keilhacker et al., Nucl. Fusion 39 (1999) 209
- [5] A. C. Riviere, Nucl. Fusion 11 (1971) 363.
- [6] T. Oikawa et. al., Proceedings of the IAEA Fusion Energy Conference (2000)
- [7] J. Wesson, *Tokamaks*, Oxford University Press, 4th ed. (2011)
- [8] J. G. Cordey in *Applied atomic collision physics; Volume 2*, edited by H. S. W. Massey, E. W. McDaniel and B. Bederson, Academic Press, Orlando (1984) 327

- [9] E. Speth, *Neutral beam heating of fusion plasmas*, Rep. Prog. Phys. 52 (1989) 57.
- [10] N. Fish, Rev. Mod. Phys. 59 (1987) 175
- [11] D. R. Mikkelson and C. E. Singer, Nucl. Technol./Fusion 4 (1983) 238
- [12] G. Duesing et al., *Neutral beam injection system*, Fus. Techn. 11 (1987) 163.
- [13] J. Pamela, *The physics of production, acceleration and neutralization of large negative ion beams*, Plasma Phys. Contr. Fusion 37 (1995) A325.
- [14] Y. Ohara, *Development of high power ion sources for fusion*, Rev. Sci. Instr. 69 (1998) 908
- [15] R.S. Hemsworth, *Long pulse neutral beam injection*, Nucl. Fusion 43 (2003) 851.
- [16] Speth et al., *Overview of the RF source development programme at IPP Garching*, Nucl. Fusion 46 (2006) S220.
- [17] U. Fantz et al., Nucl. Fusion 49 (2009) 125007
- [18] P. Franzen et al., Nucl. Fusion 51 (2011) 073035
- [19] P. Franzen et al., Fus. Eng. Des. 88 (2013) 3132

Chapter 7

Plasma wall interaction in nuclear fusion devices

Karl Krieger

7.1 Overview

A major issue for design and construction of a nuclear fusion reactor with a magnetically confined plasma is the interaction of the hot plasma with the material components of such a device. On the one hand, the plasma facing vessel components represent a sink for energy and particles released by the plasma. On the other hand, the particle bombardment of the material surface may lead to release of wall atoms and of previously implanted fuel atoms which in turn may enter the plasma.

The contamination of the plasma by impurities released from the vessel structure is one of the main problems caused by plasma wall interaction processes. An additional problem is the alteration of the material structure by the particle bombardment and the high energy flux which may limit the lifetime of the plasma facing components significantly. These problems must be solved under the constraint that the generated power has to pass through the vessel components at some location. The wall may further act as a reservoir for the hydrogen fuel isotopes leading to an uncontrollable additional source of fuel atoms, which may cause problems in maintaining stationary discharge conditions.

In the following we will first introduce a basic model of the edge plasma region in contact with the walls, the so-called scrape-off layer (SOL). Then the basic interaction processes between plasma and material walls will be discussed. This includes in particular wall erosion processes leading to impurity production and mechanisms involved in the formation of hydrogen wall inventories and the corresponding recycling processes. Finally, the main diagnostic methods for investigation of plasma wall interaction processes will be discussed.

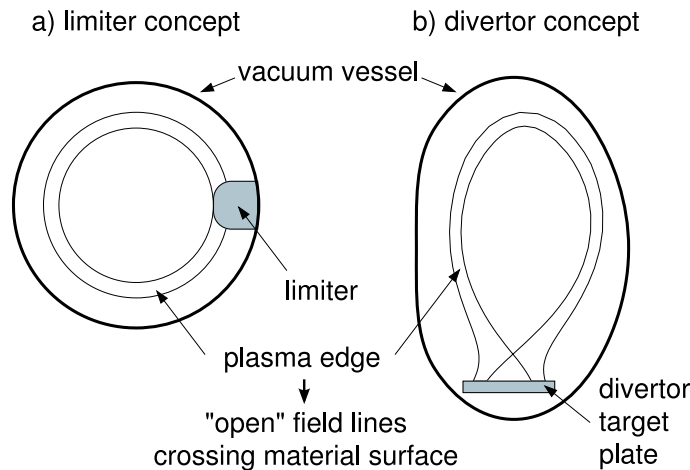


Figure 7.1: Poloidal cross-section of a limiter type (a) and a divertor type (b) plasma configuration with principal plasma facing wall components.

7.1.1 Plasma facing components

In a fusion reactor, we find several components facing the plasma directly. The largest surface consists of the first wall which surrounds the bulk region of the plasma torus. The plasma shape may be restricted by additional limiters to protect the vessel wall or equipment like antennas for radio-frequency heating which cannot withstand excessive heat loads. Finally, a very important part of the plasma facing components in current and future fusion devices are the divertor target plates. In a diverted plasma configuration these plates provide the main plasma-surface interaction zone. The fraction of the fusion power carried by the produced α -particles is coupled out to a large extent through these areas.

Fig. 7.1 shows poloidal cross-sections of a limiter type (a) and a divertor type (b) plasma configuration. In a divertor configuration the distance of the plasma wetted surface areas to the confined plasma region is much larger than for limiter configurations. Due to the correspondingly lower penetration probability of eroded material, it is much easier to maintain a low impurity level in diverted plasma discharges.

7.1.2 Bombardment of the walls with plasma particles

If the plasma is in direct contact with wall components, electrons and ions will hit the surface. This particle bombardment leads to release of atoms by collisions and, for certain materials by chemical reactions. In addition the wall material will be heated by the corresponding energy transfer. Finally, electron impact may produce secondary electrons which are reemitted back into the plasma.

The incident plasma ions will be neutralized with a fraction of them being reflected, while the remaining part will be implanted and may be released with some delay. Neutralized particles entering the plasma are ionized again by electron impact or by charge exchange processes with plasma ions. Charge exchange processes in hot plasma regions will produce neutral particles at high energies, which can escape the plasma hitting also plasma facing components without

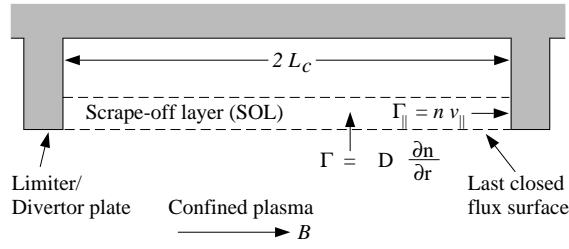


Figure 7.2: Schematic view of the scrape off layer in a magnetically confined plasma [1]. a is the minor plasma radius, B is the magnetic field, L_c is the connection length, Γ_{\perp} is the diffusive flux of particles perpendicular to B and Γ_{\parallel} is the flux of particles streaming along B .

direct plasma contact. high energetic particles and about one half of these will hit the walls again and might be reemitted with some probability.

In fusion plasmas facing components are also subject to intense irradiation by neutrons, which leads to modifications of the material structure and to corresponding degradation of mechanical stability and thermal conductivity.

Wall atoms eroded by the particle bombardment and, in case of excessive heat loads, by evaporation processes, will enter the plasma as impurities with detrimental effects on plasma performance. The erosion of wall surfaces will also limit the lifetime of the respective components. The eroded material will, however, migrate through the plasma until it is finally redeposited, which may balance the erosion to a certain extent.

7.2 The scrape-off layer

As shown in Fig. 7.1 the plasma edge in a magnetically confined plasma is either defined by a material limiter or, in the case of a diverted plasma, by a magnetic separatrix (see Fig. 7.2). Inside the so defined boundary, the magnetic surfaces are closed while in the region between the boundary and the wall surface, the so called scrape-off layer, the field lines intersect material components. The particle exhaust and the α -particle fraction of the produced power (as well as the additional heating power during start-up) are coupled out to a large extent through this region and transferred to the limiters or divertor plates.

The variation of plasma density and temperature in the scrape-off layer as a function of the minor radius can be approximately described by an exponential decay. Using a simple model of particle balance with purely diffusive transport perpendicular to the magnetic field and sonic flow along the field lines, one can estimate the decay length λ_n as a function of the perpendicular diffusion coefficient, D_{\perp} , and the ion sound velocity, c_s . The rate \dot{N}_{\perp} of particles per unit poloidal length W diffusing across the separatrix into the SOL must be equal to the rate $2\dot{N}_{\parallel}$ of particles per unit poloidal length streaming along the magnetic field lines towards the two

limiters or target plates. \dot{N}_\perp and \dot{N}_\parallel are given by

$$\begin{aligned}\dot{N}_\perp &= D_\perp \partial n / (\partial r)|_{r=a} L_c W &= D_\perp n(a) / \lambda_n L_c W &= \Gamma_\perp L_c W &\text{ and} \\ \dot{N}_\parallel &= \int_a^\infty n(a) \exp(-(r-a)/\lambda_n) dr c_s W &= n(a) c_s \lambda_n W &= \Gamma \lambda_n W ,\end{aligned}\quad (7.1)$$

where $2L_c$ is the connection length and $c_s = ((T_e + T_i)/m_i)^{1/2}$. Solving $\dot{N}_\perp = 2\dot{N}_\parallel$ one obtains an exponential decrease of n with a characteristic decay length of $\lambda_n = (D_\perp L_c / c_s)^{1/2}$. A similar analysis holds for the temperature assuming convective energy transport. Inserting typical parameters ($D_\perp = 1 \text{ m}^2/\text{s}$, $L_c = 10\text{--}100 \text{ m}$, $T_{e,i} = 10\text{--}100 \text{ eV}$), one obtains a decay length in the range from 1–5 cm which is in good agreement with measured values. The decay length of the power flux is smaller because it is determined by the product of n and T .

Since the total energy and particle flux leaving the plasma is concentrated in a very narrow region of the target plates, the incident flux will be strongly amplified over the flux across the plasma boundary. Assuming a circular shaped plasma torus with major radius R and minor radius a , one obtains a torus surface of $4\pi^2 aR$. The plasma wetted surface of a divertor or limiter in contact with the plasma boundary is $2\pi R\lambda$. The radial flux crossing the boundary of the confined plasma is therefore amplified by the ratio of these surfaces $\pi a/\lambda \simeq 100$ with $a = O(1 \text{ m})$ and $\lambda = O(1 \text{ cm})$. For a fusion machine like ITER, the α -particle heating power is $\simeq 200 \text{ MW}$. With a major plasma radius of $\simeq 6 \text{ m}$ one obtains a heat flux at the target plates of $\simeq 100 \text{ MW/m}^2$, which exceeds by far the engineering limits of any material. It is therefore necessary, to distribute the power to a larger area of the vessel, for example by increasing edge radiation from impurities and charge exchange processes.

7.3 Electric coupling of plasma and wall

When the magnetic field intersects a solid surface, the surface will charge up negatively with respect to the plasma. Consider a small plasma cube with one side limited by a wall and with electrons and ions in thermodynamic equilibrium i.e. with a Maxwellian velocity distribution. For the particle flux to the wall one obtains $\Gamma_e = n\bar{v}_e/4$ and $\Gamma_i = n\bar{v}_i/4$. With $\bar{v} = (8kT/\pi m)^{1/2}$ one sees readily that $\Gamma_e = \Gamma_i (m_i/m_e)^{1/2} \gg \Gamma_i$. A repelling potential for the electrons will build up until the fluxes are balanced which is necessary to maintain the quasi neutrality of the plasma. Because of the screening effect of the plasma, the potential is restricted to a sheath with a width of some Debye lengths $\lambda_D = (kT_e/4n_e^2)^{1/2}$.

To determine the value of the potential, we consider the balance of ion and electron flux along the field lines. The ions enter the electrostatic sheath with ion sound velocity, thus $\Gamma_i = nc_s$. The electron flux to the wall is modified by the sheath potential

$$\Gamma_e = \frac{n_e}{4} \sqrt{\frac{8kT_e}{\pi m_e}} \exp(-e\Phi/kT_e). \quad (7.2)$$

The electron hitting the wall material will produce secondary electrons which reenter the plasma with a flux $\Gamma_{es} = -\gamma\Gamma_e$ with γ being the secondary electron emission coefficient. From

the balance of ion and electron flux $\Gamma_i = (1 - \gamma)\Gamma_e$ we obtain

$$e\Phi = -\frac{kT_e}{2} \ln \left(\frac{2\pi m_e}{m_i} \left(1 + \frac{T_i}{T_e} \right) \frac{1}{(1 - \gamma)^2} \right). \quad (7.3)$$

For a cold hydrogen plasma ($\gamma \ll 1$) with $T_i \simeq T_e$ one obtains $\Phi \simeq 3kT_e/e$. Obviously, if γ increases, the argument of the logarithm will increase as well and become undetermined for $\gamma = 1$. In reality, for $\gamma \geq 0.8$, an electron space charge layer will form at the surface inhibiting any further secondary emission. In that case, the equation above does not hold anymore.

Because only the fast electrons will reach the wall, the electrons are cooled in the sheath. The ions, however, gain additional energy because they are accelerated in the sheath potential. For a Maxwellian plasma the energy flux in one direction is given by $Q = 2kT\Gamma$. The convective energy fluxes to the wall surface are then given by

$$Q_e = 2kT_e\Gamma_e = 2kT + e\frac{\Gamma_i}{1 - \gamma}, \quad Q_i = \left(2kT_i + \frac{kT_e}{2} - e\Phi \right) \Gamma_i, \quad (7.4)$$

where the contribution of $kT_e/2$ for the ions has its origin by an additional acceleration in a pre-sheath potential drop. Obviously, the major part of the energy flux is deposited by the ions because of the acceleration by the sheath potential. With increasing edge temperatures the secondary electron emission may come closer to one, thus leading to very high energy fluxes to the wall through the electron channel.

In addition the energy deposition is increased by the neutralization energy of the ions and, for hydrogen, by the recombination energy of the hydrogen atoms.

7.4 Hydrogen fuel cycle

The hydrogen isotopes used as fuel for nuclear fusion interact with most of the relevant reactor materials. This is important in particular because of

- radiological reasons: The storage of tritium in the first wall is responsible for the major fraction of the tritium inventory in fusion reactors;
- engineering aspects: Hydrogen in solids may alter their mechanical properties in an unfortunate way;
- density control of the plasma: The hydrogen inventory in the walls during a stationary discharge will be much higher than the hydrogen content of the plasma itself, leading to possible difficulties in maintaining a stable plasma density.

At low plasma temperatures, neutral atoms and ions hitting the wall will usually be reflected after transferring a part of their kinetic energy to the material.

For high plasma temperatures, the particles can penetrate deeply into the material. In this case, the recycling of the particles will be determined by kinetic reflection, but in addition, the particles may be implanted and reemitted after diffusion back to the surface. In the following, these processes will be discussed in more detail.

7.4.1 Reflection

Ions and neutral particles hitting the wall material will not be reflected right at the solid surface. Usually they will penetrate the material and be scattered by the atoms and electrons in the crystal lattice. Collisions with nuclei will lead to energy transfer and deflection while collisions with electrons will only lead to energy loss. If the path of the penetrating particles leads them back to the surface, they will be reemitted. The particle reflection coefficient R_n and energy reflection coefficient R_E defined by

$$R_n = \frac{\text{number of reflected particles}}{\text{number of incident particles}} \quad \text{and} \quad R_E = \frac{\text{energy of reflected particles}}{\text{energy of incident particles}} \quad (7.5)$$

can be determined by computer simulations where the particle trajectory and the energy transfer in the scattering processes is calculated assuming binary collisions. Experimental results are obtained from backscattering experiments, which are, however, very difficult at energies below 10 eV due to strongly decreasing detector sensitivities.

Fig. 7.3 left shows the reflection coefficients of hydrogen for two reactor relevant materials, carbon and tungsten, as a function of the energy of the incident hydrogen atoms. The reflection is mainly determined by backscattering processes and therefore increases with the target atom mass. With increasing energy the incident particles will penetrate more deeply into the bulk material, which leads to the observed decrease of the reflection coefficients towards higher energies. The simulations assume an attractive surface potential, which leads to the strong decrease of the reflection coefficients at energies below 1 eV. The determination of the precise form of the surface potential is, however, a very difficult problem. In addition, adsorbed hydrogen at the surface will strongly modify the surface potential function.

7.4.2 Implantation, diffusion and reemission

The fraction of implanted hydrogen ions which are not reflected, i.e. which do not find their way back to the surface right after penetration, are slowed down by subsequent scattering and will eventually be trapped, either at grain boundaries or at vacancies in the bulk. In addition they may be bound in form of a metal hydride.

When the ions enter the solid surface they recombine to atoms and the fraction which is not trapped within the course of the thermalization process may then travel through the material by diffusion. If the atoms reach a surface, they will recombine to molecules and may be released by thermal desorption.

Metals

Diffusive propagation of neutral hydrogen in a metal is described approximately by a transport equation for the concentration $c(x)$ of free atoms in a depth x

$$\frac{\partial c}{\partial t} = D \frac{\partial^2 c}{\partial x^2} + Q - \frac{\partial c_T}{\partial t} , \quad (7.6)$$

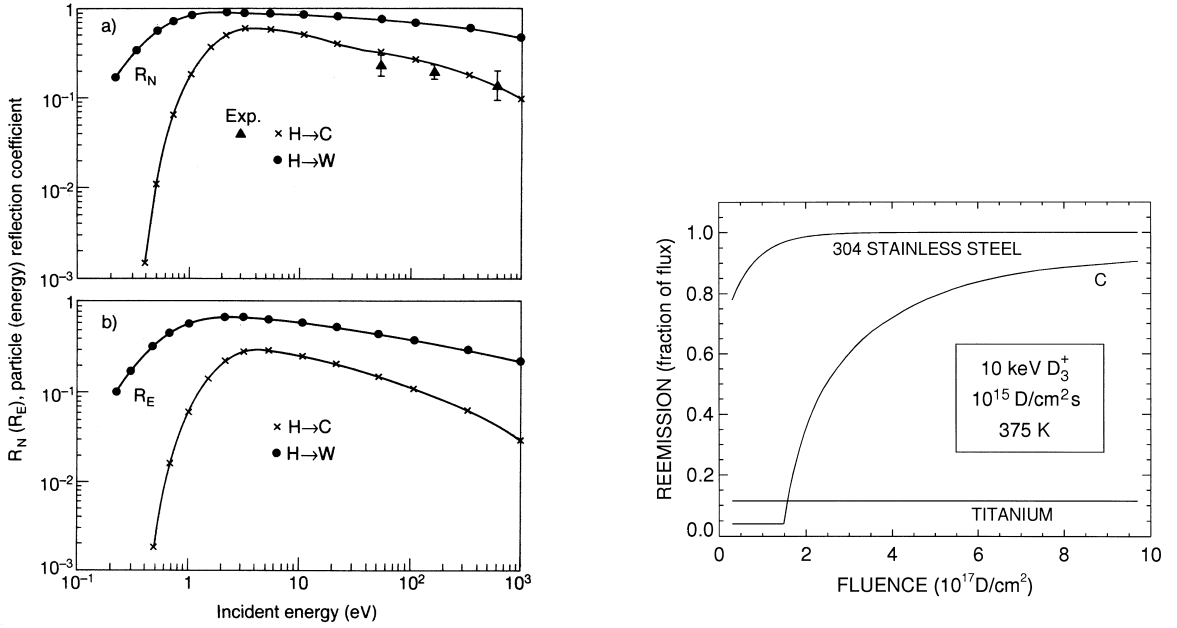


Figure 7.3: Left: Particle (a) and energy reflection coefficients (b) for hydrogen ions incident on carbon and tungsten solid surfaces as a function of the impact energy. Right: Reemission as a function of fluence (total number of implanted atoms) for different materials. The reemission is expressed in units of the implantation flux.

where Q is the source function of implanted hydrogen atoms and c_T is the concentration of trapped atoms. The maximal concentration will be found in a depth approximately equal to the mean ion range R_p . From there, the atoms diffuse back to the surface as well as deeper into the bulk material. At the surface, the rate of release is determined by the recombination rate coefficient to H_2 because energetically only molecules can be released. For the H_2 -flux one obtains

$$\Gamma_{H_2} = -D \frac{\partial c}{\partial x} \Big|_{x=0} = Kc(x=0)^2, \quad (7.7)$$

where K is the molecular recombination rate constant.

The final equilibrium distribution depends further on the solubility of the hydrogen in the material. For metals in which hydrogen dissolves exothermically like titanium, the surface is a potential barrier. Therefore, the reemission of hydrogen will be very low, the hydrogen is collected in Ti, forming TiH_2 (see Fig. 7.3 right).

In metals like steel, where hydrogen is dissolved endothermically, the reemission depends on the temperature. At low temperatures the diffusion coefficient is small and the reemission is determined by the diffusive transport. A steady state concentration builds up until the flux of implanted atoms is equal to the reemission flux (see Fig. 7.3 right). After stopping the implantation process, the hydrogen inventory in the material will be reemitted. This situation is typical for present fusion experiments with steel walls where the wall temperature remains low because of the short discharge times.

With higher temperatures (500°C for steel) the diffusion increases strongly. In that case, the reemission is mainly determined by the recombination to H₂ at the surface. This situation would occur in a fusion reactor and is important with respect to the tritium fuel. The tritium inventory in the wall will be small but on the other hand, a considerable fraction of the tritium atoms will diffuse through the wall and must be captured for example by a double wall structure with a pumped interspace.

Carbon

For carbon as wall material, the situation is different to the metals. For temperatures 400°C like in present fusion experiments with graphite as wall material, there is practically no diffusion. Implanted hydrogen will be collected until a saturation level of 0.4 H/C is reached. If the implantation continues, the additional hydrogen will be reemitted immediately (see Fig. 7.3 right). After stopping the implantation, the reemission will be much smaller than for metals. In present fusion experiments, the saturation level is reached after some discharges which may cause problems in controlling the plasma density. With so called conditioning discharges using helium, one can decrease the hydrogen inventory if necessary.

In a fusion reactor with wall temperatures above 500°C, diffusion and recombination to H₂ become important also for carbon with similar problems for the tritium handling as for the metals.

A further process leading to trapping of hydrogen in carbon will occur in devices with divertor plates made of carbon. Carbon atoms produced by erosion of the plate surfaces may be deposited at other locations where they will collect more hydrogen. This leads to a further increase of the hydrogen inventory in the vessel.

7.5 Impurity production

As mentioned in sec. 7.1, the bombardment of the wall elements by particles escaping the plasma or streaming along field lines which intersect a solid surface will produce in turn a source of neutral atoms from the wall material. Depending on the location of the surface and the plasma properties in the vicinity of the source, a certain fraction of the wall atoms will penetrate the plasma becoming ionized there. The presence of these impurities may degrade severely the plasma properties necessary for nuclear fusion. In this section, we will discuss the most important processes responsible for the contamination of the plasma.

7.5.1 Sputtering

When an ion or neutral atom is hitting a solid surface, it follows a complicated trajectory because of collisions with the lattice atoms in the solid. During this collision cascade the incident particle will be reflected or trapped as described in the previous section. In addition, if a surface atom receives sufficient energy from a collision, it is sputtered away from the solid

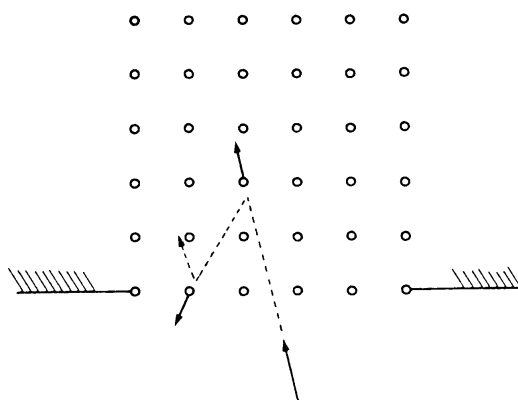


Figure 7.4: Schematic view of the physical sputtering process. The ion incident from the left is reflected in a first collision to the surface where it releases a lattice atom in the second collision.

(see Fig. 7.4). This is only possible if the energy of the incident particle is above a certain threshold E_{th} . The sputtering yield Y is defined by

$$Y = \frac{\text{average number of sputtered particles}}{\text{incident ion}} . \quad (7.8)$$

For central collisions, the fraction of the kinetic energy E_0 of an incident particle with mass m_1 which is transferred to a target atom with mass m_2 is given by $\gamma = 4m_1m_2/(m_1 + m_2)^2$. For light projectiles sputtering will occur only if the incident particle is reflected in a first collision towards the surface as shown in Fig. 7.4. Its energy after the collision is $E_0(1 - \gamma)$. To sputter a surface atom, the transferred energy in the following collision $E_0\gamma(1 - \gamma)$ must be high enough to exceed the surface binding energy E_s . This leads to a threshold energy of

$$E_{th} = \frac{E_s}{\gamma(1 - \gamma)} . \quad (7.9)$$

For most materials E_s is in the range 3.5–9 eV. Therefore, for the same projectile mass, the threshold energy is mainly determined by the mass of the target atoms. However, if m_1m_2 , e.g. if the projectile and the target atoms are the same (self sputtering), the collision cascades are much larger and the model described above does not hold any longer. In that case, the threshold energy is $E_{th} = 4E_s$.

The left part of Fig. 7.5 shows the sputtering yields Y of different targets for bombardment with D atoms. Apart from the described dependence of the threshold energy from the mass of the target atoms the position of the maximum in Y increases to higher target masses.

To determine the sputtering yield of a material exposed to a plasma, one has to integrate the sputtering yields over the energy distribution function of the incident plasma ions. In the plasma the ions usually are close to a Maxwellian distribution. Ions impinging on a solid surface are, however, accelerated by the sheath potential, which significantly increases their

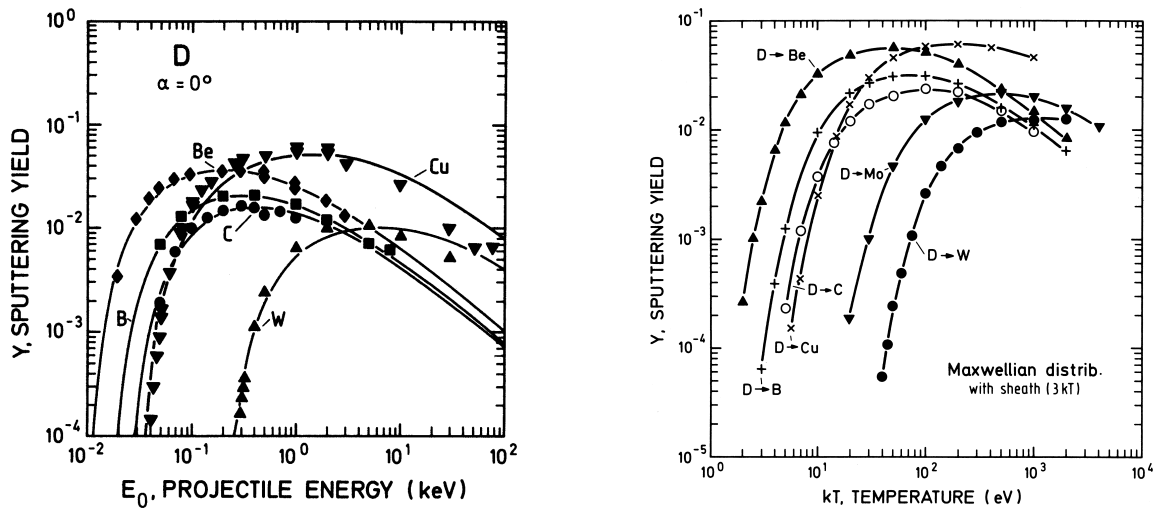


Figure 7.5: Left: Calculated sputtering yield Y of various target materials for bombardment by D ions as a function of impact energy.
Right: sputtering yields for exposure to a D-plasma as a function of the plasma temperature including acceleration by the sheath potential.

impact energy. The right plot of Fig. 7.5 shows results for a D-plasma. The ions from the high energy tail of the temperature distribution and the effect of the sheath acceleration lead to significant sputtering even at plasma temperatures fairly below the monoenergetic sputtering threshold energy.

For heavy projectiles, in particular in the case of self sputtering, the yield may even become greater than one which will lead to an unlimited increase of the impurity content in the plasma.

For light projectiles Y_{\max} is always < 1 . This is, however, only true for normal incidence. If the angle of incidence increases from the normal, the sputtering yield increases as well and may become > 1 .

The sputtered wall particles are practically all neutral. Except for single crystal targets their angular distribution is given approximately by a $\cos(\theta)$ distribution. Their energy distribution has typically a maximum at $0.5E_s \simeq 2\text{--}3$ eV. Therefore, they can deeply penetrate the plasma before they become ionized which gives them a high probability to become confined in the plasma.

7.5.2 Chemical erosion

Another erosion process will be found if the incident particles produce volatile compounds with the target material. This is observed in particular for carbon surfaces with hydrogen plasmas or with oxygen as a plasma impurity. In the first case, methane and higher carbohydrates are produced while in the latter case, production of carbon monoxide (CO) can be observed. These gases are set free very easily from the surface by thermal desorption or collisions.

For the most important case $D^+ \rightarrow C$, chemical erosion by high energy particle bombardment will occur mainly at surface temperatures in the range $500\text{--}600^\circ\text{C}$. However, if the energy of

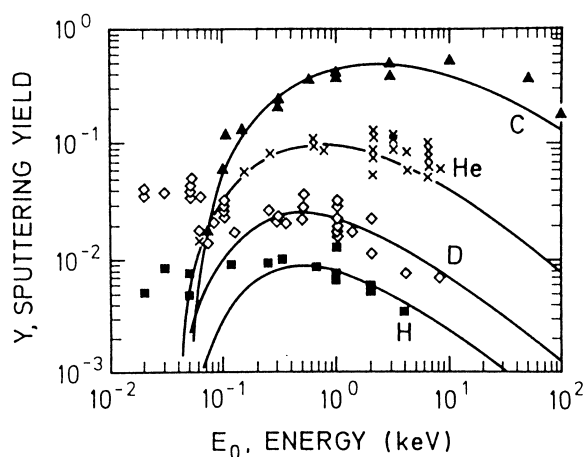


Figure 7.6: Dependence of the sputtering yield of graphite for H, D, He and C ions at normal incidence. The solid curves represent results from simulations of physical sputtering.

the incident deuterons is smaller than 100 eV, chemical erosion processes will dominate the physical sputtering processes. Fig. 7.6 shows sputtering yields for hydrogen, deuterium and helium impact on a carbon surface. The solid lines represent results from calculations with a simulation code for physical sputtering. Obviously, for hydrogen and deuterium sputtering/erosion occurs even below the threshold energy for physical sputtering.

E results from ASDEX Upgrade which is equipped with graphite wall tiles and divertor plates, confirm that the carbon content of the plasma is indeed to a large extent produced by chemical erosion of the main chamber graphite tiles.

7.5.3 Sublimation, evaporation

In a closed system, sublimation from a solid surface or evaporation of fluid material is in equilibrium with the condensation from the gas phase. The equilibrium is determined by the temperature and the steam-pressure of the material. For steam pressures above 10^{-6} mbar, sublimation or evaporation will be the dominant process. For beryllium which is considered as a possible wall material, the corresponding temperature is 800°C while sublimation of carbon will only occur for temperatures $> 2\,000^{\circ}\text{C}$.

Furthermore, laboratory experiments show that in carbon exposed to high levels of particle influx, interstitial atoms are produced which can reach the surface by diffusion where they sublime. This process starts at much lower surface temperatures ($\gtrsim 800^{\circ}\text{C}$) and could lead to increased carbon production in a fusion reactor.

7.5.4 Desorption

The surfaces inside the vacuum vessel are covered with thin layers of water, cleaning agents and residue of manufacturing processes. Depending on their surface binding energy, they will

be released from the wall by the particle bombardment from the plasma thus producing an additional source of plasma impurities. It is possible to remove the weakly bound layers by glow discharges, however, the remaining oxide layers and adsorbed water molecules cannot be removed and are the main source for the oxygen contamination of the plasma.

7.5.5 Arcing and melting

If metals are used as wall material, the surface can be destroyed by melting, if the heat load from the plasma becomes so high that it cannot be removed by conduction and cooling. Droplets of molten material from the upper vessel regions can fall into the plasma where the sudden rise of the radiation losses may cause a break down of the discharge.

As less spectacular erosion process can be observed under certain discharge conditions. Because of the potential difference between edge plasma and wall, electric arcs are ignited by field emission from ridges and peaks in the surface which last for times $1 \mu\text{s}$ with a size of some mm. After ignition the cathode spot on the material surface is heated up by ion bombardment from the arc and cooled by the melting and conduction. The cathode spot grows because of the increasing erosion and after reaching a critical size the arc breaks down and may ignite again in the vicinity.

7.5.6 Positive and negative aspects of impurity contamination

The impurity contamination of the plasma in a fusion reactor can only be tolerated below a critical level which depends mainly on the charge number of the impurity atoms. However, if one can restrict the zone with higher impurity concentration to the plasma edge and the divertor plasma, the presence of impurities can also have a beneficial effect as described below.

High-Z – cooling of the central reaction zone

Heavy impurities like tungsten, molybdenum and to a certain extent nickel and iron are not fully ionized in a fusion plasma. The power loss by their line radiation is a function of the plasma temperature which has for high-Z elements a maximum in the temperature range of 10^6 – 10^7 K relevant for nuclear fusion. Therefore, concentrations higher than 0.01% (for W, Mo) and higher than 0.1–1% (for Fe, Ni) will lead to a power losses which inhibit the ignition of the plasma.

Fuel dilution

Light impurities like beryllium, boron and carbon and also helium as a product of the fusion process will be fully ionized in the plasma core. Therefore, they do not emit line radiation in the central region in contrast to the cooler edge regions. The radiation losses in the outer plasma zone will not inhibit the ignition and the burning of the plasma. However, they still

can degrade the overall energy balance of the fusion reactions. A further negative effect is the dilution of the fuel ions in the core because of the quasi neutrality of the plasma which will decrease the fusion rate. For these reasons, the concentrations of light impurities in the confined plasma must not be higher than 2–5%.

Edge cooling and power exhaust

Under certain plasma conditions, in particular at high densities, it turned out that it is possible to confine the impurities in the divertor region of a tokamak plasma. There are attempts to use the intense line radiation produced by light impurities in this cooler zone as a means to spread the power flux generated from the plasma onto a larger area of the vessel surface thus decreasing the power load of the divertor target plates. The impurities can be introduced into the divertor plasma either by sputtering from the walls or by additional puffing of impurities in gas form. This concept is known as *radiative divertor*.

Another concept to make use of radiation to decrease the power load of the divertor plates consists basically in trying to increase the divertor density to very high values and to puff in additional gas. Then, a cold plasma zone will establish above the divertor plates in which the plasma ions streaming towards the plates are cooled by charge exchange radiation. However, in these processes, as mentioned above, fast neutral atoms are produced which may increase the wall sputtering. This concept is known as *cold gas target*.

7.6 Diagnostics for plasma surface interaction

Many diagnostics are needed to provide the information for a more detailed understanding of the edge plasma and plasma-wall interaction. A detailed description would break the size limit for this manuscript, therefore only a short overview is given over diagnostics used directly in fusion experiments and diagnostic methods used in laboratory experiments for example to analyze wall materials and surfaces.

7.6.1 In situ diagnostics

- *Electron density and temperature* are measured by Thomson scattering and from spectral emission of neutral atom beams injected into the plasma edge. A further possibility is the use of electrical Langmuir probes which allow the measurement of n_e and T_e and in addition the *floating potential* of the plasma.
- *Impurity densities and fluxes* and the *densities of molecules* are measured by spectroscopy and laser resonance fluorescence. With good spectral resolution, *impurity temperatures* can be measured as well. However, there is no good method to obtain the *temperature of the plasma ions*.
- *The composition of the neutral gas* is determined by mass spectrometry. This gives valuable information for example on the molecules produced by chemical erosion.

- *Velocity spectra of escaping neutrals* are measured by time of flight spectrometers. These provide information on the ion temperature in the plasma and allows to estimate the effects of the neutral wall bombardment.
- *Surface temperatures and heat flux deposited on surfaces* are measured by infra red cameras.
- *Surface erosion and deposition* are investigated with long term marker probes where materials are vaporized as thin layers onto surface elements. To analyze single discharges, collector probes are used which allow in addition the determination of *impurity flux, mean energy and mass* and *plasma ion fluxes and mean energy*. After exposure to the plasma for a certain time, the probes are removed and analyzed by surface analytical techniques described in the next paragraph. As a further method to measure *erosion and redeposition of thin material layers* one can measure the thickness of such layers by interferometric methods.

7.6.2 Laboratory experiments

- *Analysis of collector probes and long term exposition probes.* The surface structure of the probes is examined by raster electron microscopy. The electron beam of the microscope will produce bremsstrahlung when hitting the examined surface which is characteristic for each element and allows the determination of the material composition. A quantitative determination of the distribution of an element in the material is possible by scanning the surface with high energy ion beams (in the MeV range) of protons, deuterons or α -particles. One can measure the energy distribution of the ions from Rutherford backscattering processes (RBS) or, in case of a proton beam, the spectrum of the proton-induced X-ray emission (PIXE). A further possibility is the detection of products of nuclear reactions induced by the incident ion beam which are also characteristic for a certain element. To measure the erosion of the probe surface, a trace element is implanted in a surface layer with known thickness. The erosion rate is determined by measuring the thickness of the remaining layer after exposition of the probe.
- *Hydrogen recycling* is studied by implanting protons or deuterons in materials until steady state is reached and measuring the pressure of the reemitted atoms as a function of time after switching off the beam.
- *Sputtering coefficients* can be measured by bombarding a probe with an ion beam and measuring the weight loss after a certain exposition time. In addition, the sputtered material can be analyzed by laser resonance fluorescence.
- *Reflection coefficients* are determined by estimating the amount of trapped atoms or by detecting the reflected particles using ion spectroscopy.

References

- [1] J. Wesson, *Tokamaks*, p. 424 (1996).
- [2] W. Hofer, J. Roth (Ed.), *Physical Processes of the Interaction of Fusion Plasmas with Solids*, San Diego (1996).
- [3] R. Behrisch and D.E. Post (Ed.), *Physics of Plasma Wall Interactions in Controlled Fusion*, Proceedings of a NATO Advanced Study Institute, New York (1985).
- [4] P.C. Stangeby, *The Plasma Boundary of Magnetic Fusion Devices*, Bristol (2000).
- [5] O. Auciello, D.L. Flamm (Ed.), *Plasma Diagnostics - Surface Analysis and Interactions*, San Diego (1989).
- [6] J.C. Vickermann (Ed.), *Surface Analysis - The Principa Techniques*, West Sussex (1997).

Chapter 8

Introduction to plasma diagnostics

Hans-Jürgen Hartfuß

8.1 Introduction

Investigating hot magnetized plasmas in the frame of fusion research, a large number of different diagnostic methods must be applied. Common to all diagnostic techniques is that plasma probing is conducted without any material contact between the measuring instrument and the plasma. Material probes can only be used in the very plasma edge and only for short moments.

The physics principles underlying the various techniques originate from almost all fields of physics. They are complementing one another with respect to dynamic range or concerning certain information gained by other diagnostic systems necessary to interpret the measurements. The whole diagnostic system has redundancy which means that a given physical quantity, say the electron temperature, is measured simultaneously by a number of different measuring systems which are based on different physics principles, ensuring that systematic errors do not remain unrecognized.

Although a large number of diagnostic methods is well developed and established, growing new fields of research demand for additional information, or higher spatial and temporal resolution, stimulating the development of new methods and even more refined techniques. Recent developments are often related to turbulence characterization, measuring fluctuating plasma parameters with high time and space resolution and determining correlations between various fluctuating quantities.

Typically more than 50 different diagnostic systems are installed at modern large fusion experiments. They provide the data which form the basis for the scientific work conducted, and they provide as well the bulk of information necessary for the safe operation of the fusion experiment and the protection of its components. Diagnostic data rate of the whole system typically exceeds 100 Mbyte per second. The data must reliably be stored in such a way that data access remains possible even after many years.

To characterize the plasma in an adequate way and to understand its complex behaviour as complete as possible, a large number of different plasma parameters must be determined simultaneously. These are the density of the electrons and the ions, the composition and density

of certain impurities in the plasma, the temperature of the electrons and of the ions which can differ significantly depending on the heating scenarios conducted, the total stored energy, the plasma pressure, the radiation loss, currents and electric fields in the plasma and many others. Most of them are local quantities varying with the radial coordinate. Examples are the electron temperature and density being typically maximal at the plasma axis and approaching low values at the plasma edge varying over orders of magnitude. Most of the quantities are time dependent with characteristic times varying significantly. While fluctuating quantities are characterized by time scales of the order of $1 \mu\text{s}$, certain currents in the plasma or the energy content vary slower by five orders of magnitude. The demanded accuracy of all the diagnostic measuring systems is typically 1–10%. The spatial resolution aimed at is 1–5 cm and the time resolution of the order of 0.1 ms. This short introduction to the subject concentrates on the physics behind the most important diagnostic methods, factoring out completely the wide field of technical realizations.

8.2 Categorization

The various diagnostic methods can be arranged according to different ordering principles. A natural distinction divides into active and passive methods whereas in each case waves or particles must be considered. Moreover Langmuir-probes form a separate class of techniques which could be assigned to both passive and active particle diagnostics. Another class is formed by magnetic diagnostics.

A more physics oriented categorization distinguishes the physics processes involved: Electron or ion processes, processes leading to the emission of electromagnetic radiation, light scattering processes, processes connected with the refractive index of the plasma and so on. Other organizing principles used in literature are based on the techniques involved, like laser-, spectroscopic-, X-ray-, microwave-, atomic beam techniques, etc. We will adapt an ordering scheme according to the first one given above. The chapters following directly reflect this choice.

8.3 Sightlines

Plasma probing with waves or by particles occurs along a sightline through the plasma determined by the experimental conditions of the measuring system.

- In a single sightline arrangement one cannot distinguish from which point of the sightline the information is coming from. Only line integrated information can be gained (examples: spectroscopy, interferometry).
- Using 10 to 15 sightlines simultaneously, however, local information can be derived from a reconstruction process called Abel-inversion (multi-channel interferometry).

- Modern computer based reconstruction methods allow for the application of tomography. Local information is obtained from a large number of typically several hundreds of line-integrated signals from pinhole camera systems (soft X-ray bremsstrahlung, bolometry).
- A special case of passive wave diagnostics, gives local information from a single sight-line since the origin of radiation is connected with the frequency of the emission that mapping between frequency and location is possible (electron cyclotron emission).
- Applying active techniques with atomic or laser beams, the origin of the information detected is defined by the crossing volumes of primary beam and detection beams, resulting in local information (Thomson scattering, neutral hydrogen diagnostic beam).

All diagnostic methods out of the categories active and passive wave or particle diagnostics belong to one of these five different observation schemes. Using Langmuir-probes the location is defined by the tip of the material metallic probe. Magnetic diagnostics have no spatial resolution since they measure the total flux changes enclosed by loops outside the plasma column.

8.4 Magnetic diagnostics

Magnetic measurements are conducted with induction loops wound around the torus in various orientations. The voltage V obtained at the clamps of a loop with N turns and area A is determined by the temporal flux change enclosed by the loop

$$V = - \int_F \frac{\partial B}{\partial t} dF = -NAB\dot{.} \quad (8.1)$$

The magnetic field B is obtained by integration accomplished electronically. The most important magnetic diagnostics reveal the total plasma current with the Rogowski-coil, the loop voltage with the voltage-loop, and the total stored energy in the plasma with the diamagnetic-loop. The basic arrangements are shown in Fig. 8.1.

8.4.1 Rogowski-coil

The Rogowski-coil is a solenoid enclosing the whole plasma current i.e. the torus in one poloidal plane. It is sensitive only to the poloidal field generated by the net current I_p consisting of electron and ion currents in opposite directions. No information is gained on the current distribution. The plasma current I_p is derived by integrating the measured voltage V over time which is for a coil with n windings per unit length and area A given by

$$V = \dot{\Phi} = nA\mu_0\dot{I}_p \quad (8.2)$$

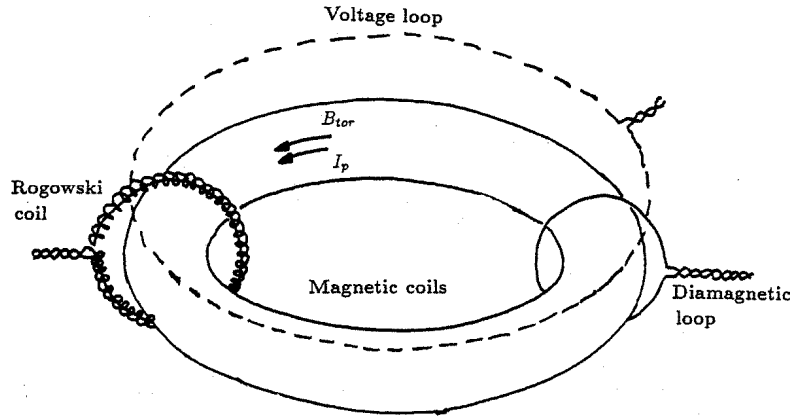


Figure 8.1: Arrangement of the most important inductive loops forming the set of magnetic diagnostics in a toroidal fusion device: The Rogowski-coil to measure the total plasma current, the voltage-loop to measure the current driving loop voltage, and the diamagnetic-loop which allows to determine the total stored energy in the plasma.

8.4.2 Voltage-loop

In tokamak experiments the plasma current is driven by the voltage generated by the external transformer. This so-called loop voltage is measured by an inductive loop consisting of a single wire which encloses the total flux generated by the transformer. The voltage loop lies parallel to the torus ring. Knowledge of the loop voltage V_l and the plasma current I_p are connected through the plasma conductivity and since the conductivity is temperature dependent, also the average electron temperature can be derived

$$\frac{I_p}{V_l} \propto \sigma \propto T_e^{3/2}. \quad (8.3)$$

8.4.3 Diamagnetic-loop

The average plasma pressure or equivalently the average energy density can also be determined from purely inductive measurements. In a magnetized plasma electrons and ions are gyrating around the field lines in a way that the external field is weakened giving rise to the plasma diamagnetism. The flux change $\Delta\Phi$ caused by the plasma built up in the magnetic field is proportional to the average plasma pressure $\langle p \rangle$ equivalently to the average energy density

$$\Delta\Phi \propto \langle p \rangle = k_B \langle n_e T_e + n_i T_i \rangle. \quad (8.4)$$

It is measured with the simple flux loop wound around the torus in poloidal direction. It must be integrated in time to get the actual stored *diamagnetic* energy.

8.5 Wave diagnostics

Wave diagnostics gain information either by analyzing the spectral composition of the emitted radiation from the plasma (standard spectroscopy) or by measuring the changes in amplitude, phase, polarisation or k -vector a wave undergoes when passing the plasma.

The hot magnetized plasma is emitting radiation in a very wide spectral range. To gain the full information contained, passive probing must therefore be done at wavelengths extending from about 10 mm to 0.1 nm over about eight orders of magnitude covering the ranges from micro-waves to X-rays. Basically also absorption spectroscopy can be done in this range. It has gained, however, only minor importance.

In active probing experiments the wave particle interaction is almost completely governed by the mobile electron component of the plasma. The electron density determines a cut-off frequency below which no propagation is possible and beyond which the refractive index of the plasma varies in a characteristic way. Largest changes occur in the mm and sub-mm spectral regions which therefore have the highest diagnostic potential.

At frequencies far above this cut-off, the refractive index approaches the vacuum value, however, electrons can still be accelerated by the wave's E -field causing wave scattering which carries important information about the scattering centres.

8.5.1 Active wave measurements

Microwave diagnostics

Propagation of an electromagnetic wave through the plasma is described by the dispersion relation connecting the wave k -vector to the frequency $k = k(\omega)$, from which the refractive index N can be derived.

Neglecting ion motion and collisions between particles in a non-magnetized plasma, the dispersion relation and the refractive index are

$$\omega^2 - \omega_p^2 = k^2 c^2 ; \quad N = \sqrt{1 - \left(\frac{\omega}{\omega_p}\right)^2} . \quad (8.5)$$

ω_p is the plasma frequency determined by the electron density

$$\omega_p^2 = n_e \frac{e^2}{\epsilon_0 m_e} . \quad (8.6)$$

Propagation is only possible for $\omega > \omega_p$. Since electron densities are typically in the 10^{19} – 10^{20} m^{-3} range, propagation is only possible beyond about $f = \omega/2\pi > 100 \text{ GHz}$. It is the mm-wave range where the strongest changes of the refractive index occur, which is therefore used for probing (see Fig. 8.2 left).

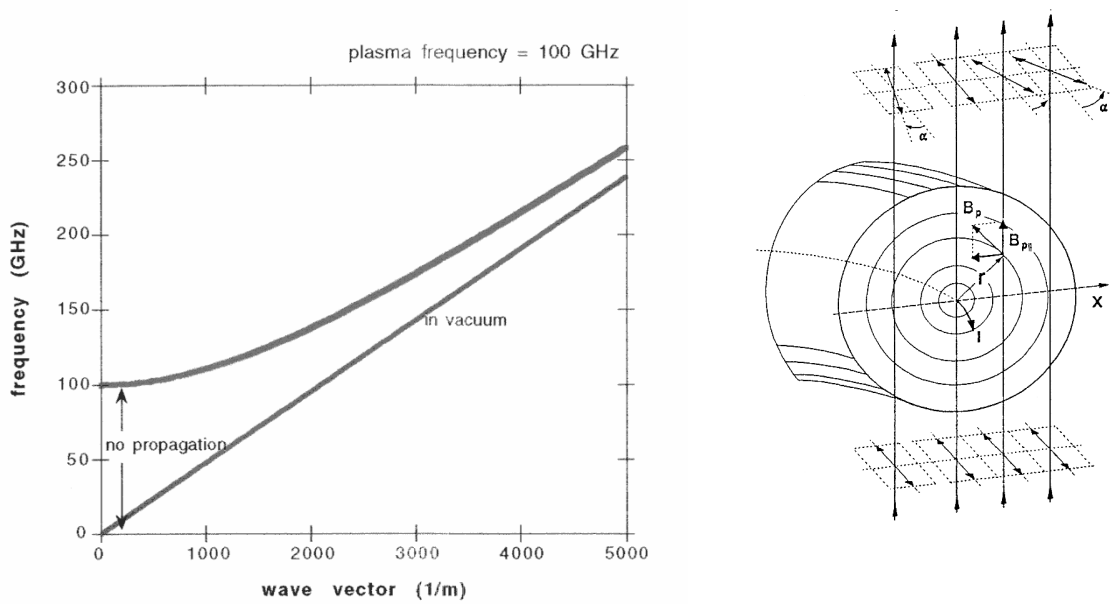


Figure 8.2: Left: Dispersion relation of a non-magnetized plasma (red). The plasma frequency is chosen 100 GHz corresponding to an electron density of $1.26 \times 10^{20} \text{ m}^{-3}$. At frequencies below the plasma frequency no propagation is possible.

Right: Principle arrangement of a polarimetry system to measure the poloidal field generated by the plasma current. The Faraday-effect gives rise to a rotation of the polarization plane by the angle α . The rays through the plasma can be used as well as interferometer channels to determine simultaneously the electron density (H. Soltwisch, Transactions of Fusion Technology **25**, 304 (1994)).

Contrary to this a magnetized plasma is a strongly anisotropic medium. General expressions for the dispersion relation are complicated.

However, in case a linear polarized wave propagates perpendicular to the B -field through the plasma with its E -field parallel to B (ordinary mode) the dispersion relation is identical to that one of the non-magnetized plasma, as given above. The relation is the basis for two important diagnostic systems interferometry and reflectometry operated under the above described conditions.

1. Interferometry

Since the refractive index depends on the electron density via the plasma frequency, measurements based on the refractive index give information on the electron density. The measurement is done by comparing the optical path difference between a microwave signal through the plasma and one through free space which can easily deduced from the phase difference of the two signals. If the probing frequency is large compared to the plasma frequency, the phase difference is proportional to the electron density integrated

along the line of sight

$$\varphi = \frac{2\pi}{\lambda} \int_{z_1}^{z_2} (N_V - N(z)) dz \propto \int_{z_1}^{z_2} n(z) dz. \quad (8.7)$$

The integral quantity determined in this way is called the line-density and is one of the most important parameters in fusion diagnostics. Local information can be gained by operating simultaneously a number of interferometers with parallel sightlines covering the plasma cross section and by applying mathematical inversion techniques (Abel-inversion).

2. Reflectometry

While interferometry uses frequencies in the range 200 GHz to 30 THz far above the plasma frequency, in reflectometry the probing frequency range is chosen just to meet it. As mentioned before plasma frequencies range from about 30–100 GHz. Reflectometry then launches a wave in this frequency range and determines the position inside the plasma where $N(\omega)$ approaches zero and from where the launched wave is reflected. The position of the reflecting cut-off layer is determined applying RADAR techniques by measuring the time delay to the cut-off layer and back. This can be done electronically in various ways, either with short microwave pulses of sub-ns duration or by sweeping the frequency of a continuous wave and measuring the resulting phase change. Other methods are basically combinations of these two. The local electron density $n_e(r)$ is determined from a scan of the probing frequency relating time delay τ and cut-off frequency $\omega(\tau)$.

3. Polarimetry

The dielectric properties of the magnetized plasma give rise to additional effects which can favourably be used for diagnostic applications. Considering here only active wave probing with propagation parallel and perpendicular to any B -field of a magnetized plasma. In case of parallel propagation, the two characteristic waves are the left and the right hand circular polarized waves. Due to the gyration motion of the electrons with frequency ω_c , the magnetized plasma is circular birefringent, which means the refractive indices of the left and right hand circular waves N_L and N_R differ. A magnetized plasma therefore shows the Faraday-effect: The polarization plane of a linear polarized wave propagating along the B -field is rotated by a small angle α given by

$$\alpha = \frac{1}{2} \frac{2\pi}{\lambda} \int_{z_1}^{z_2} (N_L - N_R) dz \approx \frac{1}{2c} \int_{z_1}^{z_2} \omega_p^2 \omega_c \frac{dz}{\omega^2} \propto \int_{z_1}^{z_2} n_e(z) B_{\parallel}(z) dz. \quad (8.8)$$

The measurement is a line-integrated measurement in an arrangement almost identical to that of an interferometer. Therefore often the two are combined to form an interfero-polarimeter arrangement measuring simultaneously the phase to determine the electron density and the rotation of polarization to determine the parallel B -field component along the line of sight. If the line of sight is chosen within one poloidal plane, the parallel B -field is the one generated by the plasma current. In case many sightlines are used simultaneously, the plasma current density can be determined (see Fig. 8.2 right).

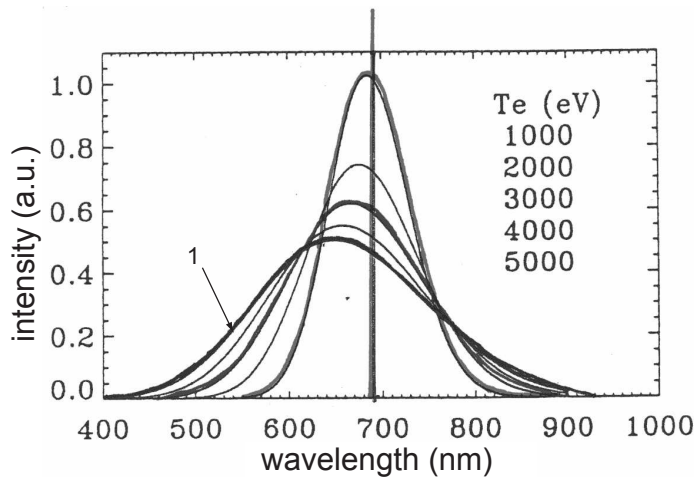


Figure 8.3: The spectra of the Thomson scattered radiation for various temperatures T_e . The primary laser line is at about 700 nm. With increasing temperature relativistic effects cause an asymmetry in the scattering spectra (line 1).

In case of propagation perpendicular to a B -field field, the two characteristic waves are linear polarized waves with the E -field parallel to B , the one used for interferometry, called ordinary wave (O-mode) and the extraordinary wave (X-mode) polarized perpendicular to B . Again the refractive indices for the two waves differ, which means the magnetized plasma is linear birefringent as well, it shows the Cotton-Mouton-effect. This means the ellipticity of a linear polarized wave composed of an X- and an O-mode component is changed when passing the plasma. Analysis of the polarization state gives line-integrated information on the electron density and the perpendicular B -field components involved.

Thomson scattering

At frequencies very large compared to the plasma frequency, the plasma refractive index approaches the vacuum value $N = 1$. However, individual plasma electrons are periodically accelerated in the E -field of a propagating wave launched as a laser beam for example. The oscillating charges are then origin of secondary radiation. The total intensity observed is composed of contributions of the individual electrons. The process is called incoherent Thomson scattering. Since the scattering centres are moving, the secondary waves have characteristic frequency shifts reflecting the particle's velocity, so carrying information about the velocity distribution function of the electrons. With a Maxwellian velocity distribution characterized by the temperature T_e of the electrons, a continuous spectrum around the primary laser frequency

$$I_s \propto \sqrt{\frac{m_e}{2\pi T_e}} n_e e^{-m_e \omega^2 / (2k^2 T_e)} \quad (8.9)$$

is observed from which the temperature can be derived (see Fig. 8.3). The scattering intensity I_s is proportional to the number of scattering centres, i.e. proportional to the electron density.

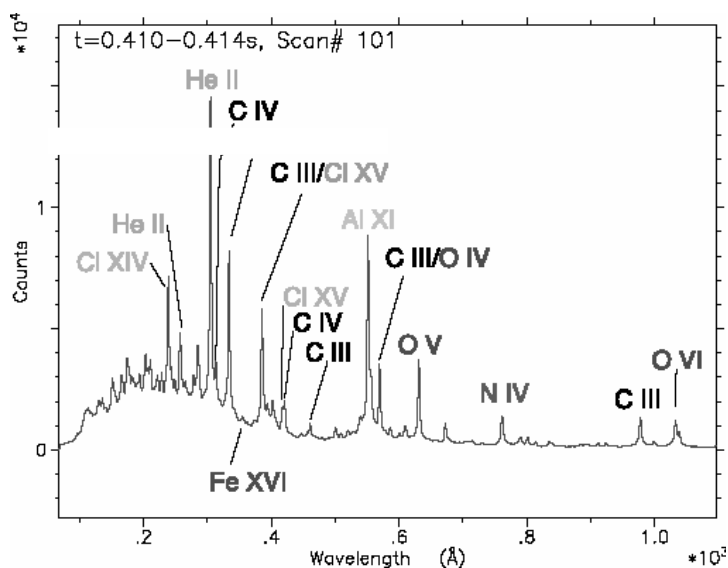


Figure 8.4: Typical VUV spectrum emitted from an impurity contaminated plasma. Characteristic lines of various charge states (roman numbers) of various elements like He, C, O, Cl, N, Al, and Fe could be identified. A continuous radiation background is also present (courtesy R. Burhenn, W7-AS).

Observation geometry and laser beam define the scattering volume. The arrangement therefore gives local information about electron density and temperature.

8.5.2 Passive wave measurements

Electromagnetic radiation emitted by fusion plasmas is composed of parts created in many different physical generation processes. In a fully ionized pure hydrogen plasma there is continuum radiation caused by bremsstrahlung owing to the accelerated motion of electrons in the field of the ions, cyclotron radiation due to the gyration motion of the charged particles in the external magnetic field, and recombination radiation after electron capture of ions. This continuous emission is superimposed by line radiation of recombined hydrogen atoms at the cool very edge of the plasma (Balmer-lines).

In addition to these unavoidable emission processes of a magnetically confined ideal hydrogen plasma, emission caused by impurities in the plasma must be considered. The impurities are ions of higher atomic number $Z > 1$. If these ions are fully ionized, they contribute to the emission with the processes listed before.

In case they are not fully ionized, which is true in particular for high Z ions, collision processes in the plasma lead to inner shell electronic excitation followed by spontaneous emission of characteristic line radiation with quantum energies typically in the keV range. Since this emission is connected with a significant energy loss, the impurity concentration of a fusion plasma must be kept sufficiently small. With regard to a future fusion reactor, impurity concentration of light atoms like C or O might reach the 1% level, however, the concentration of high- Z materials like W or Mo must not exceed the 0.1% level.

The small unavoidable impurity content can favourably be used for diagnostic purposes. The analysis of this radiation is done with regard to the wavelength which is characteristic for the element and its charge state. Analyzing also the line width and an eventual Doppler-shift, the ion temperature and collective drifts of the ions can be evaluated.

Line radiation

Main aim when analyzing the spectrum of line radiation is the determination of the impurity composition and the concentration of the various elements. To enable this, additional information is necessary. From the wavelength the element can uniquely be determined. The intensity of the emission depends on the concentration of this element but also on the excitation conditions, in particular on the local electron temperature and density. This makes the application of extensive code calculations necessary considering all excitation and de-excitation processes, to interpret the measured line intensities of the spectra.

The observation is typically along a sightline through the plasma centre. Since the plasma is optically thin a line integrated measurement results. Without additional knowledge no localization is possible.

A gross estimation, however, can be based on the fact that since the electron temperature profile is maximal in the plasma centre, the individual ionization states are not equally distributed in the plasma cross section but rather distributed like an onionskin in layers of a certain temperature range resulting in a localization of the individual charge states of an ion. The known electron temperature profile allows in this way an allocation of the emission of different charge states observed.

One of the most direct interpretations is based on the evaluation of the Doppler-broadening of the spectral lines. The line width reflects the ion temperature of the majority of ions of the bulk plasma since due to collisional interaction full thermalization is normally obtained (see Fig. 8.5 left). Measuring the line widths of elements in various charge states, the ion temperature profile can be reconstructed, at least estimated.

Continuum radiation

Continuum radiation is generated in the plasma due to the action of electric and magnetic forces on the electrons. The acceleration of the ions is small. Their emission can usually be neglected.

1. Bremsstrahlung

The accelerated motion of an electron in the field of an ion is the classical process to generate bremsstrahlung. Since the electron is before and after the interaction in a free state the process is called free-free transition. In case the electron is bound in its final state, recombined with an ion, the process is a free-bound transition. Both processes lead to the emission of continuous radiation, forming a continuous background in the spectral range from mm to X-ray regions. While recombination is dominant in the cool plasma edge, at the higher temperatures in the plasma bulk free-free transitions are dominant.

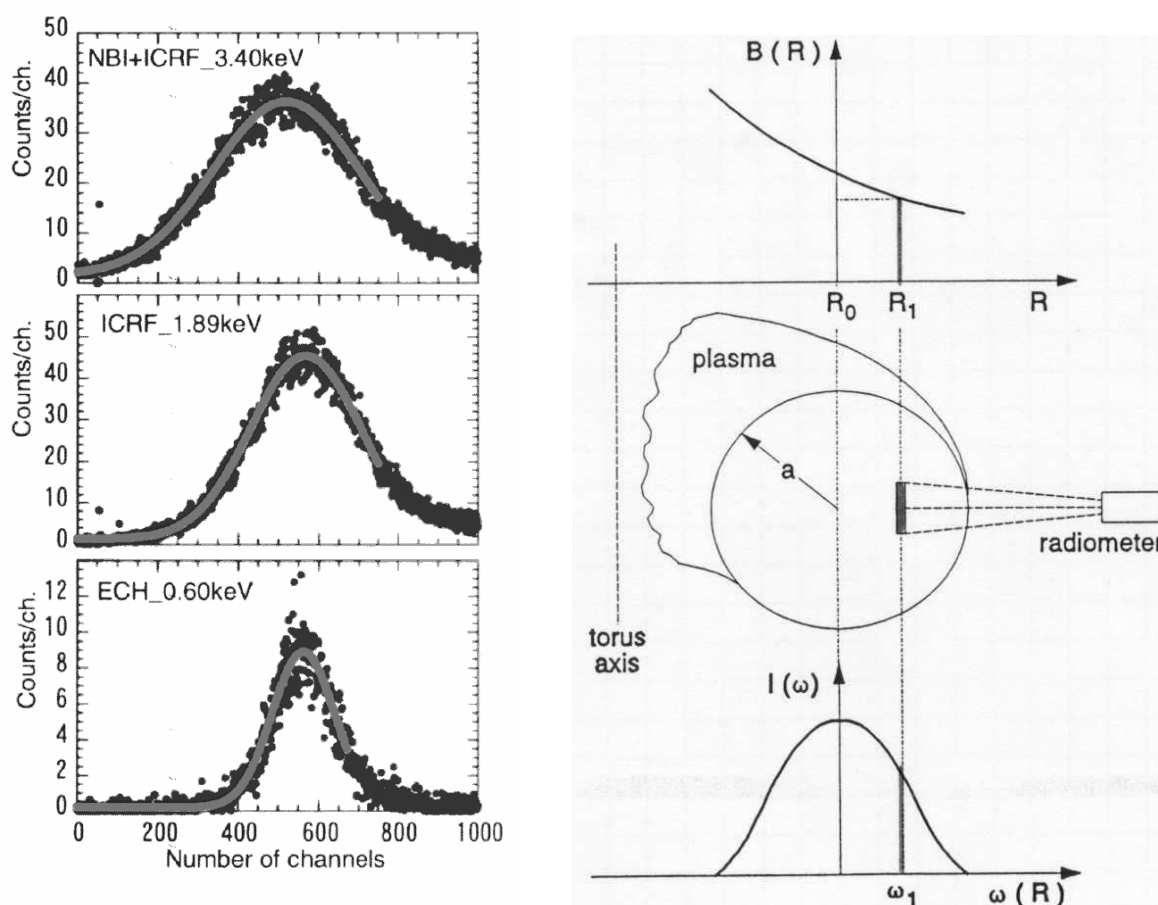


Figure 8.5: Left: The line width of a Doppler-broadened spectral line of the 20-fold ionized Ti for various heating scenarios NBI + ICRF, ICRF, and ECRH resulting in ion temperatures of 3.4, 1.89, and 0.6 keV. Measurements (dark) and simulations of the width assuming a Maxwellian energy distribution nicely agree (courtesy of S. Morita, LHD, Japan). Right: In a toroidal confinement device the B -field monotonically decreases with R across the plasma cross section. As a result the gyration frequency varies with R too. The frequency of the emission is therefore connected with the position of generation. The intensity of the emission is proportional to the local temperature.

The total power emitted within a certain finite spectral interval is proportional to the local densities of ions and electrons, the ion charge squared and to the square root of the electron temperature

$$P \propto Z^2 n_e n_i \sqrt{T_e}. \quad (8.10)$$

Due to this strong dependence on quantities which are in most cases constant on flux surfaces, bremsstrahlung emission can be used to reconstruct the flux surfaces, their shift under the action of plasma pressure as well as to determine MHD-phenomena. To limit the bremsstrahlung power loss, high- Z impurities must be avoided in a future fusion reactor.

The measurements are made in the soft X-ray spectral region using multi sightline pin-hole camera systems with hundreds of sightlines. The local emissivity is reconstructed from the line integrated measurements applying tomographic reconstruction techniques. The spectrum shows a characteristic exponential decay with frequency ω

$$I_\omega d\omega \propto e^{-(\hbar\omega)/(kT_e)} d\omega \quad (8.11)$$

from which the electron temperature can be determined without absolute calibration of the detection system.

2. Cyclotron radiation

In a magnetically confined plasma the Lorentz-force causes the electrons to gyrate around the field lines with a frequency

$$\omega_0 = \frac{e}{m_e} B . \quad (8.12)$$

This accelerated motion leads to the emission of electromagnetic radiation at the cyclotron frequency ω_0 and its harmonics. At B -fields of the order of a few T emission is in the mm-wave range. Since the energy density of the emission is proportional to the acceleration squared, the intensity of the emission caused by the ion gyration motion at the same energy is completely negligible. Only the electron cyclotron emission (ECE) has therefore gained diagnostic importance. With the line of sight in a poloidal plane perpendicular to the plasma axis, the width of the emission spectrum is dominated by the B -field variation through the plasma, resulting in a continuous spectrum with a width of typically several 10 GHz. At sufficiently high electron temperature and density, the plasma is optically thick in the range of cyclotron frequencies. The intensity of the emission then reaches the black-body level which, through Plancks law, is solely determined by the electron temperature. Since the frequency is determined by the known local field $B(R)$, a local electron temperature $T_e(R)$ can be deduced from the measured intensity $I(\omega)$. The classical Rayleigh-Jeans approximation of Plancks law then gives a linear relation between electron temperature T_e and the intensity I

$$I_\omega d\omega = \frac{\omega^2}{8\pi^3 c^2} \frac{\hbar\omega}{\exp(\hbar\omega/(kT_e)) - 1} d\omega \approx \frac{\omega^2}{8\pi^3 c^2} kT_e d\omega . \quad (8.13)$$

In this simplified picture the energy of individual electrons of a thermalized population has not been considered. It causes, as a result of the relativistic mass increase with kinetic energy, a downshift of the emission frequency, or -accordingly- at given observation frequency a shift of the emitting layer away from the so-called cold resonance into regions of higher B -field.

As a result, the emission of the electrons at the various energies of a Maxwellian distribution is smeared out over a certain radial range behind the cold resonance. However, due to the multi-step emission and reabsorption processes of the radiation on the way to the observer, radiation can escape only from a layer right behind the cold resonance whose temperature is being reflected in the observed blackbody intensity. The mechanism only

holds in case the B -field is monotonically decreasing to the observer, which is the necessary condition of the method. A radiometer calibrated against a blackbody source of known physical temperature determines basically the ECE radiation temperature T_{rad}

$$T_{rad} = T_e [1 - e^{-\tau}] \quad (8.14)$$

approaching the electron temperature T_e in case the optical depth τ is sufficiently high. The optical depth is obtained integrating the absorption along the line of sight. The leading parameters determining the absorption are the local electron density and temperature. Densities in the 10^{19} m^{-3} and temperatures of about 50 eV are sufficient to fulfil the conditions.

8.6 Particle diagnostics

Atoms and ions are injected to diagnose the plasma in various ways. While impurity pellets are injected to study their excitation, ionization, their dwell time, and motion with the passive spectroscopic diagnostics described, well collimated low and high energy H, He, or Li atomic beams are used to investigate local phenomena occurring along the beam as a result of its interaction with the plasma particles. Neutral atoms are used to avoid deflection in the magnetic field. However, also ions of high energy and mass are sent into the plasma to probe its local electric potential.

Passive particle diagnostics analyze neutral atoms escaping from the plasma after charge exchange interaction with fast H-atoms injected by a so-called diagnostic injector. Also the diagnostic of neutrons produced in fusion reactions fall into this category.

8.6.1 Active particle diagnostics

Li-beam

A well collimated beam of neutral Li-atoms is being injected into the plasma, directed to the plasma axis. Beam energy and electron density in the plasma determine the penetration depth. With energies of some 10 keV it is of the order of a few 10 cm. In electronic collision the beam atoms are excited



and the intensity of the resonance line from the $2p$ to $2s$ transition is being detected perpendicular to the beam. Arrays of detectors allow for the simultaneous observation along the beam. The intensity reflects almost directly the electron density, which can be determined in this way with high spatial resolution in the very important edge region of the plasma where density gradients are often very high and where its exact knowledge is of great importance.

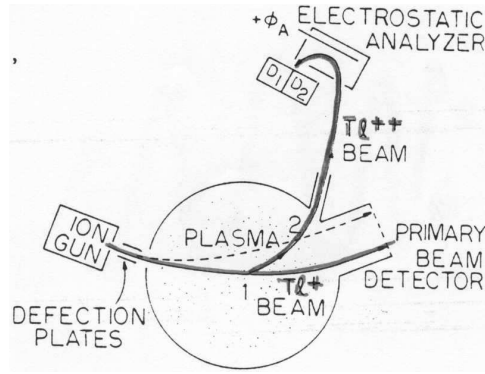


Figure 8.6: Experimental arrangement of a heavy ion beam probe diagnostic. Tl^+ ions are generated in an ion gun and launched into the plasma (trajectory 1). If the ion is further ionized to Tl^{++} , the gyro-radius is decreased (trajectory 2). From the energy change of the Tl^{++} ions, the local plasma potential at the position of the ionization can be deduced (T. Dolan, Fusion Research, p. 246).

Heavy ion beam probe

High energy, heavy mass singly charged ions are shot into the plasma in a well collimated beam of small divergence. Typical energies range from 100 keV to several MeV. Ions used for this purpose are typically Cs^+ , Ta^+ or Au^+ . Due to the Lorentz-force the ions gyrate around the field direction, with a gyro-radius larger than the plasma radius. Along the only slightly bended beam path, in electronic collisions ionization processes change the charge q of the primary beam ions from e to $2e$



As a result the ion gyro-radius

$$r_g = \frac{vM_I}{qB} \quad (8.18)$$

is decreased by a factor of two right at the location where the ionization occurs. The new trajectory of the *secondaries* now differs clearly from the primary injected ions. If the plasma has a locally varying finite electric potential $\Phi(s)$ along the beam path s , the energy of the ion passing the plasma changes by $e\Phi(s)$ reaching the initial value E_1 again when leaving it, since the plasma is electrically neutral and energy gained when entering is lost when leaving the plasma or vice versa. If, however, at position s_0 higher-ionization by one step occurs, the two-fold ionized particle leaves the plasma with an energy $E_2 = E_1 + e\Phi(s_0)$, reflecting the local potential at position s_0 . The energy difference $E_2 - E_1$ is determined via deflection in electric fields. Scanning the primary beam and the detection geometries, the potential distribution across the plasma can be determined, which is of importance to interpret transport processes in the plasma.

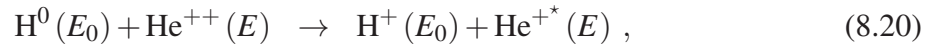
High energy neutral hydrogen injection

A beam of high energy neutral hydrogen atoms H^0 generated in a system called diagnostic injector with sufficient energy $E_0 > 50$ keV to penetrate the plasma as much as possible produces along its trajectory due to charge exchange processes with the hydrogen bulk ions neutral hydrogen atoms which can leave the plasma almost unopposed



The velocity distribution of these atoms leaving the plasma reflects the velocity distribution of the plasma ions since in the interaction process to a good approximation only charge has been transferred, not energy and momentum. Energy and momentum analysis of escaping atoms in electric and magnetic fields after a new external ionization therefore gives detailed local information about the ion energy distribution i.e. the ion temperature in the plasma. The position is defined by the overlap of the primary beam and detection geometry.

The diagnostic injector can successfully be used in a further application. For this purpose a small amount of He atoms is introduced into the hydrogen plasma as a tracer element. At the typical electron temperatures He is fully ionized. In a similar process as described before, the He^{++} ions exchange charge with the neutral hydrogen atoms of the injected beam to result in electronically excited singly charged He^+ ions



with $\lambda = 468.4$ nm . Again, since no energy is transferred in this process, the excited He^+ ions still reflect the He^{++} initial energy distribution. The Doppler-width of the spectral line at wavelength λ emitted in the de-excitation process then reflects the ion temperature of the plasma bulk ions since thermal equilibrium can be considered. The crossed beam-sightline geometry enables a local measurement of the ion temperature.

8.6.2 Passive particle diagnostics

Charge exchange neutrals leaving the plasma are already discussed together with the active diagnostics. Langmuir-probes extracting particle from the plasma are discussed in a separate chapter. Only fusion neutrons need to be briefly discussed here.

Neutron diagnostics

Neutron diagnostics will play a major role in future burning plasma experiments (BPX) like ITER where the analysis of the 14.2 MeV fusion neutrons becomes most important. In existing fusion experiments operating with mixtures of deuterium and hydrogen or with pure deuterium

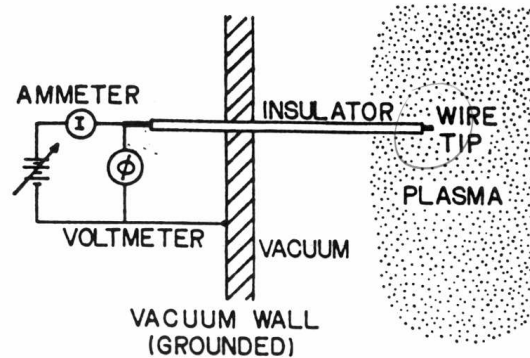
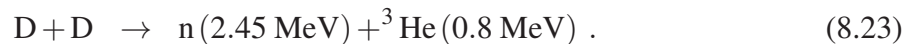


Figure 8.7: Langmuir-probes consist of a tiny electrode of about 1 mm length which is in direct contact with the plasma edge. Depending on the bias voltage, either ions or electrons are extracted from the plasma. From the measured I–V characteristic information can be gained about the electron and ion energy distribution function as well as about the plasma potential. (T. Dolan, Fusion Research, p. 239).

plasmas, neutrons are produced in two different reaction schemes with the kinetic energies of the reaction products given in brackets



The first scheme produces charged products only which can leave the plasma in nowadays medium sized experiments due to their high energy but will stay confined in future large machines. The neutrons from the second reaction, however, will leave the plasma. Energy analysis of the Doppler-broadened line at 2.45 MeV gives information about the energy of the reacting ions in the plasma.

8.7 Langmuir-probes

Langmuir-probes are counted among the oldest plasma diagnostics with still high importance in both fields fusion high temperature and in particular low temperature plasma diagnostics. The Langmuir-probe is a tiny metallic electrode in direct contact with the plasma. Retroaction to the plasma can therefore not completely excluded. In fusion experiments probes are moved into the plasma only for some 10 ms to avoid overheating of the device. Dependent on the potential applied, the small electrode either injects or extracts charged particles from the plasma. Currents to the probe are governed by the electron density and the electron temperature as well as the plasma potential. All three quantities can be derived from the measured current-voltage characteristic of the probe, which is obtained conducting a fast voltage sweep.

Table 8.1: Main methods and some important quantities. Diagnostic techniques given in the rows, most important parameters in the columns.

	f_e	f_i	n_e	n_i	n_Z	T_e	T_i	p	E	B
Magnetics						×		×		×
Particle flux	×	×	×	×		×	×		×	
Refractive index			×							×
Cyclotron emission	×					×				
Bremsstrahlung			×		×	×				
Line radiation					×		×		×	×
Scattering	×		×			×		×		
Charge exchange		×			×		×			
Nuclear reaction		(×)		×			×			

8.8 Summarizing remarks

To summarize the various techniques, Tab. 8.8 connects the main methods and some important quantities they are aiming at. The diagnostic methods briefly discussed in the frame of this introduction to the field are linked matrix-like with the physical quantities the measuring systems are diagnosing.

The various diagnostic techniques given in the rows are based on measurements of magnetic flux changes and particle fluxes from the plasma, measurements of the plasma dielectric properties, the radiometry of the cyclotron emission, the spectroscopy of the continuous bremsstrahlung and the discrete impurity line emission, on laser light scattering and charge exchange processes and based as well on nuclear reactions resulting in neutrons leaving the plasma.

The most important parameters as given in the columns are: $f_{e,i}$, energy distribution function of electrons and ions, $n_{e,i}$, electron and ion densities, $T_{e,i}$, electron and ion temperatures, p plasma pressure, E and B electric and magnetic fields. This is of course only a small part of the plasma parameters to be measured. However, to list them all would definitely go beyond the scope of this introductory chapter.

References

- [1] W. Lochte-Holtgreven, *Plasma Diagnostics*, AIP, New York, 1995
- [2] I.H. Hutchinson, *Principles of Plasma Diagnostics*, Cambridge University Press, Cambridge, MA, 1987

- [3] T.J. Dolan, *Fusion Research*, Pergamon Press, New York, 1982
- [4] T.J.M. Boyd, J.J. Sanderson *The Physics of Plasma*, Cambridge University Press, Cambridge, UK, 2003
- [5] Transaction of Fusion Technology, *Carolus Magnus Summer School on Plasma Physics*, **25**, 2T, 289-340 (1994)

Chapter 9

Computational plasma physics

Eric Sonnendrücker

9.1 Introduction

Understanding an experiment in physics relies on a model which is generally a differential equation or a partial differential equation or a system involving many of these. In sufficiently simple cases analytical solutions of these exist and then this can be used to predict the behaviour of a similar experiment. However in many cases, especially when the model is based on first principles, it is so complex that there is no analytical solution available. Then there are two options: the first is to simplify the model until it can be analytically solved, the second is to compute an approximate solution using a computer. In practice both are usually done, the simplified models being used to verify that the code is working properly. Due to the enormous development of computer resources in the last 50 years, quite realistic simulations of physical problems become now possible. Most problems in tokamak or stellarator physics rely heavily on so called numerical modelling, be it the computation of a real equilibrium, the solution of MHD equations or of kinetic models. Computational sciences have emerged next to theory and experiments as a third pillar in physics and engineering. Designing efficient, robust and accurate simulation codes is a challenging task that is at the interface of the application domain, plasma physics in our case, applied mathematics and computer science. The main difficulties are to make sure that the implemented algorithms provide a good approximation of the physics model and also that the algorithms use efficiently the available computer resources which are costly. Even though many basic simulations can be performed nowadays on a laptop, state of the art computations require huge super-computers that consists of many computing units and nowadays often heterogeneous computing elements (CPU, GPU, MIC, ...). These require parallel algorithms and often to achieve optimal efficiency a very good knowledge of the computer architecture. The programming skills and methodologies that are also very important in computational physics will not be addressed here. We refer to [3] for an introduction

The aim of this lecture will be to introduce the process of developing a simulation code and some standard methods and numerical issues. The model problem for which the scheme will be developed is the Vlasov-Poisson system, which is classical in kinetic plasma physics.

9.2 From a physics problem to a computer code

The first step is to find an appropriate model, which is often a set of coupled differential or partial differential equations. If the model is continuous the solution lives in an infinite dimensional space which cannot be represented on a computer. The first step then will be to discretise it, i.e. represent the unknowns by a large but finite number of values, typically its values on a finite grid or the coefficients of its expression on the basis of a finite dimensional linear space. Then from the equations of the starting models relations between the values representing the discrete unknowns should be found. This yields a finite number of linear or non linear equations that can be solved on a computer. This will require methods of numerical linear algebra, which are introduced in [4] or iterative methods for linear or nonlinear equations, a good introduction of which is available in [2]. We won't focus on these either as they are generally implemented in most numerical software tools like Matlab or Numpy and very efficient libraries, LAPACK, ScaLAPACK, PETSc, Trilinos, to name a few, are freely available.

There are many possible ways to discretise a differential or partial differential equation. They are not all equal and many things need to be considered, when choosing an appropriate one. The most important is naturally that the discrete model converges towards the initial model when the number of discrete values goes to infinity. Because computer arithmetics is not exact, as real numbers cannot be represented exactly on a computer, sensitivity to round-off errors is very important. Then some algorithms need more operations than other. Optimally an algorithm dealing with an unknown vector of N points can use $O(N)$ operations, but some can use $O(N \log N)$ or $O(N^d)$ or even more, which will make a huge difference for large values of N . Then again some algorithms will be easier to parallelise than others, which is an important issue when developing a simulation code on a massively parallel computer.

Also, before choosing a discretisation, it is important to understand the structure of the equations that are being discretised. Analytical theory plays an essential role in this aspect. What are the conserved quantities? Are there analytical solution in some special cases? What is the evolution of the solution or some quantities depending on the solution? And so on. The more information is available from analytical theory, the easiest it will be to check whether the code is correctly approximating the analytical model. The process of *verification* of a computer code, consists precisely in checking that the code can reproduce as expected information available from the theory. Verification of a computer code is essential to gain confidence in its correctness. Only once the computer code has been appropriately verified, one can proceed with the *validation* process, which consists in comparing the code to actual experiments and checking that those can be reproduced within the available error bars. If this is not the case, one needs to check the initial model, including initial and boundary conditions and all external parameters that could have an influence on the results. Possibly one also needs to develop more verification tests to check that there is no error in the implementation. This process of *Verification and validation (V & V)* is essential for developing a simulation code with reliable predictive capabilities. An exhaustive discussion of verification and validation for magnetic fusion is available in [5].

Let us now illustrate this procedure on the Vlasov-Poisson equations which describes the evolution of charged particles in phase space, and introduce a few discretisation methods and the main notions of numerical methods for partial differential equation.

9.3 The Vlasov-Poisson system

9.3.1 General features

The dimensionless Vlasov equation reads

$$\frac{\partial f}{\partial t} + \mathbf{v} \cdot \nabla_{\mathbf{x}} f - \mathbf{E} \cdot \nabla_{\mathbf{v}} f = 0. \quad (9.1)$$

It is an advection equation in phase space. Denoting by $\mathbf{F} = (\mathbf{v}, -\mathbf{E})^T$, it can be written

$$\frac{\partial f}{\partial t} + \mathbf{F} \cdot \nabla_{\mathbf{x}, \mathbf{v}} f = 0. \quad (9.2)$$

The Vlasov equation is coupled to the Poisson equation $-\Delta\phi = 1 - \rho(t, \mathbf{x}) = 1 - \int f(t, \mathbf{x}, \mathbf{v}) d\mathbf{v}$, $\mathbf{E}(\mathbf{x}, t) = -\nabla\phi$. Through this coupling, \mathbf{E} depends on f , which makes the Vlasov-Poisson system non linear.

The solution of the Vlasov equation can be obtained by solving a systems of ordinary differential equations which are called the characteristics of the advection equation:

$$\frac{d\mathbf{X}}{dt} = \mathbf{V}(t), \quad (9.3)$$

$$\frac{d\mathbf{V}}{dt} = -\mathbf{E}(\mathbf{X}(t), t). \quad (9.4)$$

We denote by $(\mathbf{X}(t; \mathbf{x}, \mathbf{v}, s), \mathbf{V}(t; \mathbf{x}, \mathbf{v}, s))$, or more concisely $(\mathbf{X}(t), \mathbf{V}(t))$ when the dependency with respect to the initial conditions is not explicitly needed, the unique solution at time t of this system which takes the value (\mathbf{x}, \mathbf{v}) at time s .

A straightforward computation yields $d/dt f(t, \mathbf{X}(t), \mathbf{V}(t)) = 0$, using the definition of the characteristics. Therefore the solution of the Vlasov equation can be expressed using the solution of the characteristics and the initial condition:

$$f(t, \mathbf{x}, \mathbf{v}) = f_0(\mathbf{X}(0; \mathbf{x}, \mathbf{v}, t), \mathbf{V}(0; \mathbf{x}, \mathbf{v}, t)). \quad (9.5)$$

We first notice that the Vlasov equation (9.1) can also be written in conservative form

$$\frac{\partial f}{\partial t} + \nabla_{\mathbf{x}, \mathbf{v}} \cdot (\mathbf{F}f) = 0, \quad (9.6)$$

with $\mathbf{F} = (\mathbf{v}, -\mathbf{E})^T$ such that $\nabla_{\mathbf{x}, \mathbf{v}} \cdot \mathbf{F} = 0$.

9.3.2 Conservation properties

The Vlasov-Poisson system has a number of conservation properties that need special attention when developing numerical methods. In principle it is beneficial to retain the exact invariants in numerical methods and when it is not possible to keep them all, as is the case here, they can be use to monitor the validity of the simulation by checking that they are approximately conserved with good accuracy.

The Vlasov-Poisson system verifies the following conservation properties:

- Maximum principle

$$0 \leq f(\mathbf{x}, \mathbf{v}, t) \leq \max_{(\mathbf{x}, \mathbf{v})} (f_0(\mathbf{x}, \mathbf{v})) , \quad (9.7)$$

- Conservation of L^p , norms for p integer, $1 \leq p \leq \infty$

$$\frac{d}{dt} \left(\int (f(\mathbf{x}, \mathbf{v}, t))^p \, d\mathbf{x} \, d\mathbf{v} \right) = 0 , \quad (9.8)$$

- Conservation of volume. For any volume V of phase space

$$\int_V f(\mathbf{x}, \mathbf{v}, t) \, d\mathbf{x} \, d\mathbf{v} = \int_{F^{-1}(V)} f_0(\mathbf{y}, \mathbf{u}) \, d\mathbf{y} \, d\mathbf{u} , \quad (9.9)$$

- Conservation of momentum

$$\frac{d}{dt} \int \mathbf{v} f \, d\mathbf{x} \, d\mathbf{v} = \frac{d}{dt} \int \mathbf{J} \, d\mathbf{x} = 0 , \quad (9.10)$$

- Conservation of energy

$$\frac{d}{dt} \left[\frac{1}{2} \int v^2 f \, d\mathbf{x} \, d\mathbf{v} + \frac{1}{2} \int E^2 \, d\mathbf{x} \right] = 0 . \quad (9.11)$$

9.4 Linear advection

When the electric field vanishes, then the Vlasov equation reduces to a linear advection equation for each given \mathbf{v} . Let us introduce the Finite Difference method and some general issues related to the discretisation of partial differential equations on this problem.

We consider first the linear 1D advection equation

$$\frac{\partial u}{\partial t} + a \frac{\partial u}{\partial x} = 0 \quad \text{pour } x \in [a, b], t \geq 0 . \quad (9.12)$$

Let us assume for simplicity that the boundary conditions are periodic. This means that u and all its derivatives are periodic of period $b - a$. We have in particular $u(a) = u(b)$. The constant a is given. As the problem is time dependent we also need an initial condition $u(x, 0) = u_0(x)$.

9.4.1 Obtaining a Finite Difference scheme

We first consider a uniform mesh of the 1D computational domain, i.e. of the interval $[a, b]$ where we want to compute the solution, see Fig. 9.1. The cell size or space step is defined by $\Delta x = (b - a)/N$ where N is the number of cells in the mesh. The coordinates of the grid points are then defined by $x_i = a + i\Delta x$. We then need a time step Δt and we will compute approximations of the solution at discrete times $t_n = n\Delta t$, $n \in \mathbb{N}$. As we assume the solution to be periodic of period $b - a$ it will be defined by its values at x_i for $0 \leq i \leq N - 1$ and we shall have $u(x_N, t_n) = u(x_0, t_n)$.

We shall denote by $u_j^n = u(x_j, t_n)$.

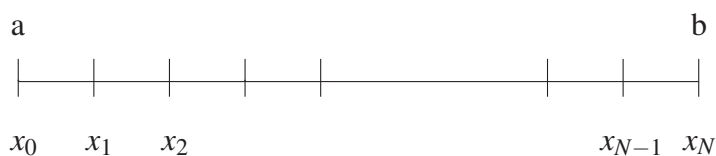


Figure 9.1: Uniform mesh of $[a, b]$.

9.4.2 Some classical Finite Difference discretisations

A Finite Difference scheme is classically obtained by approximating the derivatives appearing in the partial differential equation by a Taylor expansion up to some given order which will give the order of the scheme. As we know only the values of the unknown function at the grid points, we use Taylor expansion at different grid points and linearly combine them so as to eliminate all derivatives up to the needed order.

The same can be done for the time discretisation. For an approximation of order 1 in space and time, we can simply write

$$\frac{\partial u}{\partial t}(x_j, t_n) = \frac{u(x_j, t_{n+1}) - u(x_j, t_n)}{\Delta t} + O(\Delta t), \quad (9.13)$$

$$\frac{\partial u}{\partial x}(x_j, t_n) = \frac{u(x_j, t_n) - u(x_{j-1}, t_n)}{\Delta x} + O(\Delta x). \quad (9.14)$$

Denoting by u_j^n , the approximation of the solution at point x_j and time t_n and using the above formulas for the approximation of the partial derivatives we get the following approximation (9.12) at point x_j and time t_n :

$$\frac{u_j^{n+1} - u_j^n}{\Delta t} + a \frac{u_j^n - u_{j-1}^n}{\Delta x} = 0. \quad (9.15)$$

We thus obtain the following explicit formula which enables to compute u_j^{n+1} in function of the values of u at time t_n and points x_{j-1} , x_j and x_{j+1} :

$$u_j^{n+1} = u_j^n - a \frac{\Delta t}{\Delta x} (u_j^n - u_{j-1}^n). \quad (9.16)$$

We denote by U^n the vector of \mathbb{R}^N whose components are u_1^n, \dots, u_{N-1}^n and

$$A = \begin{pmatrix} (1 - \frac{a\Delta t}{\Delta x}) & 0 & & \frac{a\Delta t}{\Delta x} \\ \frac{a\Delta t}{\Delta x} & \ddots & \ddots & \\ & \ddots & \ddots & 0 \\ 0 & & \frac{a\Delta t}{\Delta x} & (1 - \frac{a\Delta t}{\Delta x}) \end{pmatrix}. \quad (9.17)$$

The terms at the end of the first line comes from the periodic boundary conditions. We use that $u_{-1}^n = u_{N-1}^n$ and $u_N^n = u_0^n$. Except on the two diagonals all the terms vanish.

In this case the scheme (9.16) can be written in matrix form

$$U^{n+1} = AU^n . \quad (9.18)$$

One would be tempted to replace the upwind first order finite difference formula for the spatial derivative (9.14) by the following centred formula which is of second order:

$$\frac{\partial u}{\partial x}(x_j, t_n) = \frac{u(x_{j+1}, t_n) - u(x_{j-1}, t_n)}{2\Delta x} + O(\Delta x^2) . \quad (9.19)$$

However, as we will see later, this is unstable when coupled to the first order explicit scheme in time.

The stability is enhanced when using implicit schemes in time. When using an uncentered difference scheme in the other direction for the time derivative, we get

$$\frac{\partial u}{\partial t}(x_j, t_n) = \frac{u(x_j, t_n) - u(x_j, t_{n-1})}{\Delta t} + O(\Delta t) , \quad (9.20)$$

We use the same finite difference approximation (9.14) for the space derivative as for the upwind explicit scheme. We then get the following formula

$$u_j^n + a \frac{\Delta t}{\Delta x} (u_j^n - u_{j-1}^n) = u_j^{n-1} . \quad (9.21)$$

In this case the u_j^n are defined implicitly from the u_j^{n-1} as solutions of a linear system. This is why this scheme is called implicit.

Denote by B the matrix of the linear system:

$$B = \begin{pmatrix} (1 + \frac{a\Delta t}{\Delta x}) & 0 & & -\frac{a\Delta t}{\Delta x} \\ -\frac{a\Delta t}{\Delta x} & \ddots & \ddots & \\ & \ddots & \ddots & 0 \\ 0 & & -\frac{a\Delta t}{\Delta x} & (1 + \frac{a\Delta t}{\Delta x}) \end{pmatrix} . \quad (9.22)$$

The term at the end of the first line comes from the periodic boundary conditions. We use that $u_{-1}^n = u_{N-1}^n$ and $u_N^n = u_0^n$. The terms not on the two diagonals vanish.

Going now from time step n to $n+1$ the implicit scheme in matrix form becomes

$$BU^{n+1} = U^n . \quad (9.23)$$

9.4.3 Convergence of finite difference schemes

So as to include explicit and implicit schemes, we consider a linear scheme in the following generic matrix form

$$LU^{n+1} = MU^n , \quad (9.24)$$

where the matrices L and M , are normalised such that the coefficient of u_j^n , is 1.

Let us denote by

$$V(t_n) = \begin{pmatrix} u(x_0, t_n) \\ \vdots \\ u(x_{N-1}, t_n) \end{pmatrix} \quad (9.25)$$

where u is the exact solution of the Partial Differential Equation (PDE) that is approximated by the scheme (9.24).

Definition 1 *The scheme (9.24) is called consistent of order (q, p) if*

$$\|LV(t_{n+1}) - MV(t_n)\| = \Delta t O(\Delta t^q + \Delta x^p). \quad (9.26)$$

Proposition 1 *If the exact solution is of class C^3 , the schemes (9.16) and (9.21) are consistent of order 1 in t and in x .*

This can be verified by using the Taylor expansions used for defining the finite difference schemes.

Definition 2 *The scheme (9.24) is called stable for some given norm $\|\cdot\|$ if there exist constants K and τ independent of Δt such that*

$$\|U^n\| \leq K\|U^0\| \quad \forall \Delta t \text{ such that } 0 < \Delta t < \tau. \quad (9.27)$$

Proposition 2 *The scheme (9.16) is stable for the L^∞ norm provided*

$$\frac{a\Delta t}{\Delta x} \leq 1. \quad (9.28)$$

This condition is called the **Courant-Friedrichs-Lewy or CFL condition**.

Proof. Consider the scheme (9.16). Grouping the terms in u_{j-1}^n , u_j^n and u_{j+1}^n , this scheme (9.16) becomes

$$u_j^{n+1} = \frac{a\Delta t}{\Delta x} u_{j-1}^n + \left(1 - \frac{a\Delta t}{\Delta x}\right) u_j^n. \quad (9.29)$$

As, a , Δt and Δx are positive, if $\frac{a\Delta t}{\Delta x} \leq 1$ the two factors of u_{j-1}^n , u_j^n are positive and equal to their absolute value. Hence

$$|u_j^{n+1}| \leq \frac{a\Delta t}{\Delta x} |u_{j-1}^n| + \left(1 - \frac{a\Delta t}{\Delta x}\right) |u_j^n| \leq \left(\frac{a\Delta t}{\Delta x} + \left(1 - \frac{a\Delta t}{\Delta x}\right)\right) \max_j |u_j^n|, \quad (9.30)$$

and so

$$\max_j |u_j^{n+1}| \leq \max_j |u_j^n|, \quad (9.31)$$

from which it follows that $\max_j |u_j^n| \leq \max_j |u_j^0|$ for all n , which yields the L^∞ stability. ■

L^∞ stability is linked to the notion of oscillations. If a scheme is L^∞ stable the maximal value at any time is smaller than at initial time. This is in general possible only for first order scheme. Higher order schemes introduce small oscillation, but are still stable in a different norm the L^2 norm which is in general more convenient. Limiting oscillations is still an important issue for numerical schemes and specific limiters have been developed to achieve this for hyperbolic systems [6].

9.4.4 Von Neumann stability analysis

Due to the fact that the discrete Fourier transform conserves the L^2 norm because of the discrete Plancherel inequality and that it diagonalises the Finite Difference operators (provided the original PDE has constant coefficients), it is particularly well adapted for studying the L^2 stability. The von Neumann analysis consists in applying the discrete Fourier transform to the discretised equation. To make this more precise we first recall the definition and main properties of the discrete Fourier transform.

Let P be the symmetric matrix formed with the powers of the n^{th} roots of unity the coefficients of which are given by $P_{jk} = 1/\sqrt{n}e^{(2i\pi jk)/n}$. Denoting by $\omega_n = e^{(2i\pi)/n}$, we have $P_{jk} = 1/\sqrt{n}\omega_n^{jk}$. We also denote by P^T the transpose of P , by \bar{P} its complex conjugate, and $P^* = \bar{P}^T$.

Notice that the column vector of P , $X_k = (P_{jk})_j$ corresponds, up to the normalisation constant, to a discretisation of the function $x \mapsto e^{-2i\pi kx}$ at the grid points $x_j = j/n$ of the interval $[0, 1]$. So the expression of a periodic function in the base of the vectors X_k is thus naturally associated to the Fourier series of a periodic function.

Definition 3 *Discrete Fourier Transform.*

- The *discrete Fourier transform* of a vector $x \in \mathbb{C}^n$ is the vector $y = P^*x$.
- The *inverse discrete Fourier transform* of a vector $y \in \mathbb{C}^n$ is the vector $x = P^{*-1}y = Px$.

Lemma 1 *The matrix P is unitary and symmetric, i.e. $P^{-1} = P^* = \bar{P}$.*

Proof. We clearly have $P^T = P$, so $P^* = \bar{P}$. There remains to prove that $P\bar{P} = I$. But we have

$$(P\bar{P})_{jk} = \frac{1}{n} \sum_{l=0}^{n-1} \omega^{jl} \omega^{-lk} = \frac{1}{n} \sum_{l=0}^{n-1} e^{2i\pi/n l(j-k)} = \frac{1}{n} \frac{1 - e^{2i\pi/n n(j-k)}}{1 - e^{2i\pi/n(j-k)}}, \quad (9.32)$$

and so $(P\bar{P})_{jk} = 0$ if $j \neq k$ and $(P\bar{P})_{jk} = 1$ if $j = k$. ■

Corollary 1 *Let $F, G \in \mathbb{C}^n$ and denote by $\hat{F} = P^*F$ and $\hat{G} = P^*G$, their discrete Fourier transforms. Then we have*

- the discrete Parseval identity:

$$(F, G) = F^T \bar{G} = \hat{F}^T \hat{G} = (\hat{F}, \hat{G}), \quad (9.33)$$

- The discrete Plancherel identity:

$$\|F\| = \|\hat{F}\|, \quad (9.34)$$

where (\cdot, \cdot) and $\|\cdot\|$ denote the usual euclidian dot product and norm in \mathbb{C}^n .

Proof. The dot product in \mathbb{C}^n of $F = (f_1, \dots, f_n)^T$ and $G = (g_1, \dots, g_n)^T$ is defined by

$$(F, G) = \sum_{i=1}^n f_i \bar{g}_i = F^T \bar{G}. \quad (9.35)$$

Then using the definition of the inverse discrete Fourier transform, we have $F = P\hat{F}$, $G = P\hat{G}$, we get

$$F^T \bar{G} = (P\hat{F})^T \overline{P\hat{G}} = \hat{F}^T P^T \bar{P} \bar{\hat{G}} = \hat{F}^T \bar{\hat{G}}, \quad (9.36)$$

as $P^T = P$ and $\bar{P} = P^{-1}$. The Plancherel identity follows from the Parseval identity by taking $G = F$. ■

Remark 1 *The discrete Fourier transform is defined as a matrix-vector multiplication. Its computation hence requires a priori n^2 multiplications and additions. But because of the specific structure of the matrix there exists a very fast algorithm, called Fast Fourier Transform (FFT) for performing it in $O(n \log_2 n)$ operations. This makes it particularly interesting for many applications, and many fast PDE solvers make use of it.*

Let us now consider the generic matrix form of the Finite Difference scheme introduced above:

$$LU^{n+1} = MU^n. \quad (9.37)$$

Note that on a uniform grid if the PDE coefficients do not explicitly depend on x the scheme is identical at all the grid points. This implies that L and M have the same coefficients on any diagonal including the periodicity. Such matrices, which are of the form

$$C = \begin{pmatrix} c_0 & c_1 & c_2 & \dots & c_{n-1} \\ c_{n-1} & c_0 & c_1 & & c_{n-2} \\ c_{n-2} & c_{n-1} & c_0 & & c_{n-3} \\ \vdots & & & \ddots & \vdots \\ c_1 & c_2 & c_3 & \dots & c_0 \end{pmatrix} \quad (9.38)$$

with $c_0, c_1, \dots, c_{n-1} \in \mathbb{R}$ are called *circulant*.

Proposition 3 *The eigenvalues of the circulant matrix C are given by*

$$\lambda_k = \sum_{j=0}^{n-1} c_j \omega^{jk}, \quad (9.39)$$

where $\omega = e^{2i\pi/n}$.

Proof. Let J be the circulant matrix obtained from C by taking $c_1 = 1$ and $c_j = 0$ for $j \neq 1$. We notice that C can be written as a polynomial in J

$$C = \sum_{j=0}^{n-1} c_j J^j. \quad (9.40)$$

As $J^n = I$, the eigenvalues of J are the n -th roots of unity that are given by $\omega^k = e^{2ik\pi/n}$. Looking for X_k such that $JX_k = \omega^k X_k$ we find that an eigenvector associated to the eigenvalue λ_k is

$$X_k = \begin{pmatrix} 1 \\ \omega^k \\ \omega^{2k} \\ \vdots \\ \omega^{(n-1)k} \end{pmatrix}. \quad (9.41)$$

We then have that

$$CX_k = \sum_{j=0}^{n-1} c_j J^j X_k = \sum_{j=0}^{n-1} c_j \omega^{jk} X_k, \quad (9.42)$$

and so the eigenvalues of C associated to the eigenvectors X_k are

$$\lambda_k = \sum_{j=0}^{n-1} c_j \omega^{jk}. \quad (9.43)$$

■

Proposition 4 Any circulant matrix C can be written in the form $C = P\Lambda P^*$ where P is the matrix of the discrete Fourier transform and Λ is the diagonal matrix of the eigenvalues of C . In particular all circulant matrices have the same eigenvectors (which are the columns of P), and any matrix of the form $P\Lambda P^*$ is circulant.

Corollary 2 We have the following properties:

- The product of two circulant matrix is circulant matrix.
- A circulant matrix whose eigenvalues are all non vanishing is invertible and its inverse is circulant.

Proof. The key point is that all circulant matrices can be diagonalized in the same basis of eigenvectors. If C_1 and C_2 are two circulant matrices, we have $C_1 = P\Lambda_1 P^*$ and $C_2 = P\Lambda_2 P^*$ so $C_1 C_2 = P\Lambda_1 \Lambda_2 P^*$.

If all eigenvalues of $C = P\Lambda P^*$ are non vanishing, Λ^{-1} is well defined and

$$P\Lambda P^* P\Lambda^{-1} P^* = I. \quad (9.44)$$

So the inverse of C is the circulant matrix $PA^{-1}P^*$. ■

Now applying the discrete Fourier transform to our generic scheme yields:

$$P^*LU^{n+1} = P^*MU^n \Leftrightarrow P^*LPP^*U^{n+1} = P^*MPP^*U^n \quad (9.45)$$

which is equivalent to

$$\Lambda_L \hat{U}^{n+1} = \Lambda_M \hat{U}^n, \quad (9.46)$$

where Λ_L and Λ_M are the diagonal matrices containing the eigenvalues of the circulant matrices M and L which are given explicitly from the matrix coefficients. It follows because $\|\hat{U}\| = \|U\|$ for any vector U that the scheme is L^2 stable if and only if $\max_i |\lambda_{M,i}|/|\lambda_{L,i}| \leq 1$, where $\lambda_{M,i}$ and $\lambda_{L,i}$ are the eigenvalues of M and L .

Let us now apply this technique to the scheme (9.21):

Proposition 5 *The implicit upwind scheme (9.21) is stable for the L^2 norm for all strictly positive values of Δx and Δt .*

Proof. Let us denote by $\alpha = a \Delta t / (\Delta x)$. We notice that matrix B is circulant with $c_0 = 1 + \alpha$, $c_{n-1} = -\alpha$, the other c_i being 0.

The eigenvalues of B thus are $\lambda_k = c_0 + c_{n-1} \omega^{-2ik\pi/n}$. Which implies that

$$\Re \lambda_k = 1 + \alpha \left(1 - \cos \frac{2k\pi}{n}\right) \geq 1, \quad (9.47)$$

as $\alpha \geq 0$. It follows that all eigenvalues of B have a modulus larger or equal to 1, which implies that B is invertible. Moreover the eigenvalues of its inverse all have modulus less or equal to 1, which implies the L^2 stability of the scheme. ■

Proposition 6 *The centred scheme second order in space and first order in time:*

$$u_j^{n+1} = u_j^n - \frac{a\Delta t}{2\Delta x} (u_{j+1}^n - u_{j-1}^n). \quad (9.48)$$

is unstable in L^2 .

Proof. Let us denote by $\alpha = a\Delta t / \Delta x$. The first order in time centred scheme becomes in matrix form $U^{n+1} = AU^n$ where A is the circulant matrix with three non vanishing diagonals corresponding to $c_0 = 1$, $c_1 = -c_{n-1} = \alpha/2e^{\frac{2i\pi k}{n}}$. Hence its eigenvalues are $\lambda_k = 1 - \alpha/2(e^{2i\pi k/n} - e^{-2i\pi k/n}) = 1 - i\alpha \sin 2k\pi/n$ so that $|\lambda_k| > 1$ for all k such that $\sin 2k\pi/n \neq 0$. Hence the scheme is unstable. ■

Theorem 1 (Lax) *A linear scheme of the form (9.24) is convergent if it is stable and consistent.*

Remark 2 As we saw there is a simple formula enabling to express the eigenvalues of a circulant with respect to its entries. This is very useful for stability analysis, but can also help to write very simple numerical schemes relying on the FFT. Assume a semi-discretisation in space yields a scheme whose matrix form is based on a circulant matrix. This is the case for many discretisation schemes when discretising linear partial differential equations on a uniform periodic grid. Then applying the discrete Fourier transform, using the FFT, yields a system of decoupled scalar ODEs that can be solved either analytically or using a standard ODE solver. Finally transforming back by an inverse FFT yields the solution. The cost of such a scheme is close to the cost of two FFTs as the solution of the decouple scalar ODEs is generally small.

9.4.5 High-order time schemes

As we saw, the time discretisation can be performed by finite differences as for the space discretisation. However it is generally more convenient to separate the space and time discretisation for a better understanding. The method of lines consists in applying only a discretisation scheme in space first (this can be Finite Differences or any other scheme). Then one obtains a system of ordinary differential equations of the form

$$\frac{dU}{dt} = \mathcal{A}U, \quad (9.49)$$

where $U(t)$ is the vector whose components are $u_i(t)$ the unknown values at the grid point at any time t . Then one can use any Ordinary Differential Equation (ODE) solver for the time discretisation. For example using an explicit Euler method with the upwind method in space yields the previous explicit upwind scheme and when we use an implicit Euler method we get the implicit upwind scheme.

When working with linear homogeneous equations with no source term, the simplest way to derive high order time schemes is to use a Taylor expansion in time and plug in the expression of the successive time derivatives obtained from the differential system resulting from the semi-discretization in space. Consider for example that after semi-discretization in space using Finite Differences (or any other space discretisation method) we obtain the differential systems

$$\frac{dU}{dt} = \mathcal{A}U, \text{ with } U = \begin{pmatrix} u_0(t) \\ \vdots \\ u_{n-1}(t) \end{pmatrix}, \quad (9.50)$$

and \mathcal{A} the appropriate matrix coming from the semi-discretization in space. Then a Taylor expansion in time up to order p yields

$$U(t_{n+1}) = U(t_n) + \Delta t \frac{dU}{dt}(t_n) + \dots + \frac{\Delta t^p}{p!} \frac{d^p U}{dt^p}(t_n) + O(\Delta t^{p+1}). \quad (9.51)$$

Now if \mathcal{A} does not depend on time and $dU/dt = \mathcal{A}U$, we get that

$$\frac{d^p U}{dt^p} = \mathcal{A}^p U, \text{ for any integer } p. \quad (9.52)$$

Hence, denoting U^n an approximation of $U(t_n)$, we get a time scheme of order p using the formula

$$U^{n+1} = U^n + \Delta t \mathcal{A} U^n + \dots + \frac{\Delta t^p}{p!} \mathcal{A}^p U^n = (I + \Delta t \mathcal{A} + \dots + \frac{\Delta t^p}{p!} \mathcal{A}^p) U^n. \quad (9.53)$$

For $p = 1$ this boils down to the standard explicit Euler scheme.

Writing U^n the solution in vector form at time t_n , we define the propagation matrix \mathcal{A} such that

$$U^{n+1} = AU^n. \quad (9.54)$$

Definition 4 *The numerical scheme defined by the propagation matrix A is stable if there exists $\tau > 0$ such that U^n is bounded for all $n \in \mathbb{N}$ and $\Delta t < \tau$.*

Proposition 7 *The numerical scheme defined by the propagation matrix A is stable if there exists $\tau > 0$ such that for all $\Delta t < \tau$ all eigenvalues of A are of modulus less or equal to 1.*

Stability of Taylor schemes

For a Taylor scheme of order p applied to $dU/dt = \mathcal{A}U$, we have $A = I + \Delta t \mathcal{A} + \dots + \Delta t^p/p! \mathcal{A}^p$. Then denoting by λ an eigenvalue of \mathcal{A} , the corresponding eigenvalue of A is $\mu = 1 + \lambda \Delta t + \dots + \lambda^p \Delta t^p/p!$. And one can plot the region of the complex plane in which $|\mu(\lambda \Delta t)| \leq 1$ using for example `ezplot` in Matlab, which are the stability regions. This means that the time scheme associated to the semi-discrete form $dU/dt = \mathcal{A}U$ is stable provided all the eigenvalues λ of \mathcal{A} are such that $\lambda \Delta t$ is in the stability region.

Stability of the upwind scheme

$du_i(t)/dt = -au_i(t) - u_{i-1}(t)/\Delta x$ corresponds to the circulant matrix \mathcal{A} with $c_0 = -a/\Delta x = -c_1$. So its eigenvalues verify $\lambda_k \Delta t = -a\Delta t/(\Delta x) (1 - e^{2i\pi jk/n})$. Obviously, for any integer value of k , $\lambda_k \Delta t$ is on a circle in the complex plane of radius $a\Delta t/\Delta x$ centred at $(-a\Delta t/(\Delta x), 0)$. The stability region of the explicit Euler method is the circle of radius 1 centred at $(-1, 0)$, so that in this case we see again that the scheme is stable provided $a\Delta t/\Delta x \leq 1$. For the higher order schemes the radius corresponding to the maximal stability can be found by computing the second real root (the first one being 0) α of the equation $|\mu(\lambda \Delta t)| = 1$, see Fig. 9.2. We find that for the order 2 scheme $\alpha = -2$, so that the stability condition is the same as for the order 1 scheme. For the order 3 scheme we find that $\alpha = -2.5127$ and for the order 4 scheme we find that $\alpha = -2.7853$. The value of α corresponds to the diameter of the largest circle of eigenvalues that is still completely enclosed in the stability region. This yields the stability condition $a\Delta t/\Delta x \leq |\alpha|/2$. We notice that the maximal stable time step is larger for the schemes of order 3 and 4.

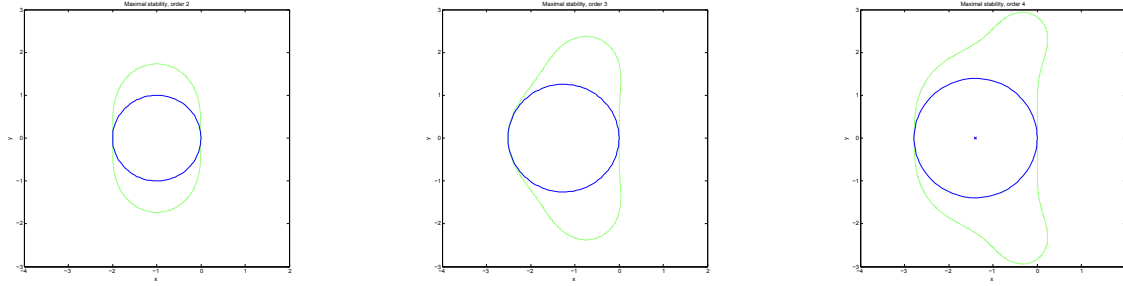


Figure 9.2: Location of eigenvalues (blue circle) corresponding to maximal stability zone for explicit time schemes of order 2, 3, 4 (left to right).

Stability of the centred scheme

$du_i(t)/dt = -au_{i+1}(t) - u_{i-1}(t)/(2\Delta x)$ corresponds to the circulant matrix \mathcal{A} with $c_1 = -a/(2\Delta x) = -c_{n-1}$. The corresponding eigenvalues are such that

$$\lambda_k \Delta t = -\frac{a\Delta t}{2\Delta x} \left(e^{\frac{2i\pi jk}{n}} - e^{-\frac{2i\pi jk}{n}} \right) = -\frac{ia\Delta t}{\Delta x} \sin \frac{2\pi jk}{n}. \quad (9.55)$$

Hence the eigenvalues are all purely imaginary and the modulus of the largest one is $a\Delta t/\Delta x$. The stability zone for the order 1 scheme is the interior of the circle centred at $(0, -1)$ of radius 1 and the stability zones for the schemes of order 2 to 4 are represented in Fig. 9.2 (green line). Note that for the order 1 and 2 scheme the intersection of the stability zone with the imaginary axis is reduced to the point 0. So that when all eigenvalues are purely imaginary as is the case here, these schemes are not stable for any positive Δt . On the other hand the schemes of order 3 and 4 have a non vanishing stability zone on the imaginary axis, larger for the order 4 scheme. By computing the intersection of the curve $|\mu(\lambda \Delta t)| = 1$ with the imaginary axis we find the stability conditions for the order 3 scheme: $a\Delta t/\Delta x \leq \sqrt{3}$ and for the order 4 scheme $a\Delta t/\Delta x \leq 2\sqrt{2}$.

9.5 Spectral solution of the Poisson equation

For the approximating a linear PDE with constant coefficients on a periodic domain the FFT is the simplest and often fastest method. If the solution is smooth it provides moreover spectral convergence, which means that it converges faster than a polynomial approximation of any order, so that very good accuracy can be obtained with relatively few points. The exact number depends of course on the variation of the solution. Let us explain how this works for the Poisson equation on a periodic domain that we shall need for our simulations.

Consider the Poisson equation $-\Delta\phi = \rho$ on a periodic domain of \mathbb{R}^3 of period L_1, L_2, L_3 in each direction. The solution is uniquely defined provided we assume that the integral of ϕ on one period vanishes.

We look for an approximation of ϕ of the form in the form of a truncated Fourier series

$$\phi_h(x_1, x_2, x_3) = \sum_{k_1=-N_1/2}^{N_1/2-1} \sum_{k_2=-N_2/2}^{N_2/2-1} \sum_{k_3=-N_3/2}^{N_3/2-1} \hat{\phi}_{k_1, k_2, k_3} e^{ik \cdot x}, \quad (9.56)$$

where we denote by $\mathbf{k} = (2\pi k_1/L_1, 2\pi k_2/L_2, 2\pi k_3/L_3)$ and by $\mathbf{x} = (x_1, x_2, x_3)$.

Remark 3 Note that in principle, it would be natural to truncate the Fourier series in a symmetric way around the origin, i.e. from $-N/2$ to $N/2$. However, because the FFT is most efficient when the number of points is a power of 2, we need to use an even number of points which leads to the truncation we use here. See Canuto, Hussaini, Quarteroni and Zang for more details [11].

We assume the same decomposition for ρ_h . Then taking explicitly the Laplace of ϕ_h we get

$$-\Delta\phi_h(x_1, x_2, x_3) = \sum_{k_1=-N_1/2}^{N_1/2-1} \sum_{k_2=-N_2/2}^{N_2/2-1} \sum_{k_3=-N_3/2}^{N_3/2-1} |\mathbf{k}|^2 \hat{\phi}_{k_1, k_2, k_3} e^{ik \cdot x}. \quad (9.57)$$

Then using the collocation principle, we identify this expression with that of ρ_h at the discretisation points $\mathbf{j} = (j_1 L_1/N_1, j_2 L_2/N_2, j_3 L_3/N_3)$ with $0 \leq j_i \leq N_i - 1$:

$$\sum_{k_1, k_2, k_3} |\mathbf{k}|^2 \hat{\phi}_{k_1, k_2, k_3} e^{ik \cdot \mathbf{j}} = \sum_{k_1, k_2, k_3} \hat{\rho}_{k_1, k_2, k_3} e^{ik \cdot \mathbf{j}}. \quad (9.58)$$

Then as the $(e^{ik \cdot \mathbf{j}})_{(k_1, k_2, k_3)}$ form a basis of $\mathbf{R}^{N_1} \times \mathbf{R}^{N_2} \times \mathbf{R}^{N_3}$ we can identify the coefficients, so that we have a simple expression of the Fourier coefficients of ϕ_h with respect to those of ρ_h for $|\mathbf{k}| \neq 0$:

$$\hat{\phi}_{k_1, k_2, k_3} = \frac{\hat{\rho}_{k_1, k_2, k_3}}{|\mathbf{k}|^2}, \quad -N_i/2 \leq k_i \leq N_i/2 - 1, \quad (9.59)$$

and because we have assumed that the integral of ϕ is 0, we have in addition $\hat{\phi}_{0,0,0} = 0$.

Now, to complete the algorithm, we shall describe how these coefficients can be computed from the grid values by a 3D discrete Fourier transform.

In 1D, $\hat{\phi}_k$ is defined by $\hat{\phi}_k = 1/\sqrt{N} \sum_{i=0}^{N-1} \phi_i e^{2i\pi jk/N}$ from which it is easy to see that $\hat{\phi}_{k+lN} = \hat{\phi}_k$ for any integer l . So after having computed $\hat{\phi}_k$ using a Fast Fourier Transform for $0 \leq k \leq N-1$ we get the negative coefficients $\hat{\phi}_k$ for $-N/2 \leq k \leq -1$ from the known coefficients by the relation $\hat{\phi}_k = \hat{\phi}_{k+N}$. Finally to go to the 3D case, it is enough to see that the 3D discrete Fourier transform is nothing but a series of 1D transforms in each direction.

Remark 4 In order to compute the electric field $\mathbf{E} = -\nabla\phi$ in the pseudo-spectral approximation, we just multiply each mode $\hat{\phi}_{k_1, k_2, k_3}$ by the corresponding $i\mathbf{k}$. Beware however, that

because we use an unsymmetric truncated Fourier series, the mode $-N/2$ of the electric field needs to be set to 0 in order to get back a real electric field by inverse Fourier transform. Indeed for a real field $(u_j)_{0 \leq j \leq N-1}$, the corresponding $N/2$ mode is $\sum_{j=0}^{N-1} (-1)^j u_j$ which is real. Hence, as ρ and then ϕ are real, their corresponding $N/2$ mode is real, and thus the same mode for E would be purely imaginary and not real unless it is 0. Note that setting this mode to 0 introduces an additional error of the order of truncation error of the series, and thus is acceptable.

9.6 A semi-Lagrangian method for the Vlasov equation

Due to the CFL constraint on the time step linked to an explicit solution of the Vlasov equation, this method is generally not used in practice. The semi-Lagrangian method uses explicitly the characteristics of the equation and allows a much larger time step. Moreover, for the Vlasov-Poisson equation, operator splitting yields a particularly simple scheme.

Operator splitting, which consists in splitting a complex operator in simpler parts to facilitate the solution is particularly useful when the split operators have a simpler structure. This is the case for the Vlasov equation where we can split the equation into the following two pieces:

$$\frac{\partial f}{\partial t} + \mathbf{v} \cdot \nabla_{\mathbf{x}} f = 0, \quad (9.60)$$

with \mathbf{v} fixed and

$$\frac{\partial f}{\partial t} + \frac{q}{m} \mathbf{E}(\mathbf{x}, t) \cdot \nabla_{\mathbf{v}} f = 0, \quad (9.61)$$

with \mathbf{x} fixed. We then get two constant coefficient advections the characteristics of which can be solved explicitly. This is obvious for (9.60) as \mathbf{v} does not depend on t and \mathbf{x} . On the other hand, integrating (9.61) with respect to \mathbf{v} , we get that

$$\frac{\partial \rho}{\partial t} = \frac{\partial}{\partial t} \int f(t, \mathbf{x}, \mathbf{v}) d\mathbf{v} = 0, \quad (9.62)$$

so that ρ and consequently \mathbf{E} does not change when this equation is advanced in time. So that $\mathbf{E}(t, \mathbf{x})$ needs to be computed with the initial f for this equation and does then depend neither on t , nor \mathbf{x} .

Semi-Lagrangian methods have become, far behind the Particle-In-Cell (PIC) method a classical choice for the numerical solution of the Vlasov equation, thanks to their good precision and their lack of numerical noise as opposite to PIC methods. They need a phase space mesh and thus are very computationally intensive when going to higher dimensions. Indeed a 3D simulation requires a 6D mesh of phase space. For this reason, semi-Lagrangian methods have become very popular for 1D or 2D problems, but there are still relatively few 3D simulations being performed with this kind of method.

The specificity of semi-Lagrangian methods, compared to classical methods for numerically solving PDEs on a mesh, is that they use the characteristics of the scalar hyperbolic equation, along with an interpolation method, to update the unknown from one time step to the next.

These semi-Lagrangian methods exist in different varieties: backward, forward, point based or cell based.

Most semi-Lagrangian solvers are based on cubic spline interpolation which has proven very efficient in this context.

Let us consider an abstract scalar advection equation of the form

$$\frac{\partial f}{\partial t} + \mathbf{a}(\mathbf{x}, t) \cdot \nabla f = 0. \quad (9.63)$$

The characteristic curves associated to this equation are the solutions of the ordinary differential equations

$$\frac{d\mathbf{X}}{dt} = \mathbf{a}(\mathbf{X}(t), t). \quad (9.64)$$

We shall denote by $\mathbf{X}(t, \mathbf{x}, s)$ the unique solution of this equation associated to the initial condition $\mathbf{X}(s) = \mathbf{x}$.

The classical semi-Lagrangian method is based on a backtracking of characteristics. Two steps are needed to update the distribution function f^{n+1} at t_{n+1} from its value f^n at time t_n :

1. For each grid point \mathbf{x}_i compute $\mathbf{X}(t_n; \mathbf{x}_i, t_{n+1})$ the value of the characteristic at t_n which takes the value \mathbf{x}_i at t_{n+1} . For a constant \mathbf{a} , we have $\mathbf{X}(t_n; \mathbf{x}_i, t_{n+1}) = \mathbf{x}_i - \mathbf{a}\Delta t$.
2. As the distribution solution of equation (9.63) verifies

$$f^{n+1}(\mathbf{x}_i) = f^n(\mathbf{X}(t_n; \mathbf{x}_i, t_{n+1})), \quad (9.65)$$

we obtain the desired value of $f^{n+1}(\mathbf{x}_i)$ by computing $f^n(\mathbf{X}(t_n; \mathbf{x}_i, t_{n+1}))$ by interpolation as $\mathbf{X}(t_n; \mathbf{x}_i, t_{n+1})$ is in general not a grid point.

These operations are represented on Figure 9.3.

Remark 5 *This semi-Lagrangian method is very diffusive if a low order (typically linear) interpolation is used. In practice one often used cubic splines or cubic Hermite interpolation, which offer a good compromise between accuracy and efficiency.*

This semi-Lagrangian method has been initially introduced for the 1D Vlasov-Poisson equation by Cheng and Knorr [17] in 1976. It was based on a trigonometric interpolation in x and a cubic spline interpolation in v and a directional Strang splitting method and is still one of the most used methods for this problem.

Let us now specify the algorithm for the 1D Vlasov-Poisson problem where the unknown is the distribution function for the electrons and in presence of motionless neutralizing background ions on a domain $[0, L]$ periodic in x and infinite in v . The equations then read

$$\frac{\partial f}{\partial t} + v \frac{\partial f}{\partial x} - E(x, t) \frac{\partial f}{\partial v} = 0, \quad (9.66)$$

$$\frac{dE}{dx} = \rho(x, t) = 1 - \int f(x, v, t) dv, \quad (9.67)$$

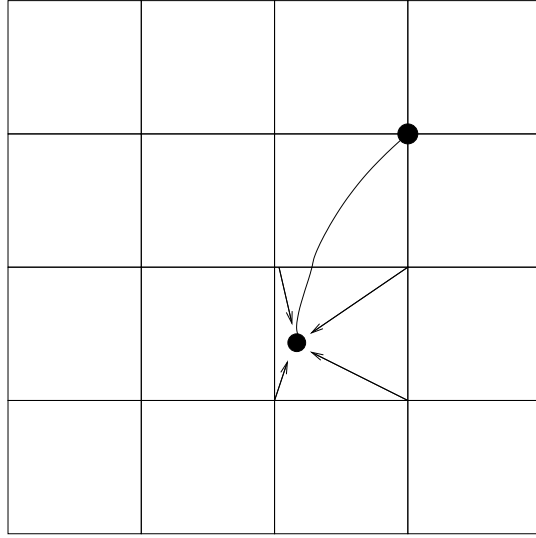


Figure 9.3: Sketch of the classical semi-Lagrangian method.

with the initial condition $f(x, v, 0) = f_0(x, v)$, verifying $\int f_0(x, v) dx dv = L$.

The infinite velocity space is truncated to a segment $[-A, A]$ sufficiently large so that f stays of the order of the round off errors for velocities less than $-A$ or larger than A during the whole simulation (in practise in the normalized examples we are going to consider, taking A of the order of 10 is very safe for all our test cases. Let us define a uniform grid of phase space $x_i = iL/N$, $i = 0, \dots, N-1$ (the point x_N which corresponds to x_0 is not used), $v_j = -A + j2A/M$, $j = 0, \dots, M$.

The full algorithm can in this case be written:

1. **Initialization.** Assume the initial distribution function $f_0(x, v)$ given. We deduce $\rho(x, 0) = 1 - \int f_0(x, v) dv$, and then compute the initial electric field $E(x, 0)$ solving the Poisson equation.
2. **Update from t_n to t_{n+1} .** The function f^n is known at all grid points (x_i, v_j) of phase space and E^n is known at all grid points x_i of the configuration space.

- We compute f^* by solving

$$\frac{\partial f}{\partial t} + E^n \frac{\partial f}{\partial v} = 0 \quad (9.68)$$

on a half time step $\Delta t/2$ using the semi-Lagrangian method.

- We compute f^{**} by solving on a full time step

$$\frac{\partial f}{\partial t} + v \frac{\partial f}{\partial x} = 0 \quad (9.69)$$

from the initial condition f^* .

- We compute $\rho^{n+1}(x) = 1 - \int f^{**}(x, v) dv$ and then the corresponding electric field E^{n+1} using the Poisson equation.

- We compute f^{n+1} by solving on a half time step

$$\frac{\partial f}{\partial t} + E^{n+1} \frac{\partial f}{\partial v} = 0 \quad (9.70)$$

from the initial condition f^{**} .

Note that the actual ρ^{n+1} can be computed using $f^{**}(x, v)$ (instead of $f^{n+1}(x, v)$), as the charge density corresponding to $f^{**}(x, v)$ is identical to that associated to $f^{n+1}(x, v)$. Indeed, we go from $f^{**}(x, v)$ to $f^{n+1}(x, v)$ by solving (9.70), and we notice, integrating this equation in v that it implies that $d/dt \int f(x, v, t) dv = 0$ and so that ρ is not modified during this stage.

9.7 Verification of the 1D Vlasov-Poisson code

The verification of Vlasov-Poisson 1D starts naturally with the testing of the different building bricks of the code: interpolation routine, Poisson solver, Vlasov solver.

Several verification tests need to be found so that as much of the potential problems that can occur will be detected. These tests will rely on analytic solution, convergence order and other known mathematical properties of the equations being validated. In particular, it is important to check that exact conservation properties of the scheme are indeed satisfied up to round off errors. It is also important to monitor the conservation properties of the equations that are not exactly verified by the scheme. This can be a good indicator of the accuracy of the code.

9.7.1 Test of the field solver

The Poisson solver can be very easily tested by the method of manufactured solutions, which consists in choosing a function compatible with the boundary conditions and computing its Laplacian to get the right-hand-side ρ . This gives us a problem with an analytical solution on which convergence and convergence order can be tested.

9.7.2 Test of the Vlasov solver with a given advection field

The first test that should be performed with the Vlasov solver, is to take a given force field, reduced in the Vlasov-Poisson case to the electric field. In particular, for the 1D Vlasov-Poisson equations one can take $E(x) = x$. The Vlasov equation then reads

$$\frac{\partial f}{\partial t} + v \frac{\partial f}{\partial x} - x \frac{\partial f}{\partial v} = 0. \quad (9.71)$$

The corresponding characteristics are

$$\frac{dX}{dt} = V, \quad \frac{dV}{dt} = -X, \quad (9.72)$$

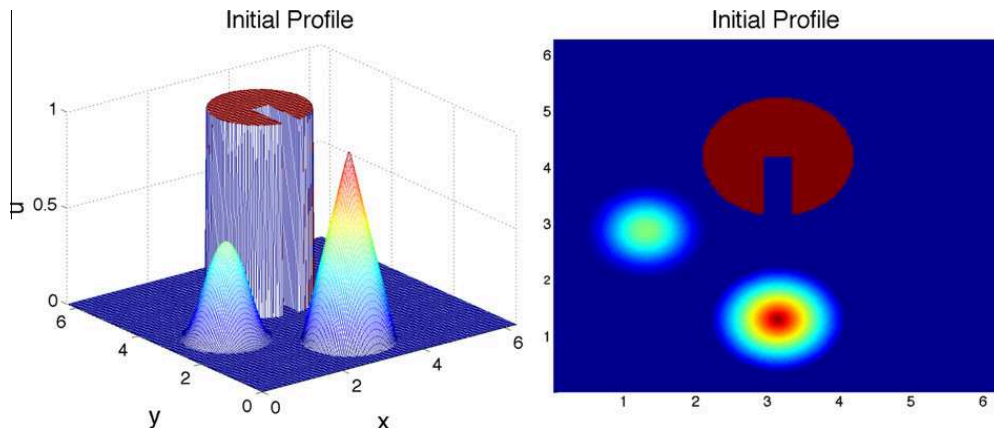


Fig. 5.2. Plots of the initial profile.

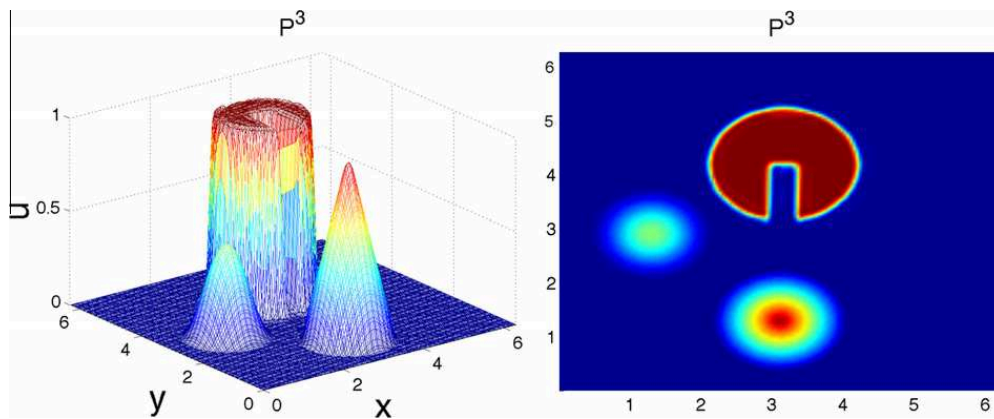


Figure 9.4: Possible initial conditions for a rotating advection field and their evolution. From Qiu-Shu J. Comput. Phys. 2011.

which corresponds to a rotation field, so that the solution after one turn $t = 2\pi$ is exactly back at the initial condition, so that one use the initial solution as an analytical solution after a complete number of terms. One can then test the solver, using first smooth initial conditions (like Gaussians) to test convergence and convergence order and then non smooth initial conditions, like the slotted cylinder or a cone to test the appearance of oscillations, see Fig. 9.4.

9.7.3 Comparison with the linearised Vlasov-Poisson system

Once all the building bricks are validated, one can come to the verification of the global code which can be done by using known solutions of the linearized Vlasov-Poisson equations. We shall here consider two classical test cases: Landau damping and two-stream instability.

The linearised Vlasov-Poisson equations can be solved analytically using a Fourier expansion in space and a Laplace transform in time. The electric field solution of the linearised Vlasov-

Poisson equations has the form

$$\hat{E}(k, t) = \sum_j \text{Res}_{\omega=\omega_j} \tilde{E}(k, \omega) e^{-i\omega t}, \quad (9.73)$$

where

$$\tilde{E}(k, \omega) = \frac{N(k, \omega)}{D(k, \omega)} \quad (9.74)$$

and the ω_j are the roots of the dispersion relation $D(k, \omega) = 0$ for fixed k . There are in general several roots of $D(k, \omega)$. In the linear phase only the dominant root matters (i.e. the one with the largest eigenvalue). Only the dominant root can be observed after some time, the contribution of the others becoming negligible. The expressions of D and N depend on the initial condition, which determines the problem being solved.

In order to compute the residues we can write the Taylor expansion of $D(k, \omega)$ in the neighbourhood of ω_j

$$D(k, \omega) = D(k, \omega_j) + (\omega - \omega_j) \frac{\partial D}{\partial \omega}(k, \omega_j) + O((\omega - \omega_j)^2), \quad (9.75)$$

and so, if ω_j is a simple root, we have $D(k, \omega_j) = 0$ and $\partial D / \partial \omega(k, \omega_j) \neq 0$. It then results that

$$\text{Res}_{\omega=\omega_j} \left(\frac{N(k, \omega)}{D(k, \omega)} e^{-i\omega t} \right) = \lim_{\omega \rightarrow \omega_j} \left((\omega - \omega_j) \frac{N(k, \omega)}{D(k, \omega)} e^{-i\omega t} \right) = \frac{N(k, \omega_j)}{\frac{\partial D}{\partial \omega}(k, \omega_j)} e^{-i\omega_j t}. \quad (9.76)$$

Computation of the zeros of an analytic function

For a given k the dispersion function $D(\omega, k)$ is analytic in ω . We are then reduced to the computation of the zeros of an analytic function that we shall denote by f in this section. An algorithm for doing this in the case f and its derivative f' can be evaluated at any complex point, which is the case for us, was proposed by Delves and Lyness [9] and a slightly more robust version of the algorithm was implemented by Kravanja *et al.* in the freely available Zeal package [7]. Another implementation was also proposed by Davies [8]. It is again based on the theorem of residues known from complex analysis [1].

If an analytic function f has a zero at a complex point z_j , then f'/f has a simple pole at z_j with multiplicity given by the corresponding residue. Hence, assuming that γ is a closed contour in the complex plane that does not go through any zero of f the theorem of residues implies that N the number of poles of f enclosed in the contour γ , including multiplicities, is

$$N = \frac{1}{2i\pi} \int_{\gamma} \frac{f'(z)}{f(z)} dz. \quad (9.77)$$

Moreover the same theorem also yields, for any $p \in \mathbb{N}$

$$s_p := z_1^p + \dots + z_N^p = \frac{1}{2i\pi} \int_{\gamma} z^p \frac{f'(z)}{f(z)} dz. \quad (9.78)$$

Delves and Lyness then introduced the polynomial P_N with zeros z_1, \dots, z_N

$$P_N(z) = \prod_{j=1}^N (z - z_j) = z^N + \sigma_1 z^{N-1} + \dots + \sigma_N. \quad (9.79)$$

The coefficients $\sigma_1, \dots, \sigma_N$ of P_N are related to the values s_1, \dots, s_N by the following Newton identities:

$$\begin{aligned} s_1 + \sigma_1 &= 0, \\ s_2 + s_1 \sigma_1 + 2\sigma_2 &= 0, \\ &\vdots \\ s_N + s_{N-1} \sigma_1 + \dots + s_1 \sigma_{N-1} + N\sigma_N &= 0. \end{aligned}$$

Then the algorithm is straightforward. The values s_j can be computed by numerically computing the contour integrals $\int_{\gamma} z^p f'(z)/f(z) dz$. Then the coefficients of the polynomial σ_j can be computed using Newton's identities, so that the problem reduces to computing the roots of a known polynomial, for which there are many known procedures especially for small degrees. One needs to be careful however that the mapping associating the σ_j to the s_j can be ill conditioned if zeros are too close or if N is too large. For this we advocate an adaptive procedure dividing the chosen contour into four smaller contours if there are convergence problems.

The algorithm then proceeds as follows:

1. The user gives a rectangular box in which the zeros are to be found.
2. Compute the number of zeros with multiplicities N if $N > 5$ subdivide the box into four sub boxes and start again for each box.

Convergence problems can still occur if a zero is too close to the contour or if two distinct zeros are too close. This can be solved by shifting slightly the contour and/or further subdividing the box. All this is done automatically in the code.

An application of this method for finding all the zeros with imaginary part larger than -2 of the Landau dispersion relation for different values of k is displayed in Fig. 9.5.

Landau damping

The initial conditions of Landau damping corresponds to

$$f_0(x, v) = (1 + \varepsilon \cos(kx)) \frac{1}{\sqrt{2\pi}} e^{-v^2/2}, \quad L = 4\pi. \quad (9.80)$$

In our numeric simulations we take $\varepsilon = 0.001$. Physically this represents a small perturbation of a Maxwellian equilibrium. This equilibrium is stable and the distribution comes back to its equilibrium after the perturbation.

In this case we find

$$D(k, \omega) = 1 - \frac{1}{2} \frac{\omega_p^2}{k^2 v_{th}^2} Z' \left(\frac{\omega}{\sqrt{2} v_{th} k} \right), \quad (9.81)$$

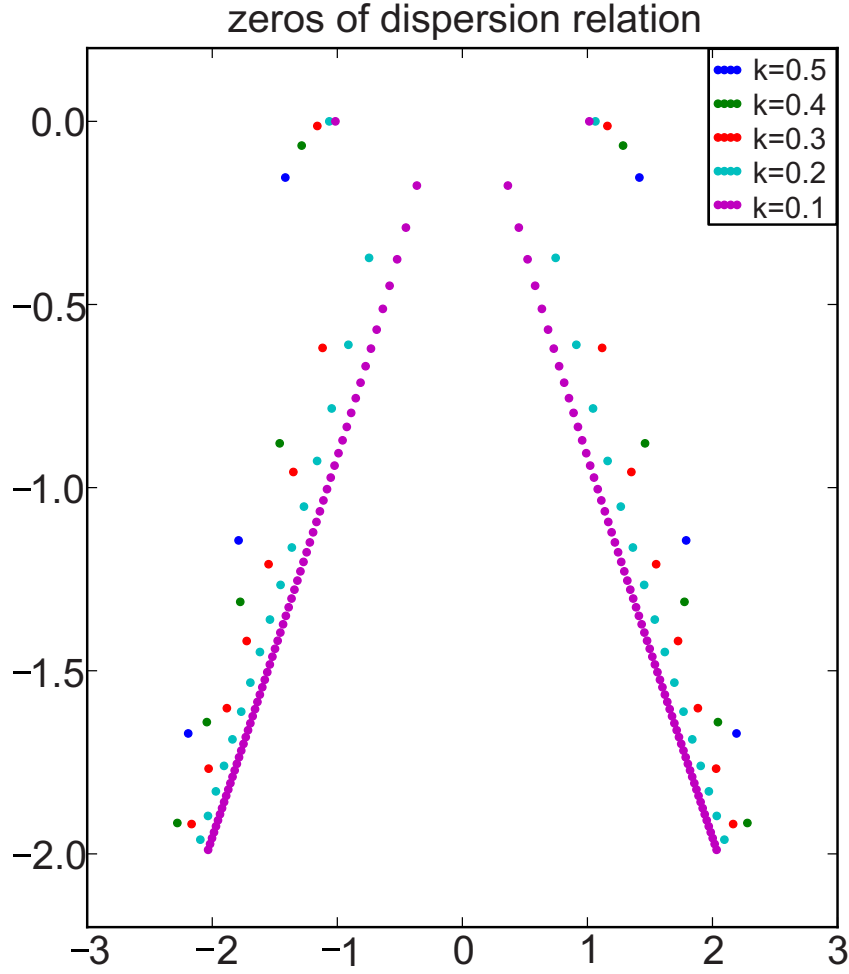


Figure 9.5: All zeros with imaginary part larger than -2 of the Landau dispersion relation for different values of k .

k	ω_j	$N(k, \omega_j) / \frac{\partial D}{\partial \omega}(k, \omega_j)$
0.5	$\pm 1.4156 - 0.1533i$	$0.3677 e^{\pm i 0.536245}$
0.4	$\pm 1.2850 - 0.0661i$	$0.424666 e^{\pm i 0.3357725}$

and

$$N(k, \omega) = g(k) \frac{n_0 e}{k^2 \epsilon_0} \frac{1}{\sqrt{2} v_{th}} Z\left(\frac{1}{\sqrt{2} \pi v_{th}}\right), \tag{9.82}$$

with $g(k) = 1/2$ for $k = -1, 1$ and 0 else. Here Z stands for the classical plasma dispersion function, which can be evaluated with standard numerical software.

Let us write down a table with the roots of $D(k, \omega) = 0$ with largest imaginary part and the corresponding value of $N(k, \omega_j) / (\partial D / \partial \omega)(k, \omega_j)$ for several values of k , see Tab. 9.7.3:

We denote by $\omega_r = \Re(\omega_j)$, $\omega_i = \Im(\omega_j)$, r the amplitude of $N(k, \omega_j) / (\partial D / \partial \omega)(k, \omega_j)$ and φ its phase. Note that we always have a root of the form $\omega_r + i\omega_j$ associated to $r e^{i\varphi}$, and a root of the form $-\omega_r + i\omega_j$ associated to $r e^{-i\varphi}$. So considering only the two root for which ω_i is

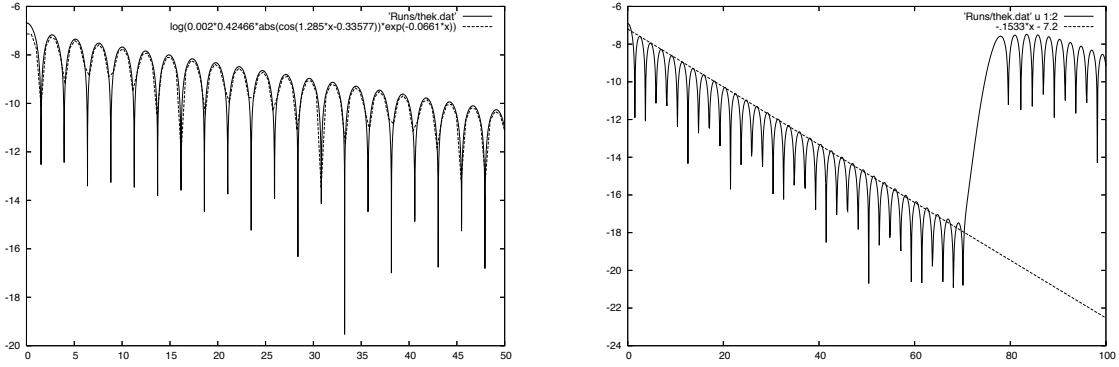


Figure 9.6: Left: Landau damping for $k = 0.4$.
Right: Landau damping for $k = 0.5$.

the largest, we have

$$\begin{aligned}\hat{E}(k,t) &\approx re^{i\varphi} e^{-i(\omega_r+i\omega_i)t} + re^{-i\varphi} e^{-i(-\omega_r+i\omega_i)t}, \\ &= re^{\omega_i t} (e^{-i(\omega_r t - \varphi)} + e^{i(\omega_r t - \varphi)}), \\ &= 2re^{\omega_i t} \cos(\omega_r t - \varphi).\end{aligned}$$

Then, we can verify that $\hat{E}(-k,t) = -\hat{E}(k,t)$, so that

$$E(x,t) \approx 4\epsilon re^{\omega_i t} \sin(kx) \cos(\omega_r t - \varphi). \quad (9.83)$$

Note that this is not the full solution, as we have only considered the dominating mode. However, as the others are decaying much faster and become negligible, this is a very good approximation of E after a short time.

Let us apply this formula by considering for example the first line of the table. The electric field for $k = 0.5$ will quickly, after the terms associated to the non dominating roots have decayed enough, be of the form

$$E(x,t) = 4\epsilon \times 0.3677e^{-0.1533t} \sin(0.5x) \cos(1.4156t - 0.536245). \quad (9.84)$$

We overlap in Figure 9.6 (left) the analytical solution including the dominating mode only of the electric field for $k = 0.4$ ($\hat{E}(k,t) = 0.002 \times 0.424666 e^{0.0661t} \cos(1.2850t - 0.3357725)$) and the solution computed numerically by a semi-Lagrangian method with a grid of 128 points in x and in v . The v mesh has been truncated to the interval $[-10, 10]$.

For the same numerical parameters, we display in Fig. 9.6 (right) the numerical solution and the slope corresponding to the damping rate, rather than the full solution. We notice that for a time around 80, the damping stops and the electric field comes almost back to its initial amplitude. This is a purely numerical phenomenon linked to the use of a uniform velocity mesh for a problem, which is periodic in space. This phenomenon is known as the Poincaré recurrence. In our case, it can be analysed by considering the free streaming equation

$$\frac{\partial f}{\partial t} + v \frac{\partial f}{\partial x} = 0. \quad (9.85)$$

v_0	ω	ω
1.3	$0.02115i$	$1.1648 - 0.00104i$
2.4	$0.2258i$	$1.3390 - 0.00242i$

Table 9.1: Roots of the dispersion relation for the two-stream instability.

The domain being periodic in x , we take the Fourier series. Mode k verifies then $df_k/dt - 2i\pi k/L v f_k = 0$. Whence $f_k(v, t) = f_k(v, 0)e^{2i\pi k/L vt}$. And as $v = j\Delta v$, f_k will be periodic in t of period $T_R = L/\Delta v$. In our case, we have $L = 4\pi$ and $\Delta v = 20/127 = 0.1574$. It follows that $T_R \approx 79.8$, which corresponds to the observed value.

The two stream instability

The two stream instability corresponds to two streams of different mean velocities, which can become linearly unstable. We consider here mean velocities v_0 and $-v_0$. Depending on k and v_0 this configuration can be stable or unstable.

The initial condition corresponding to this problem

$$f_0(x, v) = (1 + 0.001 \cos(kx)) \frac{1}{2\sqrt{2\pi}} \left(e^{-\frac{(v-v_0)^2}{2}} + e^{-\frac{(v+v_0)^2}{2}} \right), \quad L = \frac{2\pi}{k}. \quad (9.86)$$

In this case the dispersion relation reads

$$D(k, \omega) = 1 + \frac{\omega_p^2}{2k^2 v_{th}^2} \left[2 + \sqrt{\frac{\pi}{2}} \left(\frac{\omega}{v_{th}k} - \frac{v_0}{v_{th}} \right) e^{-\frac{(\omega/k - v_0)^2}{2v_{th}^2}} \left(i - \operatorname{erfi} \left(\frac{\omega/k - v_0}{\sqrt{2}v_{th}} \right) \right) \right. \\ \left. + \sqrt{\frac{\pi}{2}} \left(\frac{\omega}{v_{th}k} + \frac{v_0}{v_{th}} \right) e^{-\frac{(\omega/k + v_0)^2}{2v_{th}^2}} \left(i - \operatorname{erfi} \left(\frac{\omega/k + v_0}{\sqrt{2}v_{th}} \right) \right) \right],$$

For given values of k and v_0 , $D(k, \omega)$ admits several roots in ω . We display the dominant roots for $k = 0.2$ and several values of v_0 in the Tab. 9.1. Depending on the value of v_0 the instability is more or less strong, and for some values the configuration is stable.

We notice that the stable solutions oscillate with a very light damping and that the unstable roots correspond to purely imaginary roots and do not oscillate.

References

- [1] L.V. Ahlfors, *Complex analysis: an introduction to the theory of analytic functions of one complex variable*, McGraw-Hill, 1979.
- [2] C.T. Kelley, *Iterative methods for optimization, vol. 18*, Siam, 1999.

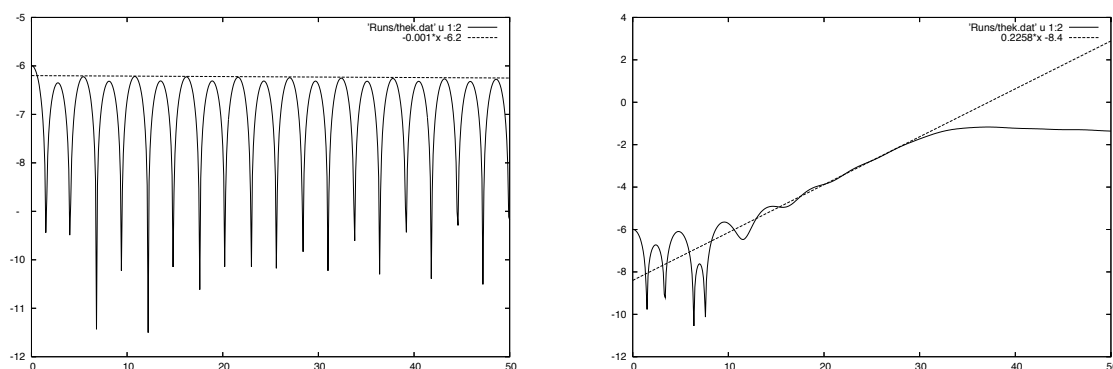


Figure 9.7: Left: Two-stream instability for $k = 0.2$ and $v_0 = 1.3$.
Right: Two-stream instability for $k = 0.2$ and $v_0 = 2.4$.

- [3] V. Eijkhout, *Introduction to High Performance Scientific Computing*, Lulu.com, 2010.
- [4] L.N. Trefethen and D. Bau, *Numerical linear algebra, vol. 50*, Siam, 1997.
- [5] M. Greenwald, *Verification and validation for magnetic fusion* in Phys. Plas. **17**(5) (2010) 058101.
- [6] R.J. LeVeque, *Finite volume methods for hyperbolic problems*, Cambridge university press, 2002.
- [7] P. Kravanja, M. Van Barel, O. Ragos, M.N. Vrahatis and F.A. Zafiroopoulos, *ZEAL: A mathematical software package for computing zeros of analytic functions* in Comp. Phys. Comm. **124**(2) (2000) 212-232.
- [8] B. Davies, *Locating the zeros of an analytic function* in J. Comp. Phys. **66**(1) (1986) 36-49.
- [9] L.M. Delves and J.N. Lyness, *A numerical method for locating the zeros of an analytic function* in Math. of Comp. (1967) 543-560.
- [10] C.K. Birdsall and A.B. Langdon, *Plasma physics via computer simulation*, CRC Press, 2004.
- [11] C. Canuto, M. Hussaini, A. Quarteroni and T.A.J. Zang, *Spectral Methods in Fluid Dynamics (Scientific Computation)*, Springer-Verlag, New York-Heidelberg-Berlin, 1987.
- [12] F.F. Chen, *Introduction to Plasma Physics and Controlled Fusion Volume 1: Plasma Physics* in Phys. Today **38** (1985) 87.
- [13] C.K. Chui, *An introduction to wavelets*, Academic press, 1992.
- [14] B.D. Fried and S.D. Conte, *The plasma dispersion function*, Academic Press New York, 1961.

- [15] R.W. Hockney and J.W. Eastwood, *Computer simulation using particles*, CRC Press, 2010.
- [16] R. Bellman and R.S. Roth, *The Laplace Transform, vol. 3*, World Scientific, 1984.
- [17] C.-Z. Cheng and G. Knorr, *The integration of the Vlasov equation in configuration space* in J. Comp. Phys. **22**(3) (1976) 330-351.

Chapter 10

Tokamaks: equilibrium, stability and transport

Hartmut Zohm

10.1 Introduction

The goal of confining a plasma in a magnetic field can be achieved in various geometries. The quality of the magnetic confinement is characterized by different criteria. For nuclear fusion, the following points are of special interest:

- The ratio of kinetic plasma pressure, averaged over the plasma volume, to magnetic pressure $\beta = \langle p \rangle / (B^2 / (2\mu_0))$. This number is a measure of the economic efficiency of the confinement since the fusion power output roughly scales as p^2 and B is the magnetic field which has to be provided externally. Usually, β is limited by the occurrence of MHD (Magneto-Hydrodynamic) instabilities.
- The energy confinement time $\tau_E = W_{pl} / P_{heat}$ which is one of the quantities appearing in the Lawson criterion $n_i \tau_E T_i \geq f(T_i)$ and characterizes the quality of the heat insulation, i.e. the transport properties of the configuration.

The simplest approach is a linear configuration (mirror, pinch) which suffers from losses appearing at the ends. These points are optimized in devices with toroidal geometry. Today, the *Tokamak* configuration is the best developed; the *Stellarator* is expected to show confinement properties of similar quality.

10.2 Plasma equilibrium

10.2.1 The steady state MHD-equations

The equilibrium of a plasma in a magnetic field can be described by the MHD equations. It is described by neglecting the temporal derivatives. If, in addition, no flow is considered ($v = 0$),

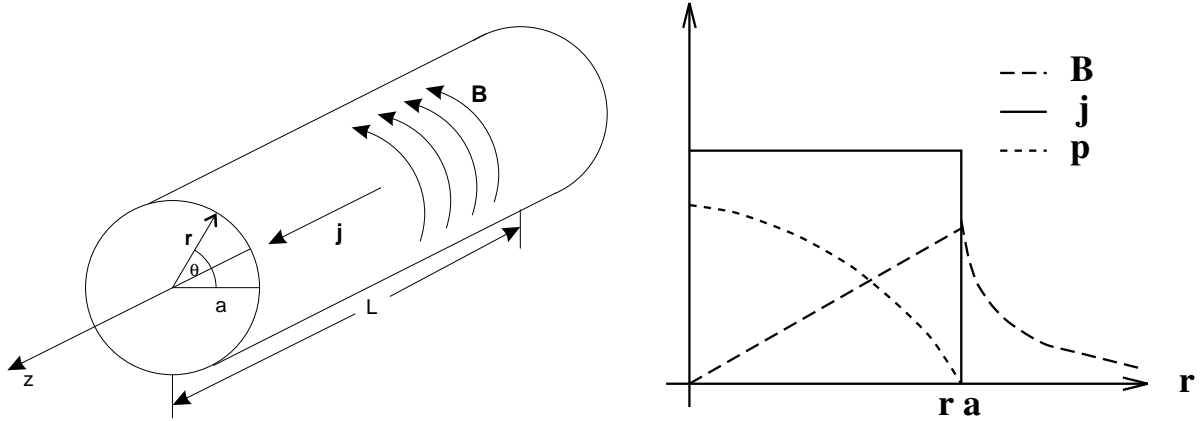


Figure 10.1: The linear z -pinch: geometry and radial profiles of j_z, B_θ and p for the example shown in the text.

the equations reduce to

$$\nabla p = \mathbf{j} \times \mathbf{B} , \quad (10.1)$$

$$\nabla \times \mathbf{B} = \mu_0 \mathbf{j} , \quad (10.2)$$

$$\nabla \cdot \mathbf{B} = 0 . \quad (10.3)$$

The first equation (10.1) is the force balance which states that a current flowing perpendicular to the magnetic field exerts a force on the fluid element. In equilibrium, this force balances the plasma kinetic pressure, i.e. everywhere in the plasma, the local pressure gradient is balanced by the Lorentz force. In particular, for $\nabla p = 0$, the fields \mathbf{j} and \mathbf{B} are collinear (*force free region*). Eq. (10.2) and (10.3) are Maxwell's equations for a static magnetic field.

10.2.2 Equilibrium in the linear pinch

A simple analytic solution of (10.1)–(10.3) can be given in the case of a linear cylindrical configuration, the so-called pinch. The simplest case is a z -pinch, i.e. a cylinder carrying a current in the z -direction (see Fig. 10.1).

Here, the magnetic field is purely azimuthal and the force balance reads

$$\frac{dp}{dr} = -j_z \cdot B_\theta . \quad (10.4)$$

To explicitly calculate the radial profile $p(r)$, we have to specify a current density profile $j_z(r)$. For simplicity, we chose $j_z = \text{const.} = j_0$ inside the plasma of radius a and $j_z = 0$ outside. Then we can solve (10.2) in cylindrical geometry to obtain

$$B_\theta = \frac{\mu_0 I_p}{2\pi a^2} r \quad \text{for } r \leq a , \quad (10.5)$$

$$B_\theta = \frac{\mu_0 I_p}{2\pi r} \quad \text{for } r > a , \quad (10.6)$$

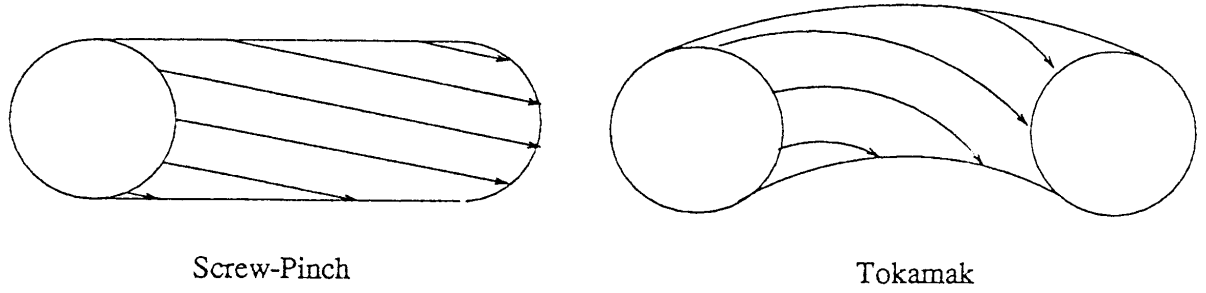


Figure 10.2: Magnetic configuration of the screw-pinch and analogous tokamak.

where $I_p = j_0 \pi a^2$ is the total current flowing in the plasma. Using this result, we can integrate (10.4) to yield

$$p(r) = \frac{\mu_0 I_p^2}{4\pi^2 a^2} \left(1 - \left(\frac{r}{a}\right)^2\right). \quad (10.7)$$

Fig. 10.1 shows a plot of the profiles. Calculating β_p , i.e. the ratio of average kinetic pressure and magnetic pressure associated with the poloidal field

$$\beta_p = \frac{2\mu_0 \langle p \rangle}{B_\theta^2} \quad (10.8)$$

we find $\beta_p = 1$ for this particular example. It can be shown that this is a general result for the z -pinch, independent of the profiles specified.

This simple equilibrium calculation does not include a stability analysis, i.e. we have shown that a state with $\partial t \rightarrow 0$ exists, but we do not know whether this is a stable solution. This will be done in the next section. For the z -pinch, one can show that it is unstable unless we add a magnetic field in the z -direction. Fig. 10.2 shows this magnetic configuration (*screw pinch*).

As can be seen, the magnetic field lines helically wind around the magnetic axis. If we bend the cylindrical screw-pinch to form a torus, we obtain a tokamak geometry. For large aspect ratio (i.e. ratio of major and minor radius $A = R/a$), a tokamak can be approximated by a screw-pinch periodic in z with period $2\pi R$. The properties of the field lines are characterized by the safety factor q defined by

$$q = \frac{\text{number of toroidal windings}}{\text{number of poloidal windings}} \quad (10.9)$$

of a field line on the torus. In the limit of the screw-pinch, the relation $q = (r/R)(B_t/B_\theta)$ holds. From stability considerations it follows that $q \geq 1$ (see below), so that $B_t \approx B_\theta q R/r$. Inserting typical tokamak values (e.g. ASDEX-Upgrade $a = 0.5$ m, $R = 1.65$ m and $q = 3$), we arrive at $B_t \approx 10B_\theta$, i.e. for this screw pinch $\beta_t = 2\mu_0 \langle p \rangle / B_t^2 \approx 1\%$. Thus stability requirements have a severe impact on the economic properties of the device.

In a screw pinch or tokamak, there is the possibility of poloidal currents that exert a force on the plasma. For $\mathbf{j}_p \times \mathbf{B}_t \uparrow \uparrow \mathbf{j}_t \times \mathbf{B}_p$, the plasma pressure balanced by the magnetic field is higher than in the pure z -pinch; in this case $\beta_p > 1$ and the poloidal current weakens the original B_t , therefore the plasma is said to be *diamagnetic*. In the opposite case, $\mathbf{j}_p \times \mathbf{B}_t \uparrow \downarrow \mathbf{j}_t \times \mathbf{B}_p$, we can sustain less pressure, and $\beta_p < 1$ (*paramagnetic* plasma).

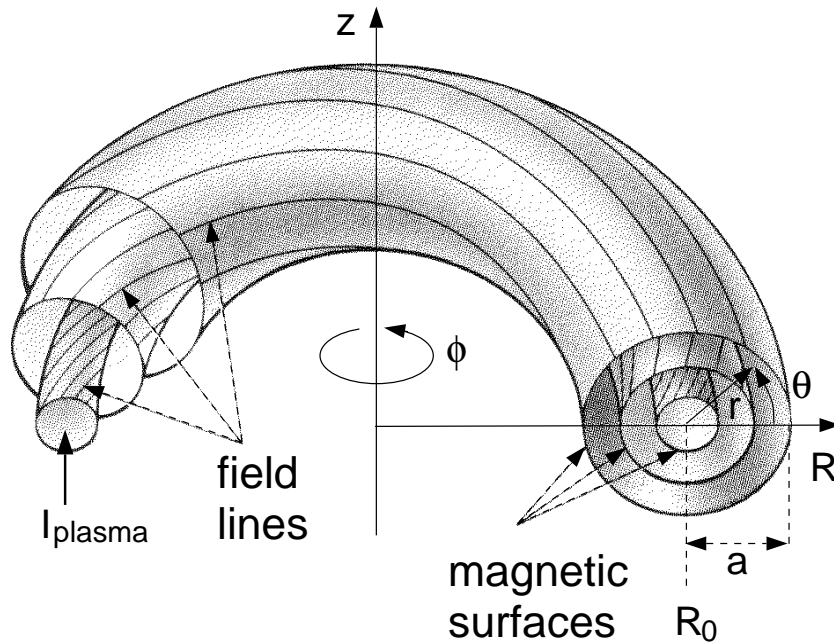


Figure 10.3: Co-ordinates used for the Grad-Shafranov equation.

10.2.3 The Grad-Shafranov equation

For an axisymmetric system like the tokamak, it is convenient to re-write the force balance (10.1). For this purpose, we need the following ideas:

- As $\nabla p = \mathbf{j} \times \mathbf{B}$, $\nabla p \cdot \mathbf{j} = \nabla p \cdot \mathbf{B} = 0$. Therefore the field lines of \mathbf{j} and \mathbf{B} lie in the surfaces of constant pressure.
- The flux integrals $\int \mathbf{B} d\mathbf{A}$, $\int \mathbf{j} d\mathbf{A}$ have a constant value on the $p = \text{const}$ surfaces for an arbitrary curve C on this surface, since \mathbf{j} and \mathbf{B} lie in this surface and thus any part of the integrals on the surface vanishes. These surfaces are therefore called *flux surfaces* and can be labelled by the (scalar) fluxes. Also, p is only a function of the fluxes.
- As $\nabla \cdot \mathbf{B} = \nabla \cdot \mathbf{j} = 0$, any flux integral $\int \mathbf{B} d\mathbf{A}$, $\int \mathbf{j} d\mathbf{A}$ has a constant value if the arbitrary surface A is surrounded by the same curve C and thus we are free to choose the surface A . This means that each flux surface can be assigned a unique value of the flux, independent of the geometry in which the flux was calculated.

On a torus, there are two topologically different types of curves: Those winding around the torus in the toroidal direction and those winding around the torus in the poloidal direction. If we chose a curve winding around in the toroidal direction, integration over the domain enclosed by this surface yields the poloidal magnetic flux function Ψ and the total poloidal current I_{pol} . Both functions are constant on the flux surface and the magnetic field can be

calculated as

$$B_\phi = \frac{\mu_0 I_{pol}}{2\pi R}, \quad (10.10)$$

$$B_R = -\frac{1}{2\pi R} \frac{\partial \Psi}{\partial Z}, \quad (10.11)$$

$$B_Z = \frac{1}{2\pi R} \frac{\partial \Psi}{\partial R}, \quad (10.12)$$

where the co-ordinates from Fig. 10.3 have been used. Note that with this definition, Ψ denotes the poloidal flux per unit length in toroidal direction ($[\Psi] = \text{Vs/m}$). Using these quantities, the force balance can be re-written as

$$-\Delta^* \Psi \equiv -\left[R \frac{\partial}{\partial R} \left(\frac{1}{R} \frac{\partial \Psi}{\partial R} \right) + \frac{\partial^2 \Psi}{\partial z^2} \right] = \mu_0 (2\pi R)^2 p(\Psi)' + \mu_0^2 I_{pol}(\Psi) I_{pol}'(\Psi) \quad (10.13)$$

known as the Grad-Shafranov equation. The prime denotes the derivative of a flux surface quantity with respect to Ψ . Eq. (10.13) is usually nonlinear in Ψ . To solve it, we can e.g. specify $p(\Psi)$ and $I_{pol}(\Psi)$ and then solve for $\Psi(R, Z)$. Usually, one will specify boundary conditions. If the plasma is surrounded by a perfectly conducting vacuum vessel, the vessel is a flux surface and therefore $\Psi = \text{const}$ at the vessel determines shape and position of the plasma boundary. To satisfy these conditions, we have to add a solution of the homogeneous equation, i.e. a function Ψ_{ext} with $\Delta^* \Psi_{ext} = 0$. Such a field is produced by external coils, i.e. the solution of the Grad-Shafranov equation with fixed boundary and profile functions tells us how to arrange external control currents to maintain the plasma in equilibrium.

10.2.4 The tokamak

The tokamak principle was already introduced in chap. 2. The plasma acts as a secondary winding of a transformer. Ramping the current in the primary coil induces a loop voltage inside the discharge vessel; after breakdown, a toroidal current flows in the plasma. This current heats the plasma via its resistance (Ohmic Heating (OH), the primary coil is also called the OH coil). The current itself creates the poloidal magnetic field, the toroidal field is produced by external coils (a stellarator produces all its field components by external coils). The poloidal field coils maintain the plasma in force equilibrium as described by (10.13). A sketch of the tokamak principle is shown in Fig. 2.9.

Fig. 10.4 shows typical examples for poloidal cross-sections calculated with (10.13). One can see that the flux surfaces are not centered to one axis, but are slightly shifted. This *Shafranov shift* is due to the forces trying to expand the torus radially outward:

- The kinetic pressure of the plasma.
- The expansion force of a current loop due to the $\mathbf{j} \times \mathbf{B}$ force.

The sum of these two forces is called *hoop force*. In Fig. 10.4 b), one can see that the plasma cross-section does not necessarily have to be circular; in fact, elongation and triangularity

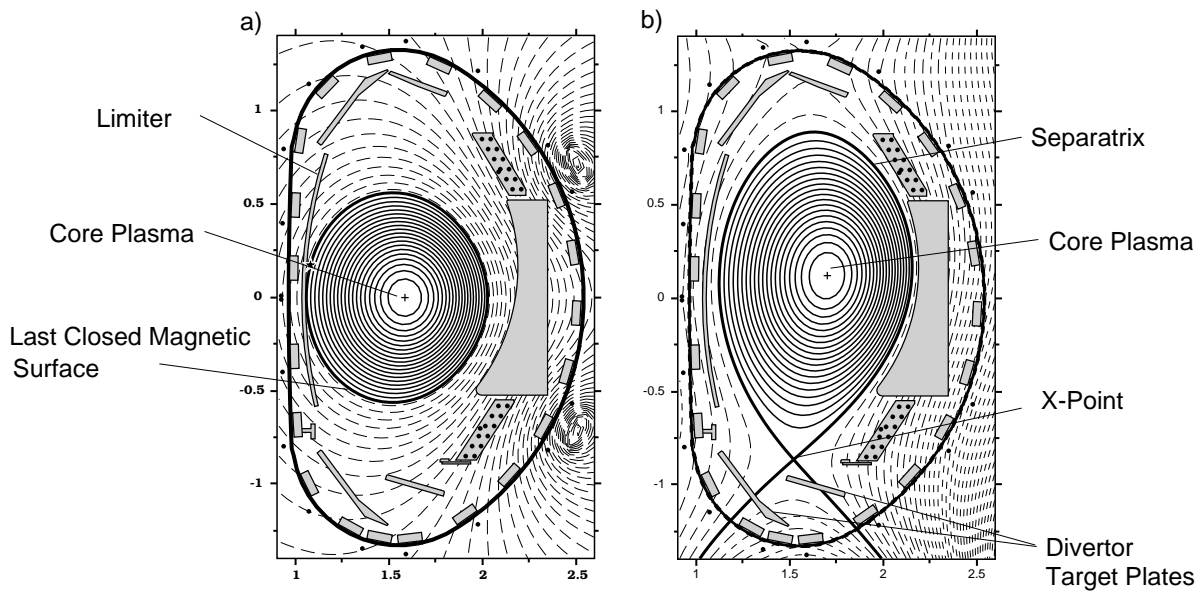


Figure 10.4: Typical poloidal cross-sections of a tokamak.

produced with additional poloidal field coils enhance plasma performance (see next section). One also sees the different ways to limit a plasma: Fig. 10.4 a) shows a so called *limiter* case, where a material limiter defines the last closed flux surface, in Fig. 10.4 b), this last closed flux surface is defined magnetically by a so-called *separatrix*; plasma crossing the separatrix flows along field lines to the material plates at the bottom of the vessel. This configuration is called a magnetic *divertor*.

10.3 Stability of an equilibrium state

As has been mentioned before, the Grad-Shafranov (10.13) describes a force equilibrium, but it does not tell us if the equilibrium is stable, i.e. if a small variation of the plasma parameters or the external control currents will lead to another equilibrium or to an unstable situation. Therefore, we have to analyze the stability properties of a configuration by a separate treatment.

MHD instabilities can deteriorate the plasma performance due to various effects: Large-scale instabilities can lead to a loss of plasma control (e.g. during a *disruption*, the plasma current collapses in an uncontrollable way) whereas small scale perturbations and MHD turbulence can significantly enhance radial transport of particles and energy. Nevertheless, in some cases instabilities may help to control parameters; e.g. ELMs (Edge Localized Modes) periodically expel impurities from the plasma edge and help keep the plasma clean.

10.3.1 Methods of stability analysis

From MHD theory, there are different ways to analyze the stability of a given equilibrium. Often, the analysis is done by introducing a perturbation of the equilibrium configuration as

a displacement ξ of a fluid element. Two methods are especially useful to check the stability against such displacements:

- The energy principle: This approach calculates the energy W_{MHD} of the configuration as a functional of the displacement vector. Stability is obtained if the second order change in energy $\delta^2 W_{MHD}\{\xi\}$ is positive for an arbitrary ξ (the linear variation is zero due to the equilibrium condition). This method is useful to prove that a configuration is *not* stable, because it is sufficient to find one unstable ξ ; on the other hand, stability is hard to prove.
- Eigenmode analysis: Here, the time-dependent MHD equations are solved with an eigenmode ansatz for the displacement ξ . An ansatz often used is the Fourier decomposition in time and space. For the screw pinch, the spatial Fourier ansatz means periodicity in poloidal and toroidal co-ordinate θ and ϕ . Note that in a real torus, symmetry in the θ direction is only an approximation and coupling of poloidal harmonics will occur. For linearized MHD equations, this leads to an eigenvalue problem for each single Fourier mode

$$\xi = \xi_{mn}(r)e^{i(m\theta - n\phi)}e^{\gamma t}. \quad (10.14)$$

The indices m and n are called poloidal and toroidal mode-numbers, for real γ , stability means $\gamma < 0$. If γ has an imaginary part, the eigenmode is called overstable and will exhibit a temporal oscillation. If γ is real and positive, it can be interpreted as a linear growth rate. The saturated amplitude of an instability can only be found by introducing nonlinear effects such as changes in the equilibrium introduced by the perturbation.

Perturbations are easily excited if the field lines do not ergodically cover a flux surface but close upon themselves after few revolutions in the torus. These flux surfaces are the ones with rational safety factor q ; they are called *resonant surfaces* and a standing wave with mode numbers $q = m/n$ can occur.

10.3.2 Classification of instabilities

In a confined plasma, an instability is driven by the free energy contained in the equilibrium configuration. In a tokamak, there are two main sources of free energy: The kinetic energy of the plasma and the energy of the magnetic field generated by the plasma. Instabilities can therefore be driven by the radial gradient of either the pressure or the current profile. At low β , the magnetic energy is much higher than the kinetic energy and the instabilities will mainly be current-driven; at high β , we expect the pressure driven instabilities to become significant.

In cylindrical approximation, the perturbed magnetic field has a radial component. The growth of this field is governed by Faraday's law. Inserting Ohm's law for the plasma yields in the linearized case

$$\frac{\partial B_{1r}}{\partial t} = -\frac{1}{r} \frac{\partial E_{1z}}{\partial \theta} = \frac{1}{r} \frac{\partial}{\partial \theta} \left(\eta j_{1z} + (\mathbf{v}_1 \times \mathbf{B}_0)_z \right), \quad (10.15)$$

where the subscript "1" refers to the perturbed quantities and the subscript "0" to the equilibrium quantities. From this we deduce that there are two ways for a perturbation to grow:

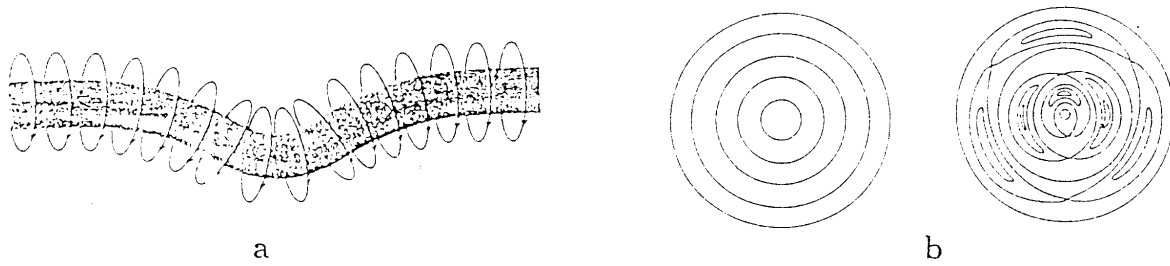


Figure 10.5: Ideal kink (a) and resistive tearing (b) instability. In (b), magnetic islands are formed.

- Ideal case (no resistivity, i.e. $\eta \rightarrow 0$): Flow of plasma perpendicular to the field lines; in this case, $\mathbf{v} \times \mathbf{B}$ balances the E -field and in the fluid frame ($\mathbf{v} = 0$), magnetic flux is conserved, i.e. \mathbf{B} moves with the fluid. This means that there is no change in the *topology*.
- Resistive case ($\eta \neq 0$): A current flows along the equilibrium field lines and generates the B -field; in this case, the topology is changed (*tearing* and *reconnection* of field lines).

Fig. 10.5 shows two examples: The so-called *kink* as a typical ideal instability, the *tearing mode* as a resistive one. In the case of the tearing mode, so-called *magnetic islands* form. Note that the magnetic island is a nonlinear solution of the MHD equations.

10.3.3 Examples

A simple example of an unstable situation is the case of an elongated plasma. In order to vertically elongate a plasma cross-section, we have to run coil currents of the same sign and order of magnitude than the plasma current. For a perfectly centered plasma, the net force is zero. However, any shift δz of the plasma current center increases the attractive force of the coil towards which the plasma moves, so that further acceleration results. The plasma experiences a vertical displacement event (VDE). As the plasma has negligible mass, this is a very fast event (on the order of the Alfvén time scale, i.e. $\approx \mu\text{s}$). In order to feedback control this instability, one therefore has to provide conducting structures that, via induction, slow down the motion to a ms timescale.

Other MHD phenomena have been shown to influence the achievable β of a configuration. An example is the *external kink* driven by current gradients near the edge imposing restrictions on the possible current profiles. Restrictions on the pressure profile come from the so-called interchange instability. Here, neighbouring flux tubes can change place, analogous to the Rayleigh-Taylor instability of a normal fluid, if the field line can shorten and thus lose magnetic energy due to this process. As can be seen in Fig. 10.6, this is the case when the radius of curvature is parallel to the pressure gradient (so-called *bad curvature*). Conversely, if the radius of curvature is anti-parallel to the pressure gradient, an interchange of plasma and magnetic field will increase the magnetic energy and thus be stabilising (*good curvature*). In a screw pinch, only the poloidal field is curved and its curvature is *bad*, i.e. potentially destabilising. Stability is then achieved by sufficient shear dq/dr so that adjacent field lines have a different pitch angle

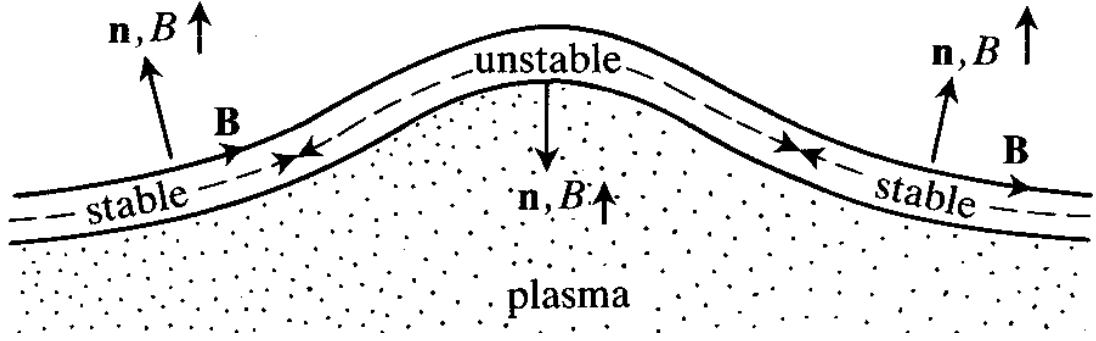


Figure 10.6: Interchange instability in a curved magnetic field.

and are not easily interchanged. In a torus, the toroidal field is also curved, exhibiting an area of good curvature on the inside and bad curvature on the outside of the torus. Thus, stability has to be determined by integrating along a field line and summing up the various stabilising and destabilising contributions. This leads to the Mercier criterion

$$\left(\frac{q'}{q}\right)^2 > -\frac{8\mu_0 p'}{rB_0^2}(1-q^2). \quad (10.16)$$

As $p' < 0$, this means stability for all pressure profiles with $q > 1$; for $q \leq 1$, the shear has to be nonzero to provide stability. At high β , however, a new type of mode, the so-called *ballooning instability*, can develop. This mode has a small perturbation component along the magnetic field, which allows a variation of the amplitude such that it concentrates on the outside of the torus, i.e. in the bad curvature region. Above a (shear dependent) critical pressure gradient, the energy gained by concentrating there is higher than the energy needed to bend the equilibrium field lines, and the mode becomes unstable.

A simultaneous optimization of pressure and current profiles yields a limit for the achievable β for given safety factor q_a and with $q_0 > 1$

$$\beta_{max}[\%] = c \frac{I[\text{MA}]}{a[\text{m}]B_t[\text{T}]} . \quad (10.17)$$

This limit is known as the *Troyon limit*, the constant c depends only on the plasma shape and varies between \approx three and five. Theory predicts an increase in c with elongation and triangularity; this is confirmed by various experiments.

Other examples for MHD instabilities are sawteeth and disruptions, each of them linked to a special rational surface ($q = 1$ and $q = 2$, respectively). This is treated in the section on experimental results of the tokamak.

10.4 Transport in a fusion plasma

10.4.1 Transport equations

For one single particle in a toroidal device, the confinement is perfect. In reality, collisions, drifts and MHD turbulence lead to a radial transport of particles and energy (i.e. perpendicular to the magnetic flux surfaces). It is this transport which determines the global energy and particle confinement times τ_E and τ_p .

To analyse the nature of transport, we define the particle flux Γ as the number of particles passing through a magnetic surface per unit area and time. For Γ we make the following ansatz

$$\Gamma = -D\nabla n + nv \quad (10.18)$$

stating that there is a diffusive part driven by the density gradient (characterized by the diffusion coefficient D) due to the statistical random walk of particles and a convective part due to a directed motion v . The equation of continuity links Γ to the temporal change in density via

$$\frac{\partial n}{\partial t} = -\nabla\Gamma + S, \quad (10.19)$$

where $S(r,t)$ is a source term describing the change in plasma density due to ionisation or recombination (i.e. processes which cannot be described as a flux into or out of the volume element). Finally, in equilibrium, n does not change in time and we obtain

$$\nabla(D\nabla n) + \nabla \cdot (nv) = S. \quad (10.20)$$

For a known source function and with given D and v , we can therefore determine the plasma density profile. On the other hand, measured density profiles are used to determine D and, with some additional assumptions, v . Transport of other quantities as e.g. energy can be treated analogously.

10.4.2 Transport coefficients

In a magnetized plasma, we distinguish between transport coefficients parallel and perpendicular to the magnetic field, e.g. D_{\parallel} and D_{\perp} . In general, the condition $D_{\parallel} \gg D_{\perp}$ holds. Since the confinement properties of a magnetic configuration are governed by the perpendicular coefficients, we will therefore focus on those.

The simplest approach to calculate diffusion coefficients comes from the random-walk ansatz. Here, we assume that, due to collisions with other particles, a particle makes a step Δx perpendicular to the magnetic field after a time Δt . If the step can be done in either direction $\pm\Delta x$ with equal probability, the process is purely diffusive and the diffusion coefficient D is given by

$$D \approx \frac{\Delta x^2}{2\Delta t}. \quad (10.21)$$

In order to estimate D , we have to evaluate Δx and Δt . The latter is given by the inverse of the collision frequency ν_c . With appropriate averaging we obtain the following relations for a 90° scattering (made up of many small angle scatterings) for electron-electron (ee), electron-ion (ei) and ion-ion (ii) collisions (we assume a pure hydrogen plasma, i.e. $Z = 1$)

$$\nu_{ee} \approx \nu_{ei} \propto \frac{ne^4}{\sqrt{m_e} T_e^{3/2}}, \quad (10.22)$$

$$\nu_{ie} = \left(\frac{m_e}{m_i}\right) \nu_{ee}, \quad (10.23)$$

$$\nu_{ii} = \left(\frac{m_e}{m_i}\right)^{1/2} \left(\frac{T_e}{T_i}\right)^{3/2} \nu_{ee}. \quad (10.24)$$

In the so-called classical approach to transport, we take Δx to be the Larmor radius r_L

$$\Delta x = r_L = \frac{\sqrt{2mkT}}{eB}. \quad (10.25)$$

However, the location \mathbf{R} of the guiding centre of the gyro-orbit is given by

$$\mathbf{R} = \frac{\mathbf{p} \times \mathbf{B}}{q_C B^2}, \quad (10.26)$$

with q_C denoting the charge of the particle. In a collision, momentum balance requires $\Delta \mathbf{p}_a = -\Delta \mathbf{p}_b$, and thus, for like-particle collisions, $\Delta \mathbf{R}_a = -\Delta \mathbf{R}_b$. Therefore, at each collision, the particles just change place so that like-particle collisions do not contribute to particle transport (note that heat can be transferred that way, because a hot particle may change place with a cold one).

The situation changes for electron-ion collisions. Here, $q_a = -q_b$ and therefore $\Delta \mathbf{p}_a = -\Delta \mathbf{p}_b$ leads to $\Delta \mathbf{R}_a = \Delta \mathbf{R}_b$. Thus diffusion is ambipolar, electrons and ions make a step of equal magnitude and direction per collision. The diffusion coefficient is then given by

$$D_{e,class} = \nu_{ei} r_{L,e}^2 = \nu_{ie} r_{L,i}^2 = D_{i,class}. \quad (10.27)$$

For the thermal conductivities, similar arguments can be applied to show that the relation $\chi_i \approx (m_i/m_e)^{1/2} \chi_e \approx 40 \chi_e$ should hold. However, experimentally determined diffusion coefficients are larger by a factor of $\approx 10^5$. Also, the electron heat conductivity is found to be comparable to that of the ions. Therefore, classical transport cannot be the dominating transport process in a fusion plasma.

So far, we did not consider the effects of the toroidal geometry. This is the subject of the so-called *neoclassical* transport theory. The main differences to classical transport theory arise from two facts:

- Along a magnetic field line, $|B|$ is not constant; a particle moving along a field line sees a higher field on the inside of the torus and, for sufficient v_\perp/v_\parallel , may be reflected in this magnetic mirror (see chap. 1). Therefore we have to distinguish between *trapped* and *passing* particles. It can be shown that the number of trapped particles is given by $n_t/n = \sqrt{2\varepsilon}$, where $\varepsilon = r/R$ is the inverse aspect ratio of the flux surface. A simple result of this effect is that the electrical conductivity is lowered in neoclassical theory as trapped particles cannot contribute to the toroidal current.

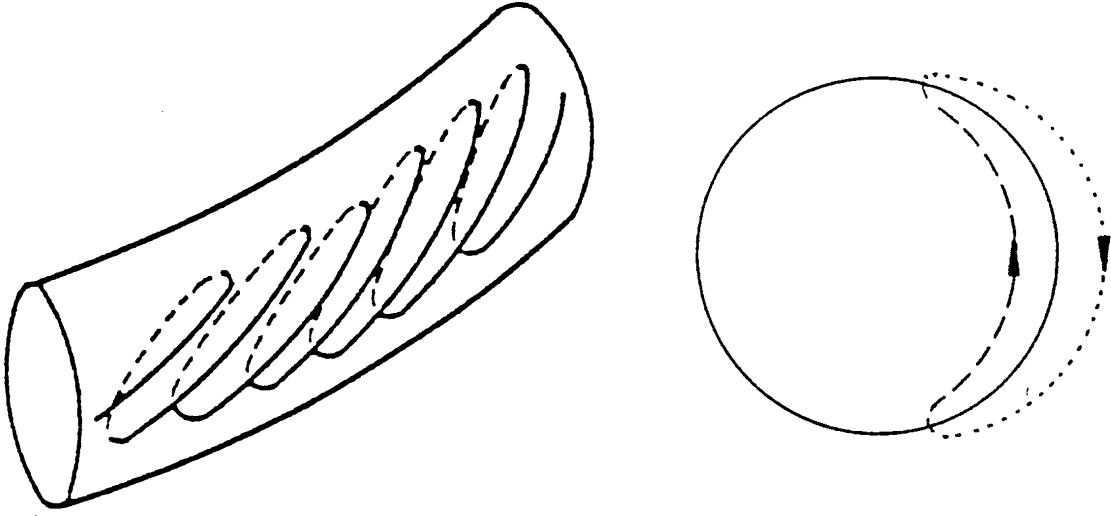


Figure 10.7: Banana Orbits in a toroidal configuration.

- Due to ∇B and curvature drifts, the path of a trapped particle deviates from the magnetic surface. Therefore, the projection of the trapped particle orbit in a poloidal plane is not a sector of a circle, but rather has a banana-like shape (see Fig. 10.7). These orbits are known as *banana orbits*. One can show that the banana width is given by

$$r_B = \frac{r_L q}{\sqrt{\varepsilon}}. \quad (10.28)$$

For trapped particles, an *effective* collision frequency $\nu_{eff} \approx \nu_c/(2\varepsilon)$, where ν_c can be any of the collisionalities discussed above, is defined. This takes into account, that a trapped particle becomes a passing one when its pitch angle has changed by $(2\varepsilon)^{1/2}$. Finally the ratio $\nu_* = \nu_{eff}/\nu_t$, where ν_t is the inverse of the time a particle needs to transit the banana, determines whether the particle can complete a banana orbit between two collisions.

There are three different regimes of neoclassical transport:

- Collisional or Pfirsch-Schlüter regime: Here, $\nu_* > 1$, particles do not complete their banana orbits but are scattered before. In this case, D is evaluated to be

$$D_{PS} = q^2 r_L^2 \nu_c = q^2 D_{class}. \quad (10.29)$$

As we have seen, q typically ranges between two and five, so transport is strongly increased.

- Banana regime: Here, $\nu_* < \varepsilon^{3/2}$, particles follow the banana orbit several times before they are scattered. We can apply the random walk argument for the $\sqrt{2\varepsilon}$ trapped particles with step size r_B and typical time interval $1/\nu_{eff}$

$$D_B \propto \sqrt{2\varepsilon} r_B^2 \nu_{eff} \approx \frac{r_L^2 q^2}{\varepsilon^{3/2}} \nu_c = \frac{q^2}{\varepsilon^{3/2}} D_{class}. \quad (10.30)$$

For typical values, e.g. $\varepsilon = 1/3$ and $q = 5$, this yields $D_B = 130 D_{class}$.

- Plateau regime: Here, $1 > \nu_* > \epsilon^{3/2}$ and one can derive $D_{Pl} \approx \nu_{th} r_L^2 q/R$. This result is independent of ν_c (hence the name). Numerical values for D_{Pl} are in between the Pfirsch-Schlüter and the Banana regimes, so that, with rising collisionality, a smooth transition occurs between the regimes.

These neoclassical terms have to be added to the classical terms, however, they completely dominate the latter. We have seen that, due to neoclassical effects, transport coefficients can be increased by two orders of magnitude, nevertheless, they still cannot explain the experimental observations, especially for the electron channel. Today, theory tries to explain this so-called *anomalous* transport by nonlinear MHD turbulence models. It is found both theoretically and experimentally that the plasma exhibits turbulent eddies of a radial extension Δx of a few cm and a lifetime Δt of several $100 \mu s$. If we calculate the diffusion coefficient according to (10.21), we arrive indeed at typical values of $1 \text{ m}^2/\text{s}$ which could explain the experimental observations. However, the precise identification of the responsible small-scale MHD instabilities is a subject of ongoing research in the field of fusion plasma physics. In particular, it has become clear that a simple description in terms of one dominant mode does not exist and several contribution must be taken into account, for the different species and the large variation of plasma parameters from the edge to the core.

Chapter 11

Experimental results from tokamaks

Wolfgang Suttrop

11.1 Tokamak plasmas

11.1.1 The tokamak principle

Nuclear fusion can be achieved in plasmas which are composed of a mixture of deuterium and tritium. At the high temperatures necessary for nuclear fusion, in the vicinity of 10 keV or 100 Million degrees K, the plasma is fully ionised, i.e. consists only of ions and electrons. In order to reach these temperatures, good thermal insulation is necessary, which can be provided by a magnetic field. The Lorentz force makes charged particles spiral (*gyrate*) around magnetic field lines. Electrons and ions can freely move along field lines. If magnetic field lines close themselves inside the plasma volume, the free parallel motion does not result in particle losses from the plasma. Consequently, toroidal field geometry (as sketched in Fig. 11.1 left) is most effective for confinement of high temperature plasmas and in fact most magnetic fusion concepts involve this topology.

The toroidal shape of the plasmas implies a non-uniform magnetic field strength. This results in a particle drift (Grad-B and curvature drift) perpendicular to the magnetic field and its gradient. This drift originates from a different gyro-radius at the low and high field sides of the particle orbit. The drift is directed parallel to the torus (vertical) axis in different directions for electrons and ions and hence leads to a separation of charge and a vertical electrical field. The electrical field induces an additional $E \times B$ drift which leads to fast radial losses of electrons and ions (see Fig. 11.1 right). Hence, a simple toroidal magnetic field is not sufficient for plasma confinement.

The losses induced by these drifts can be eliminated by introduction of an additional poloidal magnetic field. The resulting helical field directs field lines successively below and above the equator of the device so that vertical drifts result in inward and outward motion, respectively. As a result, the trajectories of the centers of the gyromotion (*gyrocenters*) are displaced from the magnetic field lines but are also closed in themselves. The magnetic moment of the gyromotion is conserved and with increasing magnetic field strength the velocity parallel to the

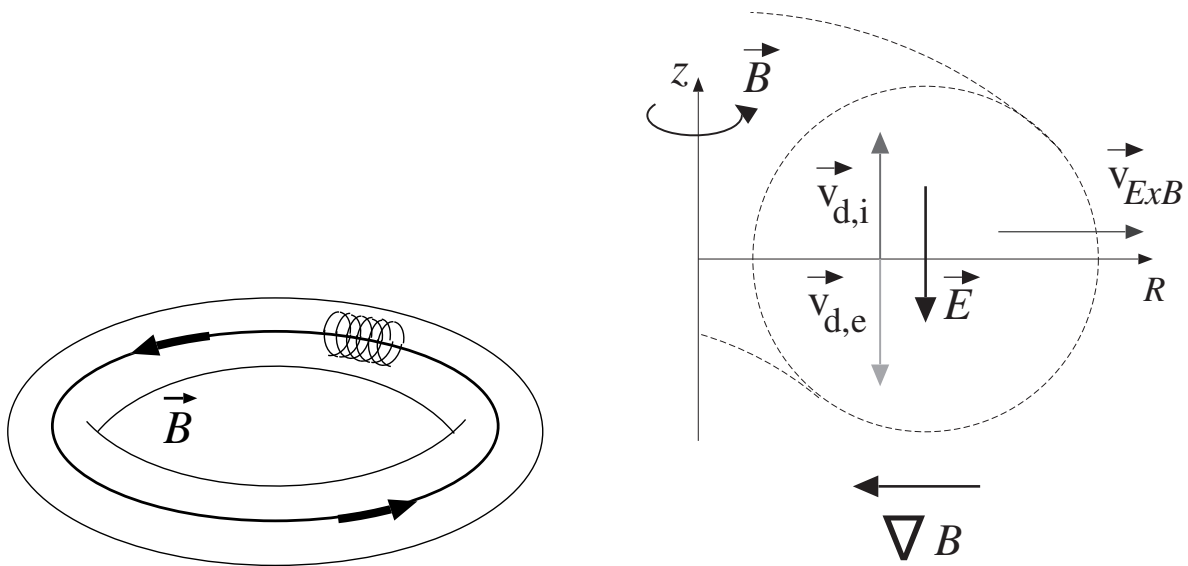


Figure 11.1: Left: Closed field lines in toroidal geometry.
 Right: Outward particle drift in toroidal geometry.

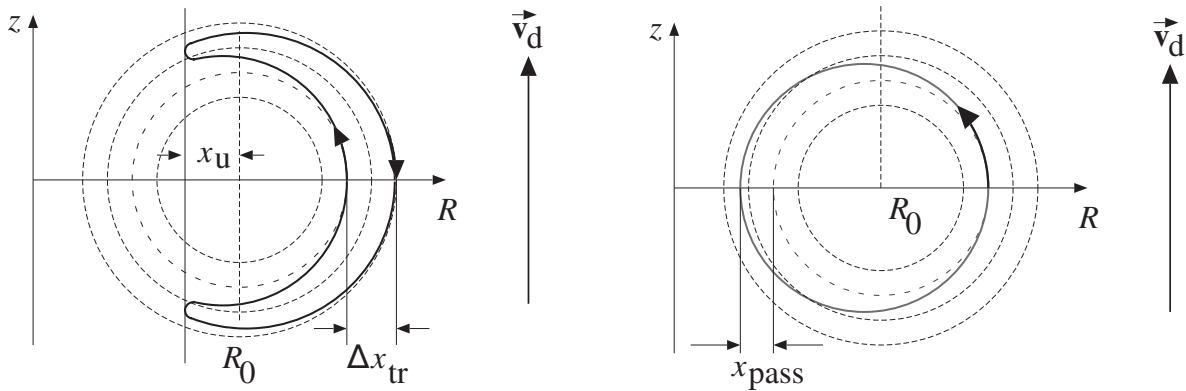


Figure 11.2: Particle trajectories in toroidal geometry:
 Left: Trapped particles,
 Right: Passing particles.

field reduces. Fig. 11.2 shows poloidal sections of two basic types of gyro-center trajectories: *Trapped particles*, see Fig. 11.2 left do not have a sufficiently large parallel velocity at the two field side to reach the location of maximum magnetic field strength. They are confined to the magnetic low field side and move in poloidally and toroidally opposite directions on the inner and outer halves of their orbit. The characteristic *banana* shape as viewn in a poloidal section gives rise to the nick-name *banana orbits* for these trajectories (see section on *magnetic mirror* above). *Passing particles* have a sufficiently large parallel velocity to continue their motion on the high field side, Fig. 11.2 right. The associated radial displacement with respect to field lines, Δx , is larger by a factor $(R/a)^{1/2} \equiv 1/(\epsilon)^{1/2}$ for trapped particles than for passing particles, where R is the *major radius* (distance from torus axis to plasma center) and a the *minor radius* (half of the diameter of the plasma column) of the toroidal plasma.

The effects of toroidicity on particle orbits have several important consequences. Cross-field

diffusion by Coulomb collisions is enhanced by the larger radial displacement of the particle orbits compared to their gyroradius (*neo-classical* diffusion). In presence of a pressure or density gradient, the average toroidal velocity of trapped particles at a given radial location is not zero. Momentum is transferred by Coulomb collisions to passing particles resulting in a plasma current (*bootstrap current*).

The additional poloidal field needed for confinement can be created in different ways. *Stellarators* generate a helical field entirely by external field coils. *Tokamaks* use a plasma current to produce the poloidal field component, while the toroidal field is generated by an axisymmetric arrangement of external coils. The word *tokamak* stems from a Russian acronym for *Toroidal chamber with magnetic coils*. In the following, we concentrate on tokamaks.

11.1.2 Components of a tokamak

The main components of a tokamak are illustrated in Fig. 11.3 left. Helical magnetic field lines span nested surfaces of constant magnetic flux (*flux surfaces*). The plasma is enclosed in a vacuum chamber (not shown) which is needed to remove air and control the hydrogen pressure outside the plasma. The axisymmetric toroidal field is produced by poloidal currents in a set of magnetic coils surrounding the plasma. A central solenoid is used to produce a time-varying poloidal magnetic flux which induces a toroidal loop voltage, and due to finite plasma resistivity, a plasma current. The plasma is subject to a poloidally and radially outward directed force which results from a finite plasma pressure gradient. This force is balanced by the $j \times B$ force acting on the plasma current due to the helical field and an additional vertical field produced by toroidal currents in external conductors (*vertical field coils*).

As an example, the poloidal cross section of ASDEX Upgrade (Axi-Symmetric Divertor Experiment) at Max-Planck-Institut für Plasmaphysik, Garching (Germany), is shown in Fig. 11.3 right. This machine can produce plasmas with major radius $R = 1.65$ and horizontal minor radius $a = 0.5$ m. An array of vertical field coils is installed which do not only produce the vertical field for compensation of the radial outward force but also can create suitable poloidal fields to create a wide range of plasma shapes. Typically, vertically elongated plasmas are produced by toroidal currents in upper and lower shaping coils which have the same direction as the plasma current. This configuration is inherently unstable against vertical displacements. A small upward displacement from the equilibrium position will result in a larger attracting force on the plasma current of the upper coil current than of the lower coil, thereby amplifying the perturbation. This position instability is damped by induced currents in a passive saddle-loop near the plasma (*passive stabilizing loop*). On time scales longer than the L/R time constant of the saddle loop (about 1 ms), the vertical position is actively controlled with an external radial field, i.e. by a differential current in the upper and lower vertical field coils.

11.1.3 Divertor tokamaks

Quadrupole currents in the poloidal field coils are also used to form a *magnetic divertor* configuration. Fig. 11.4 illustrates two basic magnetic configurations of a tokamak plasma.

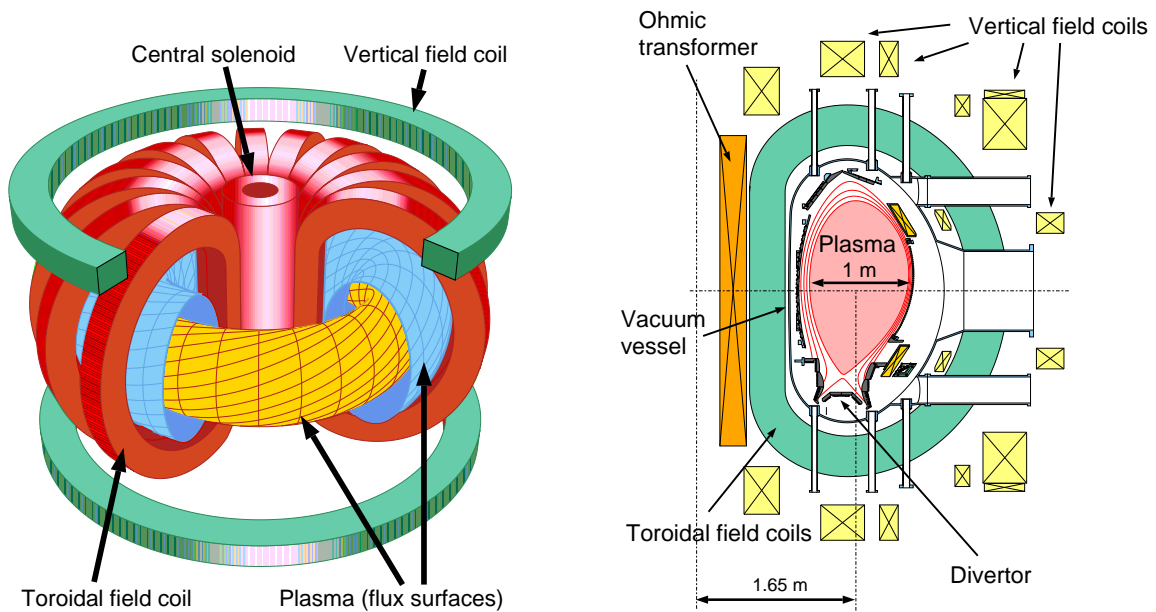


Figure 11.3: Left: Tokamak: Schematic view of main components.

Right: Cross section of ASDEX Upgrade (Axi-Symmetric Divertor EXperiment), installed at Max-Planck-Institut für Plasmaphysik, Garching, Germany.

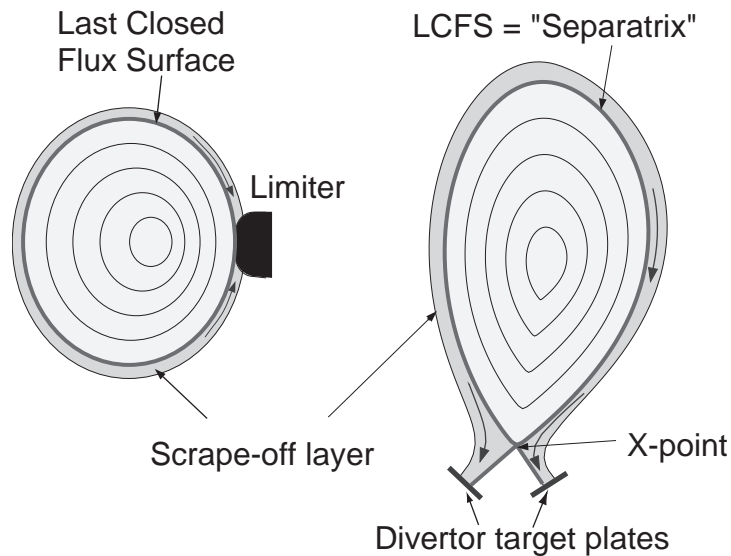


Figure 11.4: Limiter and divertor configurations.

Radial diffusion of particles and heat across the magnetic field will lead to expansion of the plasma until a material wall is intersected. Without a magnetic divertor, this first material contact will be close to the main confined plasma volume, and hence be subjected to strong heat load and particle fluxes. This region, called the *limiter*, must be appropriately designed in order to prevent excessive materials erosion. With a suitable axi-symmetric quadrupole field a magnetic X-point is introduced which defines a magnetic surface (*separatrix*) that intersects the material wall only at a distance from the main plasma. Particles and energy from the main

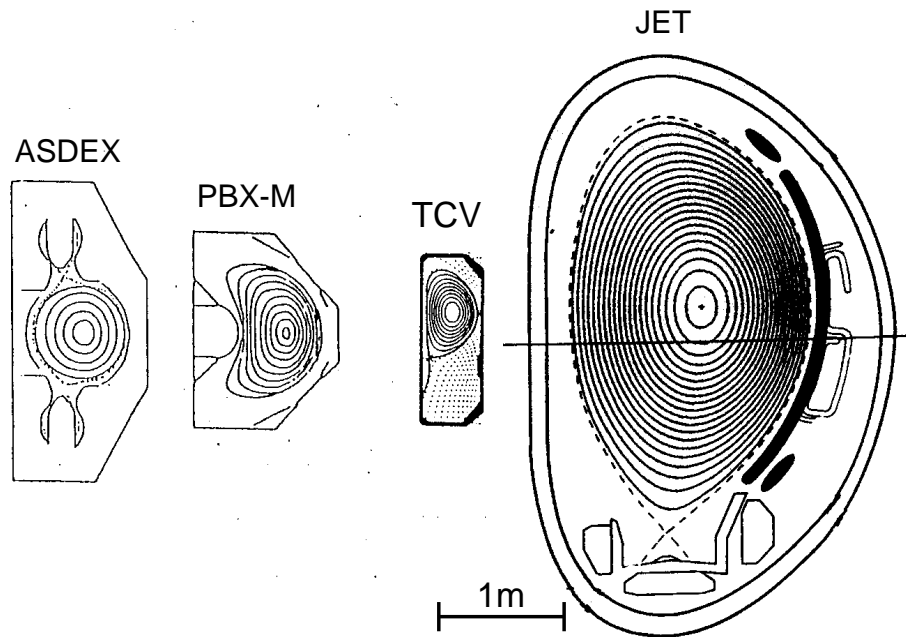


Figure 11.5: Variations of magnetic configurations (poloidal cross sections) in different experiments in shape (ASDEX, PBX-M) and plasma size (TCV, JET).

plasma flow along field lines to a separated divertor region where particles are neutralized at the material wall (*target plates*). A fraction of the neutral particles is reflected towards the separatrix, re-ionised and is streaming back again to the target plates. This recycling flux effectively increases the plasma density in the divertor region. Under normal conditions, the plasma pressure is constant along magnetic field lines, hence the plasma temperature in the divertor is smaller than that at the separatrix near the main plasma. As a result, the erosion damage at the material wall produced by ions can be strongly reduced and cleaner plasmas are obtained compared with a limiter configuration. This favourable property of divertors is exploited in most modern magnetic fusion devices, both tokamaks and stellarators. Fig. 11.5 shows cross sections of four tokamaks: ASDEX (Max-Planck-Institut für Plasmaphysik, Garching, Germany), PBX-M (Princeton Plasma Physics Laboratory, Princeton, New Jersey, USA), TCV (Centre de Recherche en Physique des Plasmas, Lausanne, Switzerland) and JET (Joint European Torus, Culham, United Kingdom). These examples illustrate a variety of plasma sizes, cross sections and divertor geometries used in tokamaks.

11.1.4 Magnetic configuration

At the densities and temperatures reached in fusion plasmas, significant kinetic pressure is obtained in the plasma core and large pressure gradients produce strong forces on the plasma column. The ∇p forces are balanced by $j \times B$ forces arising from the magnetic field interacting with internal (toroidal and poloidal) plasma currents. This force balance is often called the *magnetic equilibrium* of a plasma configuration. (It has to be stressed that this terminology

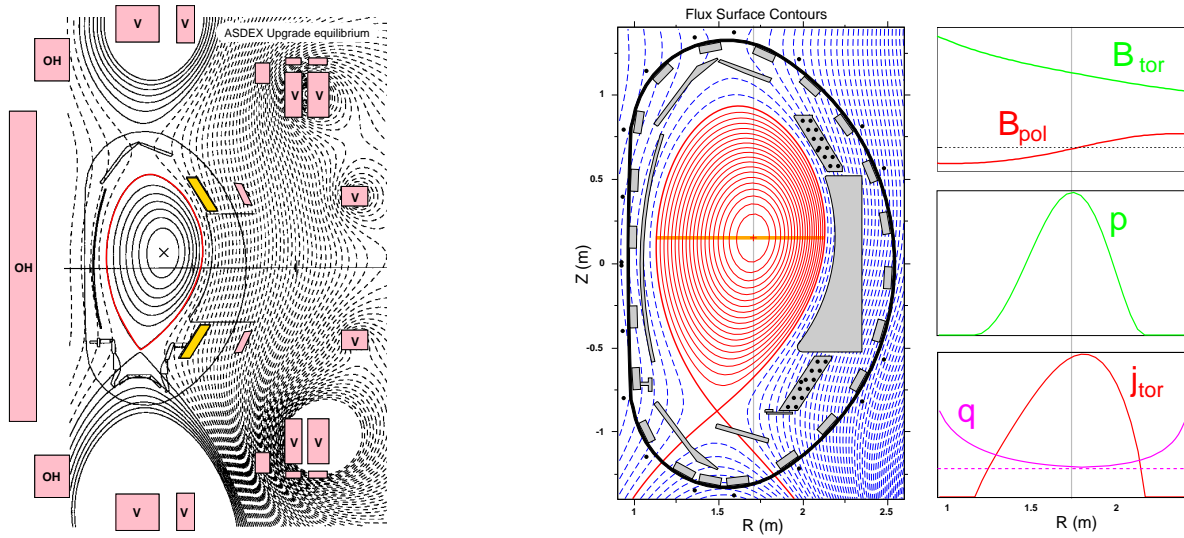


Figure 11.6: Left: Poloidal magnetic flux in and around a shaped tokamak plasma (poloidal section), which is created by toroidal currents – plasma current and a set of external poloidal field coils. Right: Tokamak equilibrium: Flux surfaces, radial midplane profiles of B_{tor} , B_{pol} , pressure p , toroidal plasma current j_{tor} and safety factor q .

does not imply the existence of a thermodynamic equilibrium state. In the contrary, because of the presence of strong heat flows into and out of the plasma, fusion plasmas are always open thermodynamic systems, far from thermodynamic equilibrium).

The poloidal magnetic field components B_R , B_z can be expressed by the derivatives of the poloidal magnetic flux ψ through a circle co-axial with the torus axis $B_R = -(1/2\pi R)\partial\psi/\partial z$, $B_z = (1/2\pi R)\partial\psi/\partial R$. From Ampere's law (toroidal derivatives vanish due to axi-symmetry) the toroidal current density can be expressed as

$$j_{tor} = -\frac{1}{2\pi\mu_0} \left[\frac{1}{R} \frac{\partial^2 \psi}{\partial z^2} + \frac{\partial}{\partial R} \left(\frac{1}{R} \frac{\partial \psi}{\partial R} \right) \right] \equiv -\frac{1}{2\pi\mu_0} \frac{1}{R} \Delta^* \psi. \quad (11.1)$$

The magnetic field lines span nested toroidal surfaces of constant plasma pressure which can be labelled with the flux ψ (*flux surfaces*). Expressing the toroidal field B_t by the *poloidal* current I_{pol} within a flux surface, $(\partial(RB_t)/\partial R) = (\mu_0/2\pi) (\partial(I_{pol})/\partial R)$, and using Ampere's law again, one obtains the famous Grad-Shafranov-Schlüter equation

$$\Delta^* \psi = -4\pi^2 \mu_0 R^2 p' - \mu_0^2 I_{pol} I'_{pol}, \quad (11.2)$$

where the prime ($'$) denotes the derivative with respect to ψ . Solutions of (11.2) describe the magnetic flux and toroidal current density for an axisymmetric magnetic equilibrium configuration characterized by toroidal current density $j_{tor}(R, z)$ (which contains plasma currents and external shaping coil currents), plasma pressure gradient p' and poloidal current profile I_{pol} .

Fig. 11.6 left shows (in a poloidal cross-section) contours of constant magnetic flux for an experimental magnetic equilibrium of a plasma in ASDEX Upgrade. The toroidal plasma

current generates poloidal magnetic flux which, in superposition with the flux generated by the poloidal field coils, defines a region of magnetic surfaces which are closed in themselves and have no intersection with a material wall. The boundary of this region (*last closed flux surface*, or *separatrix*) is highlighted in Fig. 11.6 left. Measurements of the magnetic flux are taken at many positions inside the vacuum vessel to reconstruct the experimental magnetic surfaces using (11.2). The shape of these surfaces can be controlled (feed-forward or feed-back) by the currents in the shaping coils.

Fig. 11.6 right shows a close-up of the vacuum vessel, the region of closed magnetic surfaces and profiles of the toroidal magnetic field B_{tor} , poloidal magnetic field $B_{pol} = (B_R^2 + B_z^2)^{1/2}$, plasma pressure p and toroidal current density j_{tor} along a horizontal section across the plasma center (indicated in the figure). Magnetic field lines follow a helical path on flux surfaces around the torus. A field line returns to a given poloidal position at a certain increment of the toroidal angle $\Delta\Phi$, which depends on B_t and B_{pol} along the field line. The *safety factor* $q = \Delta\Phi/2\pi$ counts how often a field line passes toroidally around the torus before it returns to the same poloidal position. For cylindrical cross-section and $R/a \gg 1$, $q(r)$ can be approximated as $q = (r/R)(B_t/B_{pol})$. The profile of q is also shown in Fig. 11.6 right. For a sufficiently peaked j_{tor} profile, q rises monotonically from the plasma center to the edge. This is typically the case if the plasma current is driven entirely by the induced loop voltage so that j_{tor} is determined by the radial resistivity profile. For irrational q , field lines span the entire flux surface. For rational q , field lines join up into themselves after a finite number of passes around the torus, so that helical perturbations can easily occur. Magnetic flux surfaces with integer or low rational q values are important for the stability of tokamak plasmas. In particular, q at the plasma edge has to be above a value of two to avoid a large scale disruptive instability (see sec. 11.2.3). This defines a minimum toroidal field for any given plasma current. The safety factor in the plasma center is usually clamped to values near or above unity by sawtooth oscillations (see sec. 11.2.3) or other types of magnetohydrodynamic activity.

11.1.5 Plasma heating

In order to balance heat losses from the plasma, a continuous heat source must exist to maintain the temperatures needed for fusion reactions to occur.

A heat source inherent for tokamaks is the Joule heat ηj^2 which originates from the plasma current and the low but finite resistivity η of a high temperature plasma (*Ohmic heating*). The plasma resistivity is proportional to $T_e^{-3/2}$ so that the Ohmic heating power reduces with increasing plasma temperatures, while the heat loss increases with increasing temperatures and their gradients. In practice Ohmic heating is limited to temperatures up to about 1 500 eV, significantly below the temperatures needed to initiate fusion reactions. Neutral particle injection (NBI) or absorption of radio-frequency waves can be used to heat the plasma to temperatures significantly higher than those achieved with Ohmic heating.

For NBI heating, a beam of ionized deuterium is produced and accelerated in an electric field. Typical particle energies are 60–140 keV and beam currents range up to 100 A per NBI source. The deuterium beam is guided through a neutralizer chamber filled with neutral deuterium gas. Charge exchange reactions occur for 60–90% of the ions (depending on beam energy).

Particles not neutralized are deflected by a magnetic field towards the wall of the chamber where they recombine and are pumped out. The fast neutral particles can pass through the tokamak periphery without being affected by the magnetic field. In the plasma, the neutral beam particles undergo charge exchange reactions which produce a population of fast ions. The plasma is heated by collisions of the fast ions with the thermal particles.

Radio frequency heating makes use of resonances in the dispersion relation for waves in plasmas, in particular resonances with the cyclotron motion of ions and electrons (*cyclotron resonance*). Electromagnetic waves are absorbed at the cyclotron resonance (and their harmonics) and the wave energy is converted into increased kinetic energy perpendicular to the magnetic field of the resonant particles. Collisions lead to thermalization of the energy distribution at increased temperature. Due to the different mass of ions and electrons different frequencies must be used. While for ion cyclotron heating (ICRH) frequencies in the range of several ten MHz are used, electron cyclotron resonance heating (ECRH) requires frequencies of the order of 100 GHz. ICRH heating systems typically use vacuum tube amplifiers, coaxial conductors and loop antennas mounted inside the vacuum vessel close to the plasma surface. ECRH power is generated by strong electron beams in a magnetic field with properly tuned magnetic fields (in devices called *gyrotrons*). The microwave power is transmitted in oversized waveguides or by quasi-optical imaging. Antennas are steerable mirrors which launch Gaussian beams that can be directed for variable power deposition positions.

11.1.6 Anatomy of a tokamak plasma

Figure 11.7 left shows for a typical tokamak discharge (example taken from the ASDEX Upgrade tokamak) several measurements as a function of time. After start-up of the discharge, the plasma current I_p is ramped up within one second to its flat-top value of 1 MA. The discharge is terminated after 6.5 s by a ramp down of I_p . The same panel shows I_{OH} , the current in the central solenoid needed to achieve the requested plasma current: Before the start of the pulse, I_{OH} is set to 40 kA. Initially, a large loop voltage (second panel) is needed for break-down. This is achieved with a fast step in I_{OH} . During current ramp up, large flux is consumed due to the inductance of the plasma. During current flat top, flux consumption depends on plasma resistivity. In our example, neutral beams are injected during two time intervals (1.5–3 s and 5–6.5 s) resulting in an increase of plasma temperature and consequently a decrease of resistivity. This results in the measured reduction of the loop voltage and reduced ramp rate of I_{OH} during the time intervals with auxiliary heating.

Details of the start-up phase of this discharge are shown in Fig. 11.7 right. A carefully dosed amount of deuterium gas (*gas prefill*) is introduced into the vacuum chamber and then a fast step of I_{OH} is applied to generate a large loop voltage. This results in ionisation of the neutral gas. The resulting free electrons are accelerated and help to further ionize the neutral gas. The plasma density (bottom panel) rises along with the plasma current. After about $t = 100$ ms, the plasma current is feedback-controlled and slowly ramped up. After $t = 200$ ms the plasma density is also feed-back controlled with the gas fuelling rate.

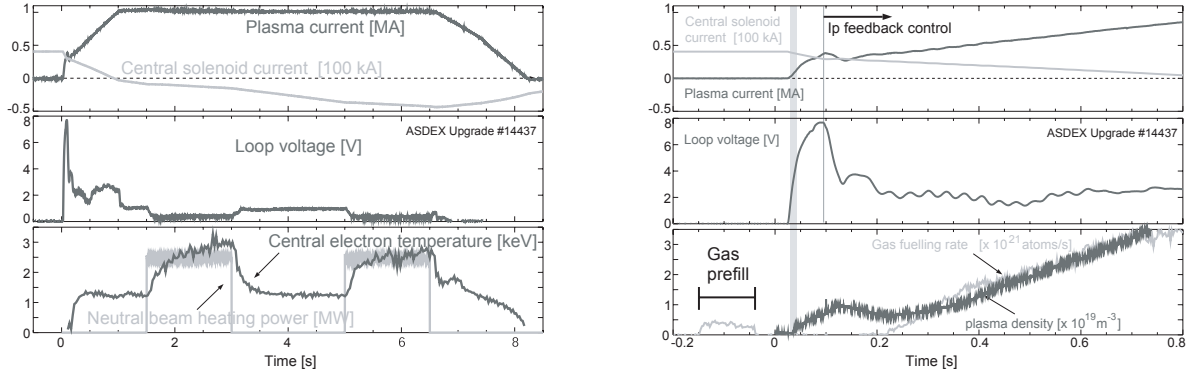


Figure 11.7: Left: Measured time traces for a tokamak plasma during start and plasma current ramp-up phase, flat-top phase, and ramp-down phase. Right: Start-up phase of a tokamak plasma: A high loop voltage, generated by a fast central solenoid current ramp, ionises an initial neutral gas prefill.

11.2 Experimental results

11.2.1 Confinement and transport

Confinement time

One of the main requirements for a nuclear fusion plasma is a sufficiently large *energy confinement time*, defined as $\tau_E = W_{th}/P_{heat}$, where W_{th} is the thermal stored energy and P_{heat} the heating power required to obtain this energy. The confinement time is a major figure of merit for tokamak performance and is relatively easy to measure. The heating power is the sum of ohmic heating ($V_{loop} \times I_p$) and auxiliary heating power, plus alpha particle power (small in today's tokamaks). The thermal stored energy can be obtained from density and temperature profiles, or approximated by the total stored energy (e.g. from diamagnetic measurements), corrected for the measured or estimated energy of fast (non-thermal) particles, which mainly depends on heating method, heating power and plasma density.

Fig. 11.8 shows a scaling of the confinement time (experimental vs. predicted τ_E) for a relatively large number of tokamak experiments with different plasma size. This scaling, termed IPB98(y), is used to predict the performance of the planned International Thermonuclear Experimental Reactor (ITER) from present-day machines and has the form

$$\tau_{E,IPB98(y)} = 0.0365 I_p^{0.97} B_t^{0.08} P_{heat}^{-0.63} n_e^{0.41} M^{0.2} R^{1.93} \epsilon^{0.23} \kappa^{0.67}, \quad (11.3)$$

$\tau_{E,IPB98(y)}$ is the predicted confinement time in seconds, I_p plasma current in MA, B_t toroidal magnetic field in T, P_{heat} auxiliary heating power in MW, n_e line averaged electron density (10^{19} m^{-3}), M ion mass number, R major radius (m), $\epsilon = a/R$, κ is the elongation (ratio of vertical and horizontal minor plasma radius). Energy confinement depends most strongly on plasma current I_p , plasma size (radius R) and elongation κ .

The experimental data base spans more than two orders of magnitude of τ_E in similar plasma types (High confinement mode, see sec. 11.2.2 below). ITER is designed for $\tau_E \approx 6$ s, which

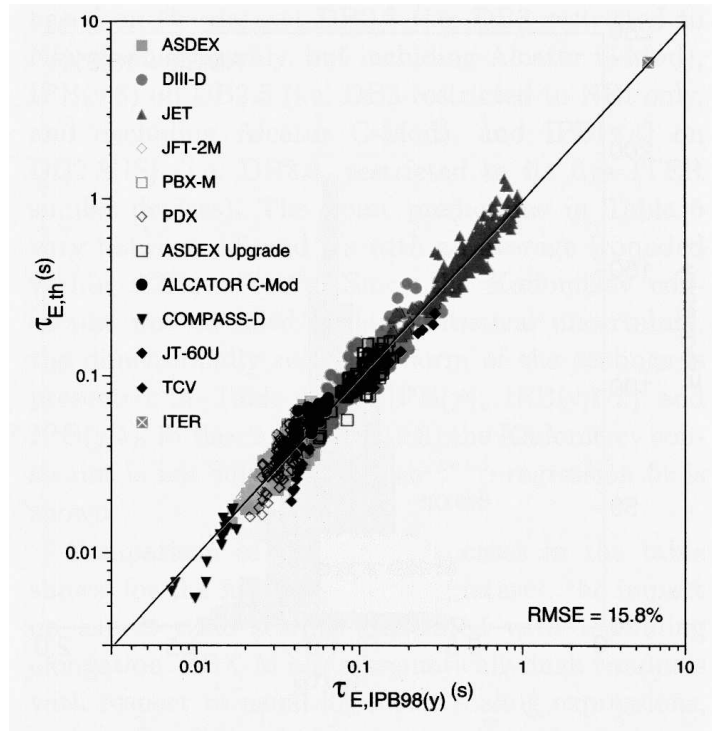


Figure 11.8: Energy confinement time scaling of the International confinement database for a large set of tokamaks.

is less than a factor of ten above the largest confinement times obtained in tokamaks to date. Naturally there are uncertainties with such extrapolations, originating from variance in the data base, and possible physics regime changes from current experimental parameters to a reactor-size plasma. It is therefore interesting to study the physics of heat transport in more detail.

Heat diffusion

Heat transport can be expressed in terms of a local power balance for the electron and ion heat conduction channels

$$q_{\perp e,i} = -n_{e,i} \chi_{e,i} \text{grad} T_{e,i} \pm Q_{e,i}, \quad (11.4)$$

where $\chi_{e,i}$ is the *heat diffusivity*, $n_{e,i}$ the density, $\text{grad} T_{e,i}$ the temperature gradient and $q_{\perp e,i}$ the heat flux of the considered species (electrons or ions). $Q_{e,i}$ is the collisional heat transfer between electrons and ions.

For *random walk* radial diffusion dominated by Coulomb collisions, one expects a diffusivity of the order of $\chi_{e,i} \approx \Delta x^2 / \tau_{e,i}$ where Δx is the radial step size (gyroradius for classical diffusion, banana orbit width for neo-classical diffusion in a toroidal plasma) and $\tau_{e,i}$ is the electron-ion collision time. However, it is found that the actual diffusivity in tokamak plasmas is normally significantly larger than the neo-classical value. In addition, heat diffusivity increases with increased heat flux. Historically, this behaviour has been termed *anomalous* transport and it is now known to originate from small-scale turbulence which creates fluctuating poloidal

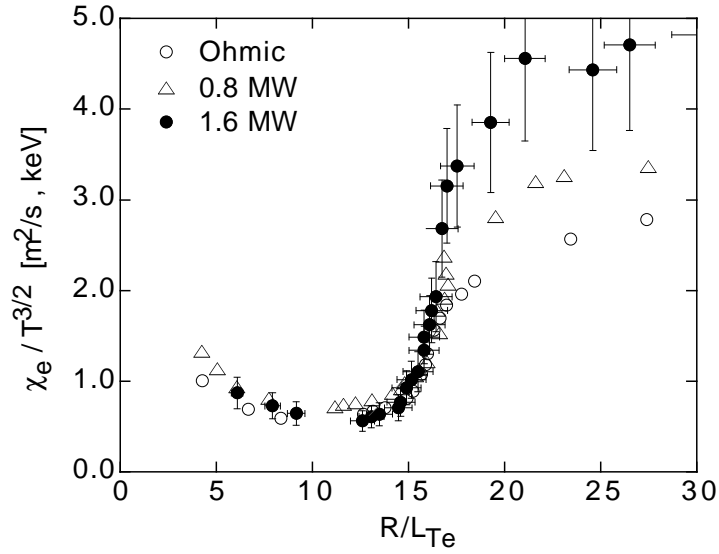


Figure 11.9: Normalized electron heat diffusivity $\chi_e/T_e^{3/2}$, measured as a function of normalized electron temperature gradient $(\nabla T_e)R/T_e = R/L_{T_e}$.

electrical fields. As a result, fluctuating radial $E \times B$ drifts occur which exchange plasma between hot and cold regions.

Various instability mechanisms exist that can drive transport-relevant turbulence. A common feature is that destabilization occurs if the temperature gradient length $L_T = T/\nabla T$ drops below a critical threshold $L_{T,crit}$. The heat diffusivity strongly depends on $L_T/L_{T,crit}$ and scales with $T^{3/2}$ (*gyro-Bohm* dependence). This behaviour is indeed found in experiments, as shown for electron by measurements of χ in ASDEX Upgrade (evaluated using (11.4)). Fig. 11.9 is a plot of electron heat diffusivity χ_e (normalised by $T_e^{3/2}$) as a function of inverse gradient length $R/L_{T_e} = R\nabla T_e/T_e$ (R is the major radius at midplane on the low-field side). Three different levels of electron heating power are employed: Ohmic heating and ECRH with 0.8 MW and 1.6 MW RF power. The data points correspond to measurements at different radial locations, central points have low heat flux and low inverse gradient length R/L_T (lower left), plasma edge data appears at high diffusivity (upper right corner of the diagram). The experiment shows the predicted increase of χ_e at $R/L_T \approx 15$. Furthermore, data with different heating power (and different temperature) is described by the same normalisation of χ_e by $T_e^{3/2}$.

The existence of a critical threshold for χ_e above which heat transport increases strongly leads to the formation of *canonical* temperature profiles, where L_T is near $L_{T,crit}$, almost independently of the heating power. This is the origin of the strong deterioration of confinement time τ_E with heating power (11.3). For fixed gradient length, the central temperature depends strongly on the edge temperature, which is limited by edge instabilities (see sec. 11.2.2 and sec. 11.2.3 below). Consequently, high edge pressure and high edge temperature help to achieve high stored energy in the core of a tokamak plasma.

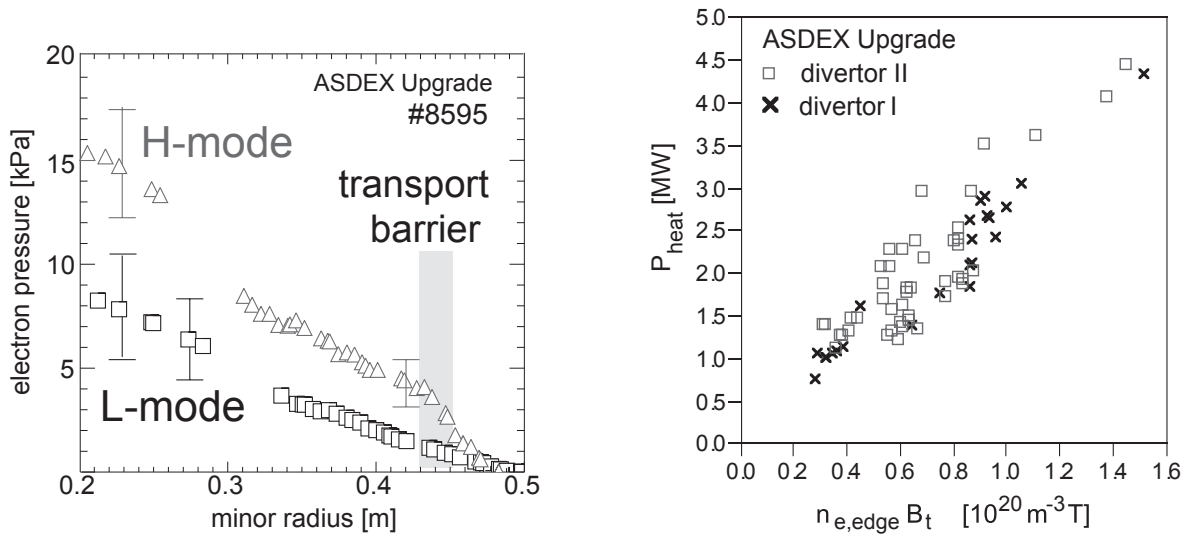


Figure 11.10: Left: Comparison of electron pressure profiles in L-mode and H-mode.
Right: Experimental power threshold for barrier formation.

11.2.2 Confinement improvement

High-confinement mode

The level of radial particle and energy transport found in tokamaks is mainly caused by small-scale turbulence. Nevertheless, suppression of this turbulence can be observed in specific cases, leading to a reduction of the particle and heat diffusivity in a restricted plasma volume. This behaviour is often called the formation of a *transport barrier*. With the introduction of a divertor, spontaneous formation of a transport barrier at the plasma edge has been found in the ASDEX tokamak (Garching, 1984). This regime has been termed the *high-confinement mode (H-mode)*. The effect of the edge transport barrier is demonstrated in Fig. 11.10 left for a discharge of the ASDEX Upgrade tokamak before and after transition to H-mode. Since the discovery of H-mode, the plasma state before the transition to H-mode is usually termed *L-mode (low confinement mode)*. In H-mode, the pressure gradient steepens up at the plasma edge (r between 0.43–0.45 m for the profile shown), giving rise to a pressure *pedestal*, i.e. additional stored energy in the plasma from the pressure offset at the edge. The temperature just inside the transport barrier is significantly higher than in L-mode, allowing (for the same gradient length $L_T = T/\nabla T$) a higher plasma core temperature gradient than in L-mode, resulting in an additional confinement benefit.

The condition to enter High-confinement mode is a minimum heating power across the plasma boundary. Empirically, the threshold power depends on the product of plasma edge density and magnetic field, $P_{\text{heat}} \propto n_{e,\text{edge}} \times B_t$. Fig. 11.10 right illustrates this dependence for the case of two divertor geometries in ASDEX Upgrade. Little influence of the divertor geometry (and other parameters such as heating method) is found.

A typical time history around the transition to H-mode is shown in Fig. 11.11 left. The heating power is being stepped up to just above the H-mode threshold at $t = 1.65$ s. Large heat flux in

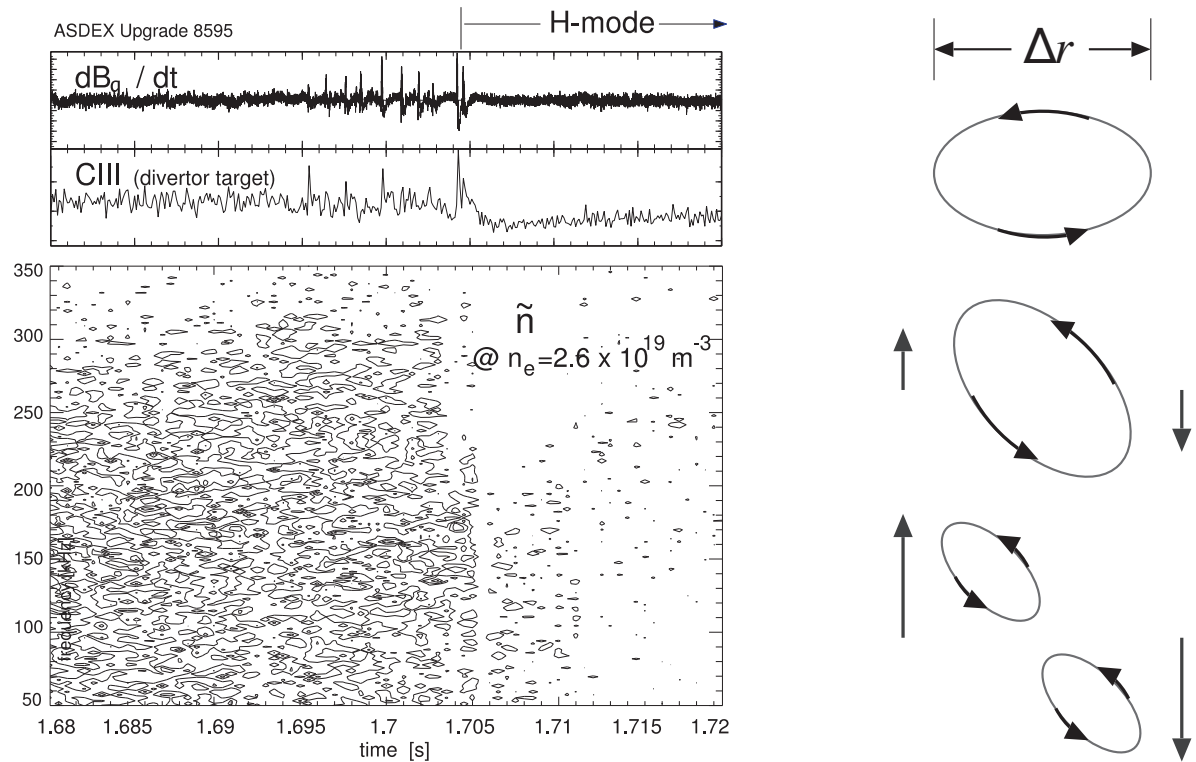


Figure 11.11: Left: Fluctuations are reduced at the transition from L-mode to H-mode.

Right: H-mode model: $E \times B$ shear flow reduces radial size of turbulent eddies.

L-mode leads to turbulence that can be seen as broad-band density fluctuations in the \tilde{n} spectrogram contour plot. Transport occurs in bursts that appear in the divertor heat flux (C-III spectral line intensity) and main plasma magnetic probes (\dot{B}). After the transition to H-mode (at $t = 1.705$ s in the example), the level of density fluctuations is much reduced and the C-III signal in the divertor drops.

While in L-mode additional heating power creates steeper gradients and thus generates more free energy to drive turbulence and enhanced losses, it can also trigger a transition to H-mode, a self-organising process that results in a bifurcation to a state of reduced transport. This transition to H-mode is accompanied with the creation of a radial electrical field gradient, corresponding to sheared rotation of the centers of the particle gyro-motion. It is believed that de-correlation of turbulent $E \times B$ convection cells by sufficiently fast sheared rotation is the origin of the transport reduction (cf. cartoon Fig. 11.11 right). However, although a number of possible mechanisms has been proposed the physics that drives the radial electrical field is still unknown and subject to ongoing research effort.

Internal transport barriers

Transport barriers can exist not only at the plasma edge, but also in the plasma core, causing steep temperature and/or density profiles, thereby increasing the central pressure. *Internal*

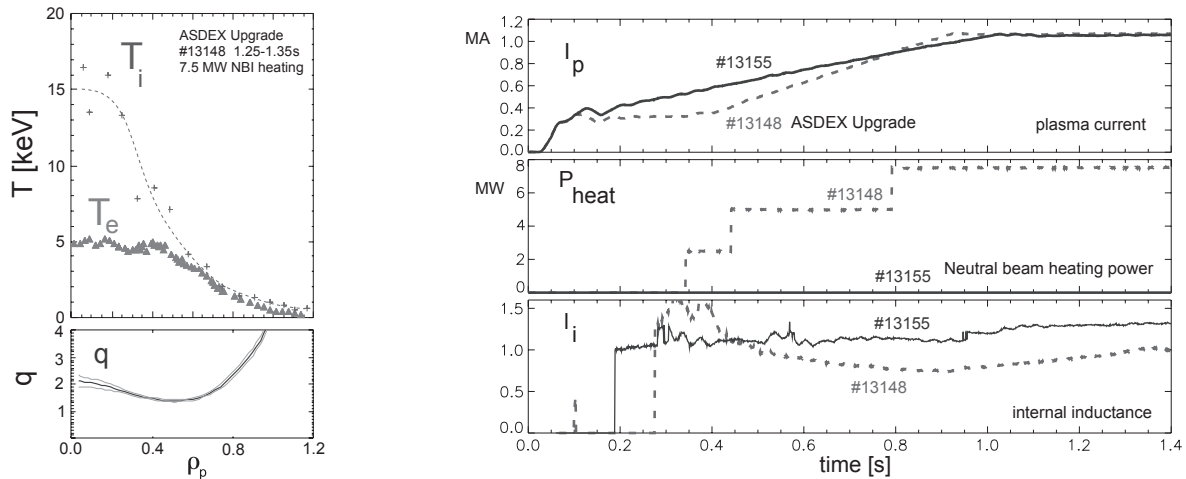


Figure 11.12: Internal transport barrier example:

Left: Profiles of T_i , T_e and safety factor q .

Right: Comparison of discharges with (13148) and without (13155): Early heating during the current ramp leads to broader current profile as seen by a reduced value of l_i .

transport barriers (ITB) arise from an influence of the magnetic shear $s = (r/q) dq/dr$ on the growth of micro-instabilities and thereby the heat diffusivity. In conventional tokamak plasmas without ITB, q increases monotonically from the center towards the edge, i.e. the magnetic shear is positive across the entire plasma radius. It is observed that heat transport can be reduced at low or negative magnetic shear.

Fig. 11.12 left shows profiles of the electron and ion temperature and the safety factor q in a discharge with ITB in the ASDEX Upgrade tokamak. The q profile is flat or slightly reversed inside a normalized radius of $\rho = 0.6$. A strong ion temperature gradient is maintained around $\rho = 0.4$, leading to a central ion temperature of 15 keV. This temperature, obtained in a tokamak much smaller than an envisaged fusion reactor, is near the optimum temperature for D-T fusion reactions. Fig. 11.12 right shows how this result is achieved. A conventional plasma (shot #13155) is compared with an ITB discharge (#13148). In the ITB pulse, heating power is applied early in the plasma current ramp, resulting in higher T_e . Due to the increased resistive skin time the initial flat or slightly hollow plasma current profile remains *frozen* for the duration of the experiment. This is seen by the slow evolution of the *internal inductance* l_i which indicates by its lower value after $t = 0.45$ s a broader (less peaked) current profile.

The advanced tokamak

For truly stationary tokamak operation the plasma current has to be driven entirely non-inductively, for example by the bootstrap effect due to the pressure gradient in the plasma. This leads to the interesting concept of the *Advanced Tokamak*, where the bootstrap current profile maintains the low or reversed shear profile required for the transport reduction which causes the ITB. Fig. 11.13 compares profiles of the pressure, toroidal current density and safety factor q (assuming pure ohmic or pure bootstrap current) for both a *conventional* (non-ITB) and an ITB plasma.

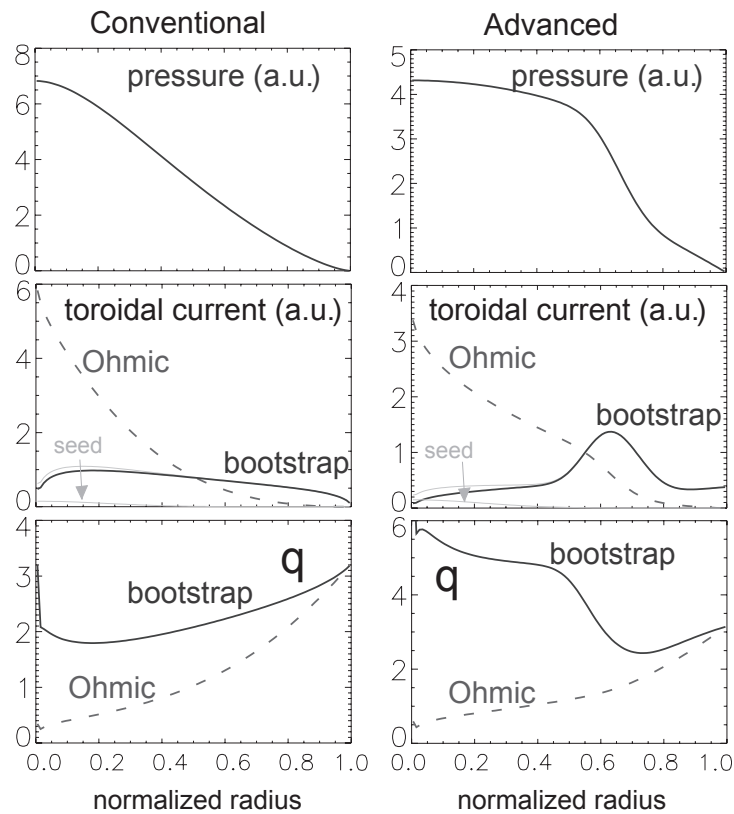


Figure 11.13: Profiles of plasma pressure p , current density j and safety factor q comparing conventional and advanced scenarios. A conventional plasma has a monotonously rising q profile. Flat or reversed reversed q profile can lead to a transport barrier. In an ideal advanced scenario, the resulting steep pressure gradient creates a bootstrap current that maintains the q -profile non-inductively in steady state. Ohmic and bootstrap contributions to j and q are shown separately.

In the conventional scenario the ohmic (inductively driven) current dominates. The ohmic current density profile is fixed by the conductivity (electron temperature) profile. A sufficiently strong transport barrier can, in principle, sustain a reversed shear profile. The strong pressure gradient produced by the transport reduction creates a strong off-axis bootstrap current. The resulting non-monotonic current profile maintains the weak or negative magnetic shear profile that allows to sustain the transport barrier. A tokamak reactor with an ITB and this type of *self-generated* plasma current could be built smaller than a conventional tokamak and would allow true steady-state operation. A crucial condition is the alignment of the reversed shear region with the region of actual strong pressure gradient, which if not matched, leads to rapid changes of the radial position of the transport barrier. A (small) current profile correction can be applied non-inductively by external current drive techniques, e.g. by electron cyclotron or lower hybrid wave heating with toroidal component of the wave vector. Advanced tokamak scenarios with a variety of current drive methods are an important topic in most current tokamak research programs.

11.2.3 Stability and operational limits

Instability occurs if a plasma perturbation amplifies itself and grows until the plasma configuration is severely modified. Free energy sources for instability growth arise for instance from large gradients of pressure and currents present in a fusion plasma. Many instabilities involve displacements of magnetic surfaces (*MHD instabilities*), but also other types of instabilities exist, for example radiation instability originating from increased radiated power with decreasing temperatures. MHD instabilities are distinguished by their scale: Micro-instabilities occur on the gyro-radius scale and are relevant for radial particle and heat transport. Macroscopic instabilities affect the plasma on the scale of the plasma dimensions and can have large effects on confinement or even terminate a plasma discharge. In toroidal geometry one can characterize unstable modes by their integer toroidal (n) and poloidal (m) mode numbers. Most macroscopic MHD modes can become unstable only at *resonant* surfaces, i.e. magnetic surfaces where $q = m/n$, and n and m are small numbers. At finite aspect ratio, modes with different poloidal mode number m couple, giving rise to complex mode number spectra.

Instabilities are important as they define the accessible plasma parameter range for stable tokamak operation. Subsequently, we discuss the basic tokamak operation range and examine several important types of instabilities and their effects.

Tokamak operational limits

For stable tokamak operation, there are upper bounds for the plasma current and the plasma density. Fig. 11.14 shows a schematic diagram of the accessible parameter range in a plot of $1/q_a$, the reciprocal edge safety factor vs. $\bar{n}_e R/B_t$ (known as *Hugill diagram*). We note that $1/q_a \propto I_p/B_t$, so the vertical axis is proportional to the plasma current. For $1/q_a \rightarrow 0.5$ the $q = 2$ surface approaches the plasma edge and a $m = 2, n = 1$ *kink* instability occurs. This is a fast-growing large scale ideal MHD mode which leads to a quick termination of the plasma discharge.

Empirically, a density limit is found which is proportional to the plasma current density. In the Hugill diagram (see Fig. 11.14) this is expressed by an upper bound of the line averaged density $\bar{n}_e R/B_t \propto I_p/aB_t$ or $\bar{n}_e \propto I_p/aR \propto I_p/a^2$ (for constant aspect ratio R/a). The physics of the density limit is quite complex, and some of its aspects are outlined in the next section.

The accessible operation range of tokamaks is bounded by these limits. High plasma density is desirable for good performance and to facilitate power exhaust with a divertor. For a tokamak reactor it is therefore desirable to operate at highest possible plasma current density. The maximum value of B_t is defined by technical limitations for toroidal field coil system. Hence, the $q = 2$ limit sets an upper bound to I_p . From these considerations, the optimum operation point is in the upper right corner of the Hugill plot.

Density limit disruptions

The density limit in tokamaks can assume quite complex phenomenology. A typical history of a density limit in a discharge with only ohmic heating is shown in Fig. 11.15 left. In this

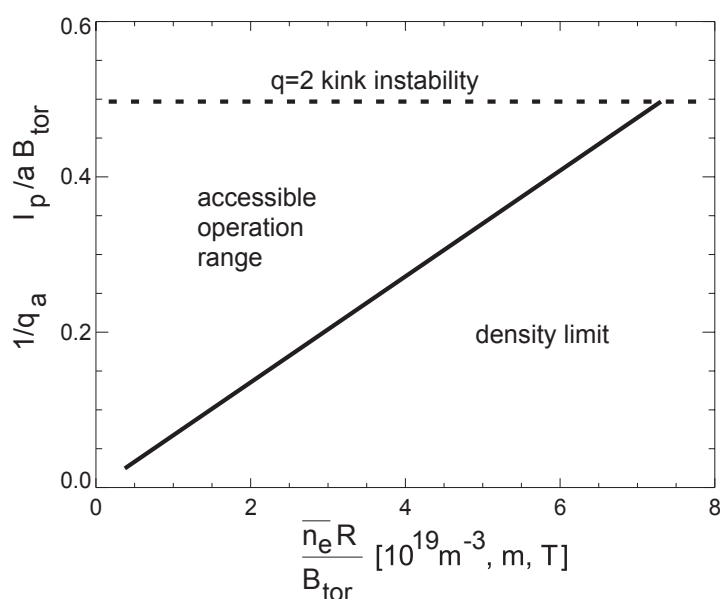


Figure 11.14: Hugill-Diagram showing the basic tokamak operational range. An upper limit to the plasma current is given by the onset of $n = 1, m = 2$ kink instability for $q = 2$ at the plasma edge. A density limit exists at $\bar{n}_e \propto B_t / (Rq) \propto I_p / a^2$.

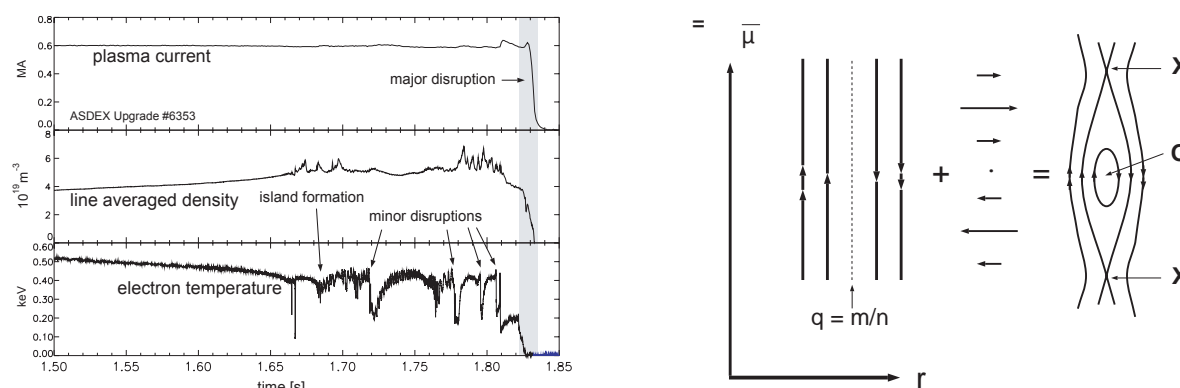


Figure 11.15: Left: History of a density limit disruption. With increasing density the plasma edge is cooled and magnetic islands grow. Finally a *major* disruption occurs with thermal and plasma current quench. Right: Formation of magnetic islands by superposition of an unperturbed sheared magnetic field and a helical B_r field.

experiment, the line averaged density is slowly raised by gas puffing. The edge electron temperature (bottom trace) reduces with increasing density. When the edge has sufficiently cooled down, *tearing mode* instability occurs which results in the formation of magnetic islands by reconnection.

Fig. 11.15 right shows the structure of magnetic islands (in helical and radial coordinates). Magnetic islands result from helically periodical perturbation currents which give rise to a radial magnetic field with helical symmetry. They can grow only at resonant rational surfaces,

i.e. where $q = m/n$. At the density limit, several islands with $m/n = 4/1, 3/1$ and $2/1$ appear. Since heat transport is faster along magnetic field lines than perpendicular to the field, radial heat flux effectively bypasses the island interior (*O-point*) and concentrates near the X-point. Consequently the temperature is flat inside the island, while near the X-point a gradient is maintained. Plasma rotation makes this modulation visible as an oscillation of the temperature (bottom panel in Fig. 11.15 left).

After islands have grown to a certain radial extent, fast confinement loss events (*minor disruptions*) occur, which lead to a flattening of the temperature profile around a resonant surface. The volume inside this surface cools down and islands on inner resonant surfaces begin to grow. After several minor disruptions, several island chains can exist simultaneously and the rotation velocity reduces to zero (*mode locking*). A *major disruption* occurs, with a fast loss of plasma energy (*energy quench*) and subsequent quench of the plasma current. Because of the inductivity of the plasma, the plasma current quench results in *halo currents* in the vacuum vessel wall, which lead to very large forces on the material structure of a tokamak. The vacuum vessel and the support structure of all magnetic coils must be designed to withstand these forces.

Nevertheless, the disruptive termination of a plasma can be avoided or at least mitigated. If the density is kept below the density limit, the phenomenology described above does not occur. If the density limit is encountered, one can delay tearing mode growth by localized electron cyclotron current drive which replaces the missing helical current in the O-point. Several techniques have been successfully applied to delay or avoid mode locking. Finally, during a disruption the kinetic and magnetic energy in the plasma can be disposed by radiation from injected impurities leading to a more even distribution of energy deposition on the walls, and a reduction of halo currents.

The physics mechanism at the onset of the density limit are still under investigation. Several observations can be made depending on the confinement regime: Increase of radial transport at the edge leading to edge cooling and breakdown of the H-mode barrier; *detachment* of the divertor, i.e. loss of the parallel pressure balance between main chamber edge and divertor due to radial momentum transfer, and formation of a poloidally asymmetric condensation instability (*MARFE*) which leads to edge cooling. Several mechanisms can drive magnetic island growth: Deformations of the current profile, and helical current perturbations due to radiation losses from the island interior or loss of the bootstrap current because of pressure profile flattening around the O-point. The interplay of these mechanisms is being studied in experiments and by complex computer simulations.

Sawtooth oscillations

In many tokamak discharge scenarios, the central temperature undergoes a characteristic oscillation: After a slow linear rise (of few to several 100 ms duration) the temperature crashes very quickly (within about 100 μ s) and the cycle repeats. This behaviour has been first observed in the central soft X-ray emissivity and has been named *sawtooth* oscillations for its peculiar time history (see Fig. 11.16 left, top panel). X-ray tomography can be used to reconstruct a two-dimensional image of the central emissivity which reveals the structure of the underlying perturbation. The lower part of Fig. 11.16 left shows the reconstructed X-ray emissivity

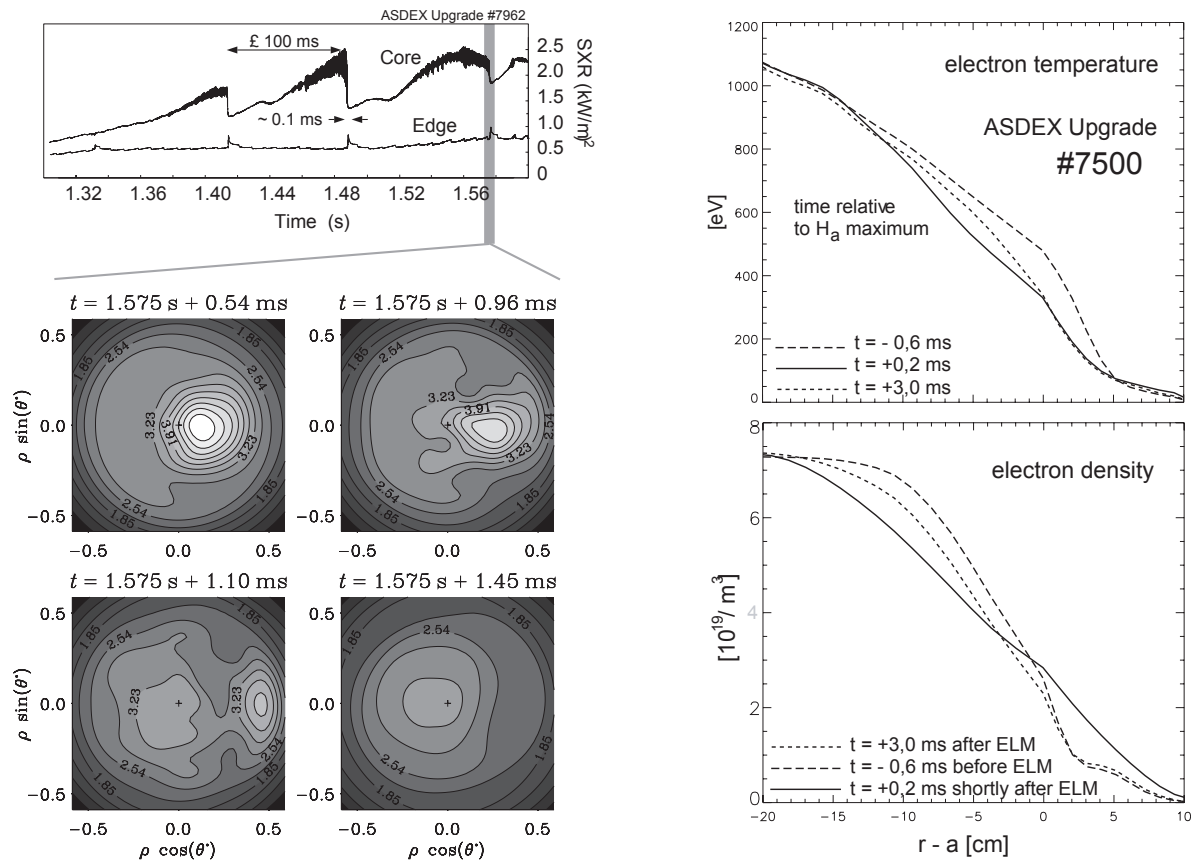


Figure 11.16: Left: Sawtooth oscillations as seen by soft X-ray measurements. Bottom right: Tomographic reconstruction of soft X-ray emissivity before, during and after the sawtooth crash. Right: Edge electron temperature and density profiles (A) before an ELM, (B) shortly after an ELM, (C) in the recovery phase in between ELMs.

for four phases before, during and after the sawtooth crash. In between sawtooth crashes the plasma center is heated and the central temperature increases. If $q(0) < 1$, an $n = 1, m = 1$ kink mode is destabilised. Because of good radial confinement the interior of this region is hot ($t = +0.54 \text{ ms}$). Because of the toroidal plasma rotation, the difference of temperatures inside and outside the kink structure appears as fast oscillations (black areas) in the X-ray signals (see Fig. 11.16 left top). With increasing central current density the structure becomes unstable and reconnection sets in ($t = +0.96 \text{ ms}$ and $t = +1.1 \text{ ms}$). Hot plasma streams into a larger volume and the peak temperature and emissivity are reduced, but the 1/1 mode re-appears and the cycle starts over ($t = +1.45 \text{ ms}$).

Fig. 11.17 left schematically shows the temporal evolution of the profiles of the central current density and associated safety factor q . In between sawtooth crashes, $j(0)$ (and $T_e(0)$) both rise, resulting in a drop of central $q(1)$. Eventually $q(0)$ falls significantly below unity (2). A quick reconnection event flattens the central j (and T_e) profile and q rises again above one; the cycle starts over.

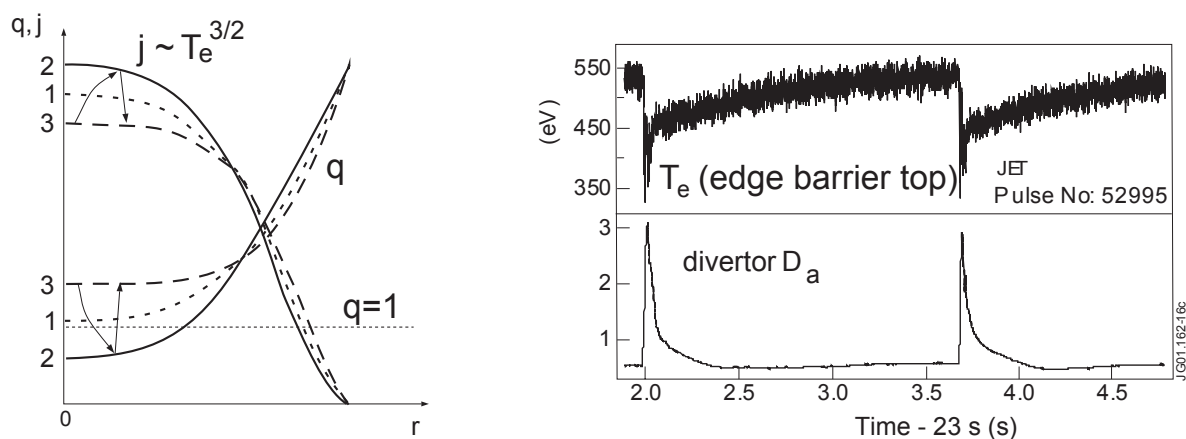


Figure 11.17: Left: Profiles of j during a sawtooth cycle.

Right: Time traces of edge electron temperature and divertor D_α showing repetitive losses at the edge and increased recycling during ELMs.

Edge localized modes

Edge Localized Modes (ELMs) are instabilities that occur in H-mode where a transport barrier leads to a steep pressure gradient at the plasma edge. The edge temperature (shown in Fig. 11.17 right, top time trace) and edge density (not shown) increase until sudden heat and particle losses occur. These losses can be detected as a characteristic spike in the D_α line radiation intensity in the divertor due to increasing recycling particle flux and increasing ionisation because of the heat loss (Fig. 11.17 right, bottom trace).

The particle and heat losses are also seen as a sudden partial erosion of the edge temperature and density profiles (see Fig. 11.16 right). Steep profiles (A) in the edge barrier region before ELMs flatten within few $100 \mu\text{s}$ (B) and recover slowly (C) by radial heat and particle transport from within the plasma core until the maximum pressure is reached again and a new ELM occurs. This results in a characteristic oscillation cycle which repeats itself many times, often hundreds of times in one plasma discharge. Along with hydrogen, also impurities are lost which otherwise tend to accumulate in the main plasma due to the very slow out-diffusion across the H-mode transport barrier. While this feature of ELMs allows for stationary H-mode plasmas, the fast energy loss during the collapse phase can present a large peak power load to the divertor structure which can cause significant erosion of the divertor structure. For this reason, ELMs with small losses occurring at a high frequency are preferred over slow and large ELMs.

The precise physical origin of ELMs and the nature of the instability are still under investigation. The phase of enhanced transport during ELMs is characterized by a broad spectrum of MHD modes with a duration of about $100 \mu\text{s}$. ELMs set in near values of the total edge pressure gradient where one expects *ballooning* instability, i.e. short wavelength modes driven by the pressure gradient at the magnetic low field side where the curvature of the magnetic field is not stabilizing. Fig. 11.18 left shows a stability diagram for ballooning modes. The attainable normalized pressure gradient (first stability limit) $\alpha = 2\mu_0 R (\nabla p) q_a^2 / B_i^2$ increases with magnetic shear $s = (r/q) dq/dr$. Interestingly, at low shear a second stable regime can exist. Low

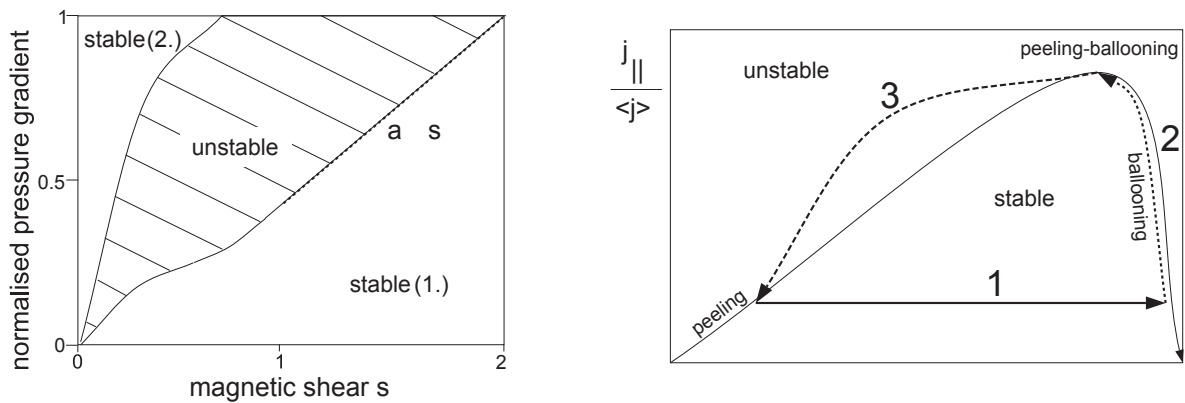


Figure 11.18: Left: Stability diagram for ballooning modes. Stability occurs for high magnetic shear (*first* stable regime) or very low magnetic shear (*second* stable regime). Access to the second stable regime is often blocked by an unstable region as shown.

Right: Schematic model for the ELM cycle: Different time scales for evolution of edge pressure gradient α and edge current density j_{\parallel} result in several stability limitations during the cycle (see text).

local shear at the magnetic low field side can be produced by suitable plasma shaping or by high edge current density.

Ballooning modes are typically small scale modes, most unstable for high mode numbers and thus do not explain the large perturbations associated with ELMs. Furthermore, it is often observed experimentally that the pressure gradient saturates well before an ELM occurs indicating a more complex physics process involved. Recent models for ELMs consider a variety of instabilities, including modes driven by the large toroidal current gradient at the plasma edge. A large edge current density originates from the bootstrap current driven by the large edge pressure gradient in the H-mode transport barrier. In this picture the ELM cycle can be described as follows (see Fig. 11.18 right).

In between ELMs (1) the (normalized) pressure gradient α rises on the transport time scale (few ms for heat and particle diffusion over a few cm) until the ballooning pressure gradient limit is reached. Small scale instability leads to enhanced losses, effectively clamping the pressure gradient while the edge current density j_{\parallel} builds up within the resistive skin time (10–100 ms for the edge of current tokamaks). Ultimately the stability limit for coupled peeling (i.e. medium- n kink) and ballooning modes is reached, leading to macroscopic instability, the ELM crash (3). Pressure and current are expelled and the cycle repeats itself. At present, the ELM cycle and stability limits are qualitatively and quantitatively described. Current theoretical and experimental work focuses to understand and predict the magnitude of the ELM losses and to tailor the plasma edge in order to reliably obtain ELM types with smaller energy losses.

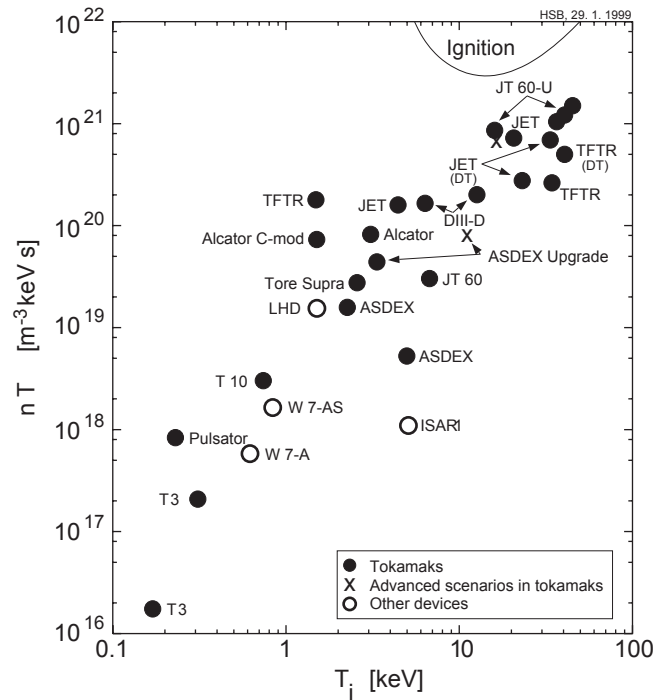


Figure 11.19: Historical performance of tokamaks and other devices, fusion triple product $nT_i\tau_E$ as a function of T_i .

11.3 Summary and outlook

Tokamaks can confine a nuclear fusion plasma with a combination of external toroidal field and poloidal magnetic field created by an internal plasma current. The plasma current can be driven inductively by a magnetic flux ramp created with a central solenoid which limits the duration of tokamak discharges. Non-inductive current drive by externally driven current or bootstrap (pressure gradient current) current can extend the pulse duration and possibly allow stationary tokamak operation. Heat and particle transport in tokamaks is usually dominated by fluctuating $E \times B$ convection from micro-instabilities which are driven by the strong temperature gradients. However, transport barriers at the plasma edge and in the plasma interior can be produced which reduce the heat diffusivity to near a level expected for collisional transport. The strong pressure and current density gradients present in a well-confined tokamak plasma can also drive a range of macroscopical instabilities, which often take the form of limit-cycle oscillations. Examples are sawtooth oscillations, associated with central $m = 1, n = 1$ kink modes that undergo fast reconnection events and a flattening of the central temperature, and Edge Localized Modes, driven by the steep pressure gradient of an edge transport barrier resulting in repetitive energy and particle losses. While these instabilities do not prevent stationary plasma operation and in some cases even help avoiding accumulation of impurities, other instabilities lead to severe confinement deterioration or even a termination of the plasma. The accessible tokamak parameter range is bounded by the conditions to avoid these instabilities.

The historical progress of nuclear fusion research can be measured by the fusion triple product $nT_i\tau_E$ which is plotted in Fig. 11.19 as a function of T_i for tokamaks and other magnetic confinement devices (mostly stellarators). The values of $nT_i\tau_E$ have increased over several orders

of magnitude in the last few decades and plasma temperatures and densities needed for a fusion reactor are obtained in contemporary tokamaks. In order to reach ignition (self-sustained plasma heating by alpha particles resulting from fusion reactions) an increase of the energy confinement time to values of several seconds is needed. This can be achieved by a larger plasma size, such as that of the planned International Thermonuclear Experimental Reactor (ITER), a tokamak with major radius $R = 6.2$, about twice as large as that of the presently largest tokamak, JET ($R = 3$ m). The step to a reactor-scale experiment with large fusion power and significant neutron production will allow to study dominant plasma heating by fast alpha particles, confinement and plasma-wall interaction, and test first-wall and low-activation structural materials needed for an integrated power plant concept. Alternative confinement concepts such as stellarators will further develop and demonstrate their attractive potential in new experiments, for example for steady state operation. Nevertheless, one can expect that tokamaks will remain at least for some foreseeable future the reliable *workhorse* and universal test-bed for magnetic fusion research they have been in the last three decades.

Further reading

General

- M. Kaufmann, *Plasmaphysik und Fusionsforschung* (in German), Teubner Verlag, Stuttgart, Leipzig, Wiesbaden 2002, ISBN 3-519-00349-X.
- F.F. Chen, *Introduction to Plasma Physics*, Vol. 1, second edition, Plenum Press, New York 1984, ISBN 0-306-41332-9.
- R.J. Goldston, P.H. Rutherford, *Introduction to Plasma Physics*, IOP Publishing, Bristol 2000, ISBN 0-750-30183-X.
- K. Miyamoto, *Plasma Physics for Nuclear Fusion*, MIT Press, Cambridge 1989, ISBN 0-262-13237-0.
- J.A. Wesson, *Tokamaks*, Oxford University Press 1987, ISBN 0-19-856328-0.

Specific topics

- F. Ryter et al., Empirical studies of electron transport, *Plasma Phys. Control. Fusion* **43** (2001) A323.
- R.J. Groebner, An emerging understanding of H-mode discharges in tokamaks, *Phys. Fluids* **B 5** (1993) 2343.
- J.W. Connor and H.R. Wilson, A review of theories of the L-H transition, *Plasma Phys. Control. Fusion* **42** (2000) R1.
- H. Zohm, Edge Localized Modes, *Plasma Phys. Control. Fusion* **38** (1996) 105.

- J.W. Connor, A review of models for ELMs, *Plasma Phys. Control. Fusion* **40** (1998) 191.
- H.R. Wilson et al., Ideal magnetohydrodynamic stability of the tokamak high-confinement edge region, *Physics of Plasmas* **6** (1999) 1925.
- J.P. Freidberg, *Ideal Magnetohydrodynamics*, Plenum Press, New York 1987, ISBN 0-306-42512-2.
- D. Biskamp, *Nonlinear Magnetohydrodynamics*, Cambridge University Press, Cambridge 1993, ISBN 0-521-59918-0.
- ITER-Team, ITER Physics Base, *Nuclear Fusion* **39** (1999) 2137-2638,
- R. Aymar et al., The ITER design, *Plasma Phys. Control. Fusion* **44** (2002) 519 and <http://www.iter.org>.
- ASDEX Upgrade: <http://www.aug.ipp.mpg.de>.

Chapter 12

Introduction to stellarator theory

Ralf Kleiber, Håkan Smith

12.1 Introduction

12.1.1 Some history

The stellarator concept was introduced in 1951 by the astrophysicist Lyman Spitzer. In order to introduce rotational transform (see sec. 12.1.2) in a toroidal configuration he proposed to twist a torus into a shape resembling the shape of the number eight (figure-eight stellarator).

Some years later the Model C Stellarator experiment was built in Princeton but was not successful: The plasma was lost very quickly. As was understood later this was mainly due to an incomplete knowledge about the behaviour of resonances in magnetic surfaces. While the Princeton stellarator experiment was still plagued by a low confinement time (a few Bohm times¹ at $T_e \approx 100$ eV) Russian scientists at the 1968 IAEA Novosibirsk conference showed that, with a confinement concept called tokamak, it was possible to achieve an electron temperature of about 1 keV for 30 Bohm times.

This historical situation resulted in the fact that tokamaks became the main line of fusion research in the world while the stellarator concept was pursued only in some places, mainly at the IPP Garching and at the University in Kyoto. Today there is a renewed interest in the stellarator concept as an alternative to the tokamak: A large stellarator of the torsatron² type (Large Helical Device (LHD)) started its operation 1998 in Japan at the NIFS. The German-EU experiment Wendelstein 7-X is being constructed in Greifswald and scheduled to start operation in 2015. Other (smaller) stellarators are in use in the USA (HSX), Spain (TJ-II) and Australia (H-1).

¹The Bohm time $\tau_B = a^2/D_B$ (a : minor radius) is defined via the Bohm diffusion coefficient $D_B = 1/16k_B T_e/(eB)$.

²The stellarator concept appears under different names, e.g. heliotron, torsatron, heliac, which mainly distinguish the way the coil systems were historically constructed. In this text we will not elaborate on this, instead we will use just the collective notion *stellarator*.

12.1.2 Some basic notions

Fig. 12.1 shows the basic torus geometry of a fusion device with the poloidal and toroidal angles ϑ and φ . The ratio $A = R/a$ of major to minor radius is called the aspect ratio.

If for a given magnetic field $\mathbf{B}(\mathbf{r})$ a function $\Psi(\mathbf{r})$ exists in a region of space such that $\mathbf{B} \cdot \nabla \Psi = 0$ then the surfaces $\Psi(\mathbf{r}) = \text{const}$ are called flux surfaces (i.e. the magnetic field is tangent to these surfaces). The existence of nested³ flux surfaces (Fig. 12.1 shows three such surfaces), at least in the main volume of the device, is an essential prerequisite for plasma confinement by a magnetic field. The innermost flux surface that is degenerated into a line is called the magnetic axis. If the equilibrium consists only of nested flux surfaces they are distinguished by a flux surface label $s \in \mathbb{R}$.

A field line on a given flux surface can be specified by a (non-periodic) function $\vartheta = f(\varphi)$. If φ increases by $2\pi n$ ($n \in \mathbb{N}$) the angle ϑ changes by an amount ϑ_n . The quantity ι defined by $\iota := \lim_{n \rightarrow \infty} \vartheta_n / (2\pi n)$ is called the rotational transform⁴ and has the same value for each field line on a given flux surface; in general ι is a function of the flux surface label. The s -derivative of the rotational transform is called shear ι' . A flux surface s_0 where the rotational transform is rational $\iota(s_0) = n/m$ ($m, n \in \mathbb{Z}$) is called a rational surface⁵. On a rational surface all field lines are closed lines while on a non-rational surface one field line fills the surface ergodically.

Even if magnetic surfaces do not exist one can obtain a good impression of the field structure by following a field line for many turns and marking with a point the positions where it intersects an arbitrarily chosen poloidal plane. The collection of these points is called a Poincaré plot (examples can be seen in Fig. 12.7, top). In such a plot a flux surface shows up by points forming a closed curve.

12.1.3 Tokamak, stellarator

The way in which the rotational transform ι is generated can be used to distinguish two classes of fusion devices: Tokamaks and stellarators. In a tokamak the plasma current, which is e.g. driven by the externally induced electric field, causes the poloidal field that in combination with the toroidal field from the (toroidal) field coils leads to a twisting of the magnetic field lines and thus to a rotational transform. Since usually the current density is highest at the center of the torus ι decreases with increasing radius.

In a stellarator the rotational transform is caused solely by a coil system externally to the plasma without any total plasma current J , i.e.

$$J := \int_{A_p} \mathbf{j} \cdot d\mathbf{A} = 0, \quad (12.1)$$

³Be M_S the set of points enclosed by a flux surface S . Then nested means that for all pairs (S_1, S_2) $M_{S_1} \subseteq M_{S_2}$ or $M_{S_2} \subseteq M_{S_1}$.

⁴In the simplest approximation ι can be regarded as the pitch of the field line on the flux surface.

⁵Since the set of rational numbers \mathbb{Q} is dense in \mathbb{R} the same is true for the set of rational surfaces with respect to all flux surfaces.

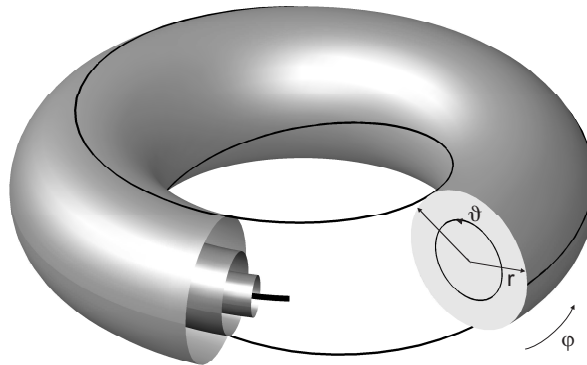


Figure 12.1: Toroidal geometry with nested flux surfaces, magnetic axis and a field line (red) with $\iota = 0.38$.

where j is the current density and A_p is a poloidal plasma cross section. Since the influence of the coils is strongest at larger radii the rotational transform increases with increasing radius.

So one main difference between tokamak and stellarator is the existence or absence of a total toroidal plasma current.

The beneficial role of a total plasma current for confinement in a tokamak has two main accompanying disadvantages: Firstly it can lead to violent instabilities called disruptions which destroy the plasma confinement and secondly – in a standard⁶ tokamak – the operation time is limited by the necessity of inducing an electric field. An advantage of the tokamak concept is that a tokamak possesses rotational symmetry and thus is a two-dimensional configuration.

The main advantages of a stellarator are that because of $J = 0$ it is inherently disruption free and can be used to achieve steady state operation. It is easy to show that the condition $J = 0$ cannot be satisfied for an axisymmetric configuration and thus a stellarator must have three-dimensional geometry. This makes stellarators geometrically and computationally more complex than tokamaks but, as we will see in the following sections, offers much more flexibility in their design which can be used for their optimisation.

Although in principle the three-dimensional geometry of a stellarator need not have any symmetries one usually imposes two symmetry requirements (see Fig. 12.2):

- Periodicity: Invariance against a rotation by $2\pi/P$ in the toroidal direction, where P is the number of – so called – field periods.
- Stellarator symmetry: Invariance against flapping around certain lines.

In a tokamak the rotational transform is of first order in the poloidal field component B_p : $\iota \sim B_p/B_0$, (B_0 is the total field). For a stellarator the first order effect of the helical field

⁶This is not the case for the so called advanced tokamak where bootstrap current (driven by density and temperature gradients) and current drive are responsible for ι .

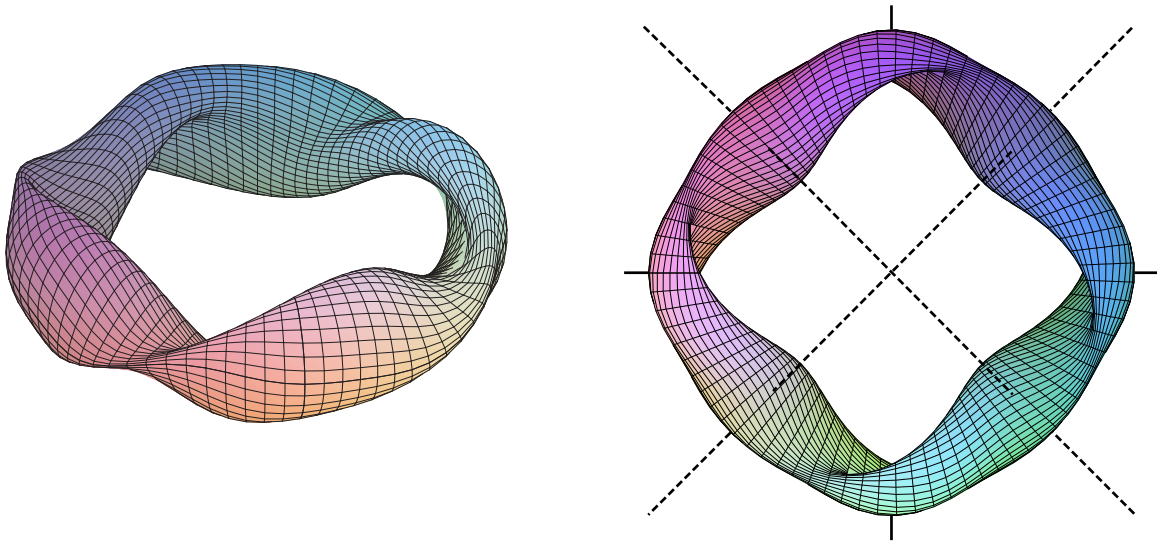


Figure 12.2: Side (left) and top (right) view of a stellarator with $P = 4$. The field periods and the lines for the stellarator symmetry are denoted by short and dashed lines, respectively (here both types of lines do have the respective complementary feature).

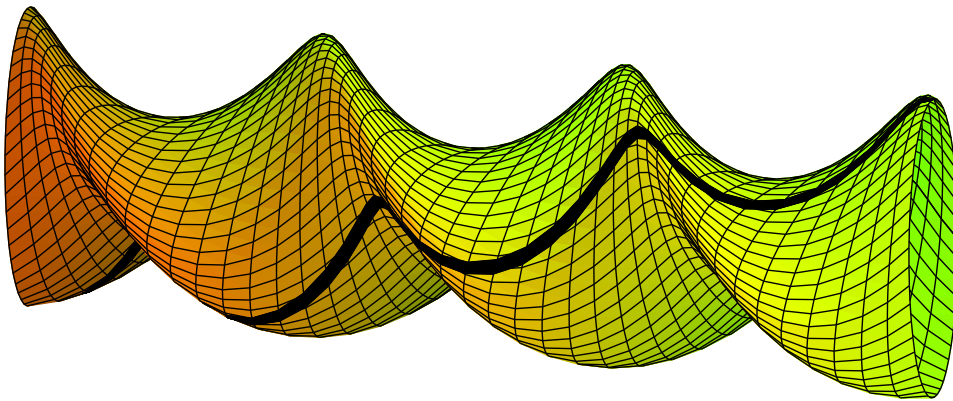


Figure 12.3: Three-dimensional view of one flux surface of a straight $\ell=2$ stellarator (three field periods). The thick black line shows one field line.

component B_h causes the field line to wiggle while the rotational transform, i.e. the poloidal shift that remains after averaging, is only of second order: $\iota \sim (B_h/B_0)^2$. This behavior of the field line can be understood if one rewrites (12.1) (using $\mu_{0j} = \nabla \times \mathbf{B}$) as a line integral around a poloidally closed curve ∂A_p giving $J = \int_{\partial A_p} B_p dl = 0$. For this integral to be zero the poloidal field component B_p has to change sign which implies an oscillating behavior of the field line.

Both effects are illustrated for a straight $\ell=2$ stellarator in Fig. 12.3; the wiggling is conspicuous while the rotation of the field line reflects the rotational transform.

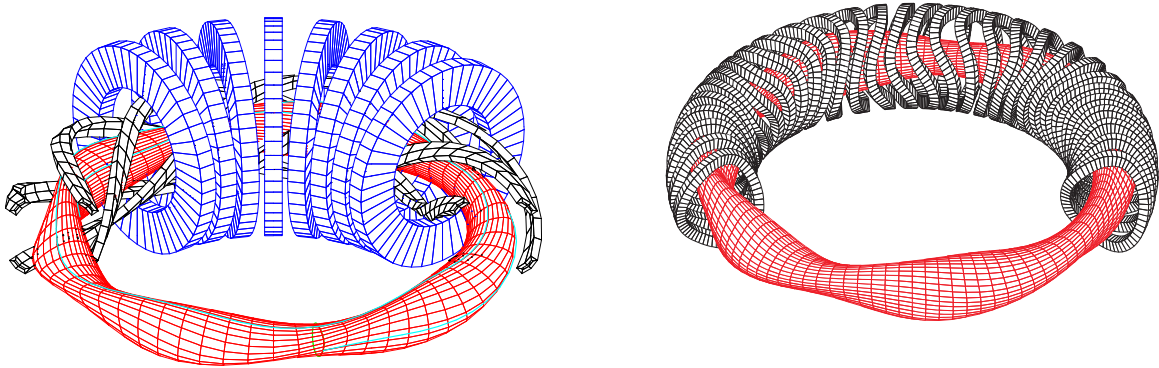


Figure 12.4: Classical (left) and modular (right) coil system for an $\ell=2$ stellarator.

12.1.4 Coil system

An important part in the engineering design of a stellarator is the question how a coil system must look like in order to produce the desired magnetic field. The classical coil system for e.g. an $\ell=2$ stellarator consists of groups of interlinked coils (Fig. 12.4 left): A set of planar coils generating the toroidal field component and four helical coils carrying currents running in alternating directions in neighboring coils⁷ responsible for the helical field components. The drawback of this kind of coil system is that strong forces can arise between the interlinked coils thus making it difficult to build. Also it can only be used for relatively simple configurations due to its low flexibility with regard to design.

Another possibility for finding a suitable coil system comes from the following observation: If in a toroidal volume V a magnetic field is given that on the boundary surface ∂V is tangential it is possible to calculate a surface current distribution on a second surface outside of ∂V that generates this field; discretizing this current distribution then leads to a coil system⁸. This way of obtaining a coil system is crucial for the design of modern optimised stellarators since it allows to start from a given plasma shape, which e.g. is obtained by stellarator optimisation (see sec. 12.6), and then calculate the corresponding – so called – modular coil system, which consists of a set of non-planar coils.

⁷A configuration with currents flowing always in the same direction is called a torsatron; it does not have toroidal field coils, but instead needs two coils generating a vertical field component.

⁸Since the corresponding mathematical problem does not have a unique solution there are many different coil systems giving nearly the same magnetic field. This allows to take into account engineering constraints in an optimisation procedure which combines aspects of field accuracy and coil flexibility.

12.2 Equilibrium

12.2.1 Equilibrium equations

The system of equations to be solved for a macroscopic fluid equilibrium follows from the general magnetohydrodynamic (MHD) equations by assuming $\partial/\partial t = 0$ and $\mathbf{v} = 0$

$$\mathbf{j} \times \mathbf{B} = \nabla p, \quad (12.2)$$

$$\nabla \times \mathbf{B} = \mu_0 \mathbf{j}, \quad (12.3)$$

$$\nabla \cdot \mathbf{B} = 0. \quad (12.4)$$

Eq. (12.2) gives the balance between Lorentz force and pressure force while (12.3) to (12.4) are Maxwells equations. One immediate conclusion is $\mathbf{B} \cdot \nabla p = 0$, i.e. the pressure is constant along a field line and consequently – assuming the existence of flux surfaces – it must be constant on each flux surface. From $\mathbf{j} \cdot \nabla p = 0$ it follows that the current can only flow in a flux surface.

12.2.2 Straight stellarator

It was mentioned in the last section that a stellarator cannot be axisymmetric, so the simplest possible stellarator is a helical symmetric configuration, i.e. all the physical quantities (using cylindrical coordinates) depend only on r and $\vartheta - kz$, where k is the parameter determining the length of a period.

For a vacuum field one has to solve the equation $\Delta\Phi = 0$ to obtain the magnetic potential (b_ℓ are free coefficients)

$$\Phi = B_0 z + \frac{1}{k} \sum_{\ell=1}^{\infty} b_\ell I_\ell(\ell kr) \sin \ell(\vartheta - kz).$$

From this follows an expression for the magnetic surfaces for a general straight stellarator

$$\Psi = B_0 \frac{kr^2}{2} - r \sum_{\ell=1}^{\infty} b_\ell I'_\ell(\ell kr) \cos \ell(\vartheta - kz) = \text{const}. \quad (12.5)$$

Fig. 12.5 shows the cross section of stellarators each having only one ℓ component; due to the helical symmetry the curves rotate around the origin for increasing z . Note that the $\ell=1$ stellarator is the only one with a non-straight magnetic axis.

Since straight configurations are only of theoretical interest we will in the following always assume toroidal topology.

12.2.3 Magnetic coordinates

Typical for a fusion plasma is the extremely high degree of anisotropy introduced by the magnetic field. As an order of magnitude estimate for the perpendicular and parallel length scale

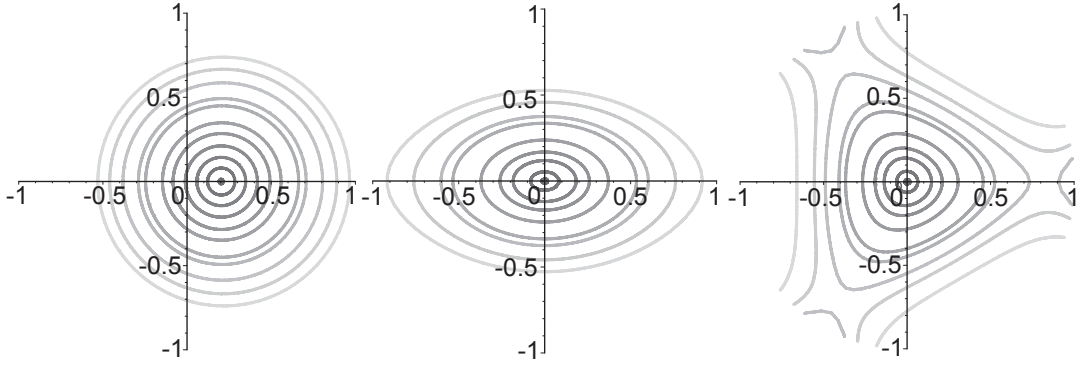


Figure 12.5: Intersection of $\Psi = \text{const}$ surfaces with the $z = 0$ plane for an $\ell = 1, 2, 3$ stellarator (from left).

one can take the ion gyroradius which is of the order of some 10^{-2} m and the parallel mean free path of a particle which is around some 10^3 m, respectively. Thus it is highly advantageous to have at one's disposal a coordinate system in which the field line can be described by a simple functional form and a separation of the perpendicular and parallel direction is easy.

The so called magnetic coordinates (s, ϑ, φ) are a special curvilinear coordinate system fulfilling these requirements. Here $s \in [0, 1]$ is the flux surface label – using magnetic coordinates requires the assumption that nested flux surfaces exist everywhere – and $\vartheta, \varphi \in [0, 2\pi]$ are angle-like coordinates. The geometric complexity of the configuration thus becomes hidden in the metric tensor g_{ij} . For calculations in this coordinate system one can use the formalism of tensor calculus.

In magnetic coordinates the magnetic field has the simple form

$$\mathbf{B} = \frac{1}{\sqrt{g}} (F_T' \mathbf{r}_{,\varphi} + F_P' \mathbf{r}_{,\vartheta}),$$

where F_T', F_P' is the s derivative of the toroidal ($F_T(s)$) and poloidal ($F_P(s)$) magnetic flux, $g^{1/2}$ is the determinant of the metric tensor and $\mathbf{r}_{,\varphi}, \mathbf{r}_{,\vartheta}$ are the covariant basic vectors. This expression shows that in magnetic coordinates the field lines are just straight lines $\vartheta = \iota \varphi$ with the rotational transform given by $\iota = F_P'/F_T'$.

12.2.4 Magnetic islands

One vital question for a fusion device is if it possesses nested flux surfaces or not.

Because of axisymmetry this question is simple to answer for a tokamak. Its symmetry allows to reduce the MHD equilibrium equations to one elliptic equation for the flux function $\Psi(r, z)$: the Grad-Shafranov-Equation

$$\left(r \frac{\partial}{\partial r} \frac{1}{r} \frac{\partial}{\partial r} + \frac{\partial^2}{\partial z^2} \right) \Psi + \mu_0 r^2 \frac{\partial p(\Psi)}{\partial \Psi} + \frac{\mu_0}{8\pi^2} \frac{\partial I^2(\Psi)}{\partial \Psi} = 0, \quad (12.6)$$

where $p(\Psi)$ and the current distribution $I(\Psi)$ are arbitrary functions. The fact that p only depends on Ψ ensures a constant pressure on each flux surface. Specifying profiles for p and

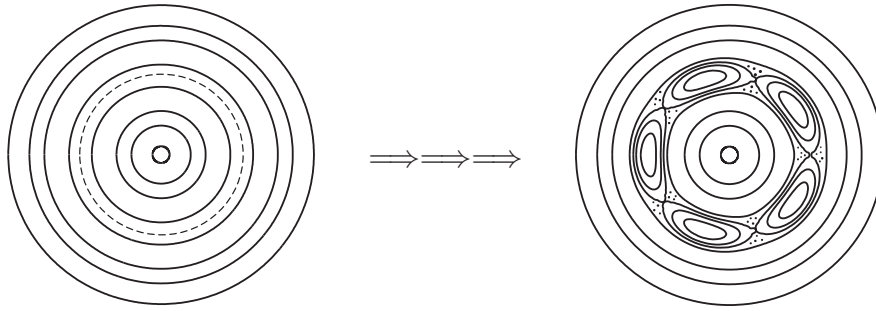


Figure 12.6: Left: Equilibrium with nested flux surfaces (the resonant surface is shown dashed).
Right: Equilibrium with perturbation, ergodic regions are indicated with dots.

I and imposing boundary conditions on Ψ (e.g. $\Psi = 0$ at the given plasma boundary) this (in general) nonlinear equation can be solved and directly gives the flux surfaces. Thus there is no problem for axisymmetric equilibria.

For three-dimensional configurations it is generally not possible to show that a flux function exists, which makes it very complicated to obtain information about the existence of flux surfaces.

The complications arising in connection with three-dimensionality can be seen by the following gedankenexperiment: Imagine bending a straight stellarator, which always possesses flux surfaces (see (12.5)), into a torus. This process can be regarded as adding perturbations with Fourier amplitude \mathcal{P}_{mn} to the original straight equilibrium in order to produce the new toroidal one. It can be shown that the surface which is in resonance with the perturbation \mathcal{P}_{mn} will break up into a chain of islands separated by X-points⁹. The latter are surrounded by ergodic regions where the field lines move chaotically filling out a volume instead of a surface¹⁰. This is illustrated in Fig. 12.6 where the effect of an $m = 5$ perturbation on an equilibrium with flux surfaces is sketched.

How this looks like for a real equilibrium is shown in Fig. 12.7. Here a chain with large islands (light grey) is located around the flux surface where the ι profile crosses 5/5 (note that the ι profile is constant inside the region occupied by the islands). For a shifted ι profile that does not contain 5/5 these islands disappear.

The width w of an island can be estimated by

$$w = 4\sqrt{\frac{R}{m\iota'}\mathcal{P}_{mn}}. \quad (12.7)$$

⁹These islands are called *natural* in order to distinguish them from island caused by effects external to the equilibrium, e.g. small errors in the coils. For natural islands the Fourier number n must be a multiple of the number of field periods.

¹⁰All this is analogous to nonlinear dynamics where it is shown that perturbations added to an integrable system lead to a destruction of the resonant tori in phase space (see the Poincaré-Birkhoff and Kolmogorov-Arnold-Moser (KAM) theorem). This analogy can be put on rigorous footing by noticing that the field lines in a torus can be described by a Hamiltonian function.

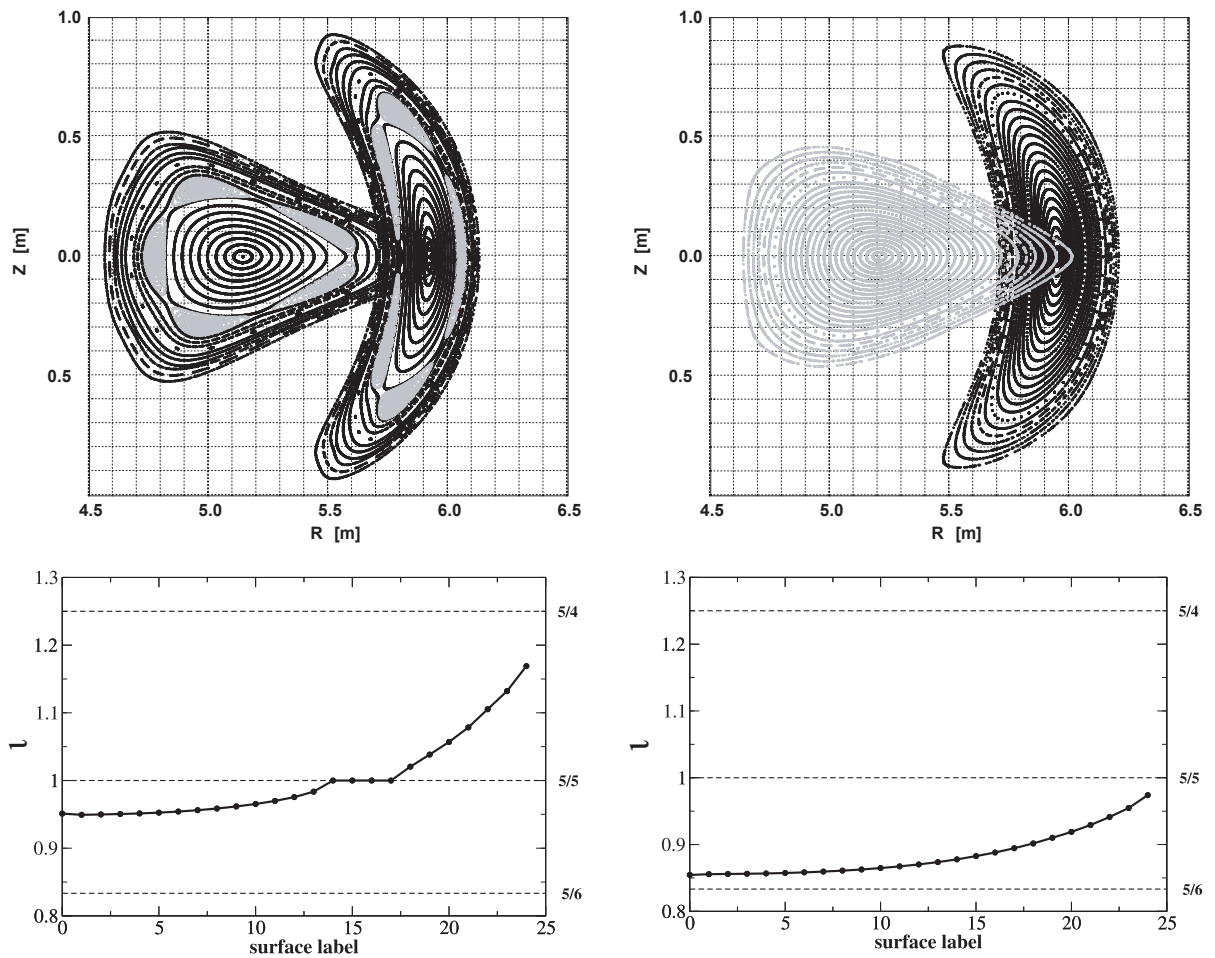


Figure 12.7: Poincaré plots of two Wendelstein 7-X variants with different ι profiles.

Left: ι profile including the 5/5 resonance.

Right: The same calculation but with a downward shifted profile avoiding this resonance.

Using e.g. values typical of Wendelstein 7-X and assuming a perturbation amplitude $\mathcal{P}_{mn} \approx 10^{-4}$ one finds that this perturbation can lead to islands of width $w/a \approx 0.2$ showing that even a small perturbation can create relatively large islands. The danger of islands lies in the fact that they normally lead to a strong deterioration of plasma confinement by allowing particles to quickly cross the region occupied by the island chain. The existence of islands in an equilibrium is an inherent feature of three-dimensional systems, so it is of major interest for stellarator theory to design configurations in such a way that islands are so small that they have nearly no effect on confinement.

Eq. (12.7) shows that rational numbers n/m with low m – so called low order rationals – produce larger islands than rationals with high m and that high shear leads to smaller islands than low shear. Hence there are two strategies to arrive at three-dimensional equilibria with small islands:

- High shear minimises the influence of low order rationals but makes it necessary for the ι profile to cross many rationals. This strategy is followed in e.g. LHD.
- Low shear allows to place the flat ι profile in a region where there are no low order rationals. This line is followed by Wendelstein 7-X.

12.2.5 3D equilibrium codes

In order to describe an equilibrium (without bootstrap current) one has to specify the radial profile of the pressure and the shape of the outer flux surface \mathcal{S} (along with the boundary condition that \mathbf{B} must be tangent to \mathcal{S}). For a stellarator the condition $J = 0$ is imposed – the ι -profile then follows – while for a tokamak either the current or the ι -profile must be given. Solution of (12.2) to (12.4) then gives the magnetic field inside \mathcal{S} .

The shape of \mathcal{S} is usually described using the parametric representation

$$\begin{aligned} R &= \sum_{m,n} R_{m,n} \cos(mU - nV), \\ Z &= \sum_{m,n} Z_{m,n} \sin(mU - nV), \\ \phi &= V, \end{aligned}$$

where $U, V \in [0, 2\pi]$ are parameters and (R, Z, ϕ) are cylindrical coordinates, together with the set of Fourier coefficients $R_{m,n}, Z_{m,n}$.

Since in three dimensions the existence of flux surfaces is not guaranteed, the structure of a solution can only be found a posteriori making it non-trivial to obtain pressure profiles which are constant on each flux surface.

The numerical calculation of stellarator equilibria is e.g. carried out with the help of two tools: The Variational Magnetic Equilibrium Code (VMEC) and the Princeton Iterative Equilibrium Solver (PIES).

VMEC

In this approach one *assumes* that the equilibrium has nested flux surfaces, i.e. one ignores the possibility of islands. As we have seen this assumption is generally not true for three-dimensional equilibria. Thus the solution given by the code serves only as an approximation to the exact equilibrium and can be rather bad if this has large islands¹¹. Whether the approximation is a good one can only be tested afterwards.

Under this assumption making the energy functional

$$W = \int \left(\frac{B^2}{2\mu_0} + \frac{p}{\gamma - 1} \right) dV$$

¹¹Instead of islands the approximative solution shows divergences in the parallel current density j_{\parallel} at the resonant surfaces. In the exact solution j_{\parallel} stays finite everywhere.

(γ : adiabatic coefficient) stationary, together with the additional constraint that the mass inside each flux surface does not change by the variation, is equivalent to solving the equilibrium (12.2) to (12.4).

The attractiveness of this approach lies in the fact that it is computationally much faster than computing an equilibrium allowing for islands. Thus VMEC has become the standard tool for calculating stellarator equilibria.

PIES

The PIES code permits islands in the equilibrium solution¹². It solves the MHD equilibrium equations employing a Picard iteration, i.e. starting with an initial guess B^0 – obtained with e.g. VMEC – it solves the equations

$$\nabla \times B^{n+1} = \mu_0 j(B^n), \quad \nabla \cdot B^{n+1} = 0,$$

where $j(B^n)$ is found from solving

$$j \times B^n = \nabla p, \quad \nabla \cdot j = 0.$$

The drawback of this approach is its extremely slow convergence making the calculation of an equilibrium very time consuming¹³.

12.3 Pfirsch-Schlüter current

One goal of fusion power plant design is to achieve $\beta := 2\mu_0 p/B^2$ values of about 5% (averaged in the confinement region). Connected with an increase in the plasma pressure is a shift of the plasma center with respect to the outer plasma surface (Shafranov shift). If this shift is too large the plasma center comes close to the outer plasma surface which may cause problems. So, cautiously one limits β to some value β_{eq} such that the plasma center keeps a safe distance from its boundary.

For an axisymmetric equilibrium and classical stellarators the Shafranov shift Δ is given approximately by $\Delta/R = \beta/\iota^2$. Usually one defines β_{eq} to be reached if $\Delta = a/2$, resulting in $\beta_{\text{eq}} \sim \iota^2/A$. Typical values are $A \approx 3$, $\iota \lesssim 1$ for a tokamak and $A \approx 10$, $\iota < 1$ for a stellarator. While this definition leads to a useful β -limit for a tokamak, a stellarator with small ι and large A has a β_{eq} which is too low for fusion applications.

The way out of this difficulty is to use the freedom given by the three-dimensional structure of a stellarator to design $|B|$ in such a way as to reduce the Shafranov shift.

First we have to understand what causes the Shafranov shift: From the MHD equilibrium relation $j \times B = \nabla p$ one obtains the diamagnetic current $j_{\perp} = B \times \nabla p/B^2$. Splitting the quasineutrality relation $\nabla \cdot j = 0$ into a parallel and perpendicular component gives $\nabla \cdot j_{\parallel} = -\nabla \cdot j_{\perp}$. The

¹²A second code allowing for islands is the HINT code which uses the time dependent MHD equations.

¹³An equilibrium calculation for the W7-X configuration using VMEC needs a few minutes computing time on an SX-5 vector computer; the analogous calculation using PIES takes approximately one week.

diamagnetic current thus gives rise to a parallel current called the Pfirsch-Schlüter (PS) current. As a result one gets

$$\nabla \cdot \mathbf{j}_{\parallel} = -\frac{2}{B^3} (\nabla p \times \mathbf{B}) \cdot \nabla |\mathbf{B}| = -\frac{2|\nabla p|}{B} \kappa_g$$

with κ_g the geodesic curvature¹⁴. Note that ∇p is normal to the flux surface and, as a consequence, only the derivative of $|\mathbf{B}|$ in the flux surface enters this expression. The geodesic curvature will also play an important role in the next section and thus will show up as a quantity of main importance for stellarators.

For a simple axisymmetric configuration this equation can easily be solved and gives the PS current as

$$j_{\parallel} = \frac{\partial p}{\partial r} \frac{2}{\iota B_0} \cos \vartheta .$$

This parallel current density – flowing in different directions at the inside respectively outside of the torus – leads to a vertical magnetic field that in combination with the toroidal and poloidal field results in an outward shift of the plasma: The Shafranov shift.

For a helically symmetric configuration with $\mathbf{B} = B(r, \vartheta - kz)$ one finds $j_{\parallel} \propto 1/(\iota - 1)$. It follows for $\iota \ll 1$ that the magnitude of j_{\parallel} (and consequently the Shafranov shift) in a helically symmetric configuration is much smaller than in an axisymmetric one. Using the VMEC code it is possible to construct quasi-helically symmetric stellarator equilibria¹⁵ for which even a β of 40% leads to nearly no Shafranov shift.

This observation shows the strategy how to reduce the Shafranov shift and increase β_{eq} for a stellarator: Using the freedom given by the three-dimensional structure one can design $|\mathbf{B}|$ and with it the geodesic curvature in such a way as to minimize the Shafranov shift (more details on this will be given later in sec. 12.6). Taking the volume averaged ratio of the parallel to the diamagnetic current $\langle j_{\parallel}^2 / j_{\perp}^2 \rangle$ as a measure for the importance of the PS current one can see the progress of stellarator design with time: While for the classical (non-optimised) stellarator W7-A this ratio is around 12 it can be reduced to three for the partly optimised W7-AS and then to 0.5 for the fully optimised W7-X (corresponding to $\beta_{\text{eq}} \approx 5\%$). This is illustrated in Fig. 12.8, where W7-AS for $\beta \approx 2\%$ shows a noticeable Shafranov shift while it is hardly visible in W7-X for $\beta \approx 5\%$.

12.4 Neoclassical transport

12.4.1 Neoclassical transport

The main aim of neoclassical (transport) theory is to calculate the collisional transport of particles and heat – e.g. radial diffusion coefficients for particle and heat fluxes – as functions

¹⁴Using a triad $(\mathbf{b}, \mathbf{n}, \mathbf{n} \times \mathbf{b})$ such that \mathbf{b} is the unit B-field vector and \mathbf{n} is the unit normal vector of the flux surface the curvature $\kappa := (\mathbf{b} \cdot \nabla) \mathbf{b}$ can be written as $\kappa = \kappa_n \mathbf{n} + \kappa_g \mathbf{n} \times \mathbf{b}$ with the geodesic and normal curvature κ_g, κ_n . In contrast to the normal curvature the geodesic curvature is an intrinsic property of the surface geometry.

¹⁵In toroidal topology helically symmetric equilibria do not exist; one has to resort to so called quasi-helically symmetric equilibria (see sec. 12.4.2).

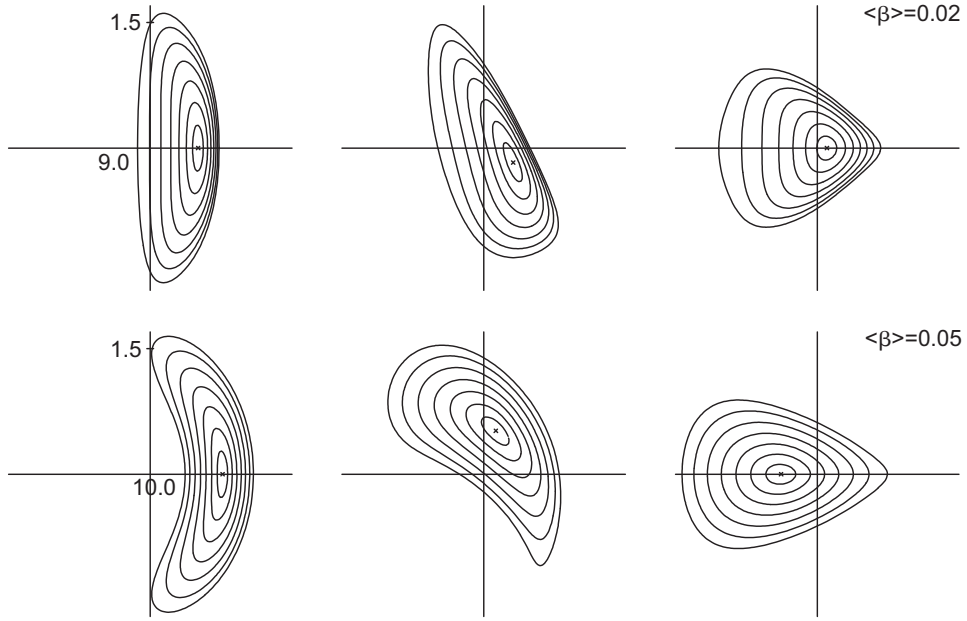


Figure 12.8: Toroidal cuts (at $\phi = 0, 2\pi/20, 2\pi/10$) for W7-AS (top) and W7-X (bottom).

of the collision rates and the electric field taking into account the toroidal geometry of a fusion device¹⁶. The theoretical base for neoclassical calculations is collisional kinetic theory especially its drift kinetic simplification.

Fig. 12.9 gives an overview on the neoclassical transport for tokamaks and stellarators. Depending on ν_{ei} (ion-electron collision frequency) one finds different regimes: The Pfirsch-Schlüter, plateau and banana regime for high, intermediate and low collisionality, respectively. The three-dimensional geometry of a stellarator can lead to regimes not present in a tokamak. In the long mean free path regime the helical variation of $|B|$ (helical ripple) for a classical stellarator leads to the so called $1/\nu$ regime¹⁷ which is of paramount importance since it can lead to extremely large neoclassical losses potentially dangerous for a stellarator fusion device.

For the PS regime a fluid treatment of radial diffusion is possible: For a cylinder the equilibrium equation and Ohm's law ($\eta = m_e/(ne^2)\nu_{ei}$)

$$\mathbf{j} \times \mathbf{B} = \nabla p, \quad \mathbf{E} + \mathbf{v} \times \mathbf{B} = \eta \mathbf{j}$$

give the perpendicular velocity of the fluid as

$$\mathbf{v}_\perp = \frac{\mathbf{E} \times \mathbf{B}}{B^2} - \frac{1}{B^2} \eta \nabla p$$

consisting of the $\mathbf{E} \times \mathbf{B}$ -drift and a radial drift induced by collisions. Using the last term to calculate the radial particle flux $\Gamma = n\mathbf{v}_\perp$ and comparing this with Fick's law $\Gamma = -D\nabla n$ leads to the classical diffusion coefficient (ρ_e : electron gyroradius)

$$D_c = \left(1 + \frac{T_i}{T_e}\right) \rho_e^2 \nu_{ei}. \quad (12.8)$$

¹⁶In cylinder geometry one speaks of classical transport theory.

¹⁷If an electric field is included a $\nu^{1/2}$ regime can also be present.

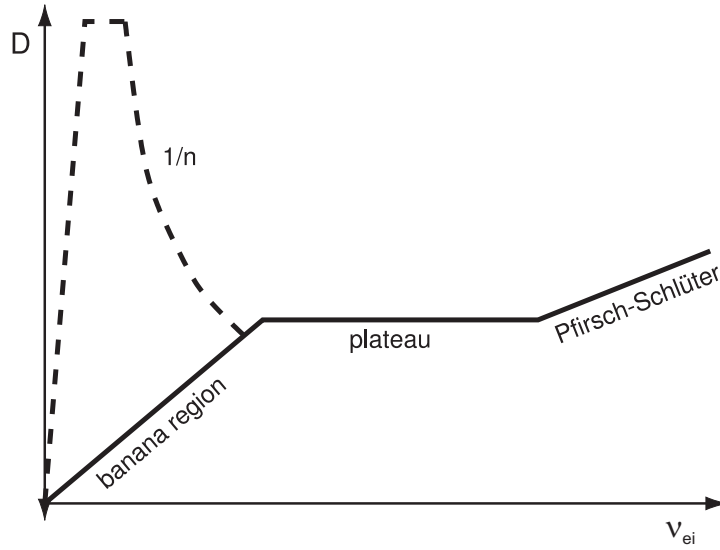


Figure 12.9: Neoclassical diffusion coefficient as a function of collision rate. Black: tokamak. Dashed: additional regimes for a stellarator.

A more complicated calculation in toroidal geometry¹⁸ including the PS current gives an additional factor (PS factor) and leads to the larger neoclassical diffusion coefficient $D_{nc} = (1 + \iota^{-2})D_c$.

To understand the origin of the banana and $1/\nu$ regime one has to look at the motion of particles. For this task it is sufficient to use the guiding center equations of motion¹⁹

$$\dot{\mathbf{R}} = v_{\parallel} \mathbf{b} + \mathbf{v}_d, \quad (12.9)$$

$$\dot{v}_{\parallel} = -\mu \mathbf{b} \cdot \nabla |\mathbf{B}|, \quad (12.10)$$

$$\dot{\mu} = 0 \quad (12.11)$$

with the perpendicular drift velocity ($\mathbf{b} := \mathbf{B}/|\mathbf{B}|$ and $\mu := v_{\perp}^2/(2B)$ the magnetic moment per unit mass)

$$\mathbf{v}_d = \frac{\mu B + v_{\parallel}^2}{B\Omega} \mathbf{b} \times \nabla |\mathbf{B}|. \quad (12.12)$$

From these equations²⁰ follows the very important fact that particles with low enough energy can be trapped around a minimum of $|\mathbf{B}|$ while for higher energies they can stream (nearly) freely. A particle trapped in a minimum of B shows a fast bouncing motion superposed onto a slow drift. This slow drift motion can be separated by averaging over the fast bouncing motion (bounce average) and gives the motion of the bounce center²¹ $\langle \mathbf{v} \rangle = 1/\tau_b \oint \mathbf{v} dt$ (τ_b : bounce time).

¹⁸This can most easily be seen by using the general relation $\Gamma = n \int \eta j^2 dS / (|\nabla p|)$ (with $\eta_{\perp} \approx 2\eta_{\parallel}$) connecting the particle flux Γ with the resistive dissipation integrated over one flux surface. Thus the additional dissipation caused including parallel (PS) currents leads to an increase in the particle flux by the PS factor.

¹⁹See the lecture "Introduction to fusion plasmas".

²⁰Note that (12.10) follows from (12.9), (12.11) and energy conservation.

²¹To obtain the drift kinetic theory the fast gyrating particle had been replaced via averaging by its slowly drifting guiding center. Now drift kinetic is further reduced to a theory with the bounce center as the slowly moving basic entity obtained by averaging over the comparatively faster bounce motion of the guiding center.

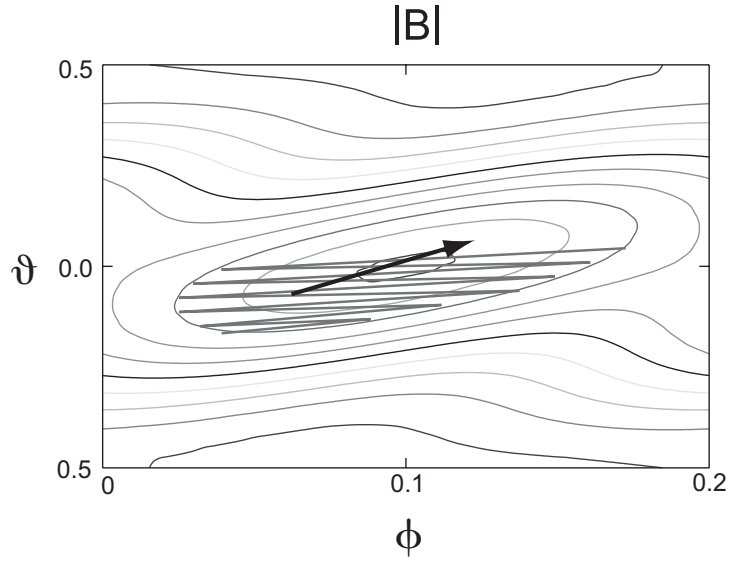


Figure 12.10: Motion of a trapped particle near a minimum of B (contour lines). The red line shows the actual motion of the guiding center while the black arrow shows the motion of the bounce center.

In a tokamak trapped particles move on so called banana orbits with radial width Δ_b . The center of a banana orbit slowly drifts toroidally but not radially, i.e. $\langle \mathbf{v} \rangle$ has only a toroidal component. Collisions cause particles to jump from one banana orbit to another thus leading to a random walk with step size Δ_b resulting in a diffusion coefficient (given by $D = l^2/\tau$, where l is the diffusion step length and τ the collision time²²) in the banana regime as $D_b = \Delta_b^2 \nu_{ei}$.

As a very simple model for $|B|$ in a stellarator one often uses

$$B = B_0 (1 - \varepsilon_t \cos \vartheta - \varepsilon_h \cos(\ell \vartheta - P\phi)) ,$$

where $\varepsilon_{t,h}$ measures the strength of the toroidal or helical component, respectively.

For $\varepsilon_t = 0$ the bounce center drifts along the helical minimum (helically trapped particle) and $\langle \mathbf{v} \rangle$ has no component in the radial direction.

Adding a toroidal component ($\varepsilon_t \neq 0$) leads to a net radial component of $\langle \mathbf{v} \rangle$ which can be computed by performing the bounce average of

$$v^r = v_d \frac{\nabla r}{|\nabla r|} = \frac{\mu B + v_{\parallel}^2}{\Omega} \kappa_g .$$

This result can be used to estimate a diffusion coefficient by noting that the diffusion step length is $l = \langle v_r \rangle / (\nu_{ei})$.

$$D_{l/v} = f_t \frac{\langle v^r \rangle^2}{\nu_{ei}} \sim f_t \frac{T^{7/2}}{nB^2} \kappa_g^2 \quad (12.13)$$

(f_t : fraction of trapped particles).

²²One can show that only collisions between unlike particle species lead to particle diffusion, while for heat diffusion collisions between like particle species are important.

This equation also shows the crucial role played by the geodesic curvature; its importance for the PS-current we have already seen in sec. 12.3. Thus decreasing the size of the geodesic curvature in the region where particles are trapped is beneficial for minimizing the neoclassical transport.

Summarizing the above picture one can say that caused by the toroidal curvature a helically trapped particle in a stellarator in general acquires a radial drift eventually leading to its loss; these particles are responsible for the $1/\nu$ regime.

One can argue more generally: Due to its axial symmetry the toroidal momentum is a conserved quantity for particle motion in a tokamak and it follows as a consequence that the maximal deviation of a (trapped or untrapped) particle from the flux surface is limited; this results in a relatively low neoclassical transport. The situation is different for a stellarator: Caused by its three-dimensional structure a conserved quantity and the related constraint on the orbit width does in general not exist²³ possibly leading to rapid particle losses showing up as the $1/\nu$ regime.

The strong dependence of $D_{1/\nu}$ on T is the cause why the $1/\nu$ regime is dangerous for a (classical) stellarator: The high temperature necessary for fusion leads to losses which are too high for a fusion power plant to work. So in order to construct a viable stellarator power plant it is of utmost importance to reduce this kind of neoclassical losses. From (12.13) one can see the possible ways how to do this: Designing a stellarator in such a way that the particles get trapped in a region with small geodesic curvature leads to a small neoclassical radial transport. This path is followed in the design of W7-X and as a result neoclassical losses in W7-X are small enough to be compatible with fusion power plant requirements.

12.4.2 Quasi symmetry

Using magnetic coordinates (s, ϑ, φ) (see sec. 12.2.3) the guiding center equation of motion for $\dot{\mathbf{R}}$ (12.9) can be written as

$$\dot{s} = \frac{1}{\sqrt{g}D} \frac{e\rho_{\parallel}}{m} (\rho_{\parallel, \vartheta} I - \rho_{\parallel, \varphi} J) , \quad (12.14)$$

$$\dot{\vartheta} = \frac{1}{\sqrt{g}D} \frac{e\rho_{\parallel}}{m} \left[-F'_p - (I\rho_{\parallel})_{,s} + \left(\tilde{\beta}\rho_{\parallel} \right)_{, \varphi} \right] , \quad (12.15)$$

$$\dot{\varphi} = \frac{1}{\sqrt{g}D} \frac{e\rho_{\parallel}}{m} \left[-F'_T + (J\rho_{\parallel})_{,s} - \left(\tilde{\beta}\rho_{\parallel} \right)_{, \vartheta} \right] \quad (12.16)$$

with $\rho_{\parallel} := mv_{\parallel}/(eB)$, $D := 1 + \rho_{\parallel} \mathbf{B} \cdot \mathbf{j} / B^2$, $\sqrt{g} := -(JF'_p + IF'_T) / B^2$ and $\tilde{\beta}$ a function that can be calculated from B .

This formulation shows that the motion of the guiding center formulated in the special coordinate system of magnetic coordinates depends *only* on the function $B(s, \vartheta, \varphi)$ (magnetic topography) but not on the spatial structure of the flux surfaces which would show up as the

²³Quasi-symmetric configurations (see next section) do have conserved quantities.

metric tensor. Formulated sloppily one can say that in magnetic coordinates the particles do not *see* the real geometry of the configuration but only the magnetic topography. This observation leads to the notion of quasi-symmetry²⁴ as a symmetry of the magnetic topography formulated in magnetic coordinates; the configuration does not need to possess a symmetry in real space.

Configurations with $B = B(s, \vartheta)$ or $B = B(s, k\vartheta - P\varphi)$ (k, P : integer parameters) are called quasi-axisymmetric or quasi-helical symmetric, respectively. They can be realized in a torus and examples are known (e.g. see Fig. 12.11). On the other hand the quasi-symmetries $B = B(s, \varphi)$ and $B = B(s)$, which would guarantee that a particle stays exactly at a flux surface²⁵, can not be achieved for toroidal systems.

For a configuration possessing a quasi-symmetry it follows from the guiding center equations of motion that there exists a conserved quantity²⁶. This conserved quantity limits the maximal excursion of a particle from the flux surface (as noted in the last section) and thus eliminates the cause for the existence of the $1/\nu$ regime. Detailed calculations indeed show that e.g. a quasi-helical symmetric stellarator shows similar neoclassical transport as a corresponding tokamak.

As an illustration Fig. 12.11 shows one flux surface of a quasi-helical symmetric configuration with six field periods. In real space it has a complicated three-dimensional structure and shows no apparent symmetries other than the ones described in sec. 12.1.3. After transformation to magnetic coordinates the helical symmetry of B becomes manifest.

Quasi-helical symmetric configurations have a bootstrap current which endangers their usefulness. Thus one considers another class of configurations, called quasi-isodynamic, where the second adiabatic invariant $J := \int v_{\parallel} dl$ (l : length along a field line) is nearly constant on the flux surfaces. In these configurations (without symmetry of B) the bounce center drifts poloidally. W7-X belongs to the class of quasi-isodynamic stellarators.

12.5 MHD stability

Since the vast field of stability quickly becomes very technical we will only give a short overview of the basic concepts of MHD stability.

Having found a plasma equilibrium configuration that meets the requirements described in the former sections it remains to show if a small perturbation applied to the system grows or decays with time. In the first case the equilibrium configuration is unstable and plasma confinement may be destroyed quickly.

Formally one uses time dependent equations, symbolically written as $\partial g / \partial t = \mathcal{M}g$ with g denoting the dynamical variables and \mathcal{M} a nonlinear operator. The solution is split into a

²⁴The qualifier *quasi* is meant to indicate that this symmetry only exists for B in a specially chosen coordinate system. Additionally it hints that quasi-symmetry is attainable in a three-dimensional configuration only to some approximation but not exactly.

²⁵A configuration fulfilling $B = B(s)$ exactly would be called isodynamic.

²⁶For e.g. quasi-helical symmetry the quantity $F_T - F_P - \rho_{\parallel}(I + J)$ is conserved.

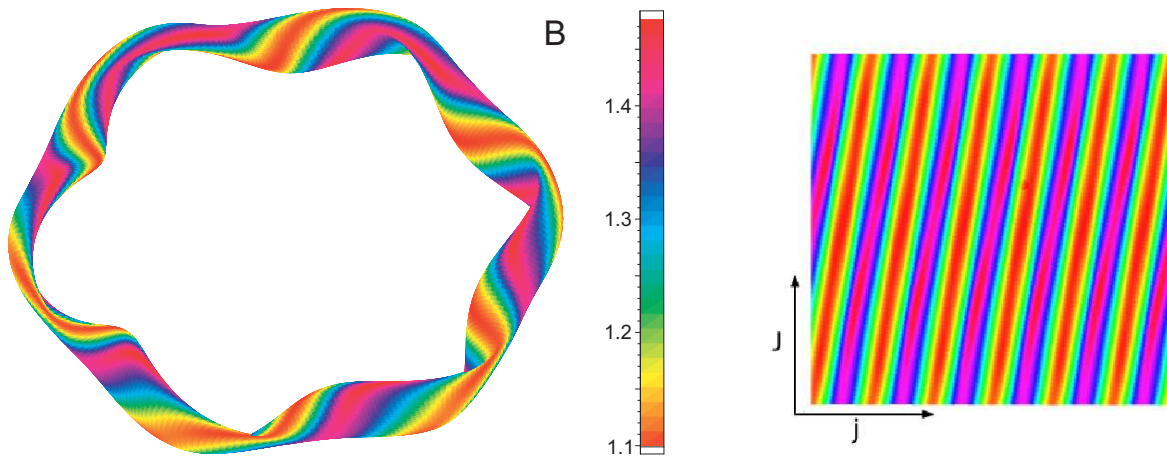


Figure 12.11: Quasi-helical symmetric stellarator in real space (left) and magnetic coordinates (right) (one flux surface is shown, color indicates the magnitude of B).

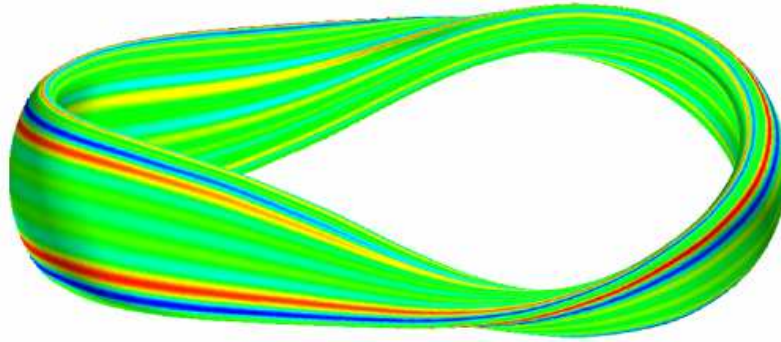


Figure 12.12: Eigenfunction for a ballooning mode. Shown is the pressure perturbation on a flux surface (high/low pressure is colored with red/green).

time independent part representing the equilibrium under investigation and a time dependent part describing the perturbation: $g(\mathbf{r}, t) = g_0(\mathbf{r}) + g_1(\mathbf{r}, t)$. Assuming small perturbations $g_1 \ll g_0$ the nonlinear operator \mathcal{M} is linearized resulting in the linear operator \mathcal{L} . Usually one is interested only in solutions behaving exponentially in time²⁷ justifying the ansatz $g_1 = \tilde{g}(\mathbf{r})e^{-i\omega t}$ (with the complex eigenvalue ω). Specification of boundary conditions on \tilde{g} then leads to the eigenvalue problem $\mathcal{L}\tilde{g} = \omega\tilde{g}$. The equilibrium is unstable if $\text{Im}(\omega) > 0$ showing that the initially infinitesimal perturbation is growing exponentially with time.

Since for MHD the operator \mathcal{L} is self-adjoint its eigenvalue problem only has solutions with $\omega^2 \in \mathbb{R}$ and can be formulated as a variational problem: The system is unstable if a perturbation $\xi(\mathbf{r})$ in the position of the plasma exists such that $\delta^2 W[\xi] < 0$ where the functional²⁸ $\delta^2 W$ is

²⁷Perturbations growing algebraically in time may exist but because of their slow growth normally are of no interest.

²⁸ $\delta^2 W$ is the second variation of the functional W from sec. 12.2.5.

given by

$$\delta^2 W[\xi] = -\frac{1}{2} \iiint [S^1 + S^2 + S^3 + S^4 + S^5] d^3 r.$$

The expressions for $S^1(\xi) \dots S^5(\xi)$ are complicated and instead of giving the details here it suffices to note their general properties: S^1, S^2 and S^5 describe the influence of field line bending, field compression and fluid compression, respectively; they act stabilizing on $\delta^2 W$. In contrast to this S^3 and S^4 are indefinite and depend on the pressure gradient p' and the parallel current density j_{\parallel} ; these two terms can cause $\delta^2 W$ to become negative. The instabilities caused by these terms are called pressure or current driven.

From the large zoo of MHD instabilities we briefly look at the kink and the ballooning instabilities: The kink instability is driven by a parallel current and consequently does not exist in a stellarator. Pressure is the energy source for the ballooning instability which bears this name since e.g. in a tokamak it has its maximal amplitude in the region of unfavorable curvature (i.e. at the outside of the torus). This instability disappears for fixed pressure gradient if the pressure is low enough and thus provides a stability β -limit. W7-X is designed in such a way that it is stable against the ballooning instability for $\beta \lesssim 5\%$. For a tokamak, large scale kink and ballooning instabilities limit the operation regime, while for a stellarator only ballooning modes have been found experimentally, hitherto. As an illustration Fig. 12.12 shows a ballooning instability in a quasi-axially symmetric stellarator above the stability β -limit. This picture also demonstrates a very general structural property of modes in a magnetized plasma: The wavelength in the direction perpendicular to the field lines is much smaller than the wavelength along the field line. This high degree of anisotropy of the instability reflects the anisotropy introduced by the magnetic field.

12.6 Stellarator optimisation

In sec. 12.2 to sec. 12.5 we have discussed four points which are of vital importance for a stellarator as a fusion device. Stellarator optimisation is the comprehensive framework where these points (and other) are put together in order to arrive at a viable design for a fusion device. Crucial for optimisation is the high degree of freedom provided by the three-dimensional structure of a stellarator.

Since the main goal of stellarator optimisation is to find equilibria that have good confinement properties one first has to quantify what one understands by *good confinement properties*. This is done by assigning to each equilibrium configuration from the configuration space Con ²⁹ a real number as a quality measure by providing a function $\mathcal{Q} : \text{Con} \mapsto \mathbb{R}$. The construction of this function requires the consideration of the physics one regards as relevant for confinement and the design targets.

In the design of W7-X one required:

²⁹Since we have seen in sec. 12.2.5 that an equilibrium (except for its profiles) can be uniquely defined by specifying its outer flux surface the space Con can be identified with the set of Fourier coefficients used in the representation of this surface.

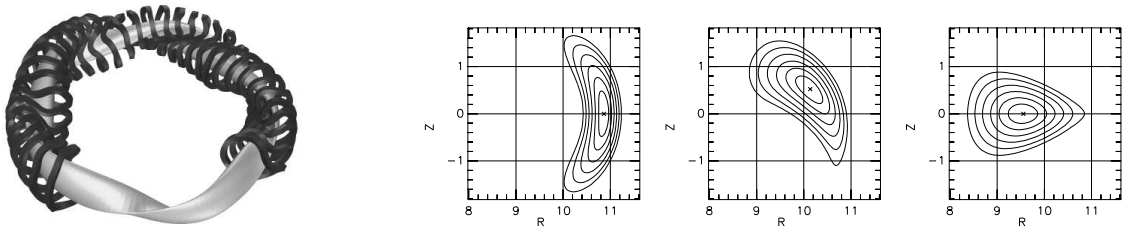


Figure 12.13: Left: Wendelstein 7-X plasma configuration with modular coils.
Right: Toroidal cuts through the equilibrium configuration at $\phi = 0, 2\pi/20, 2\pi/10$.

- Nested magnetic surfaces with small islands;
- Small Shafranov shift for $\beta \approx 5\%$;
- Small neoclassical transport;
- MHD stability, especially stability against ballooning modes for $\beta \approx 5\%$;
- Good α -particle confinement:
 α -particles are needed for the heating of the plasma and thus they must not leave the fusion device in a time shorter than their slowing down time;
- Small bootstrap current:
This is another current driven by the pressure gradient. In contrast to the PS-current it gives rise to a total toroidal current causing a shift in ι with increasing β . Since ι control is crucial for the confinement properties (see e.g. sec. 12.2.4) such a shift was considered to be undesirable³⁰;
- Feasible modular coils:
For actually building a device constraints emerge motivated by engineering considerations regarding the design of the modular coils (e.g. a minimal distance between neighboring coils must be kept, the coil curvature cannot be too large). Some of them can be taken into account in the plasma optimisation.

In the optimisation procedure, which is carried out computationally, first an outer flux surface is specified from which (using VMEC) the corresponding equilibrium configuration is computed; based on this equilibrium the function \mathcal{Q} is calculated. This procedure is repeated – employing an optimisation algorithm – with changed outer flux surface until \mathcal{Q} has reached a maximum. When the optimised equilibrium has been found the actual coil system is calculated subsequently.

Depending on the criteria and the design goals many different configurations can be found via optimisation. One possible result from this procedure, the optimised stellarator Wendelstein 7-X, is shown in Fig. 12.13.

³⁰Quasi-axisymmetric configurations are an exception to this consideration.

References

There exists no good textbook about stellarator physics (as e.g. the book by Wesson for tokamaks). So everything is scattered in articles which generally are difficult to understand for the beginner. For this reason I here give references to some of the few more basic articles.

- A.H. Boozer, “What is a stellarator”, *Physics of Plasmas*, vol. 1, p. 1647 (1998).
A more advanced introductory article with an explanation of magnetic coordinates.
- G. Grieger et al., “Physics optimization of stellarators”, *Physics of Fluids*, vol. B4, p. 2081 (1992).
Overview on the physics design for Wendelstein 7-X; very condensed.
- G. Grieger et al., “Das Fusionsexperiment Wendelstein 7-X”, *Physikalische Blätter*, vol. 49, p. 1001 (1993).
Very basic article.
- P. Helander, “Theory of plasma confinement in non-axisymmetric magnetic fields”, *Reports on Progress in Physics*, vol. 77, p. 087001 (2014).
Basic stellarator theory, recommended for students entering the field.
- P. Helander et al., “Stellarator and tokamak plasmas: a comparison”, *Plasma Physics and Controlled Fusion*, vol. 54, p. 124009 (2012).
Overview of the physics differences between tokamaks and stellarators.
- W. Lotz et al., “Optimization, MHD mode and α -particle confinement behaviour of Helias equilibria”, *Proceedings IAEA* (1992).
Describes the optimisation leading to Wendelstein 7-X; advanced reading.
- K. Miyamoto, “Plasma Physics for Nuclear Fusion”, The MIT Press (1989).
Some chapters include stellarator specific issues.
- J. Nührenberg, “Quasi-symmetries in toroidal confinement”, *Europhysics News*, p. 216 (Dez. 1998).
A short introduction into the concept of quasi-symmetries.
- F. Wagner, “Stellarators and optimised stellarators”, *Transactions of Fusion Technology*, vol. 29, p. 407 (1996).
Very good introduction, recommended.
- F. Wagner, “Topics in toroidal confinement”, *Plasma Physics and Controlled Fusion*, vol. 39, p. A23 (1997).
Experimentally oriented introduction.
- M. Wakatani, “Stellarator and Heliotron Devices”, Oxford University Press (1998).
One of the few books about stellarators but written very technically.

Chapter 13

Stellarator experiments

Thomas Windisch

13.1 Introduction

The stellarator concept was introduced by Lyman Spitzer Jr. in 1951. In a far-sighted article Spitzer described the idea of magnetic flux surfaces, i.e. a toroidal surface enclosing a certain magnetic flux $\psi = \text{const.}$, which is densely covered with magnetic field lines that lie in the surface $\mathbf{B} \cdot \nabla \Psi = 0$. If the field lines do not close they cover the toroidal surface ergodically and since they cannot cross each other, the field must proceed in the poloidal direction as it proceeds in the toroidal direction encircling the surface helically (see Fig. 13.1).

Hence, the magnetic field needs a certain twist or rotational transform ι , which is the ratio of poloidal and toroidal turns. The key element of magnetic confinement are nested flux surfaces

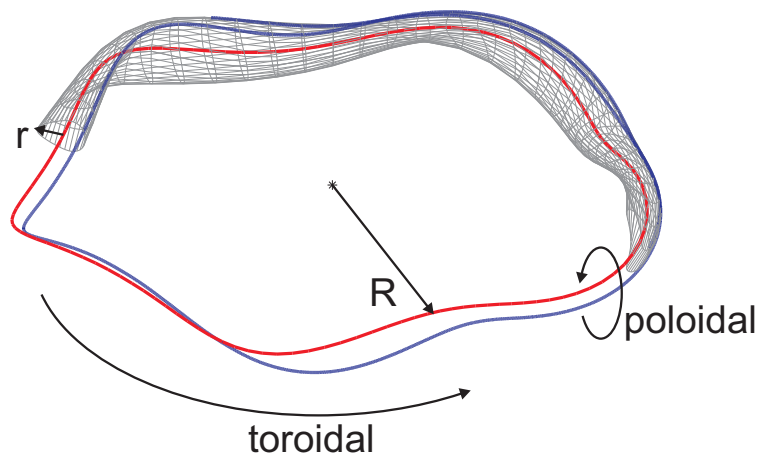


Figure 13.1: Toroidal magnetic confinement: flux surface (grey), helical magnetic axis (red) and open magnetic field line (blue).

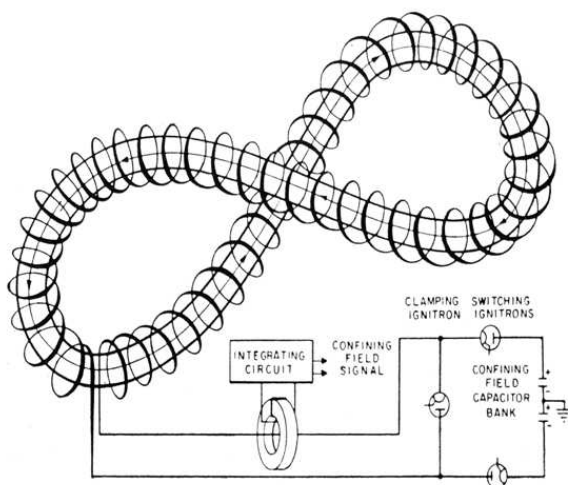


Figure 13.2: Figure-8 stellarator as proposed by Spitzer in 1951 [1].

with a small distance between the surfaces such that $|\nabla\Psi| \neq 0$ except on the magnetic axis, where the flux surface collapses to a single magnetic field line. As Spitzer recognized there are three possibilities to produce a rotational transform:

1. by a non-planar magnetic axis,
2. by an elongation and poloidal rotation of the flux surfaces, e.g. due to a transverse magnetic field whose direction rotates with distance along the magnetic axis ,or,
3. by driving a toroidal current.

Since a stellarator uses the first two concepts it allows for a large variety of non-axisymmetric helical confinement devices in which the magnetic field is solely produced by external coils without plasma currents. In contrast, the tokamak - conceptually developed also in 1951 by Tamm and Sakharov - relies only on the third method. The toroidal current is induced using ohmic transformers which makes tokamaks pulsed. Other non-inductive current drive mechanisms do exist but they are economically not efficient (a large fraction of the power produced in a fusion reactor is needed to sustain the current drive). Moreover, the tokamak suffers from current-driven instabilities leading in the worst case to disruptions. In contrast, the stellarator has a steady-state capability without plasma currents and without a hard upper density limit as a tokamak (Greenwald limit) but suffers from unconfined particle orbits as described below and a complex three dimensional geometry.

Spitzer proposed a figure-8 stellarator (see Fig. 13.2), where the rotational transform ($t/2\pi = 0.5$) is produced by the geometry. His idea was that the curvature and ∇B -induced particle drifts

$$\mathbf{v}_D = -(W_{\perp} + 2W_{\parallel}) \frac{\nabla \mathbf{B} \times \mathbf{B}}{qB^3}, \quad (13.1)$$

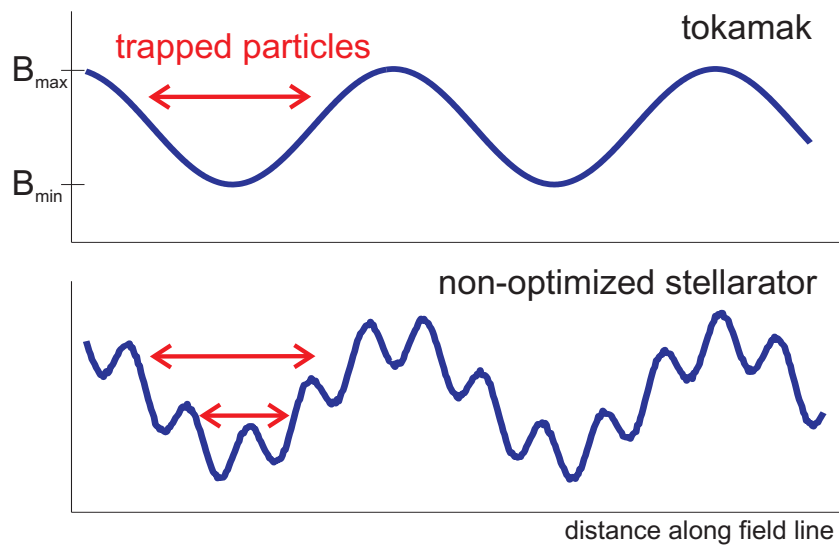


Figure 13.3: Magnetic field B along a magnetic field line for a tokamak and stellarator configuration.

where W denotes the parallel and perpendicular component of the kinetic energy, in one u-bend are compensated by the second u-bend. Without compensation the charge separation caused by the drift gives rise to an vertical electric field that leads to a rapid $\mathbf{E} \times \mathbf{B}$ -loss of the plasma.

For practical reasons the realized figure-8 stellarators, e.g. the largest being the Model-C stellarator in Princeton (1961-1969), had a racetrack-type geometry with consecutive straight and curved sections. These early stellarator experiments suffered from a small confinement time in the order of only a few Bohm times $\tau_{Bohm} = a^2/D_B$, with a being the minor radius and $D_B = T_e/(16B)$ is the Bohm diffusion coefficient and $T_e \approx 100$ eV. This was a major drawback for the stellarator concept since russian scientist reported in 1968 a tokamak confinement time of 30 Bohm times at much higher electron temperatures ($T_e = 1$ keV). The poor confinement in the early stellarator experiments were most likely caused by the large error fields induced by the transitions from straight to curved sections leading to a large fraction of unconfined particle orbits. It was soon realized that in the absence of axisymmetry of a three-dimensional stellarator field new classes of trapped particles do exist.

This is illustrated in Fig. 13.3, where the modulus of the magnetic field along a field line is displayed for a tokamak and stellarator geometry. For a tokamak, $B = |\mathbf{B}|$ varies in a periodic manner. Particles with a small velocity parallel to the magnetic field, $v_{\parallel} \leq v_{\perp}$, can be trapped in a magnetic mirror as they move from the low-field side to the high-field side. During their bounce motion between the mirror points the particles suffer from radial drift \mathbf{v}_D , which lead to so-called banana orbits in the poloidal projection of their bounce motion (see Fig. 13.4). Due to the toroidal symmetry of the tokamak magnetic field the inward and outward drift balance each other. In contrast to the axisymmetric (two-dimensional) tokamak, the stellarator exhibits in addition complex helical magnetic field ripples (cf. Fig. 13.3), i.e. local minima of magnetic field strength.

These helically trapped particles can suffer from unconfined drift orbits with large radial drifts up to a large fraction and hence spoil the confinement. As it was early realized this could be

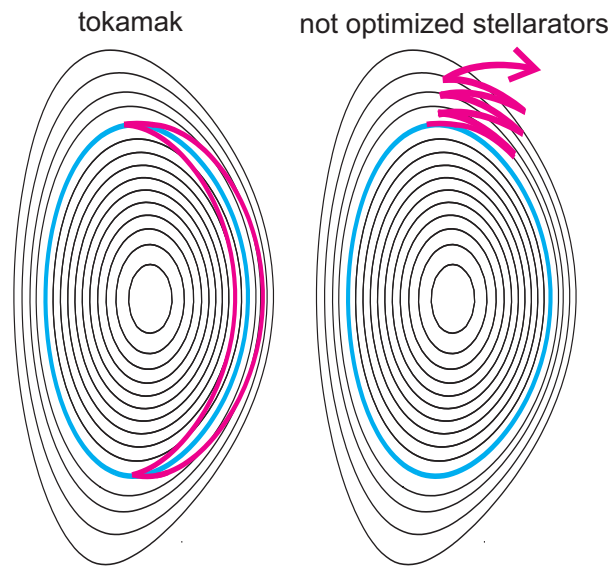


Figure 13.4: Poloidal cut of a tokamak banana trajectory and an unconfined particle orbit of a helically trapped particle in a stellarator.

a severe problem for a fusion reactor. The fast alpha particles born in the fusion process are lost to the wall and damage it before dissipating their energy by collisions with bulk plasma. But also thermal electrons and ions may be lost from the hot core and limit the energy confinement time. In the absence of turbulence, the energy and particle fluxes associated with unconfined particle orbits are described within the framework of neoclassical transport theory (see sec. 13.5). In the subsequent years following the early experiments in the 1970s one of the main goals in stellarator research was to minimize the fraction of particles with unconfined orbits by using the freedom of the three-dimensional magnetic field topology. Note, that in a stellarator the fraction can only be minimized since in the absence of turbulence and collisions the guiding-center drift orbit of every particle is confined in axisymmetric plasmas only (known as *Tamm's theorem*). An in this sense perfectly optimized stellarator would be *omni-genous*, i.e. the time-averaged radial guiding center drift of trapped particles vanishes. For passing particles this is automatically fulfilled as for particle orbits in tokamaks. This imposes some constraints on the magnetic field: In an *omni-genous* field the minimum and maximum B on any flux surface form closed curves rather than isolated points. As these curves can either close toroidally, poloidally or helically a large variety of optimized stellarator configurations is possible. Early experiments and the recent quasi-symmetric developments are introduced in the following section.

13.2 Stellarator concepts

In a *classical stellarator* (see Fig. 13.5) the poloidal magnetic field is produced by $2l$ toroidally closed helical windings with opposite current in adjacent windings, while the toroidal magnetic field is produced by additional field coils. The magnetic axis is circular. Experimental flexibility is achieved since the helical and toroidal field can be varied independently. Exam-

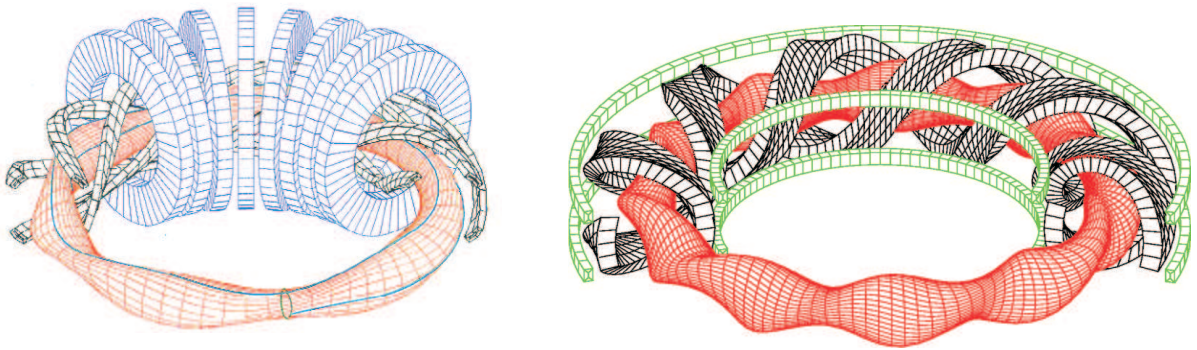


Figure 13.5: Left: A classical $l = 2$ stellarator, (W7-A). Right: *Heliotron* configuration.

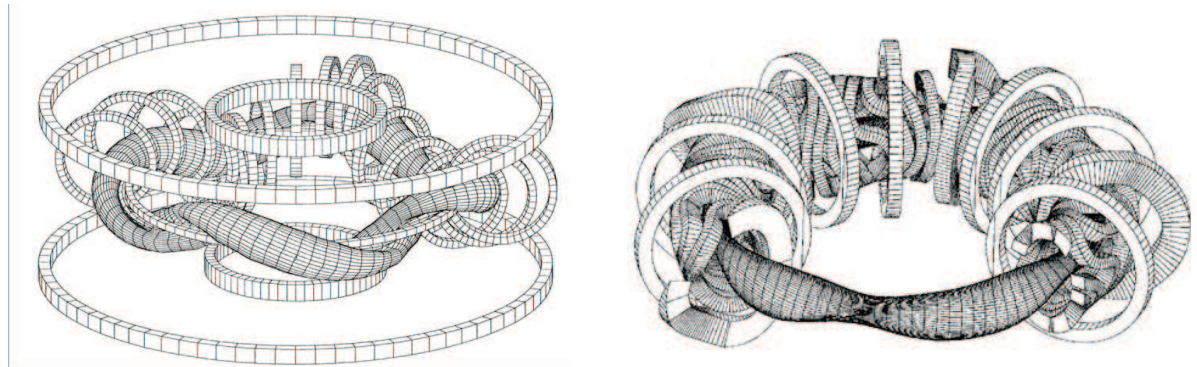


Figure 13.6: Left: Heliac configuration. Right: Advanced stellarator W7-AS.

ples are W2-A (major radius $R = 0.5$ m, $a = 0.02$ m, $l = 2$, number of field periods (toroidal turns of the helical windings) $M = 5$), and the largest ever constructed W7-A ($R = 2$ m, $a = 0.1$ m, $l = 2$, $M = 5$). The interaction between the toroidal magnetic field coils and the helical windings can lead to large radial forces acting on the helices which need heavy structural support making the concept unattractive for a fusion reactor.

In *torsatron/heliotrons* (Fig. 13.5) the poloidal and toroidal field components are produced by l helical windings with unidirectional currents. The vertical field that arises from the net toroidal current is compensated by additional poloidal field coils. Examples are *ATF* ($l = 2$, $M = 5$, $R = 2.1$ m, $a = 0.27$ m), *heliotron-J* ($l = 1$, $M = 4$, $R = 1.2$ m, $a = 0.2$ m), *CHS* ($l = 2$, $M = 8$, $R = 1$ m, $a = 0.2$ m) and largest operating helical device *LHD* ($l = 2$, $M = 10$, $R = 3.9$ m, $a = 0.6$ m, superconducting).

In a *heliac* configuration the rotational transform is produced solely by a three dimensional magnetic axis (see Fig. 13.6), i.e. circular coils placed around a helical magnetic axis. An example is TJ-II ($M = 4$, $R = 1.5$ m, $a = 0.2$ m).

In order to overcome the optimization limitations introduced by the specific concept and the large forces acting on the helical windings the concept of modular coils has been developed

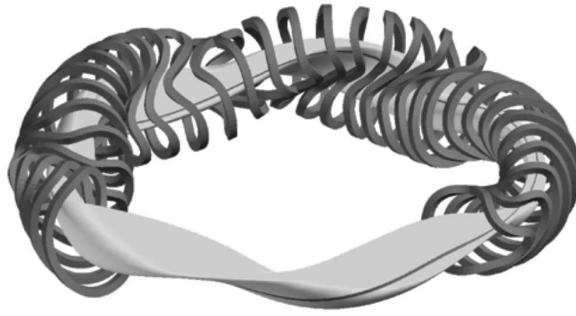


Figure 13.7: Quasi-isodynamic stellarator W7-X.

by Rekher and Wobig in 1972. The modular coil concept allows to approximate an arbitrary vacuum magnetic field inside a domain Ω tangential to the surface $\delta\Omega$ by a current sheath on this surface. The current sheath can be discretized into current lines which yield a set of modular and poloidally closed coils which than in turn reproduce this magnetic field in the domain Ω . At the same time a massive increase in computation power allowed to consider also other physics optimization criteria (see Sec. 13.3.2). The first stellarator experiment in which the magnetic configuration was the starting point to design the coils was W7-AS (see Fig. 13.6), where AS stands for advanced stellarator ($M = 5$, $R = 2$ m, $a = 0.18$ m).

As outlined in sec. 13.1 symmetries are of special importance for neoclassical confinement. The introduced quasi-symmetry of B is often only visible in certain special coordinate systems (magnetic coordinates). In a quasi-symmetric devices¹ B varies on a flux surface only through a fixed linear combination of toroidal and poloidal angles: $B(\psi, \theta, \varphi) = B(\psi, M\theta - N\varphi)$, where ψ is a flux surface label (radial), θ is the poloidal and φ the toroidal angle, respectively. Possible options are *quasi-axisymmetric* $N = 0$ (e.g. NCSX: $M = 3$, $R = 1.4$ m, $a = 0.33$ m, construction has been stopped), *quasi-poloidal symmetric* $M = 0$ and *quasihelical symmetric* $M \neq 0$ and $N \neq 0$ (HSX: $M = 1$, $N = 4$, $R = 1.2$ m, $a = 0.15$ m). In HSX it has been demonstrated that the neoclassical transport drops to tokamak level.

A different subclass of *omni-genous* optimization relies on the *quasi-isodynamic* principle, in which the parallel Pfirsch-Schlüter currents are minimized (see sec. 13.3.2). The latter increases the pressure limit and optimizes MHD stability. The *isodynamic* optimization principle has been followed in the design of W7-X ($M = 5$, $R = 5.5$ m, $a = 0.5$ m, Fig. 13.7), the successor of W7-AS. Thereby, the maximum volume averaged pressure increases from $\langle\beta\rangle = 3\%$ (W7-AS) to 5% (W7-X), making the stellarator concept economically more attractive for a fusion reactor because the fusion power scales as $P_{fus} \sim \beta^2$.

¹Quasi-symmetric devices are automatically omni-genous, meaning that all collisionless particle orbits are confined.

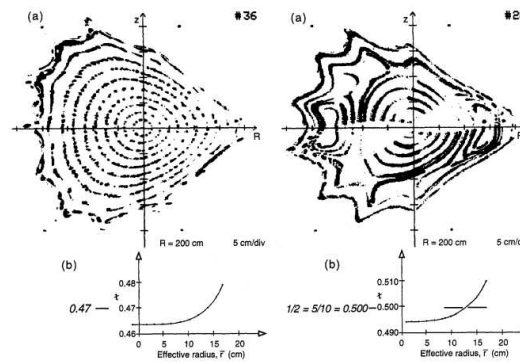


Figure 13.8: Poloidal cut of measured flux surfaces in the *W7-AS* stellarator for two different configurations of the rotational transform ι . The radial ι -profile is shown below the Poincaré plots [2].

13.3 Equilibrium

13.3.1 Vacuum magnetic field

In contrast to a tokamak, flux surfaces in a stellarator already exist in vacuum and can be measured using an electron emitter (e.g. a hot filament) and a fluorescent mesh or movable rod. The emitted electrons follow the field lines until the entire flux surface is covered (if it exists) and the fluorescence light is recorded with a camera. A poloidal cut of measured flux surfaces of two *W7-AS* scenarios with slightly different rotational transform ι are illustrated in Fig. 13.8.

On the left is a case, in which ι does not assume any low order rational value (e.g. $\iota = 1/3, 1/2, 2/3, \dots$) and unperturbed flux surfaces exist. On the right, the ι -profile covers the $\iota = 1/2$ resonance and magnetic island are clearly visible. If ι is a rational, the field lines do not cover the flux surfaces ergodically but close. Hence magnetic islands appear, if radial magnetic perturbation field with Fourier components $B_{n,m}$ (here $n = 1, m = 2$) are in resonance with the rational field line. These perturbations can be caused by external error fields (as presumably in the early figure-8 devices) or by inherent symmetries. *W7-AS* has a five-fold toroidal symmetry leading to $5/m$ -Fourier components. For this reason one observes 10 small islands ($5/10 = 1/2$) in addition to the two large islands arising from the $1/2$ -perturbation. Magnetic islands are detrimental for confinement. They offer a short circuit for radial plasma transport since they connect plasma volumes at different radii. Especially large magnetic islands can destroy the confinement due to a deterioration of flux surfaces. The width of the islands is given by $w = 4\sqrt{RB_{mn}/(m\iota')}$, where $\iota' = d\iota/dr$ is the magnetic shear. Low order rationals (low m) lead to larger island widths. The strategy of avoiding large magnetic islands is either based on a large magnetic shear (e.g. *LHD*) or by a flat iota profile that does not cover a low order rational (e.g. *Wendelstein* devices). A large magnetic shear keeps the island size small but at the same time the distance between the islands decreases and a large number of overlapping islands may exist which leads to an edge ergodic region with poor confinement. Typical radial ι -profiles of different devices are illustrated in Fig. 13.9. In stellarators the shear

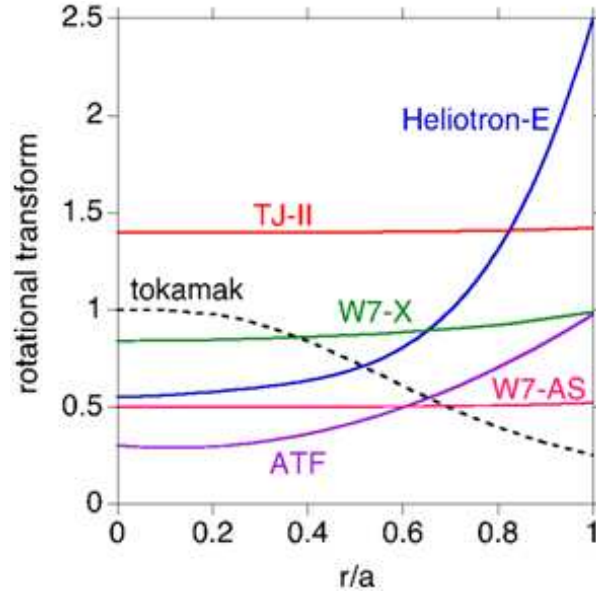


Figure 13.9: Radial profile of the rotational transform ι for different helical devices compared to a standard tokamak configuration (dashed line).

increases usually from the magnetic axis to the edge due to its generation by external coils. This corresponds to the reversed shear scenarios in tokamaks, where the shear is caused by the toroidal current in the center.

13.3.2 Plasma Equilibrium and MHD stability

In the presence of a plasma the vacuum magnetic field is altered by the currents flowing in the plasma. The MHD equilibrium of a magnetically confined plasma is determined by the radial force balance between the pressure gradient ∇p and the Lorentz force of the perpendicular current density \mathbf{j}_\perp ,

$$\nabla p = \mathbf{j} \times \mathbf{B} \quad \text{with} \quad \nabla \times \mathbf{B} = \mu_0 \mathbf{j} \quad \nabla \cdot \mathbf{B} = 0, \quad (13.2)$$

which in turn determines the perpendicular current density $\mathbf{j}_\perp = \mathbf{B} \times \nabla p / B^2$, which is called diamagnetic since it reduces the magnetic field inside the plasma. The quasi-neutrality condition $\nabla \cdot \mathbf{j} = \nabla \cdot \mathbf{j}_\perp + \nabla \cdot \mathbf{j}_\parallel = 0$ implies the existence of a parallel current in toroidal geometry, the so-called Pfirsch-Schlüter (PS) current. For an axisymmetric configuration it reads $j_{PS} \approx (2j_\perp / \iota) \cos(\theta)$. The diamagnetic and PS currents are no real currents since none of them is divergence free. In the particle picture the PS currents balance the charge separation of electrons and ions that arises from the curvature drifts (see Fig. 13.10).

The PS currents flow at different directions at the inside respectively outside of the torus. This dipole structure gives rise to a vertical field that causes a horizontal shift of the plasma axis relative to the outermost flux surface, the so-called Shafranov shift Δ . This means that the PS currents lead to a pressure induced change of magnetic field configuration. Reconstructed

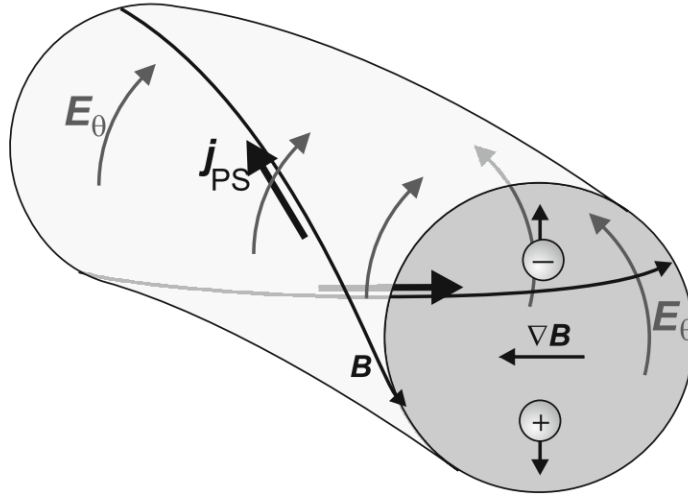


Figure 13.10: Pfirsch-Schlüter currents in a toroidal plasma [3].

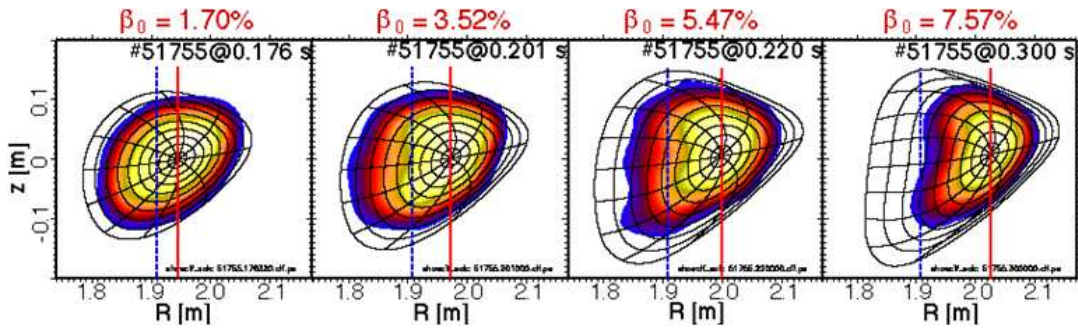


Figure 13.11: Shafranov shift observed in W7-AS for increasing plasma pressure β [Weller].

W7-AS flux surfaces for increasing plasma pressure β are shown in Fig. 13.11. The Shafranov shift of the magnetic axis is clearly observed. For a low-beta, large aspect ratio the Shafranov shift is given by $\Delta/a = R/a(\epsilon_{01}/\epsilon_t)^2 \langle \beta \rangle / (2\iota^2)$, where ϵ_{01} is the Fourier harmonic of the equilibrium field inhomogeneity associated with the toroidal curvature, $\langle \dots \rangle$ denotes the volume average and $\epsilon_t = r/R$ is the inverse aspect ratio. For a tokamak $\epsilon_{01} = \epsilon_t$. Hence, the Shafranov shift can be either reduced by reducing the aspect ratio R/a , increasing the rotational transform ι (e.g. as in torsatrons/heliotrons) or by decreasing the toroidal curvature ϵ_{01} (as e.g. in the Wendelstein devices). Along the Wendelstein optimization the factor ϵ_{01}/ϵ_t decreased from 1 (W7-A) via 0.7 (W7-AS) to 0.4 (W7-X). The reduction of the toroidal curvature can be achieved by an increase of the average elongation $\kappa = b/a$ (with b and a being the major and minor axes of an ellipse) of the flux surfaces (3D-shaping). The latter reduces the poloidal variation of B on a flux surface, which in turn also reduces neoclassical ripple losses. A result of 3D-shaped flux surfaces is shown in Fig. 13.12 for W7-AS at $\beta = 2\%$ and W7-X at $\beta = 5\%$.

Applying these optimization criteria an additional vertical magnetic field for plasma position

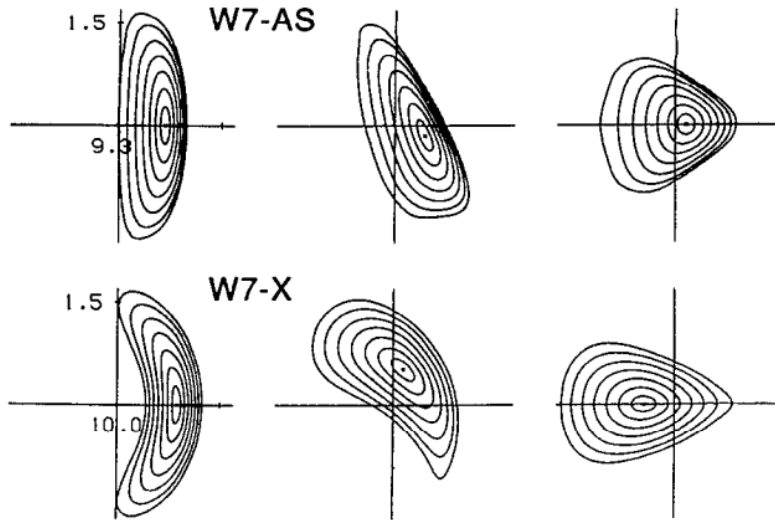


Figure 13.12: A comparison of computed flux surfaces for W7-AS ($\beta = 2\%$) and its successor W7-X ($\beta = 5\%$) [4].

control might be not necessary and the equilibria become stiff with respect to the plasma pressure. The Shafranov shift sets an operational limit for the maximum plasma pressure due to a progressive deterioration of flux surfaces. This β -limit is defined as $\Delta = a/2$, i.e. when the Shafranov shift of the magnetic axis reaches half the minor radius.

Concerning stellarator optimization small PS currents are desirable, which results in the limit $j_{PS} = 0$ in the net-current free case $\nabla \cdot \mathbf{j}_{\perp} = 0$ determined by $(\mathbf{B} \times \nabla \mathbf{B}) \cdot \nabla p = 0$ (Palumbo limit). In this *isodynamic* limit (s. Sec. 13.1) the neoclassical transport would be zero. However, the criterion cannot be fulfilled in toroidal geometry. Reducing the PS currents means reducing the geodesic curvature κ_g , since $\nabla \cdot \mathbf{j}_{PS} = -2|\nabla p|\kappa_g/\mathbf{B}$. κ_g describes the projection of the curvature vector onto the magnetic surfaces. The geodesic curvature of a magnetic field line vanishes if it is a geodesic (such as shortest airplane flight paths between two different locations on earth). In a *quasi-isodynamic* configuration the lines of constant current, i.e. the sum of the PS and diamagnetic current, $\mathbf{j}_{PS} + \mathbf{j}_{\perp}$, are poloidally closed and the net toroidal current vanishes. The situation changes at low collisionality, where the so-called bootstrap current gives rise to a net toroidal current that can alter the magnetic field configuration. The bootstrap current is caused by the pressure gradient and relies on the momentum transfer from trapped particles to passing particles, $j_b \sim (f_t/f_p)\nabla p$, where f_t and f_p denotes the fraction of trapped and passing particles, respectively. While the bootstrap current increases ι in a tokamak and thus helps to achieve a rotational transform, helically trapped particles in a stellarator lead to a j_b -component that lowers ι and thus changes the magnetic shear ι' which in turn leads to the formation of a magnetic well.² In the ATF torsatron (see Fig. 13.13) it has been demonstrated that the bootstrap current can be controlled by modifying the Fourier components of the mag-

²A magnetic well exist if the average magnetic field on a magnetic flux surface increases with enclosed volume, or in other words, if the flux surface has an average favorable curvature.

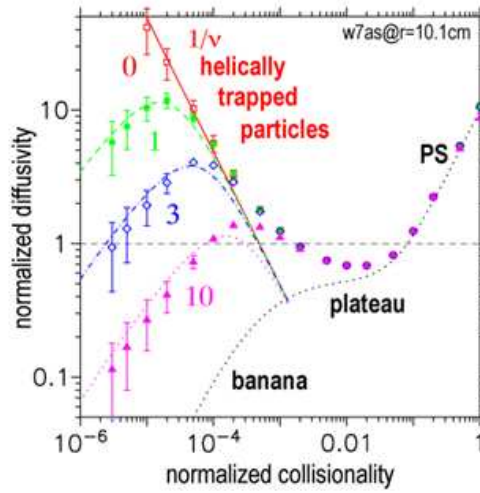


Figure 13.14: Theoretically predicted normalized neoclassical diffusion coefficient for a stellarator and tokamak configuration. The different curves in the low collisionality $lmfp$ -regime correspond to different values of the radial electric field.

coefficient is $D = d^2\nu$, where d is the step size and ν the collision frequency. The particle flux Γ is then given by Fick's law, $\Gamma = -D\nabla n$. While classical diffusion describes the situation in a homogeneous magnetic field, in which the step size is determined by the Larmor radius, the additional guiding-center drift v_D of inhomogeneous magnetic fields lead to larger step sizes. The transport associated with the guiding-center drifts in toroidal magnetic fields is described by the neoclassical theory. For a fusion reactor the long mean free path ($lmfp$) regime with high temperatures (low collisionality) is most relevant. In a stellarator the radial heat flux caused by the radial $\nabla\mathbf{B}$ -drift of ripple-trapped particles scales in the $lmfp$ -regime for small electric fields as $D \sim T^{9/2}$. At the same collisionality the heat flux in a tokamak scales in the banana regime only with $D \sim \sqrt{T}$. At higher collisionality the diffusivities in tokamaks and stellarators are comparable. A comparison of the particle diffusion coefficient as a function of normalized collisionality is shown in Fig. 13.14. In a tokamak the diffusion coefficient increases linearly with collisionality in the banana and Pfirsch-Schlüter regime. In the banana-regime toroidally trapped particles bounce between the reflection points (cf. Fig. 13.3) and can get de-trapped by a collision that displaces the banana particle by the banana width, which determines the step size. In the high-collisional Pfirsch-Schlüter regime passing particles cannot complete their poloidal orbit before experiencing a collision and thus the step size is determined by the displacement of the particles by the gradient and curvature drifts v_D , $D = v_D\tau/\tau^2$, with the collision time $\tau = 1/\nu$.

The transition region (plateau regime) is determined by a gradual decrease of the step size with increasing collisionality since the particles cannot complete their banana orbit before experiencing a collision. In a stellarator the plateau and Pfirsch-Schlüter regimes are recovered, but in the low collisionality $lmfp$ regime a $1/\nu$ -regime exists due to helically ripple trapped

particles. In the $1/\nu$ -regime the diffusion coefficient scales as³

$$D_{1/\nu} \sim (\varepsilon/\varepsilon_t)^2 \varepsilon_h^{3/2}, \quad (13.3)$$

where ε_h is the helical ripple modulation, ε is the poloidal variation of B and ε_t the inverse aspect ratio. Hence, decreasing the average toroidal curvature by elongating the plasma helps to reduce the diffusivity in the $1/\nu$ -regime. The presence of a radial electric field E_r can compensate the large diffusivity in the $1/\nu$ -regime, since the associated poloidal $\mathbf{E} \times \mathbf{B}$ -drift partly averages out the $\mathbf{B} \times \nabla \mathbf{B}$ -drift. The reduction of the diffusivity in the *lmfp*-regime for increasing E_r can clearly be observed in Fig. 13.14.

The ambipolar radial electric field is in the absence of impurities determined from the balance of thermal electron and ion fluxes $\Gamma_e = Z_i \Gamma_i$ with

$$\Gamma_\alpha = -n_\alpha \left[D_{11}^\alpha \left(\frac{\nabla_r n_\alpha}{n_\alpha} - \frac{q_\alpha E_r}{T_\alpha} \right) + D_{12}^\alpha \frac{\nabla_r T_\alpha}{T_\alpha} \right], \quad (13.4)$$

with $\alpha = e, i$ and the neoclassical radial transport coefficients D_{11} (diffusive transport) and D_{12} (flux driven by temperature gradients). In dependence on the heating method other externally driven fluxes may contribute (neutral beam injection *NBI*). In the *lmfp*-regime the solution of the ambipolarity condition has multiple roots, because the transport coefficients depend on E_r , $D_{ik} = f(E_r, \nu, r)$. For $T_e \gg T_i$ (peaked core electron temperature profiles and flat ion temperature profiles) the electron fluxes exceed the ion fluxes if $E_r = 0$. Hence, a positive E_r arises in the core that reduces the high electron flux Γ_e to the ion level. This is the so-called electron root. This regime is typically observed at low-density ECRH discharges, i.e. when the energy balance is dominated by the electrons and the ions are energetically decoupled by low collisionality leading to $T_e \gg T_i$. In contrast, at high densities (higher collisionality, $T_e \sim T_i$) the ion-root with moderate E_r in the core and strong negative E_r in the plasma edge is observed. The latter is caused by large fluxes induced by ion temperature gradients that are balanced by the negative electric field. In Fig. 13.15 a W7-AS discharge is shown that reflects the electron-root regime in the core. As in Fig. 13.15 c, often multiple solutions of the ambipolarity condition are possible (red symbols). The measured E_r follows the electron root in the core and the ion-root in the edge.

The condition of core electron-root (positive E_r) and edge ion-root (negative E_r) can lead to a large shear of the radial electric field and the associated poloidal $\mathbf{E} \times \mathbf{B}$ -drift. This is further supported by the electron flux to target plates or limiters in the region of open magnetic field lines, which causes a positive E_r . Sheared flows are an important turbulence reduction mechanism by decorrelating turbulent structures. This reduces turbulent transport, which usually exceeds the neoclassical transport in the far edge. The influence of this large turbulent, so-called anomalous, transport is e.g. observed in Fig. 13.15 d, where the estimated heat diffusivity χ_e clearly exceeds the neoclassical predictions in the edge ($r > 13$ cm).

For a fusion reactor the ion-root regime with $T_e \sim T_i$ and moderate E_r in the core is most relevant. This is somehow in contradiction to the need to overcome the poor $1/\nu$ -scaling in the *lmfp*-regime by a finite E_r . However, since the radial electric field cannot be well controlled

³For a classical stellarator the magnetic field can be written as $B/B_0 = 1 - \varepsilon \cos \theta - \varepsilon_h \cos(l\theta - M\phi)$. For a tokamak $\varepsilon \approx r/R = \varepsilon_t$ and $\varepsilon_h = 0$.

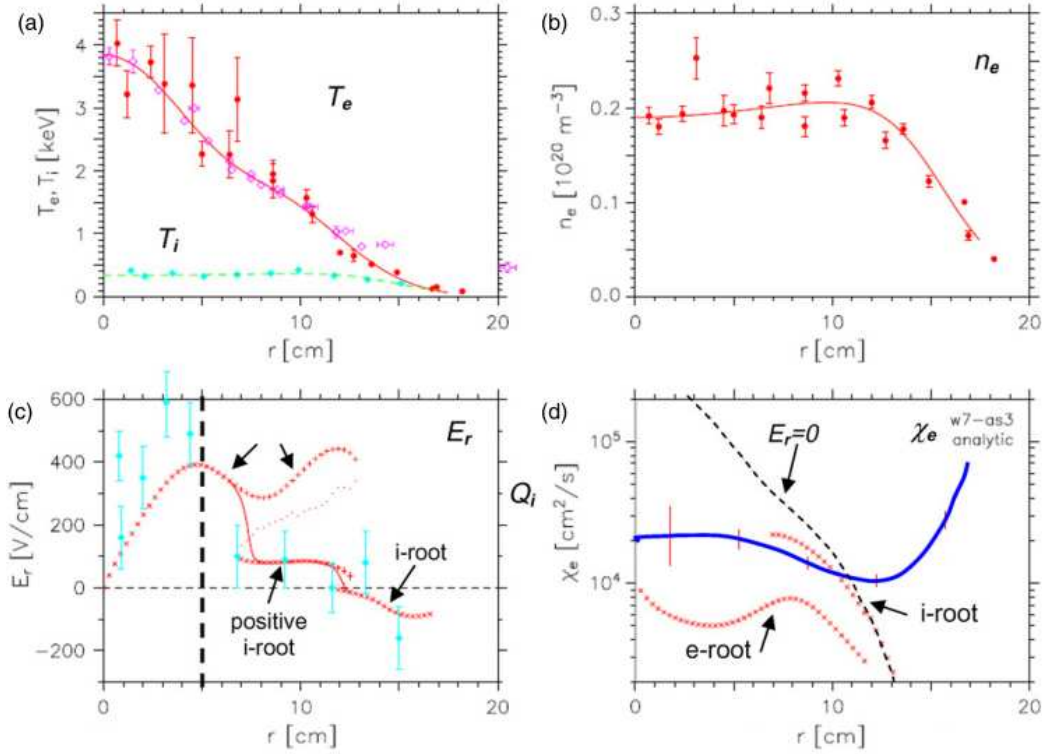


Figure 13.15: Low density core electron-root conditions observed in W7-AS. Shown are radial profiles of (a) temperatures, (b) density, (c) radial electric field and (d) electron heat diffusivity (blue: measured, dashed: neoclassical prediction) [6].

experimentally recent stellarators are optimized to have small $1/\nu$ -transport per se. An important cross-machine measure is the effective helical ripple ε_{eff} , that can be estimated from the D_{11} coefficient, $D_{11} \sim \varepsilon_{eff}^{3/2}$. Calculated radial profiles of ε_{eff} are shown Fig. 13.16 for LHD, W7-AS and W7-X. The huge reduction of ε_{eff} by optimization is nicely observed in LHD, where the magnetic axis can be shifted. With inward shifted axis the ripple decreases leading to smaller neoclassical losses as compared to the standard configuration. From W7-AS to W7-X ε_{eff} is reduced by a factor of 10.

13.5 Confinement

As outlined in the previous section, the turbulent (or anomalous) transport can significantly contribute and even exceed the neoclassical losses. Since the detailed mechanisms behind this anomalous transport are not fully understood empirical scaling laws are used to describe the dependence of the observed transport on some leading parameters. The derived *ISS04* scaling for the global energy confinement time $\tau_e = W/(P - dW/dt)$, where W is the plasma energy and P is the heating power, reads

$$\tau_e^{ISS04} = f \cdot 0.134 a^{2.28} R^{0.64} \bar{n}_e^{0.54} B^{0.84} (t_{2/3}/(2\pi))^{0.41}, \quad (13.5)$$

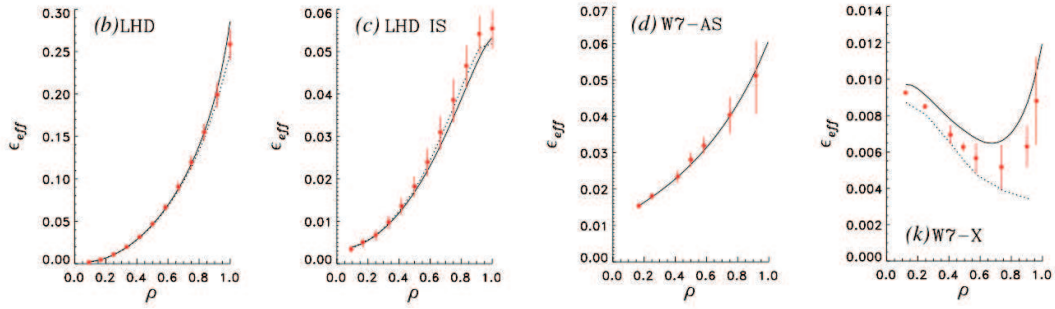


Figure 13.16: Calculated effective helical ripple ε_{eff} in the $1/\nu$ -regime. From left: *LHD* (standard), *LHD* (inverse shifted magnetic axis), *W7-AS* and *W7-X* [7].

where ι is taken at $2/3$ of the minor radius. The configuration factor f summarizes the magnetic configuration details. The maximum (best confinement) value is 1. *W7-AS* at low ι reaches $f = 1$ and *LHD* with inward shifted configuration $f = 0.93$. Similar to tokamaks a power degradation is observed: τ_e decreases with heating power. The energy confinement time of different helical devices is compiled in Fig. 13.17, together with typical tokamak data. Stellarator and tokamak have comparable confinement times. The influence of the magnetic configuration on the stored plasma energy is illustrated in Fig. 13.18 for net-current free discharges in *W7-AS*. The plasma energy shows pronounced maxima if boundary value of ι is close to a low-order rational ($\iota = 1/3, 2/5, 1/2$). An empirical model relying on an enhanced electron heat conductivity on rational surfaces is able to explain the observations (solid line in Fig. 13.18) but leaves the involved physical processes open. An explanation of the radial transport processes near or at rationals is missing.

The high confinement (*H*-mode) regime first observed in tokamaks also exists in stellarators as demonstrated first in *W7-AS* in 1992. In general, the *H*-mode is related with a sheared radial electric field at the plasma edge that suppresses turbulence and hence increases the confinement typically by a factor of two. As a result steep gradients of the plasma parameter develop at the edge. The necessary shear of the radial electric field can be driven, for example, by neo-classical fluxes. The *H*-mode goes along with an improved particle and impurity confinement which lead in the absence of ELMs (edge localized modes) to a degradation of the plasma energy if the impurities radiate a fraction 50–60% of the energy. ELMs relax the pressure gradient and expel particles and energy from the core. For a large distinct ELM the particle and energy losses are typically 5%. The so-called quiescent *H*-mode without ELMs is prone to impurity accumulation leading to a radiative collapse. An example of a *W7-AS* quiescent *H*-mode accessed during a density ramp is shown in Fig. 13.19. At the transition the edge radial electric field decreases dramatically leading to a large shear rate. In the following the plasma energy W increases but also the radiation (obtained from bolometry) due to improved impurity confinement. If the radiation reaches a certain threshold the stored energy decreases and the quiescent *H*-mode falls back to an ELMy *H*-mode. Since the large particle and energy fluxes associated with ELMs can severely damage the plasma facing components in a fusion reactor ELM-free high confinement modes as the High Density *H*-Mode (*HDH*-mode) are envisaged. The *HDH*-mode became accessible in *W7-AS* with successful island divertor operation

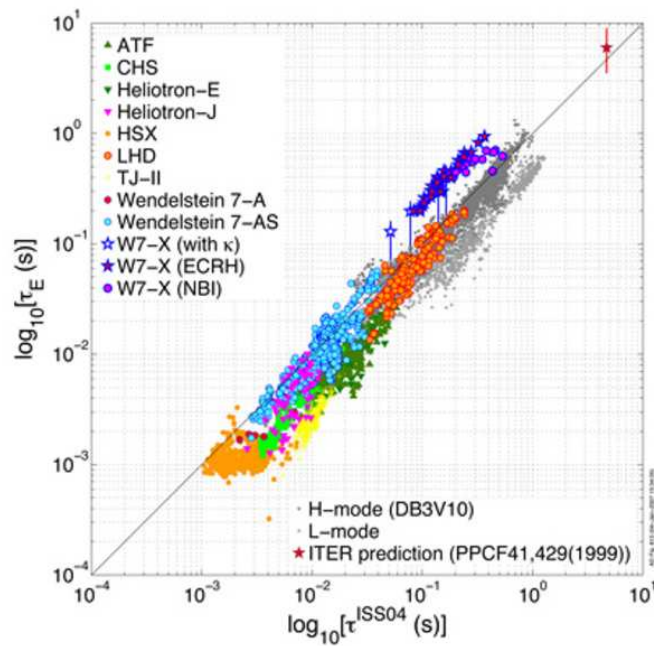


Figure 13.17: Energy confinement data of helical devices and properly rescaled tokamak configuration vs. the ISS04 scaling [<http://ipp.mpg.de/ISS>].

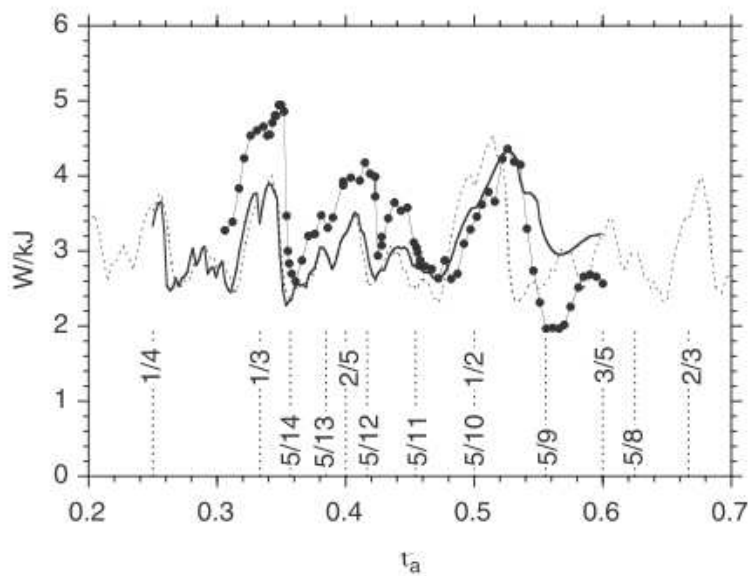


Figure 13.18: Plasma energy as a function of the edge τ value in net-current free W7-AS discharges (dotted: measurement, solid: model) [8].

at densities $n > 10^{20} \text{ m}^{-3}$. The *HDH*-mode is characterized by large decrease of the impurity confinement time due to impurity screening as indicated in Fig. 13.20.

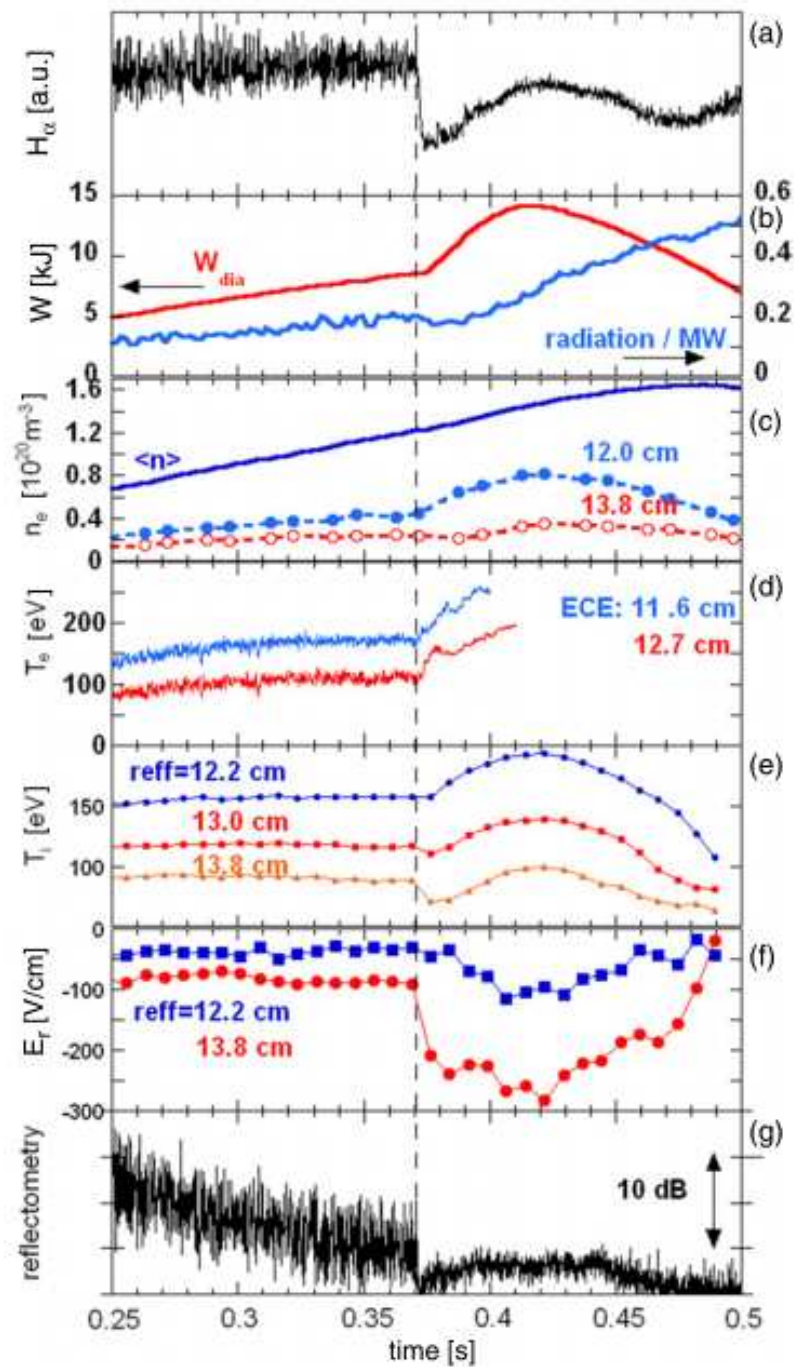


Figure 13.19: Transition into a quiescent H -mode by ramping the density. The transition time is indicated by the dashed line [9].

13.5.1 Impurity transport and divertor concepts

As discussed in the last section radiation losses due to impurity accumulation limits the pulse length and acts as a soft density limit in stellarators. For a steady-state device these losses have to be avoided. The impurity dynamics is determined by three different interaction zones:

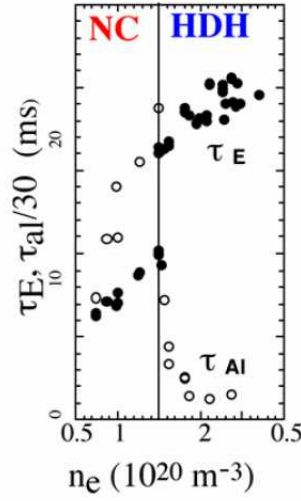


Figure 13.20: Energy confinement time τ_e and Aluminum impurity confinement time τ_{Al} during the transition from normal confinement (NC) to the HDH-mode [10].

1. Plasma-facing components with recycling and erosion of wall material,
2. The region of open flux surfaces (the so-called scrape-off layer (*SOL*)), which regulates the impurity influx to the confined region with closed field lines and
3. the plasma core.

The impurity influx from the wall can be reduced by proper wall conditioning and the flux across the *SOL* can be partially controlled by the magnetic configuration and edge density. However, the impurity transport in the confined region is determined by neoclassical transport

$$\Gamma_z = -n_Z D_z \left[\frac{\nabla_r n_Z}{n_Z} + \gamma_Z \frac{\nabla_r T_i}{T_i} - Z \left(\frac{\nabla_r n_i}{n_i} + \gamma_i \frac{\nabla_r T_i}{T_i} \right) \right], \quad (13.6)$$

where E_r has been replaced by the standard ion-root solution (cf. (13.4)). While the factor γ_i in front of the thermal gradient can be negative for a tokamak (impurity or temperature screening if ions are in the banana regime) it is almost always positive for stellarators. This means that for peaked ion temperature profiles impurity accumulation is always predicted. This does not hold for the low-density electron-root, but this is not important as this scenario has no fusion reactor relevance. A possible answer to the problem is to shield the impurity influx to the core in the *SOL*. An effective impurity retention can be achieved by a proper divertor. A divertor regulates the particle and power exhaust by channeling the fluxes to cooled target plates, where the neutralized particles can be pumped. The divertor concept has been proposed by Spitzer already in 1951 in order to overcome the direct contact of the plasma with a limiter and to increase the pumping efficiency of neutrals, i.e. the helium ash in fusion reactor, by an increased neutral pressure in the divertor chamber.

Different divertor concepts are compiled in Fig. 13.21 a. In all concepts particles leaving the confined plasma core with closed flux surfaces are diverted in the open field line region along magnetic field lines that terminate on target plates. Tokamaks have additional coils that produce one or two Null point(s) (X-point) in the poloidal plane (single or double null configurations). In low-shear stellarator experiments naturally occurring islands provide a natural separation between the confined and unconfined region (local island divertors). In large shear experiments (e.g. LHD) a stochastic ergodic layer exists (see sec. 13.1). After passing this region the particles follow one of the four divertor legs produced by the two helical coils (helical divertor). The subtle divertor dynamics in tokamaks and stellarators is quite different, which is mainly caused by the different diversion field line pitches Θ at the divertor target plates. For a tokamak $\Theta = B_{pol}/|\mathbf{B}| \approx 0.1$ while for an island divertor $\Theta = w l' a/R \approx 0.001$. Due to the smaller pitch angle the connection length L_c , i.e. the distance the particles have to travel before hitting the target, can become much larger in a stellarator. At the same time the perpendicular distance from the X-point to the target is much smaller. While in a tokamak the *SOL* transport is mainly determined by parallel heat conduction q_{\parallel} along the open field lines, the larger L_c and smaller target-to-core distance of a stellarator enhance the perpendicular transport across the magnetic islands.

In reducing the neutral inventory two effects are important: First, the islands screen the core from penetrating neutrals. If the island density (associated with the density n_{es} upstream from the targets) is sufficiently large and the island temperature is kept above the ionization energy the neutral penetration length becomes very small, i.e. the neutrals are ionized in the island. Hence, a barrier exists for the neutrals. If n_{es} is low the islands are transparent to the neutrals, which then can enter the confined region. As a consequence of this high n_{es} barrier fewer neutrals reach the confined region and the neutral core-fueling rate decreases. In order to further increase the core plasma density this island neutral screening effect has to overcome. This can be achieved by further increase n_{es} to cool the islands and decreasing the ionization rate in the islands. In the experiment this is achieved by strong gas puffing, which has to be applied to enter the HDH regime. A second important aspect to understand the HDH regime is the cross-field heat flux associated with magnetic islands as mentioned above. The cross-field transport can short-circuit the parallel temperature gradients between the target plates and the plasma upstream from the target plates. In reducing the parallel thermal force ($\sim \nabla_{\parallel} T_i$), which drives the neutrals into the SOL, the friction force ($\sim n v (v_{\parallel}^i - v_{\parallel}^z)$) becomes dominant in the parallel momentum balance and the impurities are dragged back to the targets. Numerical modeling results of the W7-AS local island divertor show a large decrease of the carbon impurity density in the SOL with increasing upstream density. When the density is further increased beyond the HDH-threshold, a large fraction (80-90%) of the power in the SOL is radiated by impurities within a radiation layer that shifts from the target plates towards the confined region (detachment). For a detached divertor the energy and particle fluxes to the target plates nearly vanish, which is beneficial for a fusion reactor. However, due to the complex three-dimensional island dynamics a stable detachment has not been achieved in W7-AS and LHD. The typical power deposition on a target plate as observed by a thermographic camera is shown in Fig. 13.22 for the attached and partially detached regime. The total power flux to the target is highly reduced in the detached regime although a hot spot remains.

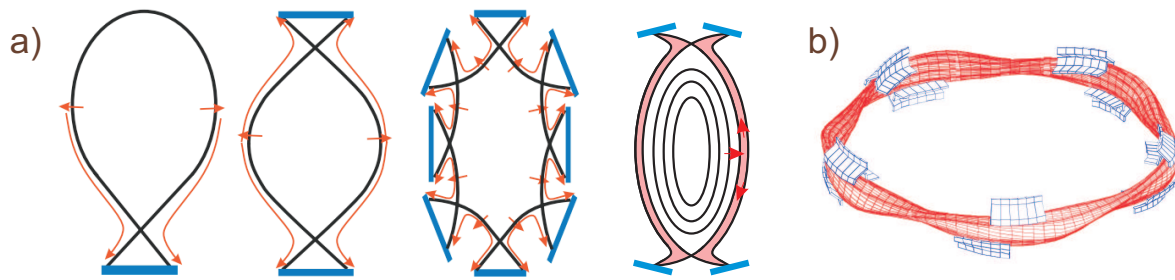


Figure 13.21: (a) Overview of divertor configurations (from left): tokamak single null, tokamak double null, island divertor, helical divertor (*LHD*). The target plates are shown in blue. (b) Local island divertor of W7-AS utilizing the 5/9 island [adapted from [11].

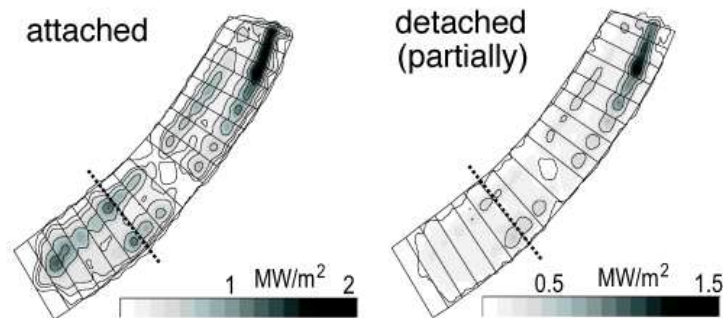


Figure 13.22: Thermographic measurement of the W7-AS local island divertor in the attached and partially detached regime [11].

13.6 Helical reactor concepts

Due to the potential to operate in steady state without current drive and the optimization success of the latest devices, the stellarator concept became (again) attractive to realize a fusion reactor. Since mechanical stability problems that arise from forces acting on the coil windings (see sec. 13.1) are limiting the possible configuration, only the heliotron and modular coil concept remain as a serious option. The developed force-free heliotron reactor (*FFHR*) relies on an upscaled *LHD* concept. In contrast, the *HELIAS* reactor relies on the modular coil concept and is an upgraded version of *W-7X*. The main parameters of *LHD*, *FFHR*, *W7-X* and the *HELIAS* reactor (*HSR 5/22*) are compiled in Tab. 13.6. The high magnetic field $B = 12\text{T}$ in the *FFHR* reactor allows to operate at fairly small β -values leading to stiff confinement properties.

parameter	<i>LHD</i>	<i>FFHR</i>	<i>W7-X</i>	<i>HSR 5/22</i>
major radius R [m]	3.9	20	5.5	22
av. minor radius a [m]	0.65	2	0.52	1.8
plasma volume V [m ⁻³]	32.5	1579	30	1407
magnetic field B [T]	4	12	3	4.75
av. plasma- β [%]	5	0.7	5	4.24
fusion power P [GW]	0	3	0	3

13.7 Summary

Starting with enthusiastic developments in the 1960's and 1970's, the stellarator concept experienced many drawbacks with respect to plasma confinement that raised skepticism. While the first devices were limited by neoclassical transport losses the outlined route of optimization lead to a dramatic increase in the confinement time. Nowadays, optimized stellarators have confinement times that are equivalent to tokamaks of comparable size. More recently, attractive confinement regimes became accessible using the island divertor concept, which is an option for power and particle exhaust in a fusion reactor. With the operation of W7-X (the commissioning of the device started already) the next optimization step towards a fusion relevant steady state plasma will (hopefully) be realized.

Recommended literature

- C. Beidler, *Helical Confinement Concepts in Fusion Physics* edited by: Kikuchi et. al, IAEA (2012).
- M. Hirsch, *Major results from the stellarator Wendelstein 7-AS*, Plasma Phys. Control. Fusion **50** 053001 (2008).
- G. Grieger, *Physics optimization of stellarators*, Phys. Fluids B **4** 2081 (1992).
- H. Wobig, *The theoretical basis of a drift-optimized stellarator reactor*, Plasma Phys. Control. Fusion **35** 903 (1993).
- P. Helander, *Theory of plasma confinement in non-axisymmetric magnetic fields*, Rep. Prog. Phys. **77** 087001 (2014).
- A. Boozer, *What is a stellarator?*, Phys. Plasmas **5** 1647 (1998).

References

- [1] T. Coor: *Experiments on the Ohmic Heating and Confinement of Plasma in a Stellarator* , Phys. Fluids **1** (1958) 411.
- [2] R. Jaenicke: *Detailed investigation of the vacuum magnetic surfaces on the W7-AS stellarator*, Nucl. Fusion **33** (1993) 687.
- [3] U. Stroth: *Plasmaphysik: Phnomene, Grundlagen, Anwendungen*, Wiesbaden: Vieweg (2011).
- [4] G. Grieger: *Physics optimization of stellarators* , Phys. Fluids B **4** (1992) 2081.
- [5] M. Murakami: *Bootstrap-current experiments in a toroidal plasma-confinement device*, Phys. Rev. Lett. **66** (1991) 707.
- [6] J. Baldzuhn: *Measurement and calculation of the radial electric field in the stellarator W7-AS*, Plasma Phys. Control. Fusion **40** (1998) 967.
- [7] C. Beidler: *Benchmarking of the mono-energetic transport coefficients results from the International Collaboration on Neoclassical Transport in Stellarators (ICNTS)* , Nucl. Fusion **51** (2011) 076001.
- [8] R. Brakel: *Electron energy transport in the presence of rational surfaces in the Wendelstein 7-AS stellarator* , Nucl. Fusion **42** (2002) 903.
- [9] M. Hirsch: *Major results from the stellarator Wendelstein 7-AS* , Plasma Phys. Control. Fusion **50** (2008) 053001.
- [10] C. Beidler: *Helical confinement concepts*, in *Fusion Physics*, edited by M. Kikuchi et al., IAEA (2012).
- [11] Y. Feng: *Physics of island divertors as highlighted by the example of W7-AS* , Nucl. Fusion **46** (2006) 807.

Chapter 14

Safety and environmental aspects of fusion

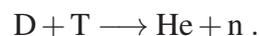
Hans-Werner Bartels

14.1 Introduction

Future fusion reactors will operate with radioactive materials: Tritium is radioactive and very mobile and the neutrons produced in the fusion reactions will activate the components near the plasma. To assess the radiological hazards of fusion, the inventories and possible release mechanisms are discussed. The behaviour of the plant during normal operation and accident situations is analyzed together with the waste management. The control of the mobile tritium is a key issue in reducing the effluents in normal operation. Associated with this is the design goal of minimizing the tritium inventories which can be released in accidents. The absence of chain reactions and the moderate decay heat densities in a fusion reactor are inherent safety-enhancing differences to fission plants. Since the neutron-induced radioactivity strongly depends on the materials used in a fusion-reactor, appropriate material selection offers the possibility of significantly influencing the amount of radioactivity produced. Generally, the decay times of fusion waste are much shorter than those of fission waste. Recycling of reactor materials after 50 to 100 years of cooling time is a potential waste management option instead of geological disposal.

14.2 Inventories

The safety implications of nuclear fusion can immediately be seen from the fundamental reaction equation



Two distinct classes of radioactive inventories follow from this:

- Tritium as part of the fuel is radioactive.

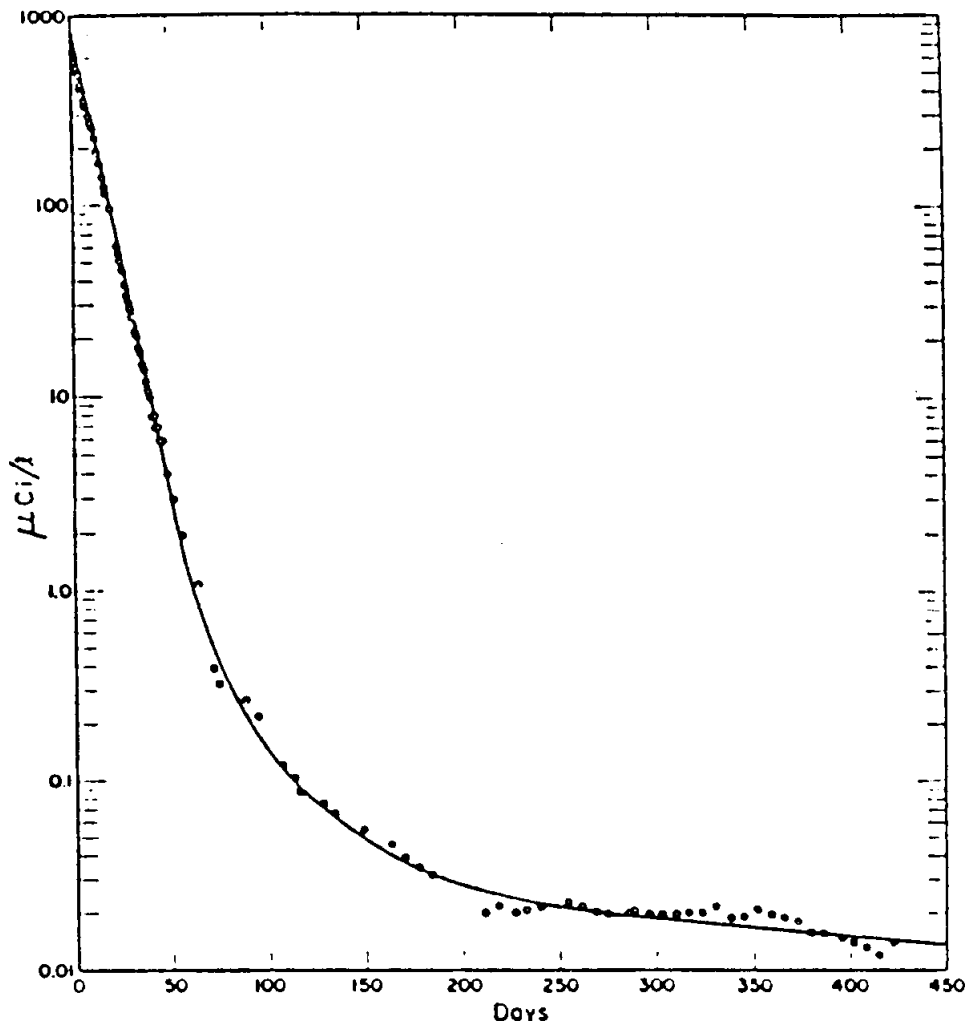


Figure 14.1: Time-dependent tritium concentration in a human after a single accidental incorporation of HTO.

- Neutrons leaving the plasma do not just produce tritium by nuclear reactions with lithium (breeding). They also perform nuclear reactions with other materials in the reactor, mainly those of structures near the plasma (first wall). Many of these reactions lead to radioactive end-products.

Tritium

The expected tritium inventory of a fusion plant amounts to a few kg. Although just 0.5 g of tritium will be inside the hot plasma, much larger amounts will be present in other systems such as the blanket, pumping system, tritium processing plant and storage.

Tritium is a weak β^- emitter with a half-life of 12.3 years. Its mean β^- energy is 5.7 keV, its maximum energy 18.5 keV. Due to the rather low energy, its mean range in organic matter is below $6 \mu\text{m}$, whereas the human skin is covered by a horny layer which is $70 \mu\text{m}$ thick. Thus tritium does not pose any hazard as an external radiator. The situation changes when tritium

is incorporated into the body via ingestion, inhalation, or skin absorption. The most common chemical species of tritiated molecules are HTO (tritiated water) and HT (tritiated hydrogen gas). Both forms are very mobile since their behaviour is similar to the non-tritiated species H_2O and H_2 . Especially HTO can easily be absorbed into the human body. Once in the body it is rapidly dissolved in the human water cycle.

Fig. 14.1 shows the decrease of tritium in the body of a technician working in a tritium laboratory who accidentally inhaled a significant amount of HTO. The measurements show a decay with three time constants. The dominating decay time of about 10 days reflects the recycling in the water compartment of the human body. A reference person weighing 70 kg has a water compartment of 42 l and a daily water exchange of about 3 l leading to a biological half-life of ten days. The longer components of about 30 and 300 days in Fig. 14.1 pertain to the exchange between water and the organic compartment. On the average the slow component accounts for roughly 10% of the tritium dose. Thus the *effective* biological half-life of tritium in the human body is 11 days.

The intake of a certain amount of tritium measured in activity A (unit: Bq = decays per second) leads to the following energy deposition in the human body

$$\varepsilon = A \cdot \tau \cdot \langle E_{\beta^-} \rangle \cdot m^{-1}$$

with ε is the energy density [J/kg], A the activity [Bq], τ the effective biological lifetime [s], $\langle E_{\beta^-} \rangle$ the average β^- energy [J] and m the mass of reference person [kg].

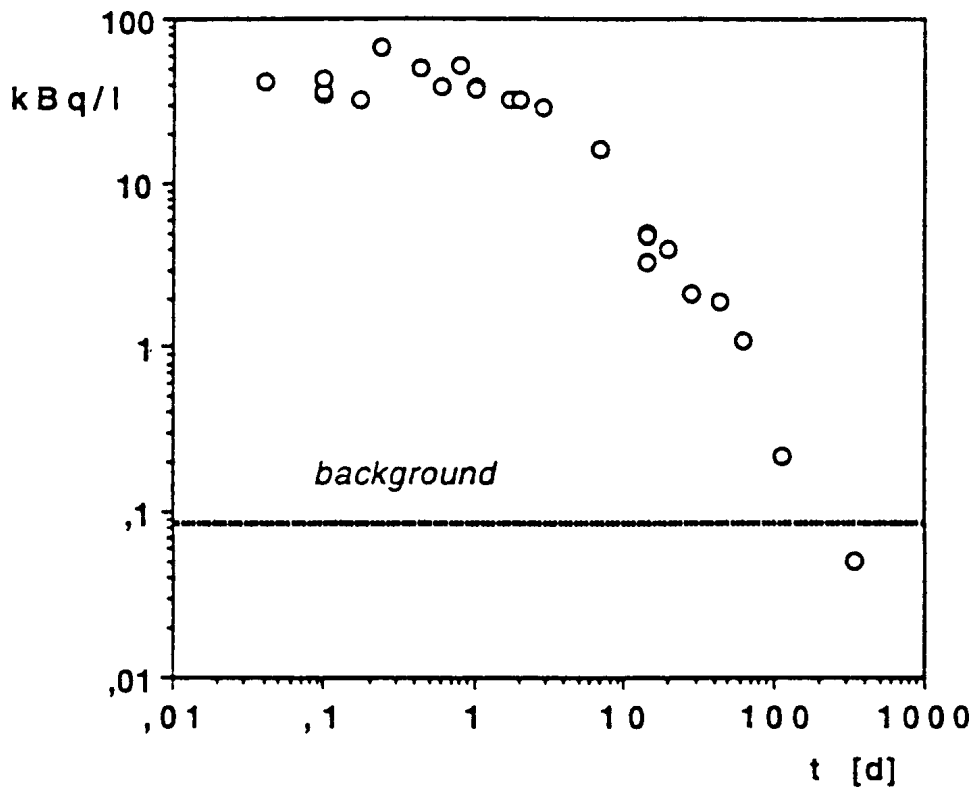
Generally, the energy dose has to be multiplied with a quality factor to account for radiation forms more hazardous than γ -rays, e.g. α -radiation is assigned a quality factor of 20. The resultant quantity is the radiation *dose* measured in units of Sievert (Sv) and allows quantification of radioactive radiation hazards to humans. For tritium the international consensus is to use $Q = 1$, but some experiments tend in the direction of $Q = 2-3$ for tritium since the low β -energy leads to localized ionization.

With $Q = 1$, the intake of 1 Bq HTO leads to a dose of 1.8×10^{-11} Sv. Intake of tritium in organic form, e.g. by eating contaminated food, would increase the dose by a factor of 2.5. This is due to a larger fraction of tritium transferred into the body compartments with longer biological lifetimes. For a given air concentration, tritiated gas (HT) is 10 000 times less hazardous than HTO since the uptake and incorporation into the body is strongly reduced. Tab. 14.2 shows a comparison of doses for different radioisotopes. It can be clearly seen that the amount of radioactivity measured in units of activity (Bq) is not a good indicator of the associated hazard. Tritium produces smaller radiation doses per Bq because the average energy per release is much smaller than for other isotopes and the effective lifetime in the human body is also shorter.

The special concern with tritium is its high volatility and the associated problems in keeping it inside the fusion plant. Once released, tritium is still very volatile. In Fig. 14.2 the specific tritium activity in soil surface water is shown versus time after a controlled release experiment in Canada. In the first year the tritium concentration dropped by a factor of 1 000 and reached the background values which were measured before the experiment. Thus strong contamination of large areas which lasts for many decades is not expected in the event of a major tritium

Table 14.1: Dose conversion factors for different isotopes.

Isotope	Dose Conversion Factor	Pathway	Relation to Tritium
Tritium	1.8×10^{-11} Sv/Bq	ingestion	1
	1.8×10^{-11} Sv/Bq	inhalation	1
Cs-137	1.4×10^{-8} Sv/Bq	ingestion	800
Pu-239	1.0×10^{-7} Sv/Bq	ingestion	5 500
	1.0×10^{-4} Sv/Bq	inhalation	5 500 000

**Figure 14.2:** Time-dependent specific activity in the soil humidity of the top 20 cm after a controlled tritium release experiment (Canada 1987).

release. Instead, most tritium will end up in the oceans, which carry a natural tritium inventory of a few kg. This tritium is formed by nuclear reactions of cosmic rays entering the earth's atmosphere (e.g.: $n + {}^{14}\text{N} \rightarrow {}^{12}\text{C} + \text{T}$). During the period of extensive nuclear weapon testing in the fifties and sixties, the earth's inventory was increased to about 500 kg. Today the residual inventory has been reduced by decay of tritium to about 80 kg.

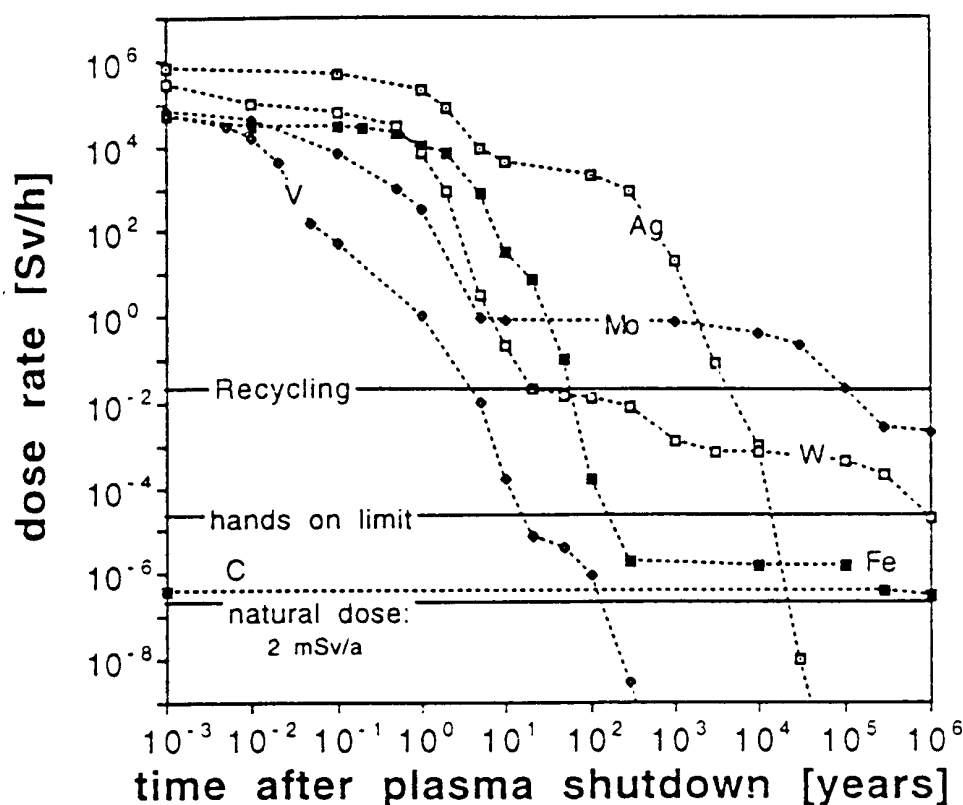


Figure 14.3: Dose rate of several elements after neutron irradiation of 12.5 MWa/m^2 .

Activation products

The expected neutron wall loading is in the range between $2\text{--}5 \text{ MW/m}^2$, which will lead to considerable radiation damage of the components near the plasma. Thus a regular exchange of these components after 2.5–5 years of operation is envisaged. A target for fusion materials is a possible neutron fluence of about 12.5 MWa/m^2 . The development of such materials is a very challenging task.

The amount of activation products in future fusion reactors strongly depends on the choice of materials. Fig. 14.3 shows the dose rates of some elements in the first wall. The total amount of radioactivity in a fusion plant will be governed by the activation products. If conventional steels are used, a level of about 50% of the radioactivity in fission plants is reached.

There is a clear distinction between the inventories of tritium and activation products, i.e. the volatility. The radioactivity inside the structural material is very hard to mobilize by definition since the structure has to withstand large forces during normal operation.

Special attention has to be given to the first-wall dust eroded by the plasma, because it can easily be mobilized. The use of very low activation materials such as carbon, beryllium, or boron would strongly reduce the hazard of this dust (see Fig. 14.3 for the dose rate of C). If high-Z materials have to be used in the plasma facing components (e.g. tungsten in the divertor), the dust inventory could pose problems similar to those of the tritium inventory. As indicated, a main issue of the activation products is waste management, which will be treated

later. The environmentally most attractive elements for structural materials in a fusion plant are vanadium, chromium, and titanium.

14.3 Normal operation effluents

During normal operation, it is the volatile tritium which has to be properly controlled. Experience of tritium handling in large facilities is available from a special type of fission reactor working with natural uranium and heavy water as moderator, the Canadian CANDU reactors. In this type of fission reactor, inventories of a few hundred grams are produced from n-capture in D₂O. Experience with these CANDU reactors allows the extrapolation that with present technology tritium effluents can be limited to 2 g per year or 50 Ci/day (1 Ci = 3.4 × 10¹⁰ Bq). In Los Alamos, USA, the largest fusion-oriented tritium laboratory, with a maximum inventory of 200 g, is in operation. The experience from this laboratory (TSTA: Tritium Systems Test Assembly) has demonstrated that one might even do better than the extrapolation above. This laboratory was closed for three month after an unexpected release of 0.4 Ci HT, which demonstrates the high safety level of the plant.

If we assume a daily release of 50 Ci in the more hazardous form HTO from a 100 m high stack, the resultant dose to the most exposed individual (MEI) living at the fence has to be calculated. It is assumed that food and sometimes also water originate from the location of the MEI. A conservative estimation of the dose to the MEI is very simple: The source term S [Bq/s] will be diluted by atmospheric dispersion. For a 100 m high stack, the plume will reach the ground at about $R_{max} = 1\,000$ m, leading to a maximum ground level air concentration c_{air} of

$$c_{air} = S \cdot \frac{1}{v_{wind}} \cdot \frac{f}{2\pi R_{max}} \cdot \frac{1}{2h_{stack}}$$

with S being the source term in [Bq/s], v_{wind} the wind speed in [m/s], f a factor accounting for nonuniform wind rose, R_{max} the downwind distance from the source in [m], and h_{stack} the height of the source in [m].

A conservative assumption is $f = 3$ and a typical average wind speed is 6 m/s at a height of 100 m. Given the air concentration, one can transform this to a concentration in the air humidity

$$c_{H_2O,air} = c_{air} / \rho_{H_2O,air} ,$$

$\rho_{H_2O,air} = 10 \text{ g/m}^3$ is a typical value for the Central European growing season.

Assuming complete equilibration of the specific tritium activity of the air humidity with that of soil water, plant water, animals, and humans, the average tritium concentration in the MEI is equal to $c_{H_2O,air}$ leading to a dose rate D of

$$D = c_{H_2O,air} \cdot \langle E_{\beta^-} \rangle .$$

Table 14.2: Energy inventories and characteristic time scales for their release in a fusion reactor (water volume in the primary loop: 400 m³, heat of evaporation at 1 bar: 900 GJ).

Source	Energy [GJ]	Time Scale
Plasma	2	< 1 s
DT in Plasma	250	1 min
Coils	100	1 min
Cooling Water	300	10 min
Decay Heat	80	1 hour
	550	1 day
	2 000	1 week

For a source term of 50 Ci/d this simple approach results in an annual dose of 23 μ Sv/a, which is about 1% of the dose received from natural sources of radioactivity. More sophisticated models predict doses to the MEI which are 2–3 times smaller.

14.4 Accidents

With respect to safety in the event of accidents, the most important characteristic of fusion is self-termination of the fusion process under such conditions. So-called *passive safety* appears to be achievable in fusion power plants because of the absence of chain reactions. The energy sources that could drive accidents are low compared with those in fission, whereas the volumes and surface areas are large. Tab. 14.4 lists some relevant energy inventories together with typical time scales of release.

After shutdown of the reactor, the decay of radioactive nuclei constitutes a heat source, known as decay heat. Passive removal of the decay heat is a key safety feature. In the event of loss of coolant accidents (LOCA), the core of a fission reactor is prone to melting if no additional cooling can be applied. In the case of fusion, the decay heat is much smaller and is distributed over large surfaces. If all cooling media are lost, just thermal conduction and radiation are left as heat removal mechanisms. Fig. 14.4 shows a detailed analysis of such a situation for the ITER device. This is a good example of passive safety since the removal of the decay heat is managed by physical mechanisms that do not rely on engineering systems, which can always fail with a certain probability. Thermal radiation will never fail. The maximum temperatures in the fusion device stay well below the melting point of the steel structures (1 400°C).

The safety studies in fusion are prompted by the large radioactive inventories involved, but the fundamental difference between fusion and fission reactors is the fact that in the former major accidents are not driven by the nuclear system itself. Instead most safety studies focus on conventional hazards. The most important accident initiators are

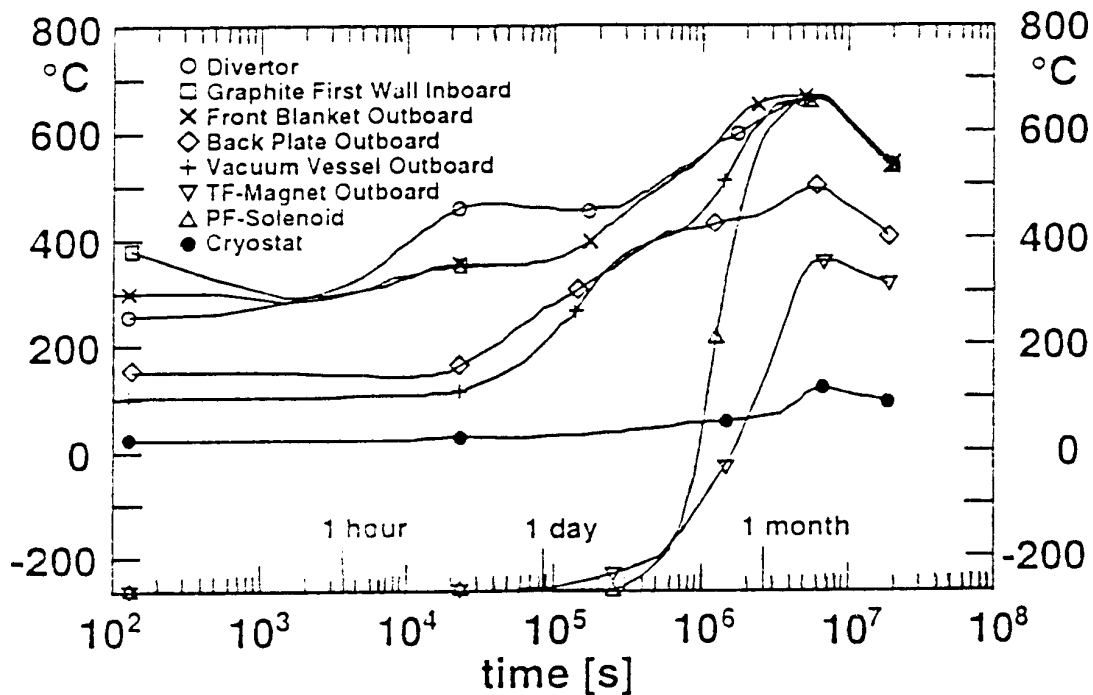


Figure 14.4: Temperature transient up to seven months for loss of all active cooling accident in ITER.

- loss of vacuum accidents with air ingress into the plasma chamber;
concerns: chemical reactions (fire), transport of tritium
- loss of coolant accidents;
concerns: pressurization, formation of hydrogen (explosion hazard)
- loss of offsite electric power;
concerns: loss of coolant flow, quench of magnets
- electric arcs in the coil system;
concerns: melting of adjacent systems, tritium release to the building
- coil deformation and displacement;
concerns: damage of adjacent components, loss of vacuum, missile generation
- volume change of cryogenic helium;
concern: pressurization
- explosions in the hydrogen isotopic separation system;
concerns: damage of building, tritium release
- fire in the long-term tritium storage beds;
concern: tritium release

The most detailed analyses have been performed for the ITER conceptual design phase. One example is air ingress into the plasma chamber, which is of concern since then one major

confining barrier is breached. For a design where the majority of the first wall is covered by carbon, chemical reactions of this material were investigated. No self-sustained fire can develop in such a case since the plasma would definitely extinguish and the first-all cooling would very effectively reduce the carbon temperatures. Even if the active cooling was simultaneously, the inertia of the cooling system would be sufficient to cool the carbon below its ignition temperature. The mobilized material, mainly tritium in the carbon dust and pumping system, would be released into the adjacent rooms. Here it would be confined in the second of three confinement barriers.

Generally, the aim of fusion safety studies is to ensure that future fusion plants are designed so that any internal accident and all conceivable external events should entail consequences confined inside the fusion plant by passive means. No internal accident should be able to destroy the buildings. The strategy is to provide a robust multi-confinement system, reduce all radioactive and energy inventories as far as possible, apply passive safety features and use high-quality nuclear components. Active systems can also play an important role to reduce any damage inside the plant.

In fusion reactors large amounts of lithium will be used to breed the necessary tritium. This could be done very efficiently by using liquid lithium. In this case the lithium could also serve as coolant since it has very good thermal properties which would simplify the design. Technical problems are still presented by the large pressure losses of liquid metals flowing in magnetic fields (MHD effect). Another serious drawback are safety concerns arising from violent chemical reactions of liquid lithium with air, water, nitrogen, and concrete. The potential energy release of the lithium inventory is about 7 000 GJ. Any contact with water produces large amounts of hydrogen with the unpleasant tendency to trigger detonations, which can seriously threaten the confinement buildings.

An alternative approach is the use of lithium ceramics such as Li_2O , Li_4SiO_4 , Li_2ZrO_3 , and other candidates which eliminate the chemical hazard caused by elemental lithium. Unfortunately, the need for a self-sufficient tritium breeding ratio calls for the neutron multiplier, beryllium (${}^9\text{Be}(n,2n)2\text{He}$), in almost all ceramic breeder designs. Beryllium is a very toxic material which builds up significant tritium inventories during neutron irradiation. In addition, there are questions about the abundance of beryllium on earth. At temperatures above 600–700°C some violent chemical reactions can also occur with air and water. Consequently, attempts are being made to push the design of ceramic breeder blankets to the extreme so as to eliminate the beryllium. Li_2O is the best candidate for these studies since it has the highest lithium atom density of all lithium ceramics. The lithium density in Li_2O is even higher than in metallic lithium. In addition the neutron activation of Li_2O is extremely small.

Another option is to use $\text{Li}_{17}\text{Pb}_{83}$, which has a melting point of 235°C and is thus a suitable liquid metal. Its chemical reactivity is much smaller than that of liquid lithium, but the use of lead poses technical problems because of its weight and there are safety concerns because of the neutron activation of lead.

The final choice of the breeder material will strongly influence the safety and environmental properties of future fusion plants.

Table 14.3: Specific dose to the most exposed individual of the public (MEI) at a distance of 1 km from the release point.

Source	Specific Dose	Type of Dose
tritium as HTO	0.5 mSv/g-T	early
	2.5 mSv/g-T	chronic
tritium as HT	0.04 mSv/g-T	early
AISI-316 first-wall steel	0.03 mSv/g	early
ITER conditions	2 mSv/g	chronic

Accidental doses to the public

The early dose is defined as the dose received during the first week after an accident, excluding the ingestion pathway. This dose definition is the basis for considering evacuation. Above 100 mSv evacuation is triggered in many countries. The chronic accidental dose integrates over 50 years of exposure time and includes all pathways. In Germany 50 mSv is the legal upper limit for public exposure after *design basis accidents*, i.e. accidents which have to be controlled by design.

Detailed studies for atmospheric accidental tritium and activation product releases have been performed. Specific doses for the most exposed individual of the public (MEI) at a distance of 1 km from the release point are presented in Tab. 14.4. The dose due to inhalation and skin absorption is 0.5 mSv/g-T (early dose) for ground level releases in the chemical form of HTO. If ingestion is included, the dose values are about five times higher (chronic accidental doses). For gaseous releases (HT), doses are at least a factor of ten lower. The earlier mentioned difference in radiotoxicity of 10 000 between HTO and HT is levelled out by the fact that HT released to the environment will diffuse into the soil, where it is rapidly oxidized by micro-organisms and subsequently re-emitted as HTO. Specific doses for steel dust envisaged during the conceptual design of ITER are about one order of magnitude below the tritium values, but for the chronic accidental doses similar values result.

Under the German licensing procedure, it has to be shown that in design basis accidents the releases stay below 20 g for tritium in the form of HTO for ground level releases. This is achievable as long as the confinement building remains intact. To avoid evacuation, tritium releases have to be kept below 200 g in all circumstances. This is the reason for setting up the safety target of keeping the tritium inventory below 150 g for all single components.

If we compare the potential hazard of the tritium and steel dust of a fusion plant with the hazard of the J-131 and Cs-137 inventories of a fission plant, fusion is 500 times more benign.

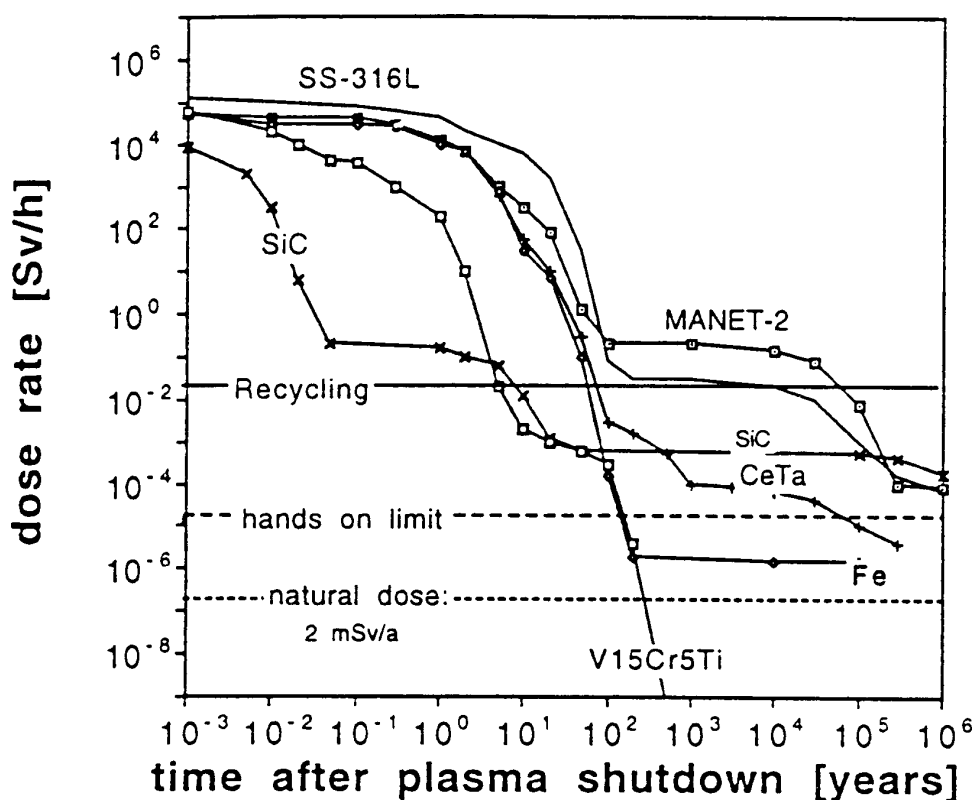


Figure 14.5: Time-dependent dose rates for technologically important materials irradiated by a neutron fluence of 12.5 MW/m^2 ; a standard steel (SS-316L), a fusion optimized steel (CeTa, KfK), the theoretical lower limit for iron based steels (Fe), a ceramic (SiC), and a vanadium alloy (V15Cr5Ti) are shown.

14.5 Waste management

The majority of the radioactive waste in a fusion reactor will arise from replacement of divertor, first wall, and blanket segments and decommissioning of the whole tokamak, including the vacuum vessel and the magnets. These components will be activated by the intense flux of 14 MeV neutrons. Due to the shielding effect of the materials involved, there will be a steep gradient in the activation when going away from the plasma.

The relatively short life of the majority of the radioisotopes produced and the absence of very toxic actinides (α -emitters) causes the ingestion hazard index of the fusion waste to be more than 1 000 times less than for fission waste after 100 years of cooling time. The basis of comparison is the total waste produced during the lifetime of the plants.

The volume of packed waste is estimated to add up to about $25\,000 \text{ m}^3$ for a fusion reactor life. This is comparable to the amount of packed waste from a typical PWR plant life, including reprocessing. Without reprocessing the volume of packed fission waste will be 30–50% smaller. The fission waste still requires much more repository consumption due to the significantly larger heat production in the waste, which limits the packing density in geological repositories.

Fig. 14.4 shows the dose rates of some technologically important materials irradiated at the first wall. Given moderate progress in the development of fusion-optimized materials, the reuse of activated material in new reactors is a potential option of waste management. For reduced-activation steels, recycling of components is estimated to be feasible up to contact dose rates of 25 mSv/h by remote handling techniques. The most activated component, which is the first wall of the plasma chamber, would reach this level 50–100 years after being dismantled from the reactor.

If new classes of low-activation materials, such as vanadium alloys, could be used in fusion reactors, *hands-on recycling* might be feasible after a few decades of cooling time. The benefit will be strong simplification of recycling procedures and thus greater economic attractiveness. However, great care must be taken to keep undesirable impurities to a low level in order to retain the radiological attractiveness, e.g. below 0.1 ppm for silver (see Fig. 14.3).

14.6 Conclusion

A board of independent scientists from different fields are regularly asked to review the European Fusion Programme. The following extract from the last *Fusion Programme Evaluation Board* (Colombo report, July 1990) is quoted to conclude this overview:

It is essential to expand the effort on technology, not only on the Next Step, but also on longer term issues, particularly in relation to the new emphasis on environmental and economic constraints. Environmental and safety criteria should as of now be considered as essential elements in governing the evolution of the Fusion Programme. Problems concerning materials, the use of tritium, the maintainability of the reactor should all be faced in time avoiding freezing of design or engineering concepts which might lead to environmentally unacceptable fusion reactors or make their design excessively complex.

Environment and safety must assume high priority in the European Fusion Programme and in its wider international extension...

It would be particularly important for fusion to qualify in two respects:

1. It must be clearly shown that the worst possible fusion accident will constitute no major hazard to populations outside the plant perimeter that might result in evacuation.
2. Radioactive wastes from the operation of a fusion plant should not require isolation from the environment for a geological timespan and therefore should not constitute a burden for future generations.

Chapter 15

Frontiers of dense plasma physics with intense ion and laser beams and accelerator technology, and application to inertial fusion energy¹

*M. Roth**,

*A. Blazevic[°], N.A. Tahir[°], D.H.H. Hoffmann**

G. Schaumann, M. Schollmeier*, S. Udrea*, D. Varentsov[°]*

* Institut für Kernphysik, Technische Universität Darmstadt, Schloßgartenstr. 9, 64289 Darmstadt, Germany

[°] Gesellschaft für Schwerionenforschung, GSI-Darmstadt, Plasmaphysik, Planckstr. 1, 64291 Darmstadt, Germany Interaction phenomena of intense ion- and laser radiation with matter

have a large range of application in different fields of science, from basic research of plasma properties to application in energy science. The hot dense plasma of our neighbouring star the sun provides a deep insight into the physics of fusion, the properties of matter at high energy density, and is moreover an excellent laboratory for astroparticle physics. As such the sun's interior plasma can even be used to probe the existence of novel particles and dark matter candidates. We present an overview on recent results and developments of dense plasma physics addressed with heavy ion and laser beams combined with accelerator- and nuclear physics technology.

¹The material presented is in part taken from a paper submitted to *Physica Scripta* as review material for the Plasma Physics Summer School, held in June 2005 in Kudowa, Poland. It is intended for internal use of the IPP summerschool only and not permitted for journals publications.

15.1 Introduction

In the familiar environment we live in, matter occurs predominantly as baryonic matter in the solid, liquid or gaseous phase. This is, however, not common to the situation in the universe at large, where most of the matter is in the form of dark matter [53] or dark energy and we don't know anything about their nature except that the gravitational interaction is observable [54]. Only 4% of the total mass of the universe is made up of baryons that we are familiar with and most of the visible matter exists as plasma.

Very often plasma is called the fourth state of matter, following the idea that as heat is added to a solid, it undergoes a phase transition to a liquid. If more heat is added the phase transition to a gas occurs. The addition of still more energy leads to a regime, where the thermal energy of the atoms or molecules forming the gas is so large, that the electrostatic forces which ordinarily bind the electrons to the atomic nucleus are overcome. The system then consists of a mixture of electrically charged particles like ions and electrons and neutral particles as well. In this situation, the long-range Coulomb force is the factor that determines the statistical properties of the sample. On earth plasmas occur naturally only as a transient phenomenon in lightning or in the aurora. The practical application of man made plasmas is very extensive and ranges from material modification, surface cleaning, and micro fabrication of electronic components to the future prospects of energy production in fusion plasmas.

There are a number of methods to produce plasma, like electrical discharges in a gas or laser irradiation of a sample. Intense heavy ion beams add on to the previously existing methods since they became available from powerful ion accelerators. They contribute a number of interesting features to plasma research because they are of dual use, in the sense that they can produce the plasma by irradiation of the sample and they also provide at the same time excellent diagnostic methods to analyze the plasma properties [18, 26, 51, 52]. Moreover, they are a unique tool to generate plasma at high density. The quest for a deeper understanding of dense plasma phenomena that govern the properties of matter under extreme temperature and density conditions is the driving motivation for high energy density plasma physics research with intense heavy ion and laser beams at GSI.

15.2 Accelerator and laser facilities at GSI-Darmstadt

The GSI-heavy ion accelerator laboratory in Germany operates the most powerful and versatile heavy ion accelerator worldwide and in addition to this there is an approved project to build a new accelerator facility at GSI called FAIR (Facility for Antiproton and Ion Research). This new accelerator will consist of two powerful heavy ion synchrotrons a number of storage rings and experimental facilities for various research projects [15]. The centerpiece of the accelerator assembly will be a 100 Tm heavy ion synchrotron. This will extend the available beam deposition power from the current level of 50 GW/g by at least two orders of magnitude up to 12 000 GW/g. Many aspects of high power beam physics associated with inertial confinement fusion driven by intense heavy ion beams can be addressed there, even though this facility will not provide enough beam power to ignite a fusion pellet [16].

GSI-FAIR Accelerators

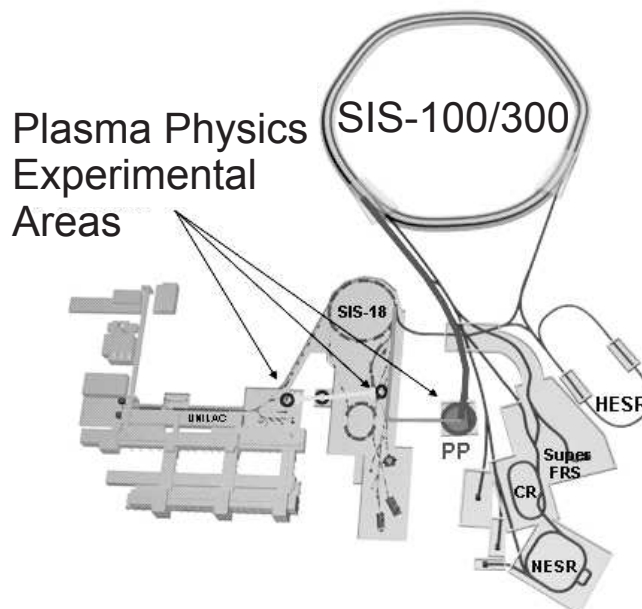


Figure 15.1: Schematic layout of the planned FAIR accelerator facility at GSI with the experimental areas for plasma physics. The FAIR project at GSI will greatly improve the option for beam-plasma experiments. The arrows point to the existing experimental areas of plasma physics and the future installation at FAIR. Each experimental area is already, or will in the future be served with heavy ion beams from the accelerator and an intense laser beam.

GSI-Darmstadt is also the first accelerator laboratory worldwide where in addition to a powerful and intense heavy ion beam a high-energy laser beam is available for experiments using laser and particle beams simultaneously. The already existing laser facility *nhelix* (nanosecond high energy laser for ion experiments) is currently complemented by a new laser PHELIX (Petawatt High Energy Laser for Ion Experiments). This is a laser system in the kJoule regime with the option to produce ultra-short, high-intensity light pulses with a total power above 1 PW (10^{15} Watt). It will be able to produce a light pulse pressure exceeding the pressure in the interior of the sun. The full potential of the PHELIX laser will be exploited in high energy density physics experiments with the high intensity heavy ion beams of the future accelerator at GSI. The unique combination of ion and laser beams facilitates novel and pioneering beam-plasma interaction experiments to investigate the structure and the properties of matter under extreme conditions of high energy density, which are similar to those deep inside stellar objects with keV temperatures and more than 100 times solid density.

15.3 High energy density physics

The properties of matter under conditions of high density and pressure are often summarized by an equation that relates the pressure or energy density to the matter density of the sample. Such an equation is called the equation of state (EOS) of the material. The determination of the proper equation of state is a topic of intense research effort experimentally as well as theoretically with ion and laser beams [8, 11, 12, 47]. Especially interesting is the occurrence of phase transitions in cold compressed material [9], e.g. the insulator to metal transition of diamond at 10 Mbar, the insulator to metal transition of solid hydrogen above 5 Mbar, or the plasma phase transitions at temperatures of about 1 eV [46].

In laser matter interaction experiments it is the intensity I measured in W/cm^2 and the total power which are the relevant experimental parameters. Due to the nature of ion matter interaction, where ions penetrate deep into the target volume, the important parameter is the energy E_s , deposited per gram of matter [J/g] and the deposition power P_s measured in W/g. Hence the physics of beam induced high energy density matter is governed by three equations

$$E_s = (1.6 \cdot 10^{-19}) \frac{dE/dx \cdot N}{\pi r^2} \quad [\text{J/g}], \quad (15.1)$$

where dE/dx is the stopping power of the material, N is the number of beam ions delivered by the accelerator πr^2 is the focal spot area. In order to achieve high deposition energy the accelerator has to provide the maximum beam intensity and the experiment has to care for an effective focusing. The stopping power is given by nature and we will show later that it may be a very different situation if the matter is in an ionized state or not. The time t_H to deliver this energy is limited, due to the hydrodynamic response of the beam heated material, and is approximately given by

$$t_H \propto \left(\frac{L^2}{P} \right)^{1/3}, \quad (15.2)$$

where L is the target dimension. For a cylindrical target this is the target radius and t_H is essentially given by the time a rarefaction wave needs to travel over the distance L .

Combining these two equations yields the total deposition power P_s

$$P_s = \frac{E_s}{t_H}. \quad (15.3)$$

Thus it is obvious, that high energy density induced by heavy ion beams requires that an intense, bunch of short time duration is focused into a sample with a small focal spot size [45]. The presently available beam from the SIS 18 is focused by a fine focus system. Until recently a plasma lens [3] was in operation and a beam spot radius of $250 \mu\text{m}$ was achieved by a 400 kA discharge current of the plasma lens [4, 27]. A specific power deposition up to 10 GW/g is achieved and results in a pressure inside the investigated target of about 10 kbar [10].

As most of the previous experiments to study high energy density matter were based on shock wave techniques starting from ambient pressure and solid density, these phase transitions were

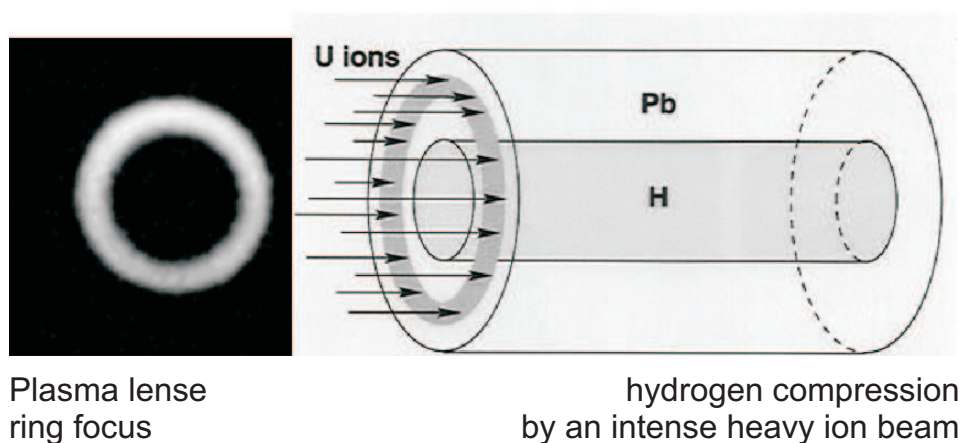


Figure 15.2: An annular beam focus, achieved by plasma lens focusing is used to compress a hydrogen sample.

not accessible because in a single planar shock only fourfold compression is possible. Higher compression ratios require multiple shocks or even isentropic compression. Heavy ion heated systems with their intrinsic large time and length scales offer a promising alternative to explore these phase transitions in precision experiments. To illustrate this capability two-dimensional numerical simulations have been carried out with respect to the parameters for hydrogen metallization. The experimental scenario makes use of the inherent cylindrical beam geometry where the compression is achieved by imploding multi-layered cylindrical targets. In the simulation the target is irradiated with an intense uranium beam at an energy of 1 GeV/u with a total number of 5×10^{11} particles. Our simulations show that hydrogen metallization is well within reach for the new accelerator facility [46, 47, 48].

The energy deposition characteristics of high-energy heavy ion beams in dense matter favor a cylindrical geometry. A simple experimental scenario is therefore a quasi-cylindrical plasma volume created by focusing an ion beam. A more complicated scenario with higher compression yields can be achieved with special beam focus geometry, e.g. a hollow cylindrical beam focus at the target position, as sketched in Fig. 15.2. This is a very challenging problem for the beam transport and focusing system [49, 50]. However, a ring focus was demonstrated experimentally, which was achieved by carefully tuning nonlinear field gradients of the plasma lens [27]. Thus hollow cylindrical implosions become possible, and the simulations show that in such case the initial pressure, which is generated by the direct heating of target material, can be enhanced by more than a factor of ten. Alternative schemes to achieve a hollow beam are based on high frequency rotation of a beam spot on target. A careful analysis of the rotation frequency as a function of beam bunch length has shown that it is possible to overcome initially imprinted beam irradiation inhomogeneities [30, 31, 50].

15.4 Interaction experiments of heavy ion beams with plasmas

The investigation of interaction processes of high-energy heavy ion beams with matter is a research topic with a long tradition at accelerator laboratories. At least for simple collision systems a basic understanding of the dominant atomic and nuclear interaction mechanisms has been achieved. However, energy loss and charge exchange reactions with dense, ionized matter have added new and interesting aspects to this field [19]. Interaction processes between intense ion beams and plasmas are an ideal tool to probe high energy density plasmas and to investigate their properties. The kinetic energy of the heavy ions can exactly be tailored to the experimental conditions. The ions penetrate deeply into the volume of the plasma target. Energy loss and the final charge state distribution of the ions are the typical signals which reveal the beam plasma interaction processes, and which allow to draw conclusions for the plasma target properties [18]. The general interest in these measurements is the determination of the deposition power with high accuracy, an analysis of recombination and charge exchange processes, and the hydrodynamic response of matter irradiated with high intensity heavy ion beams [5, 24].

First beam-plasma interaction experiments at GSI, have been carried out to compare the stopping power of hydrogen gas and fully ionized hydrogen plasma. Plasmas in linear discharge geometry and a dense z -pinch plasma [19, 20] have been employed to cover the density regime from $n_e = 10^{16}$ – 10^{19} cm⁻³. These experiments clearly demonstrated the increased stopping power of fully ionized plasmas, due to the interaction of beam ions with free electrons in plasma.

The beam energy in these first experiments was varied between 1–6 MeV/u for different ion species from carbon to uranium and the stopping power enhancement accounted for was roughly a factor three. This enhancement, as seen in Fig. 15.3 was mainly attributed to the efficient energy transfer to free electrons in small angle collisions. For lower kinetic energies, where the projectile velocity is comparable to the thermal velocity of the plasma electrons, the energy loss behavior is even more dramatic. An enhancement factor close to 40 was measured [23], and the main contribution in this case is the higher effective charge state Z_{eff} of the beam ions, due to the reduced recombination processes in highly ionized plasma. The dynamic equilibrium between ionization and capture processes is shifted towards higher charge states. Free electrons are difficult to capture for the beam ions, since energy and momentum conservation requirements are difficult to be fulfilled at the same time with free electrons. With bound electrons, however, momentum conservation is generally no problem due to the strong binding energy. The resulting reduction in electron capture cross section depends strongly on the ionization degree of the plasma. Therefore hydrogen gas was the first choice as a plasma target, because it is the only material which can be transformed from a solid to a liquid, a gas, a plasma and finally a completely ionized plasma with only a negligible amount of remaining bound electrons. Charge state analysis of beam ions penetrating the fully ionized hydrogen plasma clearly showed the effect of an enhanced average charge state [13]. The effect is well understood and described for ideal plasmas by the well known Bethe-Bohr-Bloch stopping

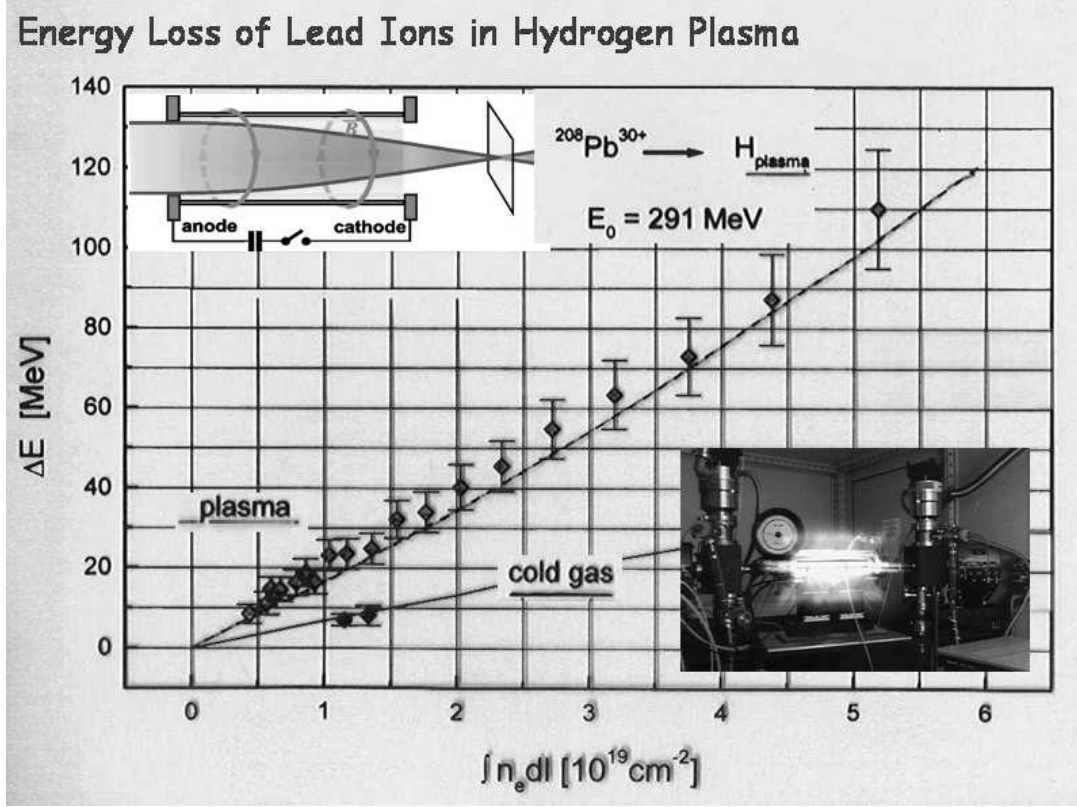


Figure 15.3: Energy loss of Pb ions in hydrogen gas and hydrogen plasma. The plasma was generated by a discharge.

theory

$$-\frac{dE}{dz} = \frac{16\pi a_0^2 I_H^2 \overbrace{Z_p^2}^{\text{effective projectile charge}}}{P m_e v_p^2} \left[\underbrace{\sum_{Z=0}^{Z_K} (Z_K - Z) n_z \ln \left(\frac{2m_e v_p^2}{I_Z} \right)}_{\text{bound electron contribution}} + \underbrace{n_e \ln \left(\frac{2m_e v_p^2}{\hbar \omega_p} \right)}_{\text{free electron contribution}} \right]. \quad (15.4)$$

The stopping power of an ionized medium is described by contributions from bound and free electrons to the electronic energy loss. For fully ionized plasma the bound electron contribution is zero.

Laser heated plasmas provide higher temperatures and densities than gas discharges. Consequently, a powerful Nd:YAG/Nd:glass laser system at the Z6 experimental area of GSI has been installed [22, 37, 38]. With this device it was possible to investigate plasmas of the critical density 10^{21} cm^{-3} corresponding to the laser wavelength (1064 nm). The temperatures of these plasmas exceeded $kT = 60 \text{ eV}$. Because of the difficulty to focus heavy ion beams and the restriction, that the target plasma size has to exceed the ion beam radius, the laser irradiated area had to be larger than 1 mm^3 . This constraint led to the necessity of a high energy pulse laser. The laser system consists of a Nd:YAG oscillator providing a laser pulse of 15 ns FWHM operating in a MOPA (master oscillator / power amplifier) scheme. The pulse is amplified in six amplification stages of up to 64 mm diameter until it has a maximum energy above 100 J.

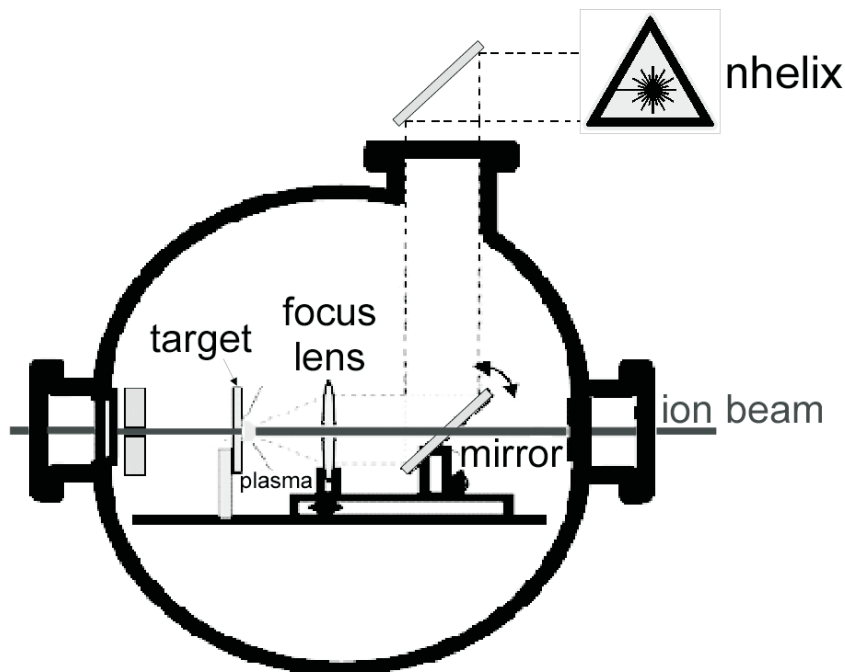


Figure 15.4: Experimental set up. The laser beam from above is focused onto the target, while the ion beam is guided through apertures to the laser plasma. The energy loss of the ion beam is measured by time of flight methods.

In the experimental set up shown in Fig. 15.4 both the laser and the heavy ion beam are transported to the target in parallel, which is possible because the ion beam is penetrating the final focusing optics through small apertures. As the laser heated area of the target is much larger in diameter than the target thickness, the expansion of the laser heated target is mainly normal to its surface. Thus during the first phase of expansion the ions face an almost constant line density. The mainly one-dimensional expansion of the target could be recently be confirmed clearly by high resolution spectroscopy experiments. It could be shown, that strongly collimated jets emerge out of the plasma. This collimation is probably enhanced by strong magnetic fields, which can be generated by high gradients in the target plasma. The plasma jets contain ions of kinetic energies in the MeV-range, as spatially resolved X-ray spectroscopy showed [35].

Future interaction experiments will benefit from planned improvement of the laser performance at the experimental area. Within the next years the installation of the Petawatt/kJoule system PHELIX will be completed and can provide target plasmas of improved homogeneity, higher temperatures and higher densities. Fully ionized plasmas with atomic numbers up to and above six (carbon) will then be available. New target materials and designs give access to a more precise spectroscopic determination of the plasma parameters and new fields of investigation. Thus the development of thin cryogenic hydrogen films for laser plasma-ion beam interaction experiments will extend the stopping power studies for hydrogen plasmas to densities of almost solid state density. An improvement of spectroscopic techniques and new models of calculation will enable us to find more precise descriptions of the interaction of

heavy ion beams with high density plasmas, answering the questions that have been raised in the recent experiments.

15.5 Application to inertial fusion energy

An inertial confinement fusion (ICF) capsule or target is a small, millimeter-sized, spherical capsule whose hollow interior contains a thin annular layer of liquid or solid DT fuel (a mixture of deuterium and tritium isotopes of hydrogen). The outer surface of the capsule is rapidly heated and ablated either directly by intense laser or ion particle beams (drivers), called direct drive (see Fig. 15.5 a), or indirectly by absorption of soft X-rays in the outer capsule surface. These soft X-rays are generated by driver beams hitting a nearby metal surface, a process called indirect drive (see Fig. 15.5 b).

The rocket effect caused by the ablated outer capsule material creates an inward pressure causing the capsule to implode in about four nanoseconds (a nanosecond is one billionth of a second). The implosion heats the DT fuel in the core of the capsule to a temperature of about 50 million degrees Celsius, sufficient to cause the innermost core of the DT fuel to undergo fusion. The fusion reaction products deposit energy in the capsule, further increasing the fuel temperature and the fusion reaction rate. Core fuel ignition occurs when the self heating of the core DT fuel due to the fusion reaction product deposition becomes faster than the heating due to compression. The ignition of the core will then propagate the fusion burn into the compressed fuel layer around the core. This will result in the release of much more fusion energy than the energy required to compress and implode the core.

An inertial fusion power plant would typically fire a continuous series of targets at a pulse rate of 6 Hz. The series of fusion energy releases thus created in the form of fast reaction products (helium alpha particles and neutrons) would be absorbed as heat in the low activation coolants (fusion chamber) that surround the targets. Once heated, the coolants would be transferred to heat exchangers for turbine generators that produce electricity. The inertial fusion power plant example shown below uses jets of molten salt, called Flibe, surrounding the targets inserted into the fusion chamber. The molten salt jets absorb the fusion energy pulses from each target while flowing from the top to the bottom. The molten salt is collected from the bottom of the chamber and circulated to steam generators (not shown) to produce steam for standard turbine generators. This particular power plant example uses a ring-shaped ion beam accelerator as a driver, but there are also laser driver possibilities.

The minimum driver energy required to implode the capsule fast enough for ignition to occur is typically about a megajoule, the caloric equivalent of a large doughnut. Since this driver energy must be delivered in a few nanoseconds, however, a power of several hundred terawatts ($1 \text{ TW} = 10^6 \text{ MW}$) will be needed. For reference, the entire electrical generating capacity of the United States is about one half terawatt.

In a sense the ICF concept can be compared to a commonly known Diesel engine, where fuel is compressed and thereby heated to the point of ignition and yields more energy than required for the compression. A further difference between MCF and ICF is that once ignition has been achieved gain is provided automatically because of the inertia of the fuel. Also ICF has already

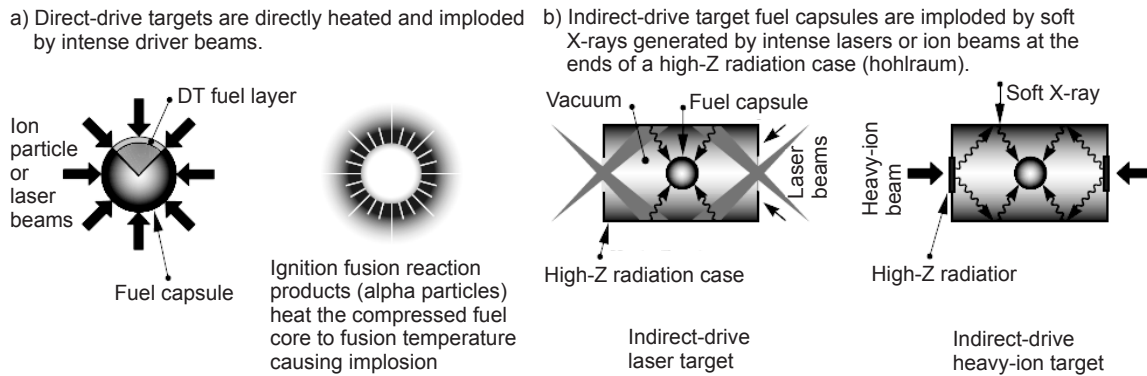


Figure 15.5: Schematics of ICF concepts.

demonstrated its feasibility. In the 1980's a successful experiment has demonstrated ignition. The main purpose of the currently constructed large laser facilities (NIF and LMJ have the size of a football stadium) is to demonstrate laser driven ICF at the lowest possible driver energy where ignition reliably can be achieved. Finally a large difference to the MCF reactor design is the de-coupling of the expensive driver from the main reactor chamber. The laser or heavy ion accelerator can be located distant from the reactor not being exposed to the large amount of fusion neutrons, which is highly desirable with respect to activation and material damage.

Inertial Fusion Energy concepts take advantage of the fact that ion and laser beams offer the opportunity to concentrate energy in space and time in such a way that matter can be transformed into plasma of high density and high temperature on a very short time scale. The target material then generally consists of a mixture of electrically charged ions, electrons and neutral particles as well. In this situation collective effects, determine the statistical properties of the sample. Atoms and ions immersed in a plasma environment experience perturbations from the plasma. As a result the atomic and ionic states turn out to be mixed, and strongly different from pure, unperturbed atomic states and they are different as well from the situation of a cold matter environment. Consequently not only the spectral characteristics of radiation emission and absorption by the atoms and ions in a plasma are substantially different from spectra of the unperturbed species, but also bulk matter properties. These can be expressed in terms of an equation-of-state, relating pressure and temperature to the matter density of the sample, by the electrical, and thermal conductivity, and radiation transport properties. In general these properties turn out to be vastly different from those of matter under ordinary conditions.

Heavy ion beam scenarios for inertial fusion energy have to take into account the specific properties of ion beams and their energy deposition characteristics in cold and ionized matter as well. A schematic comparison of heavy ion beam and laser energy deposition properties is shown in Fig. 15.6. Due to their mass, heavy ions which have been accelerated to high energy are very efficient carriers of energy. Moreover the accelerating mechanism in rf-accelerators is also very effective to convert rf-energy into kinetic energy of heavy ions. Heavy ion beams deposit their energy inside the target volume, whereas laser beams are absorbed close to the surface.

In this way heavy ion beams couple their kinetic energy in a very efficient way to the tar-

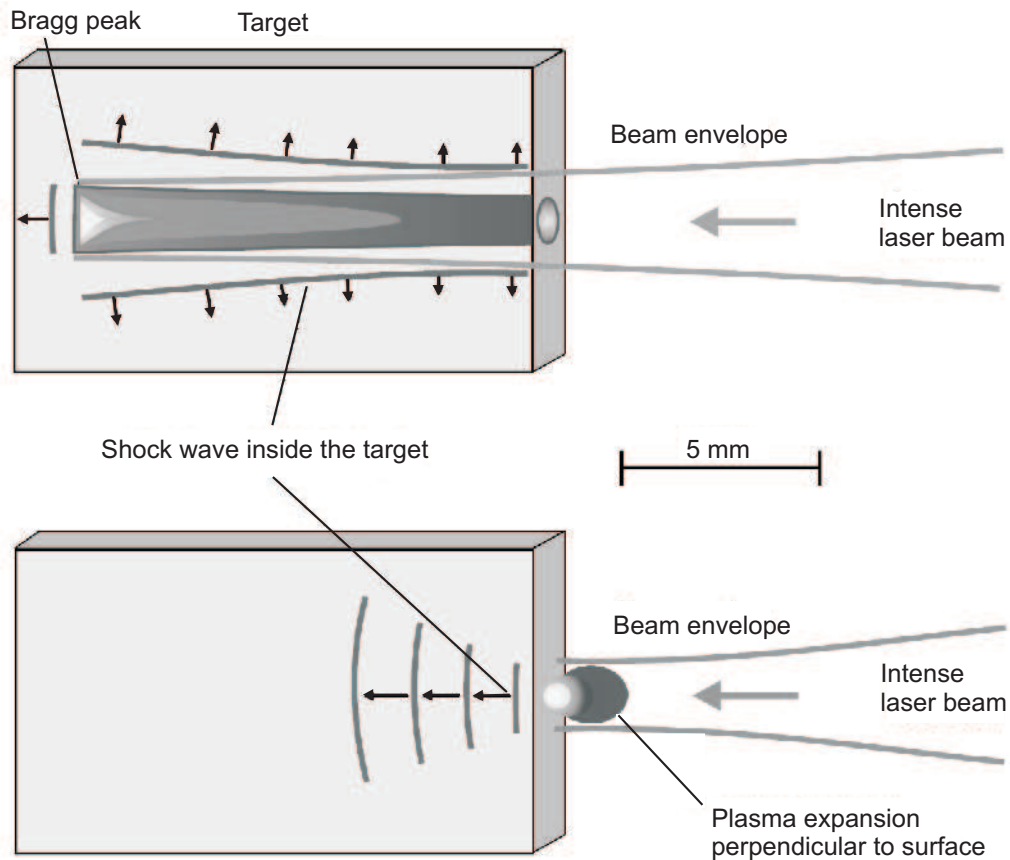


Figure 15.6: Schematic comparison of the energy deposition of an intense heavy-ion beam and that of a high performance laser in a solid target. Ion beams penetrate deep into the material, whereas laser beams are absorbed only below the critical density n_c , where the plasma frequency ω_p of the material is smaller than the laser frequency ω_{laser} .

get material. However, in an inertial fusion confinement concept where the fusion capsule is irradiated in a direct manner this effective energy coupling mechanism may turn into a disadvantage, since irradiation inhomogeneities are imprinted onto the capsule, and may lead to a decreased robustness against Rayleigh-Taylor instabilities. Until now no efficient transport mechanisms to smoothen out these initial inhomogeneities are known. This is still a topic of current research and a possible cure depends on the detailed knowledge of material properties such as equation-of-state and transport properties in high energy density conditions.

15.5.1 Basic issues of ICF target development for heavy ion beams

A necessary condition to achieve ignition and high gain is the irradiation symmetry of the pellet. Due to the efficient energy coupling- and transfer-mechanisms of heavy ions to the target material irradiation asymmetries may be generated right at the start of the ablation and compression phase. This is especially true for a low number of beams, where the symmetry requirement is difficult to achieve in a direct drive scheme already for principal geometric

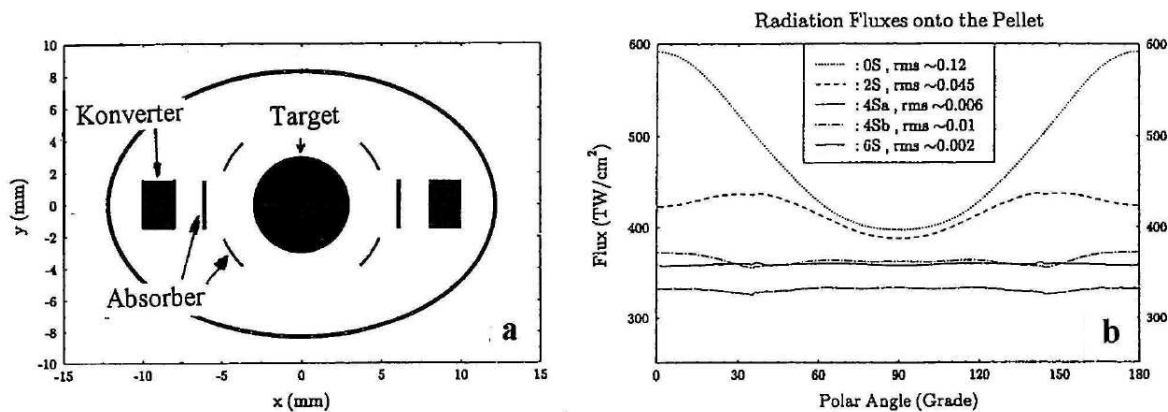


Figure 15.7: Left: For a two sided target illumination it is necessary to introduce shine shields between the converter target and the pellet.
 Right: Simulation results [25] show that this additional shielding can reduce the radiation asymmetry to the required level.

reasons. Since the first proposal of a two-side irradiated cylindrical hohlraum enclosing a radiatively imploded spherical fusion capsule by Livermore researchers in 1993 by Lindl, different approaches of indirectly driven targets have been investigated. This has recently been summarized in [2, 6, 7]. Therefore it is of fundamental interest to study if the introduction of additional shine shields into the capsule may lead to the necessary radiation symmetry. Fig. 15.7 shows an example where the introduction of a varying number of radiation shields inside the hohlraum reduced the irradiation asymmetries below the required level of approximately 1% [25].

Since a two sided illumination of the target seems to be the most suitable irradiation symmetry for intense heavy ion beams it is necessary to convert the ion beam energy into radiation and distribute it into almost 4π (steradians surrounding the implosion capsule). In the example shown in Fig. 15.7 radiation shields are used with sufficient success. A different system was suggested by Tabak and Miller [7, 41], where the converter target is distributed in solid angle to achieve the desired radiation symmetry. The case-to-capsule ratio is of course an important issue, which affects the energy gain of the fusion pellet. Two-dimensional integrated calculations show, however, that for an optimized heavy ion target a gain of 130 can still be expected in a close-coupled version of the distributed radiator target. Optimized high gain targets have been designed and investigated by a number of research groups [33] contributing to the European Study Group on heavy ion driven inertial fusion (HIDIF).

The effort to optimize case-to-capsule ratio results has the effect that the resulting hohlraum geometry tends to become smaller. Therefore the demands on the final beam spot are also increasing and the demands on final focusing, space charge neutralization in the reactor chamber, beam transport and emittance growth in the accelerator increase likewise.

15.5.2 Physics of dense plasmas and fast ignition

For the design of an efficient IFE target with high gain the basic processes of beam-plasma interaction and the hydrodynamic response of matter need to be understood on a microscopic level. The detailed knowledge of heavy ion energy deposition in a target that is partly ionized and in a state of high energy density is obviously a prerequisite for the design of the target as well as for realistic simulations of target hydrodynamics. With the facilities available now, the regime of hydrodynamic expansion of beam-heated matter can be investigated. However, for experiments to measure the conversion of kinetic beam energy into radiation, in the regime of radiation-dominated plasmas, the available beam intensity is not sufficient. Laser facilities such as the projected PHELIX laser facility at GSI combined with the new heavy ion synchrotron SIS 100, will allow to address beam plasma interaction phenomena in high-density high temperature plasmas.

15.5.3 Ultra-intense lasers

High power lasers are the most advanced drivers in inertial confinement fusion (ICF) research. The advent of ultra-intense laser systems [29] has opened the regime of relativistic plasma physics and further increased the possibilities of generating high energy density in matter. One of the most interesting new phenomena was the generation of ultra-intense, high-energetic electron beams, which penetrate deep inside the irradiated target. Because of its importance in applications like isochoric heating or fast ignition (FI) in ICF the transport of these electrons into the matter is a subject of extended research world-wide. The recent discovery of intense, well-collimated, picosecond-duration ion beams being generated by these electrons in laser solid interaction [40] has raised the hope of using the ion beam in order to explore electron transport. Moreover, because of the unique properties of the laser produced ion beams and the close correlation to the transport of the electrons inside the target the investigation of the latter is vital in order to control the beam properties for applications like diagnostics for high temperature plasmas, proton based FI [36], material science and as next generation ion sources for high energy physics.

15.5.4 Ion acceleration

The discovery of intense, collimated, energetic beams of protons off the back surface of solid targets has been the subject of great interest. Very briefly, targets of millimetre size and of several tens of micrometres thickness were irradiated with laser pulses having an intensity of up to 10^{20} Wcm^{-2} . Relativistic electrons generated from the laser-plasma interaction, having an average temperature of several megaelectronvolts, envelope the target foil and form an electron plasma sheath on the rear, non-irradiated surface. The electric field in the sheath can exceed 10^{12} Vm^{-1} , which field ionizes atoms on the surface and accelerates the ions very rapidly normal to the rear surface. Protons, having the largest charge to mass ratio, are preferentially accelerated in favour of heavier ions, over a distance of a few microns up to tens of megaelectronvolts in a collimated beam. The proton energy distribution resembles a Maxwellian with $kT = 5\text{--}6 \text{ MeV}$. This acceleration mechanism produces intense ion beams which are highly

laminar and could be an important new capability for a variety of applications. It is common understanding that the high laminarity, or low emittance, of these beams stems from the fact that the acceleration process takes place on the rear, non-irradiated surface of the target.

15.5.5 Fast ignition

Already in 1994 a new concept for the ignition of an inertial fusion target was proposed. The new scheme is known to the community as Fast Ignition and allows to ignite a fusion target with a considerably reduced amount of energy for the primary driver beam. Simply speaking, the concept of Fast Ignition resembles the change from a Diesel engine to a regular gasoline engine, where the fuel is less compressed and at the moment of maximum compression a separate ignition spark is applied to the fuel.

In conventional inertial fusion, ignition and propagating burn occurs when there is a sufficient temperature (5–10 keV) reached within a sufficient mass of DT fuel characterized by a density-radius product greater than an alpha particle range $(\rho r)_\alpha > 0.3 \text{ g/cm}^2$. The necessary conditions for propagating DT burn are achieved by an appropriate balance between the energy gain mechanisms and the energy loss mechanisms. Mechanical work (PdV), alpha particle energy deposition, and, to a smaller extent, neutron energy deposition are the principal energy gain mechanisms in deuterium-tritium fuel. Electron heat conduction and radiation are the principal energy loss mechanisms. When the rate of energy gain exceeds the rate of energy loss for a sufficient period of time, ignition occurs. Because of the short burn time and the inertia of the fuel the contribution of expansion losses are negligible.

Fast ignition (FI) was proposed as a means to increase the gain, reduce the driver energy, and relax the symmetry requirements for compression, primarily in direct-drive Inertial Confinement Fusion (ICF). The concept is to pre-compress the cold fuel and subsequently to ignite it with a separate short-pulse high-intensity laser or particle (electron or ion) pulse. Fast Ignition is being extensively studied by many groups worldwide, using short pulse lasers or temporally compressed heavy-ion beams. There are several technical challenges for the success of laser-driven FI. Absorption of the ignitor pulse generates copious relativistic electrons, but it is not yet known whether these electrons will propagate as a stable beam into the compressed fuel to deposit their energy in a small volume.

For indirect drive, the use of a laser ignitor is prohibited by the absorption of the laser light in the hohlraum wall and the ablation plasma. In principle, heavy-ion beams can have advantages for FI. A focused heavy-ion beam may maintain an almost straight trajectory while traversing the coronal plasma and compressed target, and ions have an excellent coupling efficiency to the fuel and deliver their energy in a well defined volume due to the higher energy deposition at the end of their range (Bragg peak). However, a major problem for heavy-ion fast ignition is to achieve the necessary beam brightness (small spot size, short pulse length) required to deposit sufficient energy to ignite the fuel. Transport of the ion beam over a few meters inside a reactor chamber to reach the target will result in a larger than optimal beam spot size, which will require a higher than necessary ion pulse energy in order to heat the deposition volume to the ignition temperature.

An interesting alternate route to fast ignition was triggered by the discovery of intense, short, energetic, directed beams of protons off the rear surface of solid targets irradiated by ultra intense lasers [40]. The initial idea of FI already dealt with the problem, that laser light is stopped and absorbed at a point along the rising slope of the density, orders of magnitude below the region, where the compressed fuel has to be ignited. So for the fast ignitor there is the need for energy deposition in a small volume in a short time, by particles that can be created by e.g. the laser and are not likely the subject of instabilities or other uncontrollable phenomena. With the discovery of those intense, short, energetic bursts of ions with excellent beam quality the idea of using those beams for FI was introduced [36]. Protons do have several advantages compared to other ion species and electrons. First, because of their highest charge to mass ratio, they are accelerated most efficiently up to the highest energies. They can penetrate deeper into a target to reach the high density region, where the hot spot is to be formed, because of the quadratic dependence of the stopping power on the charge state. And finally they do, like all ions, exhibit a characteristic maximum of the energy deposition at the end of their range, which is desirable in order to heat a localized volume efficiently.

The usual concept of ignition as shown in Fig. 15.8 is based on spherical compression to form an ignition spark in the center of the shock-compressed fuel. From this spark area a propagating burn wave is launched and propagates throughout the fuel. Fast ignition is based on the idea to decouple the compression and ignition process. As shown in Fig. 15.8 the fuel is first compressed in a standard way by the power of an intense heavy ion beam. Ignition is then independently achieved in a separate process. Early discussions about fast ignition involved an external laser pulse of ultra short duration and extremely high intensity [32] as the beam has to propagate through overdense plasma, which is a regime where the plasma frequency corresponding to the plasma density is higher than the laser frequency. Classically an electromagnetic wave cannot propagate under these conditions. Interaction processes of the ultra short high intensity laser beam will create a relativistic electron beam, which travels towards the highly compressed fuel core.

The physics of this process is not yet fully understood but experimental as well as theoretical investigation worldwide is addressing this problem vigorously, since laser beams with intensities exceeding 10^{19} W/cm² are available now with the advent of ultra-intense short pulse lasers [40] experiments have also demonstrated that such laser beams impinging on a curved target surface can create a high-energy intense proton beam [36] can be used to propagate towards the highly compressed fuel and finally ignite it. The scenario depicted in Fig. 15.9 combines all ICF schemes that have been treated separately. The power of highly efficient heavy ion beams is converted to radiation in the converter targets of a hohlraum. The hohlraum is heated to approximately 300 eV and the pellet inside the hohlraum is compressed. During the final stage of the process an ultra short high intensity laser pulse is fired towards the hohlraum casing producing an intense beam of protons that propagates to the compressed fuel core and achieves ignition. In this scenario laser fusion, light ion beam fusion and heavy ion beam fusion finally unite into one scenario. The next decade will probably see a breakthrough in the physics of inertial fusion based on the development of ultra short lasers combined with intense particle beams.

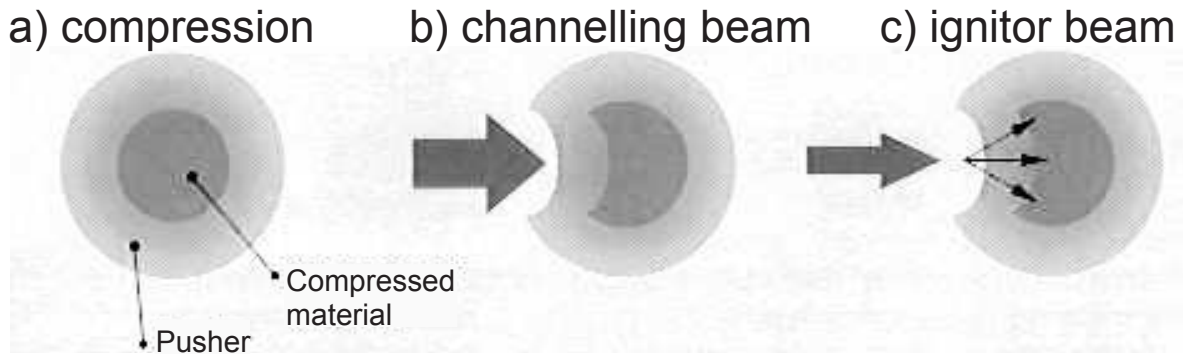


Figure 15.8: Schematic concept of fast ignition. In step a) the fuel is compressed in the standard way by high power beams, however, with lower requirements on spherical symmetry. A channeling beam b) is then used to drill a hole into the dense plasma environment and in c) the power of an ultra-short high intensity laser pulse is converted into a particle beam penetrating towards the dense core, where the compressed fuel is finally ignited.

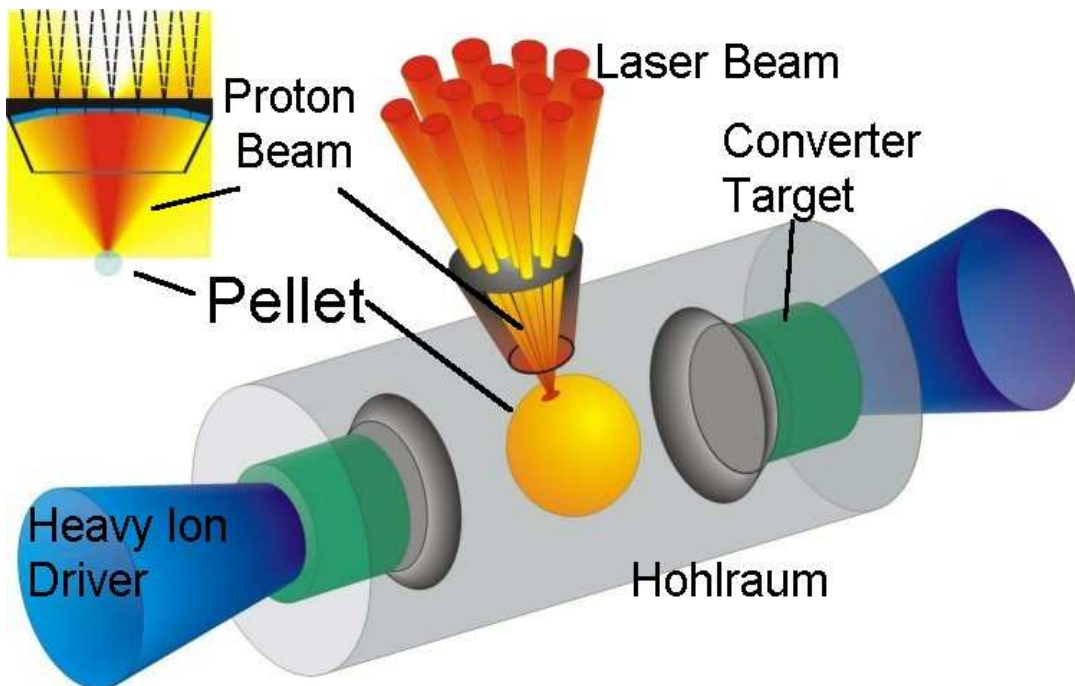


Figure 15.9: Indirectly driven fast ignition using heavy ions, laser beams and laser accelerated proton beams. The dimensions are not to scale. The surface of the laser target is shaped to focus the ion beam into the spark volume.

15.5.6 Conclusion

Inertial Fusion Energy with heavy ion beams is an area of active basic research while some aspects are already technically feasible. Currently the two big laser facilities under construc-

tion in the US and in France are the main projects towards inertial fusion. Heavy ion laboratories such as GSI-Darmstadt are continuously increasing the heavy-ion beam power for experiments. With a high power laser beam from the PHELIX laser and the intense heavy ion beam key issues of high energy density physics can be addressed to study the properties of matter under extreme conditions of temperature and pressure. A major development is the upcoming of ultra-short pulse lasers in recent years. The detailed knowledge about interaction phenomena of intense fields with matter will certainly also influence the development towards inertial fusion. As pointed out the fast ignitor scenario holds the prospects of combining the advantages of lasers light ions and heavy ion beams into one inertial fusion energy scheme. It reduces the demands on the accelerator with respect to the total beam energy to be delivered to the target.

Since inertial fusion is still an aim for some hopefully not too far distant future, it is obvious that at present all basic physics issues should be addressed carefully. Investigation of interaction processes of heavy ion beams with ionized matter had originally been motivated by inertial fusion physics, where intense heavy ion beams were proposed to ignite a fusion target [1, 21, 34]. Inertial fusion energy today is an area of active basic research while some aspects of the fusion scenario are already technically feasible. Currently the two big laser facilities under construction in the US and in France are the main projects towards inertial fusion. Accelerator laboratories like CERN in general, and heavy ion laboratories such as GSI-Darmstadt are continuously increasing the beam power for experiments. Failure of beam transport components in this case may cause already serious problems since the energy contained in a beam pulse is sufficient to melt an appreciable amount of material and even transform it into high energy density matter [42, 43, 44]. With a high power laser beam from the PHELIX laser and the intense heavy ion beam key issues of high energy density physics can be addressed to study the properties of matter under extreme conditions of temperature and pressure. The detailed knowledge about interaction phenomena of intense fields with matter will certainly also influence the development towards inertial fusion.

Acknowledgement

The authors like to acknowledge the support of various funding agencies: German-Israeli Project (DIP), INTAS; WTZ.

The authors also want to acknowledge the contribution from the CAST collaboration, the PHELIX laser team at GSI and all members of the Plasma Physics team at GSI.

References

- [1] J.J. Barnard, L.E. Ahle, F.M. Bieniosek, C.M. Celata, R.C. Davidson, et al., *Integrated experiments for heavy ion fusion*, Laser and Particle Beams **21** (4), 553-560 (2003)
- [2] M.M. Basko, M.D. Churazov, A.G. Aksenov, *Prospects of heavy ion fusion in cylindrical geometry*, Laser and Particle Beams **20** (3), 411-414 (2002)

- [3] E. Boggasch, B. Heimrich, D.H.H. Hoffmann, *Focusing behavior of plasma lenses compared to conventional quadrupole systems*, Nuclear Instruments & Methods in Physics Research Section A - Accelerators Spectrometers Detectors and Associated Equipment **336** (3), 438-441 (1993)
- [4] E. Boggasch, A. Tauschwitz, H. Wahl, K.G. Dietrich, et al., *Plasma lens fine focusing of heavy-ion beams*, Applied Physics Letters **60** (20), 2475-2477 (1992)
- [5] E. Boggasch, J. Jacoby, H. Wahl, K.G. Dietrich, D.H.H. Hoffmann, et al., *Z-Pinch plasma lens focusing of a heavy-ion beam*, Physical Review Letters **66** (13), 1705-1708 (1991)
- [6] D.A. Callahan, M.C. Herrmann, M. Tabak, *Progress in heavy ion target capsule and hohlraum design*, Laser and Particle Beams **20** (3), 405-410 (2002)
- [7] D.A. Callahan-Miller, M. Tabak, *Increasing the coupling efficiency in a heavy ion, inertial confinement fusion target*, Nuclear Fusion **39** (11), 1547-1556 (1999)
- [8] C. Constantin, C. Niemann, E. Dewald, S. Udrea, J. Jacoby, D. Varentsov, et al., *Density measurements of heavy-ion-beam-induced stress waves in solid matter by a sensitive laser deflection technique*, Review of Scientific Instruments **75** (5), 1268-1273, Part 1 (2004a)
- [9] C. Constantin, E. Dewald, C. Niemann, D.H.H. Hoffmann, S. Udrea, et al., *Cold compression of solid matter by intense heavy-ion-beam-generated pressure waves*, Laser and Particle Beams **22** (1), 59-63 (2004b)
- [10] C. Constantin, E. Dewald, C. Niemann, N.A. Tahir, A. Shutov, Kozyreva, et al., *Experimental investigations of multiple weak shock waves induced by intense heavy ion beams in solid matter*, Laser and Particle Beams **20** (3), 521-526 (2002)
- [11] E. Dewald, C. Constantin, C. Niemann, S. Udrea, J. Jacoby, J. Wieser, et al., *Fundamental studies of intense heavy-ion beam interaction with solid targets*, IEEE Transactions on Plasma Science **31** 31 (2), 221-226 (2003)
- [12] E. Dewald, C. Constantin, S. Udrea, J. Jacoby, D.H.H. Hoffmann, C. Niemann, et al., *Studies of high energy density in matter driven by heavy ion beams in solid targets*, Laser and Particle Beams **20** (2002)
- [13] K.G. Dietrich, D.H.H. Hoffmann, E. Boggasch, J. Jacoby, H. Wahl, et al., *Charge state of fast heavy-ions in a hydrogen plasma*, Physical Review Letters, **69** (25), 3623-3626 (1992)
- [14] A. Golubev, M. Basko, A. Fertman, A. Kozodaev, N. Mesheryakov, et al., *Dense plasma diagnostics by fast proton beams*, Physical Review E **57** (3), 3363-3367, Part B (1998)
- [15] W.F. Henning, *The future GSI facility*, Nuclear Instruments & Methods in Physics Research Section B - Beam Interactions with Materials and Atoms **214**, 211-215 (2004)
- [16] D.H.H. Hoffmann, A. Blazevic, P. Ni, O. Rosmej, M. Roth, N.A. Tahir, et al., *Present and future perspectives for high energy density physics with intense heavy ion and laser beams*, Laser and Particle Beams **23** (1), 47-53 (2005)

- [17] D.H.H. Hoffmann, J. Jacoby, K. Zioutas, *Gravitational lensing by the sun of non-relativistic penetrating particles*, *Astroparticle Physics* **20** (1), 73-78 (2003)
- [18] D.H.H. Hoffmann, V.E. Fortov, I.V. Lomonosov, V. Mintsev, N.A. Tahir, et al., *Unique capabilities of an intense heavy ion beam as a tool for equation-of-state studies*, *Physics of Plasmas* **9** (9), 3651-3654 (2002)
- [19] D.H.H. Hoffmann, K. Weyrich, H. Wahl, D. Gardes, R. Bimbot, C. Fleurier, *Energy-loss of heavy-ions in a plasma target*, *Physical Review A* **42** (4), 2313-2321 (1990)
- [20] D.H.H. Hoffmann, K. Weyrich, H. Wahl, T. Peter, J. Meyer-ter-Vehn, et al., *Experimental-observation of enhanced stopping of heavy-ions in a hydrogen plasma*, *Zeitschrift für Physik A - Hadrons and Nuclei* **330** (3): 339-340 (1988)
- [21] H. Hora, *Developments in inertial fusion energy and beam fusion at magnetic confinement*, *Laser and Particle Beams* **22** (4), 439-449 (2004)
- [22] O. Iwase, W. Suss, D.H.H. Hoffmann, M. Roth, C. Stockl, M. Geissel, et al., *Laser-produced plasma diagnostics by a combination of Schlieren method and Mach-Zehnder interferometry*, *Physica Scripta* **58** (6), 634-635 (1998)
- [23] J. Jacoby, D.H.H. Hoffmann, W. Laux, R.W. Muller, H. Wahl, K. Weyrich, et al., *Stopping of heavy-ions in a hydrogen plasma*, *Physical Review Letters* **74** (9), 1550-1553 (1995)
- [24] J. Jacoby, D.H.H. Hoffmann, R.W. Muller, K. Mahrtolt, R.C. Arnold, et al., *Hydrodynamic motion of a heavy-ion-beam-heated plasma*, *Physical Review Letters* **65** (16), 2007-2010 (1990)
- [25] K.H. Kang, J.A. Maruhn, *Reduction of radiation asymmetry with radiation shields in indirectly driven inertial confinement fusion hohlraum targets*, *Fusion Technology* **31** (3), 251-264 (1997)
- [26] S. Neff, A. Tauschwitz, C. Niemann, D. Penache, D.H.H. Hoffmann, et al., *Gas density measurements with heavy ion beams*, *Journal of Applied Physics* (2003)
- [27] U. Neuner, R. Bock, M. Roth, P. Spiller, C. Constantin, U.N. Funk, et al., *Shaping of intense ion beams into hollow cylindrical form*, *Physical Review Letters* **85** (21), 4518-4521 (2000)
- [28] C. Niemann, F.B. Rosmej, A. Tauschwitz, S. Neff, D. Penache, et al., *Spectroscopic density and temperature measurements and modelling of a discharge plasma for neutralized ion-beam transport*, *Journal of Physics D - Applied Physics* **36** (17), 2102-2109 (2003)
- [29] M. Perry, G. Mourou, *Science* **64**, 917-924 (1994)
- [30] A.R. Piriz, M. Temporal, J.J.L. Cela, N.A. Tahir, D.H.H. Hoffmann, *Symmetry analysis of cylindrical implosions driven by high-frequency rotating ion beams*, *Plasma Physics and Controlled Fusion* **45** (9), 1733-1745 (2003a)

- [31] A.R. Piriz, N.A. Tahir, D.H.H. Hoffmann, M. Temporal, *Generation of a hollow ion beam: Calculation of the rotation frequency required to accommodate symmetry constraint* Physical Review E **67** (1), art. no.-017501, Part 2 (2003b)
- [32] A. Pukhov, J. Meyer-ter-Vehn, *Laser hole boring into overdense plasma and relativistic electron currents for fast ignition of ICF targets*, Physical Review Letters **79** (14), 2686-2689 (1997)
- [33] R. Ramis, J. Ramirez, J.J. Honrubia, J. Meyer-ter-Vehn, A.R. Piriz, J. Sanz, et al., *A 3 MJ optimized hohlraum target for heavy ion inertial confinement fusion*, Nuclear Instruments & Methods in Physics Research Section A - Accelerators Spectrometers Detectors and Associated Equipment **415** (1-2): 93-97 (1998)
- [34] U. Ratzinger, H. Liebermann, O. Meusel, H. Podlech, R. Tiede, et al., *High current ion beam RF acceleration and perspectives for an inertial fusion driver*, Laser and Particle Beams **21** (4), 627-632 (2003)
- [35] F.B. Rosmej, D.H.H. Hoffmann, W. Suss, A.E. Stepanov, Y.A. Satov, et al., *The generation of fast particles in plasmas created by laser pulses with different wavelengths*, Journal of Experimental and Theoretical Physics **94** (1), 60-72 (2002)
- [36] M. Roth, T.E. Cowan, M.H. Key, S.P. Hatchett, C. Brown, W. Fountain, et al., *Fast ignition by intense laser-accelerated proton beams*, Physical Review Letters **86** (3), 436-439 (2001)
- [37] M. Roth, C. Stockl, W. Suss, O. Iwase, D.O. Gericke, R. Bock, et al., *Energy loss of heavy ions in laser-produced plasmas*, Europhysics Letters **50** (1), 28-34 (2000)
- [38] M. Roth, W. Suss, M. Geissel, U.N. Funk, R. Bock, A. Tauschwitz, et al., *Heavy ion interaction experiments with plasmas*, Physica Scripta **T80A**, 40-42 (1999)
- [39] G. Schaumann, M.S. Schollmeier, G. Rodriguez-Prieto, A. Blazevic, E. Brambrink, M. Geissel, et al., *High Energy heavy ion jets emerging from laser plasma generated by long pulse laser beams from the NHELIX laser at GSI*, Laser and Part. Beams **23**, 503 (2005)
- [40] R.A. Snavely, M.H. Key, S.P. Hatchett, T.E. Cowan, M. Roth, T.W. Phillips, et al., *Intense high-energy proton beams from petawatt-laser irradiation of solids*, Physical Review Letters **85** (14), 2945-2948 (2000)
- [41] M. Tabak, D. Callahan-Miller, *Design of a distributed radiator target for inertial fusion driven from two sides with heavy ion beams*, Nuclear Instruments & Methods in Physics Research Section A - Accelerators Spectrometers Detectors and Associated Equipment **415** (1-2), 75-84 (1998)
- [42] N.A. Tahir, A. Adonin, C. Deutsch, V.E. Fortov, N. Grandjouan, B. Geil, et al., *Studies of heavy ion-induced high-energy density states in matter at the GSI Darmstadt SIS-18 and future FAIR facility*, Nuclear Instruments & Methods in Physics Research Section A - Accelerators Spectrometers Detectors and Associated Equipment **544** (1-2), 16-26 (2005a)

- [43] N.A. Tahir; B. Goddard, V. Kain, R. Schmidt, A. Shutov, I.V. Lomonosov, et al., *Impact of 7-TeV/c large hadron collider proton beam on a copper target*, Journal of Applied Physics **97** (8), art. no.-083532 (2005b)
- [44] N.A. Tahir, V. Kain, R. Schmidt, A. Shutov, I.V. Lomonosov, V. Gryaznov, *The CERN large hadron collider as a tool to study high-energy density matter*, Physical Review Letters **94** (13), art. no.-135004 (2005c)
- [45] N.A. Tahir, A. Kozyreva, P. Spiller, D.H.H. Hoffmann, A. Shutov, *Necessity of bunch compression for heavy-ion-induced hydrodynamics and studies of beam fragmentation in solid targets at a proposed synchrotron facility*, Physical Review E **6303** (3), art. no.-036407, Part 2 (2001a)
- [46] N.A. Tahir; D.H.H. Hoffmann, A. Kozyreva, A. Tauschwitz, A. Shutov, et al., *Metalization of hydrogen using heavy-ion-beam implosion of multilayered cylindrical targets*, Physical Review E **6302** (2), art. no.-016402, Part 2 (2001b)
- [47] N.A. Tahir, D.H.H. Hoffmann, A. Kozyreva, A. Shutov, J.A. Maruhn, U. Neuner, et al., *Equation-of-state properties of high-energy-density matter using intense heavy ion beams with an annular focal spot*, Physical Review E **62** (1), 1224-1233, Part B (2000a)
- [48] N.A. Tahir, D.H.H. Hoffmann, A. Kozyreva, J.A. Maruhn, U. Neuner, et al., *Hydrogen metallization in heavy-ion imploded multi-layered targets*, Journal de Physique IV **10** (P5), 327-330 (2000b)
- [49] M. Temporal, J.J.L. Cela, A.R. Piriz, N. Grandjouan, N.A. Tahir, D.H.H. Hoffmann, *Compression of a cylindrical hydrogen sample driven by an intense co-axial heavy ion beam*, Laser and Particle Beams **23** (2), 137-142 (2005)
- [50] M. Temporal, A.R. Piriz, N. Grandjouan, N.A. Tahir, D.H.H. Hoffmann, *Analysis of a multilayered cylindrical target compression driven by a rotating intense heavy ion beam*, Laser and Particle Beams **21** (4), 609-614 (2003)
- [51] D. Varentsov, N.A. Tahir, I.V. Lomonosov, D.H.H. Hoffmann, J. Wieser, V.E. Fortov, *Energy loss dynamics of an intense uranium beam interacting with solid neon for equation-of-state studies*, Europhysics Letters **64** (1), 57-63 (2003)
- [52] D. Varentsov, P. Spiller, U.N. Funk, D.H.H. Hoffmann, A. Kozyreva, N.A. Tahir, et al., *Time-resolved energy loss spectroscopy of energetic heavy ion beams generating a dense plasma*, Nuclear Instruments & Methods in Physics Research Section B - Beam Interactions with Materials and Atoms **174** (1-2), 215-221 (2001)
- [53] K. Zioutas, D.H.H. Hoffmann, K. Dennerl, T. Papaevangelou, *What is dark matter made of?*, Science **306** (5701), 1485-+ (2004a)
- [54] K. Zioutas, K. Dennerl, L. DiLella, D.H.H. Hoffmann, J. Jacoby, T. Papaevangelou, *Quiet-sun X-rays as signature for new particles*, Astrophysical Journal **607** (1), 575-579, Part 1 (2004b)